Studies of Lateral Dispersion in the Ocean

by

Miles Aaron Sundermeyer

B.A. University of California, Santa Cruz, 1991
M.S. Massachusetts Institute of Technology / Woods Hole Oceanographic Institution, 1995

Submitted in partial fulfillment of the
requirements for the degree of

DOCTOR OF PHILOSOPHY

at the

MASSACHUSETTS INSTITUTE OF TECHNOLOGY

and the

WOODS HOLE OCEANOGRAPHIC INSTITUTION

September 1998

Signature of Author .....
Joint Program in Physical Oceanography
Massachusetts Institute of Technology / Woods Hole Oceanographic Institution
August 7, 1998

Certified by .....
James R. Ledwell, Thesis Co-Supervisor
Associate Scientist, WHOI

Certified by .....
Kenneth H. Brink, Thesis Co-Supervisor
Senior Scientist, WHOI

Accepted by .....
W. Brechner Owens
Chairman, Joint Committee for Physical Oceanography
Massachusetts Institute of Technology / Woods Hole Oceanographic Institution

Studies of Lateral Dispersion in the Ocean

by

Miles Aaron Sundermeyer

Submitted in partial fulfillment of the requirements for the degree of
Doctor of Philosophy at the Massachusetts Institute of Technology
and the Woods Hole Oceanographic Institution
August 7, 1998

Abstract

This thesis is written in two parts. The first part deals with the problem of lateral dispersion due to mesoscale eddies in the open ocean, and the interaction between the mesoscale strain and horizontal diffusion on spatial scales less than 10 km. The second and major part examines lateral dispersion over the continental shelf on scales of 100 m to 10 km and over time scales of 1–5 days.

PART I: Lateral Dispersion and the North Atlantic Tracer Release Experiment

Mixing and stirring of Lagrangian particles and a passive tracer were studied by comparison of float and tracer observations from the North Atlantic Tracer Release Experiment. Statistics computed from the NATRE floats were found to be similar to those estimated by Ledwell et al. (1998) from the tracer dispersion. Mean velocities computed from the floats were $(\overline{u}, \overline{v}) = (-1.2\pm0.3,\ -0.9\pm0.2)$ cm s^{-1} for the (zonal, meridional) components, and large-scale effective eddy diffusivities were $(\kappa_{e11}, \kappa_{e22}) = (1.5\pm0.7,\ 0.7\pm0.4)\times10^3$ m^2 s^{-1}. The NATRE observations were used to evaluate theoretical models of tracer and particle dispersal. The tracer dispersion observed by Ledwell et al. (1998) was consistent with an exponential growth phase for about the first 6 months and a linear growth at larger times. A numerical model of mesoscale turbulence that was calibrated with float statistics also showed an exponential growth phase of tracer and a reduced growth for longer times. Numerical results further show that Garrett's (1983) theory, relating the effective small-scale diffusivity to the rms strain rate and tracer streak width, requires a scale factor of 2 when the observed growth rate of streak length is used as a measure of the strain rate. This scale factor will be different for different measures of the strain rate, and may also be affected by temporal and spatial variations in the mesoscale strain field.

PART II: Lateral Dispersion over the New England Continental Shelf

Lateral dispersion over the continental shelf was examined using dye studies of the Coastal Mixing and Optics (CMO) program. Four experiments performed at intermediate depths and lasting 3 to 5 days were examined. In some cases, the dye patches remained fairly homogeneous both vertically and horizontally throughout an experiment. In other cases, significant patchiness was observed on scales ranging from 2–10 m vertically and a few hundred meters to a few

kilometers horizontally. The observations also showed that the dye distributions were significantly influenced by shearing and straining on scales of 5–10 m in the vertical and 1–10 km in the horizontal. Superimposed on these larger-scale distortions were simultaneous increases in the horizontal second moments of the dye patches, with corresponding horizontal diffusivities based on a Fickian diffusion model of 0.3 to 4.9 $m^2\ s^{-1}$. Analysis of the dye data in concert with shear estimates from shipboard ADCP observations showed that the existing paradigms of shear dispersion and dispersion by interleaving water-masses can not account for the observed diffusive spreading of the dye patches. This result suggests that some other mechanisms provided an additional diffusivity of order 0.15 to 4.0 $m^2\ s^{-1}$. An alternative mechanism, dispersion by vortical motions caused by the relaxation of diapycnal mixing events, was proposed which could explain the observed dispersion in some cases. Order-of-magnitude estimates of the effective lateral dispersion due to vortical motions showed that this mechanism could account for effective horizontal diffusivities of order 0.01 to 1.1 $m^2\ s^{-1}$. The upper range of these estimates were within the range required by the observations for two of the four experiments examined.

Thesis Co-Supervisor: James R. Ledwell
Title: Associate Scientist, WHOI

Thesis Co-Supervisor: Kenneth H. Brink
Title: Senior Scientist, WHOI

Acknowledgments

The work in Part I relating to the North Atlantic Tracer Release Experiment was supported by the National Science Foundation under grant OCE90-05738. The work in Part II relating to the Coastal Mixing and Optics program was funded by the Office of Naval Research under grant N00014-95-1-0633 (tracer experiments) and grant N00014-95-1-1063 (AASERT fellowship). The support from these agencies is gratefully acknowledged.

Part I of this thesis represents work done in collaboration with Jim Price (Sundermeyer and Price, 1998; WHOI contribution number 9682). Many thanks to Jim for advising and supporting me during my first three years in the Joint Program. He and Phil Richardson were responsible for the Sound Fixing and Ranging (SOFAR) floats deployed during the North Atlantic Tracer Release Experiment. Chris Wooding and Marg Zemanovic did the initial processing of those data. The original code for the numerical model used in Part I was written by Bill Dewar and Glenn Flierl. Some additional code was also provided by Audrey Rogerson and Joe LaCasce. Sincerest thanks to Jim Ledwell, Andy Watson, and Cliff Law for sharing data from their tracer release experiment, and especially to Jim Ledwell for many stimulating discussions relating to that work.

Part II of this thesis would not have been possible without the dye experiments headed by Jim Ledwell as part of the Coastal Mixing and Optics (CMO) program. Many thanks to him for advising me during the last three years and for his encouragement and support; I have benefited greatly from his expertise and thoughtful advice. The CMO dye studies also benefited from much hard work by Tim Duda, Harvey Seim, Terry Donoghue, Cindy Sellers, Stew Sutherland, Chris Rehmann, Craig Marquette, Brian Connoly, Brian Guest, Scott Madin, Dave Ciochetto and the able crew of the R/V Oceanus. Thanks also to Tim Duda, Harvey Seim, Neil Oakey, and Chris Rehmann for insightful discussions about the data. The ADCP data discussed in Part II was processed by Harvey Seim. Much of the initial processing of the dye data was done by Stew Sutherland, and Cindy Sellers. Thanks also to Neil Oakey and Blair Greenan for sharing their microstructure data from the 1996 and 1997 CMO dye cruises and to others at the Bedford Institute, Nova Scotia who contributed to those efforts.

My co-advisor, Ken Brink, and thesis committee members, Glenn Flierl, Rocky Geyer, Jim Price, Paola Rizzoli, provided many useful discussions and comments on the written thesis. It has been a pleasure to learn from them and from the many other talented scientists and staff who work at WHOI and MIT. Thanks also to John Toole for chairing my thesis defense.

Many of my classmates in the Joint Program have also taught me a great deal over the last few years, including Jay Austin, Natalia Beliakova, Derek Fong, Lyn Harris, François Primeau, Jamie Pringle, Bill Williams, Melissa Bowen, and Gwyneth Packard. Thanks also to my friends in Woods Hole who made graduate student life even more enjoyable, especially Ewann and Gary Berntson, Gwyneth and Greg Packard, Craig Lewis, Rebecca Thomas, Jen Miksis, Bonnie Ripley, Diane Di Massa, Bill Williams, Sarah Zimmermann, and the underwater hockey and the ultimate Frisbee crowds.

Various parts of this thesis were proofread by Diane DiMassa, Sue Pittenger, Mary Ann Lucas, and Barbara Gaffron. Thanks especially to Diane for proofing nearly every page, and to Sue for much moral support during the final crunch of the writing.

Finally, thanks to my parents and to my siblings for their love and encouragement, and for impressing upon me that I can achieve anything that I set out to do. This thesis is dedicated to them.

Contents

Chapter 1

Introduction

Lateral dispersion in the ocean is not solely the result of molecular processes, but rather is significantly enhanced by shearing and straining on scales ranging from millimeters to hundreds of kilometers. The goal of this thesis is to understand the role of such motions in the open ocean and over the continental shelf, and to quantify their effects from the mesoscale down to scales of a few hundred meters.

The importance of lateral dispersion in the ocean ranges from its influence on climate to its role in distributing nutrients and microscopic organisms that are the base of the oceanic food chain. On basin scales the distributions of heat and salt are the fundamental driving forces for the thermohaline circulation. Thus the advection and diffusion of these quantities play a vital role in determining the Earth's climate. On smaller scales, lateral dispersion also sets the rate at which nutrients are distributed from their sources, such as river outflows and upwelling regions. Hence, on these scales, advection and diffusion also have a large influence on biological productivity.

The broad-reaching implications of lateral dispersion in the ocean have made it a widely explored field. However, our understanding of the mechanisms of dispersion in the ocean remain limited, partly due to the difficulty of making observations, and partly because of the complexity of the random and turbulent processes that are often encountered in oceanic

environments. Two powerful approaches which have made studies of oceanic dispersion more tractable are the use of Lagrangian tracers and floats. These provide means of examining the dispersal of marked fluid particles in an integral sense, which then allow direct estimates of dispersion at the scales of interest.

In this thesis, tracer- and float-release studies from the North Atlantic Tracer Release Experiment (NATRE) and from the Coastal Mixing and Optics (CMO) dye studies are used to examine the rates and mechanisms of lateral dispersion in the ocean. In Part I, the rates of lateral dispersion in the open ocean due to mesoscale stirring are estimated from Lagrangian floats released as part of NATRE. Dispersion rates on scales ranging from 1–10 km up to 1000 km are shown to agree with the theoretical model of Garrett (1983) for mixing and stirring by the mesoscale strain field. In Part II, lateral dispersion on scales of a few hundred meters to 10 km is examined using the CMO dye experiments. It is shown that the existing paradigms of lateral dispersion by vertical shear dispersion, lateral intrusions of differing water-masses, and diffusive interleaving cannot explain the observed dispersion based on dye experiments. An alternative mechanism, dispersion by vortical motions caused by the relaxation of diapycnal mixing events is shown to be consistent with the observations and in some cases may explain the observed dispersion.

For each part of this thesis, separate introductions and conclusions will be given. The final chapter of the thesis will then provide a synthesis of the two separate studies.

Part I

Lateral Dispersion and the North Atlantic Tracer Release Experiment

Chapter 2

Observations and Numerical Simulations of Lagrangian Particles and a Passive Tracer [1]

2.1 Introduction

The kinematics of tracer dispersal provides a basis for describing the distribution of natural and anthropogenic tracers in the ocean. In this paper we examine the horizontal dispersion of a localized tracer observed during the North Atlantic Tracer Release Experiment (NATRE). Our goal is to understand what these observations can tell us about both small and large-scale advective and diffusive processes in the ocean.

2.1.1 Stirring and Mixing in a Turbulent Ocean

To begin, it is helpful to imagine that tracer dispersal is a combination of two different types of processes: "mixing" processes, which act to reduce tracer gradients, and "stirring" processes,

[1] This chapter to appear in slightly modified form as: Sundermeyer, M. A. and J. F. Price, 1998. Lateral mixing and the North Atlantic Tracer Release Experiment: Observations and numerical simulations of Lagrangian particles and a passive tracer. *J. Geophys. Res.* In press. Reprinted with permission; copyright by the American Geophysical Union.

which act to increase tracer gradients [*Eckart*, 1948]. Put another way, "mixing" processes are those which can (or must) be modeled by diffusion, i.e., molecular or very small-scale advective processes in which individual exchange events are not resolved, while "stirring" processes are resolved events, e.g., the streaking and folding of tracer within a resolved eddy field. The distinction between these two types of processes is in practice one of small versus large scale, or, in a modeling context, sub-gridscale parameterized motions versus resolved motions.

Classical theory can predict the rate of tracer dispersal in the presence of a purely diffusive and very simple advective process [e.g., *Fischer et al.*, 1979]. However, when shearing and straining occur on different scales, as in a turbulent ocean, the analysis is far more complex, and models must be built with uncertain approximations.

Consider the fate of a localized release of passive tracer into a turbulent ocean. A useful simplification, suggested by *Garrett* [1983], is to model the dispersal of tracer in three distinct stages. During the first stage, while the scale of the tracer patch is much smaller than that of the straining eddies, the patch growth can be modeled as a mixing or diffusive process. For such times, assuming a patch radius of 2σ, where σ^2 is the patch variance, the area, A, occupied by the tracer will grow linearly in time, i.e.,

$$A = 8\pi\kappa_s t, \tag{2.1}$$

where κ_s is an effective small-scale diffusivity. *Young et al.* [1982] predicted that the magnitude of this small-scale diffusivity is of order $\kappa_s \approx (N^2/f^2)\kappa_z$, where N is the buoyancy frequency, f is the Coriolis parameter, and κ_z is the vertical diffusivity. For the NATRE region, *Ledwell et al.* [1998] found that this prediction yields $\kappa_s \approx 0.08$ m^2 s^{-1}, and was consistent with the initial dispersion of their tracer injection streaks.

As the size of the patch grows, it will eventually reach a size where the mesoscale strain field begins to advect the tracer into long thin streaks. (For a point release, this will occur after time $t \approx \frac{1}{2\gamma_{\rm rms}}$, where $\gamma_{\rm rms}$ is the rms mesoscale strain rate.) The rate of dispersal may then accelerate

to a second stage in which the streak length, L, grows exponentially in time, $L = L_o e^{\lambda t}$, where $L_o = 2\sqrt{\kappa_s/\gamma_{\rm rms}}$ is the transition scale of the patch. *Garrett* [1983] presumed that the streak growth rate, λ, should be nearly equal to the rms strain rate, i.e., $\lambda = \alpha\gamma_{\rm rms}$, where α is an order one coefficient to be determined. Meanwhile, the width of the streaks is presumed to be set by a balance between the narrowing tendency of the convergent strain field and the small-scale diffusion or mixing, which acts to widen the streak, i.e., $\sigma^2_{\rm rms} = \kappa_s/\gamma_{\rm rms}$, where $\sigma^2_{\rm rms}$ is the rms cross-streak variance. (Given observations from a tracer release experiment such as NATRE, $\gamma_{\rm rms}$ cannot be measured directly and must be inferred from the streak growth rate, which is the only accessible measure of strain.) During the second stage of dispersal, based on this combination of along- and cross-streak dynamics, the tracer area is expected to grow exponentially in time,

$$A = 4\pi(\kappa_s/\gamma_{\rm rms})e^{[\alpha\gamma_{\rm rms}(t-\frac{1}{2}\gamma_{\rm rms}^{-1})]} \tag{2.2}$$

(this follows equation 2.3 of *Garrett* [1983], except for the leading factor of 4 in our result and a factor of 1/2 in the exponent rather than 1/4 which arise from different definitions of length and time scales).

Exponential growth will continue until the horizontal scale of the tracer patch exceeds that of the mesoscale eddies. At that time, the tracer dispersal enters a third stage in which continued stirring by the eddies causes streaks to wrap around one another, eventually making the patch more homogeneous. Subsequently, for times much longer than the Lagrangian integral time scale (about 10 days; see below for definition), the rate of dispersal of the patch as a whole may again be modeled as a diffusive process, with area increasing linearly in time,

$$A = 8\pi\kappa_e t, \tag{2.3}$$

where κ_e is the effective eddy diffusivity due to the mesoscale eddies, and is typically of order 10^3 m^2 s^{-1}.

This framework has proven useful for describing tracer dispersal in numerical models. For

example, simulations by *Haidvogel and Keffer* [1984] showed rapid development of tracer streaks that were consistent with an exponential growth (see section 2.5 for further discussion of their definition of the rms strain rate). Their simulations also showed an initial increase in small-scale tracer variance, possibly corresponding to the initial sharpening of tracer gradients by the mesoscale strain, followed by a slow smooth decay, consistent with the expected transition to diffusive spreading for large times. The evolution of a continuous tracer with a large-scale concentration gradient has been studied by *Holloway and Kristmannsson* [1984] who showed that an effective eddy-diffusivity formulation can also be used in that case, and that such a diffusivity agrees with simple mixing length arguments. The idea of an effective eddy diffusivity is also supported by numerous observational studies of Lagrangian particle dynamics, [*e.g., Freeland et al.*, 1975; *Colin de Verdiere*, 1983; *Davis*, 1985]. The relationship between Lagrangian particle and passive tracer has also been discussed, for example, by *Davis* [1983, 1987] and *Bennett* [1987]. These studies have furthered our understanding of how tracer and particle dispersal would be influenced by turbulent stirring; however, until recently there had been little opportunity to compare them directly with oceanic observations of a localized release of passive tracer.

2.1.2 Goals and Outline

The 1992 North Atlantic Tracer Release Experiment (NATRE) provided unique observations of the dispersal of a passive tracer and Lagrangian particles in open-ocean conditions. A thorough description of the lateral dispersion characteristics of the tracer was provided by *Ledwell et al.* [1998]. In the present work, we examine particle statistics computed from the NATRE float data and use both the tracer and float data in conjunction with a numerical model to study lateral mixing and stirring in the open ocean. We address three questions:

1) How do the statistics computed from the NATRE float data compare with similar statistics computed from the NATRE tracer data?

2) Is *Garrett's* [1983] model of a three-stage tracer dispersal qualitatively consistent with

the observed dispersion rates estimated from the NATRE field experiment?

3) What are the biases and uncertainties associated with using *Garrett's* [1983] model to make quantitative estimates of the strain rate, streak width, and small-scale diffusivity?

In section 2, we introduce some statistical tools for quantifying the dispersal and diffusion of Lagrangian particles and passive tracer. Section 3 provides an overview of the NATRE experiment and the tracer results along with a statistical description of the float dispersal. Also in section 3, we address questions 1 and 2 by examining the observations in the context of the initial streakiness of a passive tracer and the concept of effective eddy diffusivity for long times [*Garrett*, 1983; *Taylor*, 1921]. In section 4, we introduce a numerical model which is used to simulate tracer and float dispersal. We show that the simulated tracer behavior is qualitatively consistent with the theoretical model of *Garrett* [1983]. Question 3 is then addressed using our numerical results as a quantitative test of *Garrett's* [1983] scaling arguments. In section 5, we offer a discussion of the possible biases and uncertainties associated with applying this scaling to a temporally and spatially varying strain field. Finally, in section 6 we summarize our results and their implications for the NATRE field study.

2.2 Theoretical Background

2.2.1 The Formation of Tracer Streaks

In the present study, we are particularly interested in the second and third stages of dispersal, when the tracer is under the influence of the mesoscale strain field. Consider a patch made up of fully developed tracer streaks that have not yet begun to merge. During this second stage of dispersal, *Garrett* [1983] suggested that the mean streak width is set by a balance between the strain rate and small-scale diffusivity, and that the growth of the area of the tracer patch should scale as the product of the along-streak growth rate times the mean streak width. For the purpose of quantitative diagnosis, e.g., using observed streak length and width to estimate strain rate and small-scale diffusivity [*Ledwell et al.*, 1993, 1998], we now examine an exact

solution to the advection-diffusion equation and consider the effects of time dependence on this result.

Consider the case of a two-dimensional linear strain field in which the strain rate, $\gamma = \partial u/\partial x = -\partial v/\partial y$, is allowed to vary in time, but not in space (spatial dependence and eddy diffusivity are discussed in the next subsection). Furthermore, assume that small-scale dispersion processes can be parameterized in terms of an effective diffusivity, κ_s. In this case, the concentration of tracer θ can be described by the familiar advection-diffusion equation,

$$\frac{\partial \theta}{\partial t} + \gamma x \frac{\partial \theta}{\partial x} - \gamma y \frac{\partial \theta}{\partial y} = \kappa_s \nabla^2 \theta. \tag{2.4}$$

If we assume an initial condition for θ which is Gaussian in x and y (as might result from a purely diffusive process at scales small compared to the strain field), the concentration as a function of space and time can be expressed as

$$\theta = \theta_m(t) e^{\left(-\frac{x^2}{2\sigma_x^2} - \frac{y^2}{2\sigma_y^2}\right)}, \tag{2.5}$$

where the along- and cross-streak variances, σ_x^2 and σ_y^2, are governed by

$$\frac{d\sigma_x^2}{dt} - 2\gamma\sigma_x^2 = 2\kappa_s, \tag{2.6}$$

and

$$\frac{d\sigma_y^2}{dt} + 2\gamma\sigma_y^2 = 2\kappa_s, \tag{2.7}$$

respectively. $\theta_m = M/\sigma_x\sigma_y$ is the peak concentration, with M equal to the total mass of tracer, and $\gamma > 0$ is assumed (this analysis is similar to that of *Townsend*, 1951).

For a small initial patch, $\sigma_x, \sigma_y \ll \sqrt{\kappa_s/\gamma}$, and for small times, the effects of the strain are negligible, and (2.6) and (2.7) reduce to the diffusive limit which characterizes stage one. For longer times when the strain is important, a temporal average of (2.7) shows that the

cross-streak variance satisfies

$$\langle \gamma \sigma_y^2 \rangle = \langle \gamma \rangle \langle \sigma_y^2 \rangle + \langle \gamma' \sigma_y^{2'} \rangle = \kappa_s, \tag{2.8}$$

where primed variables represent fluctuations about the mean values, and we have assumed $\langle d\sigma_y^2/dt \rangle = 0$, which may apply following a tracer parcel in a stationary turbulent flow. Meanwhile, in the along-streak direction, (2.6) is satisfied by the general solution

$$\sigma_x^2 = \sigma_{xo}^2 e^{2\Gamma} + e^{2\Gamma} \int_0^t 2\kappa_s e^{-2\Gamma} dt, \tag{2.9}$$

with the exponential growth rate $\Gamma = \int_0^{t'} \gamma(t) dt$. If we identify $4\sigma_y$ as the streak width, and $4\sigma_x$ as the streak length, in the limiting case of steady γ, (2.8) and (2.9) are similar to *Garrett's* [1983] equation 2.3 for the second stage of dispersal.

There are two points to be made regarding this solution. First, even after neglecting spatial dependence of the strain rate, (2.8) suggests that the strain rate and the streak width may hold a more subtle relationship than scaling arguments alone can reveal. For example, in this case there is a covariance term generated by the product of γ and σ_y^2. Second, if we intend to use *Garrett's* [1983] results for quantitative purposes, then we must define an appropriate measure of the strain rate and streak width for tracer in a fully turbulent flow. These two points lie near the heart of this study, and will be discussed in some detail in section 2.5.

2.2.2 Particle Dispersal and Effective Eddy Diffusivity

During the third stage of tracer dispersal, the concept of effective eddy diffusivity can be applied based on statistical considerations of particle dispersal in a turbulent flow [*Taylor*, 1921]. We now define a number of statistical quantities which will be useful in later sections to characterize the large-scale flow field. In what follows, we assume an unbounded ocean which is horizontally homogeneous and statistically stationary over the scales of interest. This ocean has been seeded with a large number of Lagrangian particles or neutrally buoyant floats.

Given such an ensemble of Lagrangian particles, a measure of the spatial and temporal scales of the flow can be obtained from the spatial correlation functions (SCFs) and Lagrangian auto-correlation functions (LACFs), respectively. The isotropic SCFs, $S_{ii}(\xi)$, are defined as

$$S_{ii}(\xi) = \frac{\langle v_i'(d) v_i'(d+\xi) \rangle}{\overline{\langle v_i'^2 \rangle}}, \tag{2.10}$$

where ξ is the separation distance from an arbitrary position, d, and v_i' $(i = 1, 2)$ represent the transverse and longitudinal components of velocity, respectively. The double subscripts $ii = [11, 22]$ denote [transverse, longitudinal] spatial correlation functions. Angled brackets denote averages for an ensemble of Lagrangian particles, while the over-bar denotes a temporal average.

The LACFs, $R_{ii}(\tau)$, are defined as

$$R_{ii}(\tau) = \frac{\langle u_i'(t) u_i'(t+\tau) \rangle}{\overline{\langle u_i'^2 \rangle}}, \tag{2.11}$$

where τ is the time lag from an arbitrary time, t, and u_i' $(i = 1, 2)$ now represent zonal and meridional components of the Lagrangian velocity. The double subscripts $ii = [11, 22]$ denote [zonal, meridional] auto-correlation functions. The characteristic or integral time scale is rigorously defined as

$$I_{ii} = \int_0^\infty R_{ii}(\tau) d\tau, \tag{2.12}$$

provided this integral converges (for isotropic turbulence, $I_{11} = I_{22}$).

Taylor [1921] showed how to estimate large scale stirring from Lagrangian observations. Given the assumptions above and assuming the motion has zero mean, the mean squared particle displacement, i.e., the dispersion, is related to the eddy kinetic energy through the exact relation

$$\langle x_i'^2(t) \rangle = 2\overline{\langle u_i'^2 \rangle} \int_0^t \int_0^T R_{ii}(\tau) d\tau dT. \tag{2.13}$$

(In what follows, the mean eddy kinetic energy, EKE, is defined as $\frac{1}{2}\overline{\langle u_i'^2 \rangle} = \frac{1}{2}\overline{\langle u_1'^2 + u_2'^2 \rangle}$.) If

τ is small, R_{ii} does not differ appreciably from unity, and (2.13) simplifies to

$$\langle x_i'^2(t)\rangle = \overline{\langle u_i'^2\rangle}\, t^2, \tag{2.14}$$

which says that the dispersion is proportional to the time since release squared and the eddy kinetic energy. For long times R_{ii} should approach zero in a turbulent flow, so that the first integral in (2.13) becomes saturated,

$$\int_0^T R_{ii}(\tau)d\tau = I_{ii} = \text{const}, \tag{2.15}$$

and (2.13) reduces to

$$\langle x_i'^2(t)\rangle = 2\overline{\langle u_i'^2\rangle} I_{ii} t = 2\kappa_{e_{ii}} t. \tag{2.16}$$

Thus for long times particles disperse at a constant rate which is proportional to the mean squared eddy velocity and the integral time scale of the turbulence. This constant rate of dispersion, $\kappa_{e_{ii}} = \overline{\langle u_i'^2\rangle} I_{ii}$, defines the effective eddy diffusivity of a stationary homogeneous turbulent flow, and corresponds to stage three of *Garrett's* [1983] model. (The limit of small τ in Taylor's single particle theory has no direct analog in Garrett's model.)

2.3 Observations

The NATRE field experiment was performed in an open ocean region 1,200 km west of the Canary Islands. The main experiment involved the controlled release in May 1992 of the passive tracer sulfur hexafluoride, SF_6, along a target density surface within the main pycnocline [*Ledwell et al.*, 1993, 1998]. The subsequent tracer concentration was observed over a series of sampling cruises with the primary objectives of estimating the diapycnal diffusivity across the main pycnocline and studying lateral mixing and stirring on scales from 10 km to 1000 km in the open ocean. The latter is the focus of the present study. In conjunction with the tracer, ten neutrally buoyant SOund Fixing and Ranging (SOFAR) floats were also released to help track

the tracer and to characterize the large-scale velocity field. The floats were pre-programmed to spend the majority of their time at nearly the same depth as the tracer, and were tracked for up to one year following deployment, thus allowing simultaneous observation of a passive tracer and Lagrangian particles.

2.3.1 NATRE Tracer

The tracer injection performed in May 1992 consisted of a series of closely spaced streaks in an area approximately 400 ($\pm$100) km^2 in horizontal extent [*Ledwell et al.*, 1998]. The target surface had a potential density of $\sigma_{0.3} = 28.05$, which corresponded to a depth of approximately 310 m. Sampling of the tracer began immediately after its release and was conducted on five cruises spanning $2\frac{1}{2}$ years. Sampling was performed during the 2 weeks after release, 5 and 6 months later (October to November 1992), 1 year after release (April to May 1993), and $2\frac{1}{2}$ years after release (November 1995). A thorough analysis of the injection and subsequent dispersal of the tracer is given by *Ledwell et al.* [1998], and we discuss some of their results here, as they relate closely to our numerical simulations in section 2.4.

The horizontal distribution of tracer observed during the first 6 months is shown in Figure 2.1. This series of "snap-shots," as measured by the NATRE sampling cruises, provides a vivid image of mixing and stirring in the open ocean. Of notable interest is the streak-like character of the tracer distribution observed during the October and November 1992 surveys. There appeared to be two significant length scales which characterized the tracer distribution at this time. One was the radius of curvature of the streaks, which was set by the dominant length scale of the mesoscale eddies. The second was the rms width of the streaks, which was presumably set by a balance between the effective small-scale diffusion (on scales less than the streak width) and the mesoscale strain.

The ideas of section 2.1.1 may be applied to the NATRE observations in order to estimate an effective small-scale diffusivity, κ_s. Assuming that after 6 months the entire tracer patch was distributed in streaks similar to those observed, an exponential growth of streaks, $L = L_o e^{\lambda t}$,

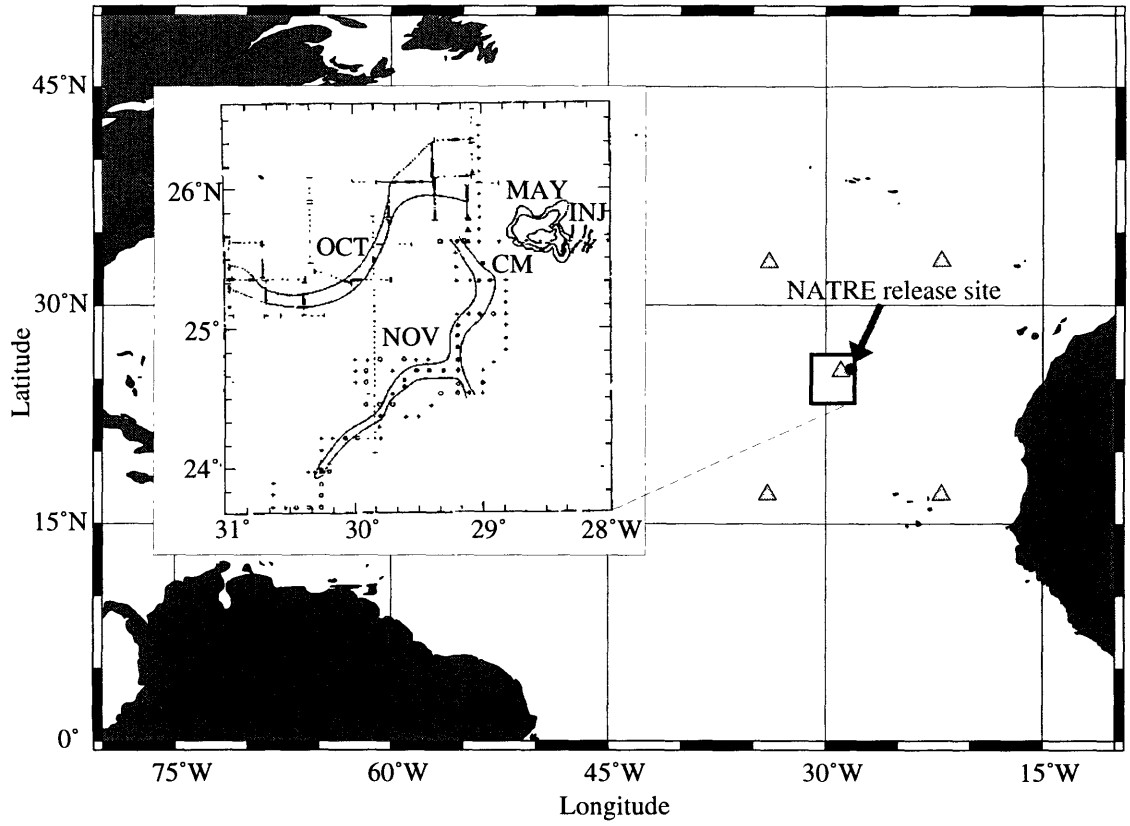

Figure 2.1: Horizontal distribution of tracer, expressed as the depth-integrated concentration, for the first 6 months of NATRE. The inset (taken from *Ledwell et al.*, [1993]) shows the location of the initial tracer injection streaks (marked INJ), contours of tracer 2 weeks after injection (marked MAY), and the two streaks observed in Fall 1992 (marked OCT, NOV). The triangles are the locations of the five Subduction moorings.

implied a streak growth rate of $\lambda \approx 3 \times 10^{-7}$ s^{-1}. Given the observed rms cross-streak width of $\sigma_{\rm rms} \approx 3$ km, and using λ as a proxy for the rms strain rate, (i.e., $\gamma_{\rm rms} = \lambda$ exactly), the cross-streak balance between the strain rate and cross-streak diffusivity, $\kappa_s = \sigma^2_{\rm rms}\lambda$, yielded an effective small-scale (less than 10 km) lateral diffusivity of $\kappa_s \approx 3$ m^2 s^{-1}. As discussed by *Ledwell et al.* [1993, 1998], this value of κ_s can be compared to that predicted for shear dispersion by internal waves, $\kappa_s \approx 0.08$ m^2 s^{-1}, that is presumed to act on scales of order 100 m [*Young et al.*, 1982]. The forty-fold discrepancy between these estimates of κ_s is intriguing and suggests that there was some horizontal mixing process acting at scales of order 1–10 km

which was not anticipated by *Young et al.* [1982]. This result is based on the assumption that the exponential growth of tracer streaks and the approximate cross-streak balance between the convergent strain field and small-scale diffusion described by *Garrett* [1983] are valid in a fully turbulent flow. Numerical results discussed in section 2.4 support these assumptions.

Ledwell et al. [1998] further reported that by May 1993 the tracer patch had become much more filled in compared to Fall 1992 surveys. Hence for the May 1993 and November 1994 surveys they estimated a large-scale effective eddy diffusivity, κ_e, using the relation $2\kappa_e = \partial\sigma^2/\partial t$ where σ^2 now represents the large-scale variance of the tracer patch. From this they obtain an effective eddy diffusivity of $\kappa_e \approx 1 \times 10^3$ m^2 s^{-1}, a value consistent with estimates based on single particle dispersion rates computed below from the NATRE float data.[2]

At this point it is interesting to compare the qualitative nature of the NATRE tracer dispersal to the theoretical predictions of section 2.1.1 (Figure 2.2). For the exponential growth phase, consistent with *Ledwell et al.* [1993, 1998], we use a small-scale diffusivity $\kappa_s = 3$ m^2 s^{-1}, and use λ as a proxy for the rms strain rate, $\gamma_{\rm rms} = \lambda = 3 \times 10^{-7}$ s^{-1}. For the linear growth phase at large times, we assume for simplicity an isotropic large-scale eddy diffusivity $\kappa_e = 1 \times 10^3$ m^2 s^{-1} (see above). To account for the finite size of the initial NATRE tracer patch, we plot the observations with a time offset of approximately 40 days, which corresponds to the time it would take for a point release of tracer to obtain an along-streak scale equal to that of the NATRE initial condition, *i.e.*, $2\sigma = \sqrt{400 \text{ km}^2/\pi} = 11$ km.

Comparison of the patch area estimates of *Ledwell et al.* [1998] with the theoretical predictions suggests that the lateral dispersal of the NATRE tracer was consistent with an exponential growth phase followed by a linear growth at large times. The correspondence of these two growth regimes with the observed streakiness and later homogenization of tracer is the most

[2]The mean drift of the center of mass of the tracer patch was also estimated by *Ledwell et al.* [1998] from the May 1993 tracer distribution. The mean westward component inferred from the tracer data was consistent with flow estimates from hydrographic data, while the southward component inferred from the tracer was somewhat smaller. That there were only minor discrepancies between these Lagrangian and Eulerian estimates suggests that the movement of the center of mass of tracer was primarily due to an Eulerian mean flow, and not Lagrangian effects such as might arise from a large-scale gradient in eddy diffusivity [*Freeland et al.*, 1975].

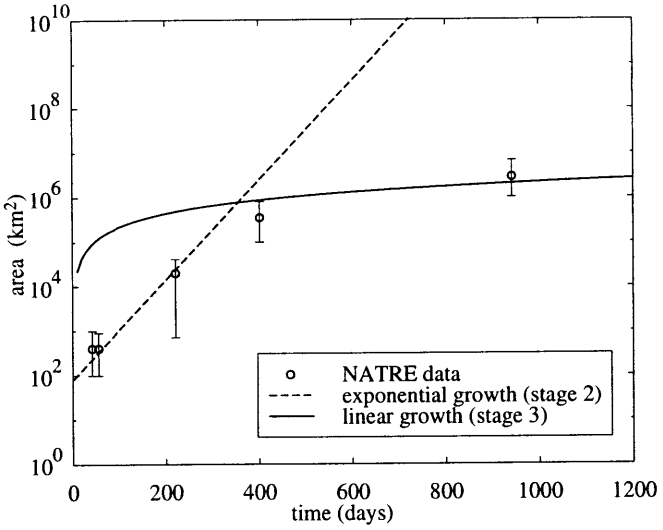

Figure 2.2: Exponential (dashed lines) and linear (solid lines) growth phases (stages 2 and 3 of section 1) of tracer area for a theoretical point release of passive tracer in a turbulent flow and for the five sampling periods of NATRE (open circles). Theoretical curves are for $\kappa_s = 3$ m^2 s^{-1}, $\gamma_{\rm rms} = 3 \times 10^{-7}$ s^{-1}, and $\kappa_e = 1 \times 10^3$ m^2 s^{-1}. Patch area estimates for the NATRE data were taken from *Ledwell et al.* [1998] and have been plotted with a time offset as described in the text.

persuasive observational evidence in support of *Garrett's* [1983] model.

2.3.2 NATRE Floats

The ten SOFAR floats released during NATRE were deployed along with the tracer in May 1992 and were tracked for up to 1 year after deployment, providing a total of about 57 float months of data (Figure 2.3). Each float was pre-programmed to make daily excursions through a portion of the water column, while spending the majority of the day at a depth approximately equal to that of the tracer target density surface. The floats were tracked acoustically, with fixes of their positions given twice per day by an array of moored listening stations. Zonal and meridional velocity components were computed from the float positions using a cubic spline interpolation method.

All of the 10 NATRE floats provided reasonable velocity data during the time that they were transmitting, although two of the floats apparently experienced failure of either their

pressure or temperature sensors. It is possible that these two floats settled to a deeper level than did the others; however, based on EKEs computed from individual float records, it does not seem that they were in a less energetic portion of the water column. We thus retain these data in our statistical analysis (in any case, the inclusion or exclusion of these data does not alter the main results of this study).

For the purpose of computing ensemble statistics, the ten NATRE floats provided a somewhat limited sampling of the Lagrangian flow. Therefore, in the following analysis, we also incorporate data from four SOFAR floats of the Subduction Experiment which were deployed about 600 km northeast of the NATRE site in May 1991. The Subduction floats were of the same type as those used in NATRE except that they were equipped to transmit data for 2 years after deployment. The four floats of interest provided a total of 84 float months of data and were advected to the southwest through the site of the NATRE experiment slightly above the target density surface between May 1991 and May 1993 (Figure 2.3). Based on XBT profiles taken during the Subduction mooring deployment cruises [*Trask and Brink*, 1993], the average depths of these four Subduction floats were 285 m, 155 m, 170 m, and 170 m. Although three of these four Subduction floats were at shallower depths than the NATRE floats, we include them in our analysis in an attempt to obtain more robust statistics. It is possible that we thus bias our statistics (EKEs of each of the four Subduction floats were about 2 times larger than the NATRE floats); however, this should not affect the major results of this study, which depend on the comparison of numerical model results with theoretical predictions of tracer dispersal. A more detailed analysis of the combined float data set was given by *Sundermeyer* [1995].

Mean velocities computed from the full float data set are $(\overline{u}, \overline{v}) = (-1.2 \pm 0.3,\ -0.9 \pm 0.2)$ cm s^{-1}, while the zonal and meridional components of the combined time and ensemble-averaged EKE are $\frac{1}{2}\overline{\langle u'^{2}_{(1,2)} \rangle} = (8.1 \pm 1.0,\ 8.0 \pm 0.9)$ cm^2 s^{-2}. Errors on means are given by the square root of the variance divided by the number of degrees of freedom, where the number of

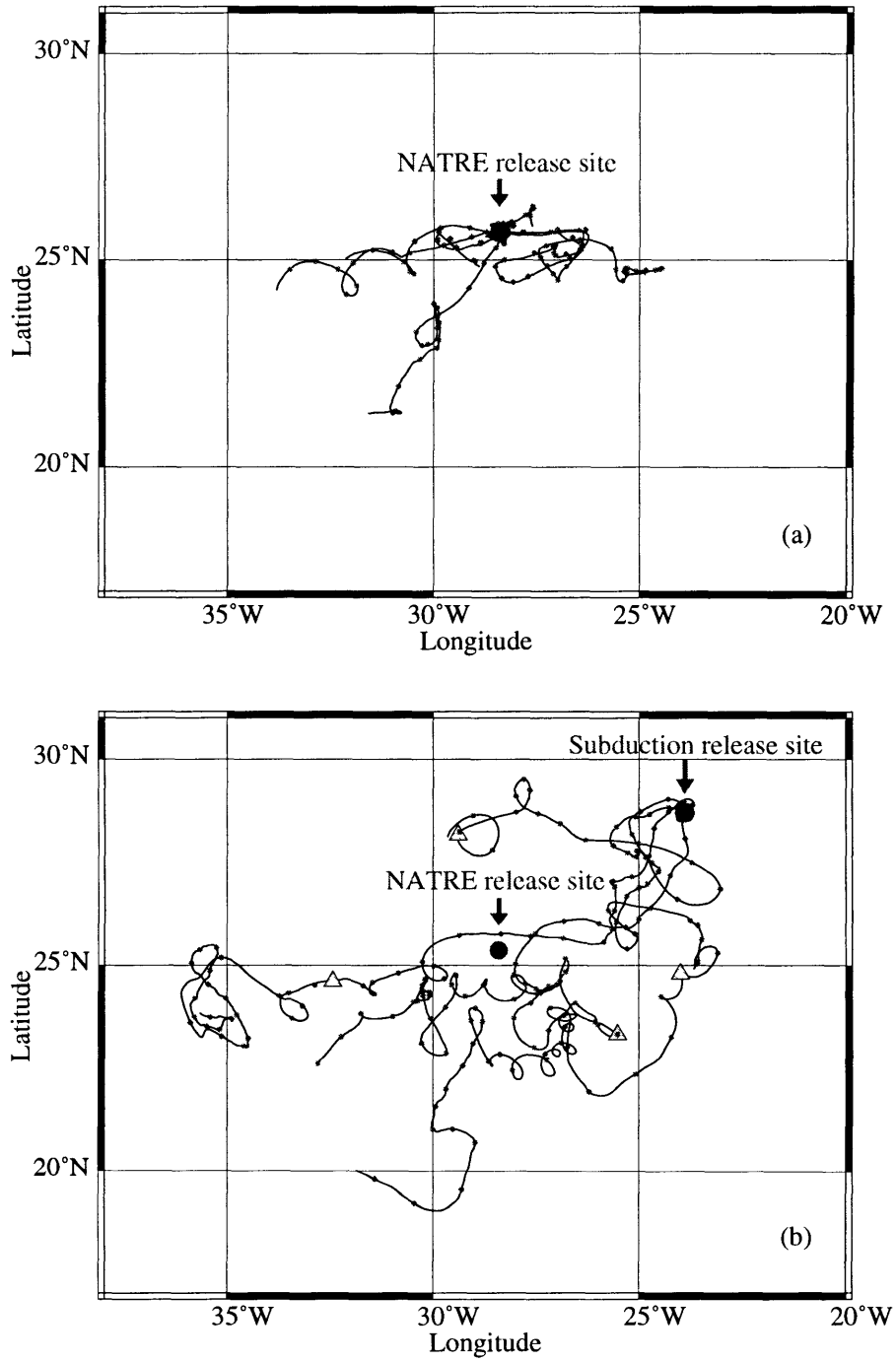

Figure 2.3: Float trajectories for (a) 1992–1993 NATRE floats (tr55–64) and (b) 1991–1993 Subduction floats (sb14,15,19,26). Triangles mark the locations of the four Subduction floats at the time of the NATRE release. Tick marks along trajectories correspond to 30 day intervals since release.

degrees of freedom is computed as the record length divided by twice the integral time scale ($[I_{11}, I_{22}] \approx [10.6, 5.4]$ days, see below).[3] The mean velocities computed from the float data are roughly in agreement with those estimated above from the tracer data, suggesting that the floats and tracer were advected similarly.

The ensemble-averaged particle dispersion, $\langle x_i'^2(t) \rangle$, is plotted in Figure 2.4. In the limits of small and large t, the curves are roughly consistent with the predicted t^2 and t growth rates, respectively. For small times (2.14) implies that on a log–log plot of dispersion *vs.* time the EKE should be given by the height of the dispersion curves (i.e., it is proportional to the slope of these curves for small times). Figure 2.4 thus suggests EKE values of $\frac{1}{2}\overline{\langle u'^2_{(1,2)} \rangle} = (2.6 \pm 3.0,\ 2.4 \pm 4.7)$ cm^2 s^{-2}, where the uncertainty is computed as the square root of the variance divided by the number of independent pieces of data. The fact that values of EKE are somewhat lower than those made from the full record may reflect a bias at small t; that is, the floats may have been released into a flow feature which was less energetic than the average flow (see footnote 3). Since the above direct estimates of EKE utilize the full data record, and hence limit such bias by incorporating a larger number of degrees of freedom, we use those to compute the eddy diffusivities below.

For long times (2.16) suggests that the diffusivities, $\kappa_{e_{ii}}$, can be estimated by the slope of the dispersion curves. A weighted least squares fit (on a linear-linear scale) between $t = 100$ and $t = 400$ days, where the dispersion at time t is weighted by the variance in the mean, σ_i^2, yields $\kappa_{e_{(11,22)}} = (5.9 \pm 2.3,\ 1.9 \pm 0.7) \times 10^3$ m^2 s^{-1}. These estimates of κ_e are approximately 2–6 times larger than those estimated above from tracer distributions in Spring 1993 and Fall 1994. This discrepancy may be a result of the small number of independent float observations used in the calculation (see previous paragraph). We suspect this because estimates of κ_e based on the product of the integral time scale and EKE (see below) give closer agreement

[3]Ensemble means were computed under the assumption that each float represented an independent particle. This seems sensible, except for times shortly after release when floats are likely to be within the same flow features and behave in a spatially coherent fashion. Thus we may have slightly (by less than about 30%) overestimated the number of degrees of freedom.

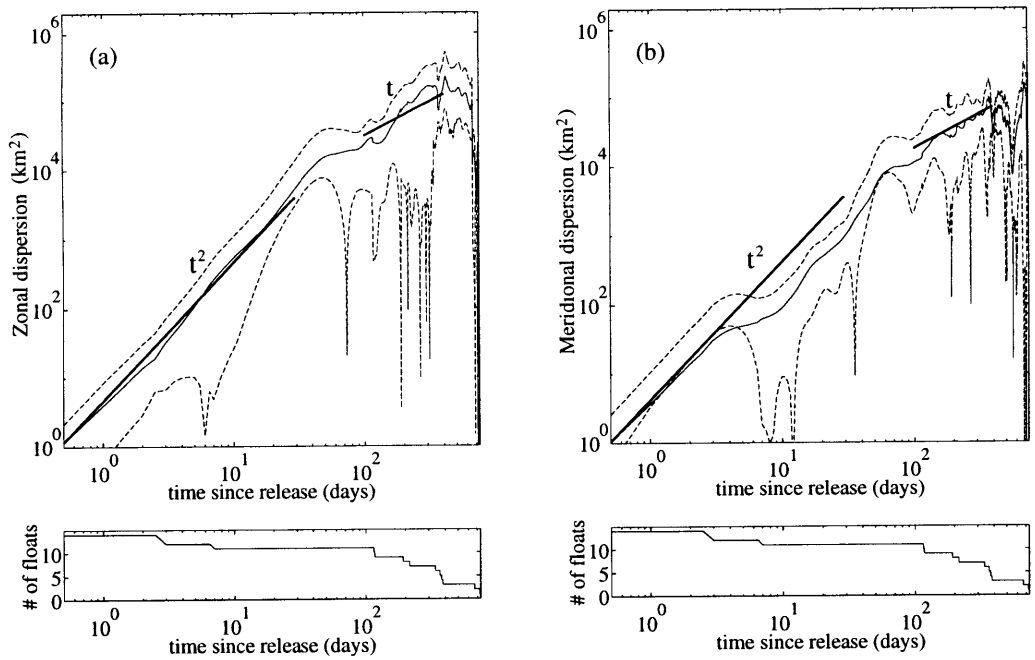

Figure 2.4: Time dependent (a) zonal and (b) meridional ensemble-averaged single particle dispersion, $\langle x_i'^2(t) \rangle$, computed from NATRE and Subduction floats showing t^2 and t growth rates for short and long times, respectively. Solid lines are dispersion curves while dashed lines indicate the uncertainty. Bold solid lines indicate t^2 and t growth rates. Lower panels show the number of floats as a function of time that made up the ensemble averages.

with values estimated from tracer distributions.

Spatial and Lagrangian auto-correlation functions were computed from the float data according to the definitions given in section 2.2.2 (Figure 2.5). The first zero crossing of the transverse correlation function occurs at approximately 70 km, which is, not surprisingly, roughly comparable to the diameter of the loops formed by the float trajectories in Figure 2.3. Comparing the zonal and meridional LACFs, a slight anisotropy is apparent, with the meridional auto-correlation function showing a small negative lobe after its first zero crossing. Some degree of anisotropy was also evident in the tracer distributions [*Ledwell et al.*, 1998]. The first zero crossings of the LACFs occur between approximately 20 and 35 days, while it appears that the integrals of the LACFs are probably saturated after lags of about 40 days for the zonal correlation function and 60–70 days for the meridional correlation function. The

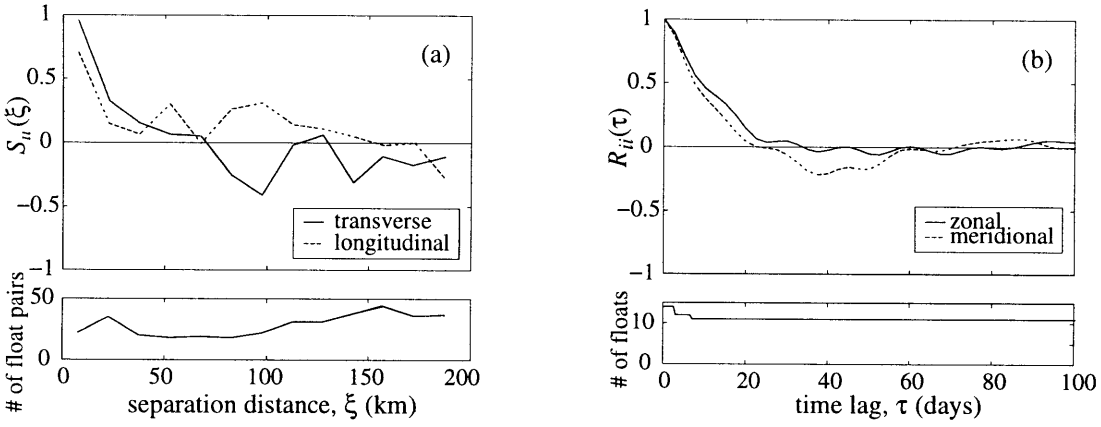

Figure 2.5: (a) Transverse (solid line) and longitudinal (dashed line) spatial correlation functions computed from NATRE and Subduction floats along with the number of float pairs used for a given separation distance. The covariances were averaged over 15 km bins of separation distance. (b) Zonal (solid line) and meridional (dashed line) ensemble-averaged Lagrangian auto-correlation functions computed from NATRE and Subduction floats along with the number of floats used for a given time lag.

locations of the changes in slope of the dispersion curves in Figure 2.4 imply similar saturation times of approximately 50 days for the zonal correlation function and 60–70 days for the meridional correlation function. Integrating the LACFs using 100 days as the upper limit of the integral of $R_{ii}(\tau)$ in (2.12) gives the integral time scales $I_{(11,22)} = (10.6 \pm 4.8,\ 5.4 \pm 2.8)$ days for the (zonal, meridional) components, where uncertainties represent 95% confidence limits estimated using a bootstrap method [e.g., *Press et al.*, 1986].

From these integral time scales and the combined time and ensemble-averaged EKE, a second estimate of the zonal and meridional diffusivities yields $\kappa_{e_{(11,22)}} = (1.5 \pm 0.7,\ 0.7 \pm 0.4) \times 10^3$ m^2 s^{-1} where error estimates are based on the uncertainties of EKE and I_{ii} computed above. These estimates of κ_e are in close agreement with those computed by *Ledwell et al.* [1998] from the tracer data.

2.4 Numerical Simulations

The results of the NATRE field experiment suggest that the theoretical ideas of *Garrett* [1983] and *Taylor* [1921] are relevant to the analysis of mesoscale stirring in the ocean. However, the NATRE tracer observations alone do not provide a means of quantitatively testing Garrett's theory, since we have no independent information about the strain and small-scale diffusivity. To address this, we now turn to numerical simulations of tracer dispersal in the presence of small-scale diffusion and a turbulent mesoscale strain field, where we do have knowledge of these quantities. A two-layer quasigeostrophic vorticity model is calibrated so that the statistics of model floats agree as closely as possible with the NATRE floats. The main goal is to understand the possible biases and uncertainties associated with estimates of strain rate and small-scale diffusivity from the NATRE observations.

2.4.1 The Model

We used a pseudo-spectral model (originally by W. K. Dewar, later modified by G. R. Flierl) with two active layers and a mean vorticity gradient in the y-coordinate direction. The model solves

$$\frac{\partial q_i}{\partial t} + J(\psi_i, q_i) = -\mu\nabla^2\psi_i + \nu\nabla^4\psi_i \qquad i = 1, 2 \tag{2.17}$$

[e.g., *Pedlosky*, 1979], where the Jacobian operator $J(a,b) = \frac{\partial a}{\partial x}\frac{\partial b}{\partial y} - \frac{\partial a}{\partial y}\frac{\partial b}{\partial x}$, μ and ν terms represent bottom friction (lower layer only) and Newtonian viscosity, respectively. The quasi-geostrophic potential vorticity, q_i, is given by

$$q_i = \nabla^2\psi_i - F_i(\psi_i - \psi_j) + f_o + \beta_i y, \qquad j = 3 - i, \tag{2.18}$$

where ψ_i is the geostrophic stream function for the ith layer, which satisfies

$$(u_i, v_i) = \hat{k} \times \nabla\psi_i = \left(\frac{-\partial\psi_i}{\partial y}, \frac{\partial\psi_i}{\partial x}\right), \tag{2.19}$$

$F_i = f_o^2/g'D_i$ is the inverse deformation radius squared, $g' = g\Delta\rho/\rho$ is the reduced gravity, and $(f_o + \beta y)$ is the planetary vorticity.

Forcing was achieved by imposing a westward mean flow, $\overline{u_1}$, in the upper layer to serve as a source for baroclinic instability. A corresponding energy sink was provided by Newtonian viscosity in both layers plus bottom friction in the lower layer.[4] This configuration is identical to that used by *Haidvogel and Held* [1981], except that they used a biharmonic diffusion to dissipate enstrophy at small scales while we use an exponential filter at high wavenumbers [*Canuto et al.*, 1988]. An overview of the dynamics of two-dimensional vorticity models can be found in *Rhines* [1977]. A more recent discussion of vortex dynamics in two-dimensional turbulence was given by *McWilliams* [1990].

Having computed the stream function in both layers from (2.17), the upper layer stream function is used to compute the evolution of a passive tracer field via the advection-diffusion equation

$$\frac{\partial\theta}{\partial t} + J(\psi_1, \theta) = \kappa_s \nabla^2\theta, \tag{2.20}$$

where κ_s is the explicit small-scale diffusivity. The motion of Lagrangian particles in the upper layer is computed using only the left hand side of (2.20). Particles which are advected across the periodic boundaries are tracked as having done so, hence the total excursion of model floats may be larger than the model domain size.

The model was run on a square domain, with doubly periodic boundaries, and 512 grid points in each horizontal direction. Re-dimensionalization was done by relating model EKE and planetary β to values appropriate to the NATRE experiment. Having set these two parameters,

[4] Additional simulations not discussed here were also run for a barotropic fluid using different forcing and dissipation mechanisms than are described above. In particular, a random Markovian formulation was used to force the perturbation stream function across a narrow wavenumber band (160–210 km scales; e.g., *Maltrud and Vallis*, [1991]), and an inverse Laplacian was used to dissipate energy at the largest scales [e.g., *Babiano et al.*, 1987]. These simulations can be compared to those of *Haidvogel and Keffer* [1984], the primary difference being the form of the forcing and dissipation mechanisms used to maintain the flow. We found that this barotropic model had to be rather heavily forced in order to achieve realistic time and space scales [*Sundermeyer*, 1995]. However, insofar as the tracer analysis went, no apparent differences were found between the barotropic and the present baroclinic simulations once a calibration had been achieved.

Parameter	Symbol	Nondimensional value	Dimensional value
domain size		$2\pi \times 2\pi$	628 km × 628 km
number of gridpoints		512	512
grid spacing	Δx	0.012	1.2 km
time step	Δt	0.0005	0.35 hours
spin-up time		12.42	1.0 year
run time		6.21	0.5 year
baroclinic deformation radius	$1/\sqrt{F_1 + F_2}$	.25	25 km
aspect ratio	F_2/F_1	0.33	0.33
planetary vorticity gradient	β	5.19	2.07×10^{-8} km^{-1} s^{-1}
Newtonian viscosity	ν	7.5×10^{-4}	3.0 m^2 s^{-1}
bottom friction (layer 2 only)	μ	0.23	9.2×10^{-8} s^{-1}
tracer diffusivity	κ_s	2.5×10^{-3}	10 m^2 s^{-1}
mean flow (layer 1 only)	$\overline{u_1}$	-.78	-3.1 cm s^{-1}

Table 2.1: Parameter settings used in the model solution described in the text. Non-dimensional model units are scaled to dimensional physical units via $U = 4$ cm s^{-1}, $L = 100$ km, and $T = 2.5 \times 10^6$ s.

the following characteristic velocity, space, and time scales are obtained:

$$U = 4 \text{ cm s}^{-1} \tag{2.21}$$

$$L = 100 \text{ km} \tag{2.22}$$

$$T = 2.5 \times 10^6 \text{ s} \approx 29 \text{ days.} \tag{2.23}$$

This non-linear system can be characterized by an advective time scale, $T \approx L/U$, so that once U is chosen, L and T are no longer independent. Other values of model parameters are given in Table 1.

2.4.2 Model Spin-up and Calibration

The flow was spun up for 1 year from an initial condition in which the perturbation stream functions were set to zero in the lower layer, and assigned a random phase and an amplitude in the upper layer such that its energy spectrum was similar to the expected equilibrium spectrum. Model calibration was achieved by adjusting the relative strengths of the imposed mean flow, $\overline{u_1}$ (note, this was the only forcing in the model), and the bottom friction, μ; the objective being to achieve an upper layer flow that was similar in a statistical sense to that of

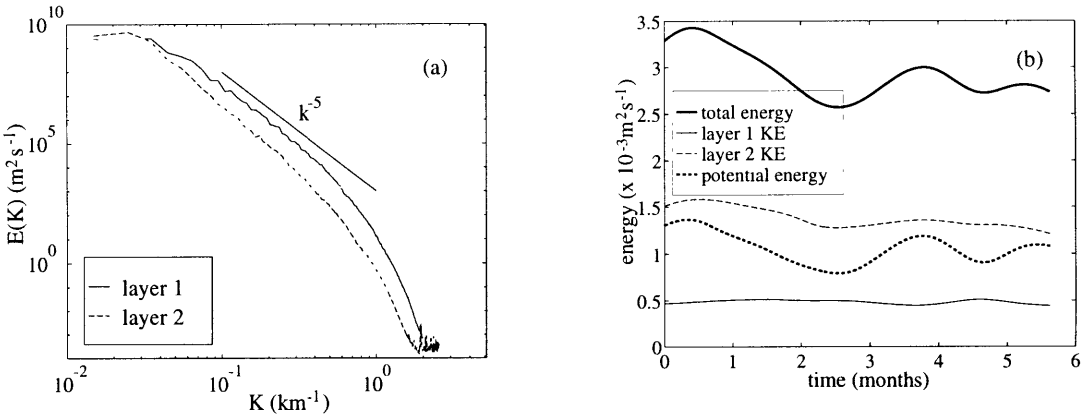

Figure 2.6: (a) Model energy spectra for upper and lower layer of a typical model run and (b) total (domain-averaged) Eulerian energy budget for a typical 6 month integration.

the NATRE region. Three diagnostics were used to determine this: the eddy kinetic energy, the spatial correlation function, and the Lagrangian auto-correlation function. In all cases, model float statistics were computed in the same way as for the NATRE floats (see below). Parameter settings for a typical model solution that met these calibration criteria are listed in Table 1.

An ensemble of 10 tracer simulations was run by re-initializing the model tracer every 6 months during a total simulation period of 5 years (not including spin-up). Figure 2.6 shows typical energy wavenumber spectra for the fully spun-up upper and lower layer along with a time series of the energy balance of the system. The k^{-5} dependence of spectra at high wavenumbers is similar to that found by *Haidvogel and Keffer* [1984], and is notably steeper than the k^{-3} slope predicted from simple energy and enstrophy conservation arguments for two-dimensional turbulence. Several investigators [*e.g., Basdevant et al.*, 1981; *Bennett and Haidvogel*, 1983; *Babiano et al.*, 1985; *Maltrud and Vallis*, 1991] have shown that steep spectral slopes may result from space-time intermittence and coherent structures of two-dimensional turbulence.

Floats were released into the upper layer, in a closely spaced array of 37 floats (intended to track the tracer; Figure 2.7), superimposed on a uniformly spaced array of 100 floats which

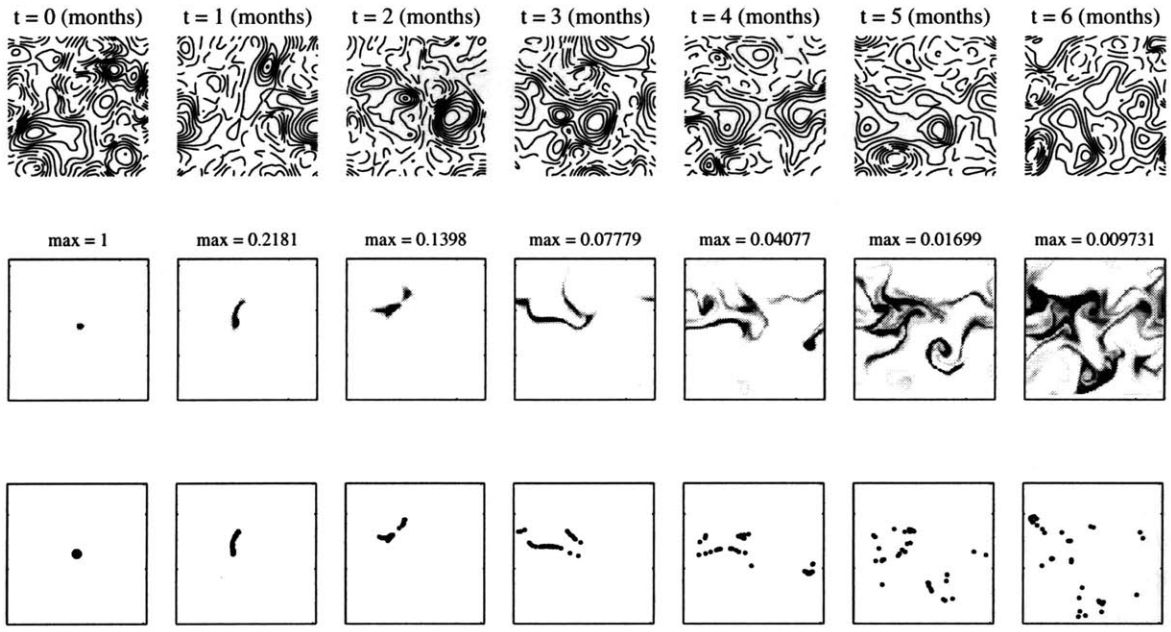

Figure 2.7: Perturbation streamfunction, tracer, and float positions (only those released within the tracer patch, see text) for a typical model run. Successive frames from left to right correspond to intervals of 1 month, with each frame representing an area of 628×628 km^2. Tracer maps are drawn with shading relative to the instantaneous maximum concentration, so that the concentration corresponding to the darkest shading decreases with time. Note the initial period of rapid streak formation followed by a more gradual "filling in" of tracer.

spanned the model domain (in order to insure robust statistics). For this example, mean velocities computed from the full array of floats were $u_{(1,2)} = (-3.2 \pm 1.6,\ 0.1 \pm 1.3)$ for the (eastward, northward) components, and were of course consistent with our specified value of $\overline{u_1}$. The time- and ensemble-averaged EKE were $(6.4 \pm 5.0,\ 7.0 \pm 4.8)$ cm^2 s^{-2} for the (eastward, northward) components, and were within 20% of the EKE computed from the NATRE floats. The model SCFs (Figure 2.8) are similar to the SCFs computed from the NATRE floats (see Figure 2.5), with the transverse SCF having a first zero crossing at 70 km. Model zonal and meridional LACFs (Figure 2.8) both have their first zero crossings at approximately 28 days, which is also consistent with LACFs computed in section 2.3 from the NATRE observations. Given these results, we consider this solution to be calibrated.

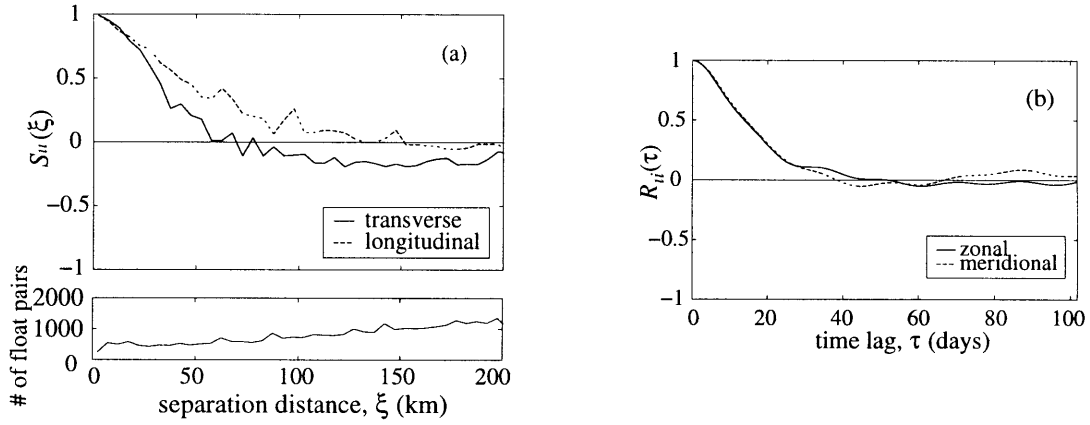

Figure 2.8: (a) Transverse (solid line) and longitudinal (dashed line) spatial correlation functions computed from model floats along with the number of float pairs used for a given separation distance. The calculated covariances were averaged over 5-km bins. (b) Ensemble-averaged zonal (solid line) and meridional (dashed line) Lagrangian auto-correlation functions computed from model floats. The number of floats used for a given time lag was 137.

2.4.3 Simulated Tracer Fields

A tracer was released into the fully spun-up upper layer. The initial tracer distribution was a Gaussian patch

$$\theta(x, y, t_o) = e^{-(x^2+y^2)/2\sigma^2} \tag{2.24}$$

of radius $2\sigma = 12.5$ km, intended as an idealization of the NATRE initial tracer distribution. The small-scale diffusivity in the model was set to 10 m^2 s^{-1}, or about 3 times larger than that inferred from the NATRE tracer observations. This was done to insure that tracer streaks were well resolved in the model, even in the presence of large strain rates.[5]

The evolution of the tracer field for a representative model solution is shown in Figure 2.7. By comparing the floats and tracer, it can be seen that the two are advected together, as was expected. Qualitatively, the dispersal of model tracer appears consistent with both theoretical

[5]Numerical experiments using a steady linear strain field, $\psi = -\gamma xy$ (not shown), were able to reproduce *Garrett's* [1983] result, $\sigma^2_{\rm rms} = \kappa_s/\gamma_{\rm rms}$, provided that the streaks were well resolved, i.e., that they were always greater than about 8–10 gridpoints in width. For poorly resolved streaks, say 5 gridpoints wide, the observed streak width was about 50% greater than predicted by the relevant steady theory, presumably because of numerical diffusion.

expectations and observations from NATRE. Immediately after release, there is a period of rapid streak formation, characterized by a fairly well defined streak width. For longer times, the streaks begin to wrap around one another and merge, gradually filling in the model domain. The tracer concentration and area are not considered for times greater than about 6 months, at which time the tracer has wrapped around the model domain.

We now mimic the analysis of the NATRE tracer (section 2.3.1), assuming no *a priori* information about the flow, and attempt to infer the small-scale diffusivity via estimates of streak width and strain rate. Using $T = 3$ months from our representative model solution (streak length in this simulation becomes ambiguous after this time; see frames 5–7 of Figure 2.7), we estimate a streak length of approximately 800 km, or $L = 2\sigma \approx 400$ km, which would imply a streak growth rate of $\lambda \approx 4.5 \times 10^{-7}$ s^{-1}. Using λ as a proxy for the rms strain rate (i.e., taking $\gamma_{\rm rms} = \lambda$ exactly), and using a value for the rms cross-streak variance $\sigma^2_{\rm rms} \approx 28$ km^2 estimated from sections of the tracer (Figure 2.9), the assumed balance $\kappa_s = \sigma^2_{\rm rms}\gamma_{\rm rms}$ yields a small-scale diffusivity of $\kappa_s = 13$ m^2 s^{-1}, which is about 30% larger than the explicit small-scale diffusivity set in the model. Repeating this analysis for the set of 10 simulations, we obtain on average $\kappa_s = 19.0 \pm 10.5$ m^2 s^{-1}, or approximately twice the explicit small-scale diffusivity set in the model (the uncertainty here is twice the sample standard deviation).

This is one of the most significant results of our numerical simulations. It shows that if λ is used as the strain rate in the expression for the cross-streak balance, then the predicted κ_s is biased by a factor of 2, but is otherwise fairly robust. An unbiased estimate obtains if we use $\sigma^2_{\rm rms} = \kappa_s/(\lambda/2)$. This suggests that the more than order of magnitude discrepancy between κ_s estimated by *Ledwell et al.* [1998] and that predicted for shear dispersion by *Young et al.* [1982] is very reliable. (*Polzin et al.* [in preparation] have suggested that shear dispersion associated with the vortical mode, which is not accounted for in *Young et al.*'s [1982] theory, may be responsible for this discrepancy. However, further investigation of this process is beyond the scope of the present study.)

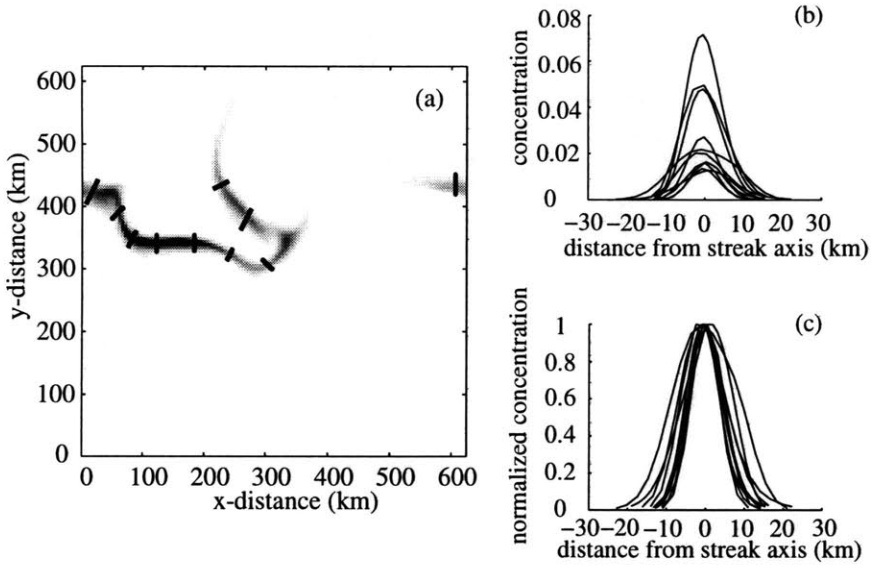

Figure 2.9: Cross-streak profiles of model tracer mimicking those obtained during the October and November NATRE cruises showing a "well-defined" rms streak width. (a) The model tracer distribution is the same as in frame 4 of Figure 7, corresponding to approximately 3 months since release. Solid lines represent the locations of tracer sampling sections. (b) Absolute and (c) normalized concentrations along the sections are plotted with the streak axis centered at zero.

Next, we compare qualitatively the growth of the model tracer area to that predicted from theory. For the small-scale diffusivity, we use the model value $\kappa_s = 10$ m^2 s^{-1}, while for the rms strain rate, we again use the streak growth rate $\lambda = 4.5 \times 10^{-7}$ s^{-1}, estimated above. For the large-scale effective eddy diffusivity we use $\kappa_e = 1 \times 10^3$ m^2 s^{-1}, consistent with estimates from NATRE. The area of the tracer patch of our representative solution, computed as the area within the highest contour bounding 95% of the tracer, is plotted along with the corresponding theoretical curves in Figure 2.10. As with the NATRE observations, there is a clear exponential growth phase followed by a reduced growth rate, perhaps approaching a linear regime, at long times (the linear growth phase for long times is not sampled adequately here due to limitations in model domain size).

Pertinent to the above calculations, the clear exponential growth seen in Figure 2.10 associated with rapid streak formation is the most compelling argument for using *Garrett's* [1983]

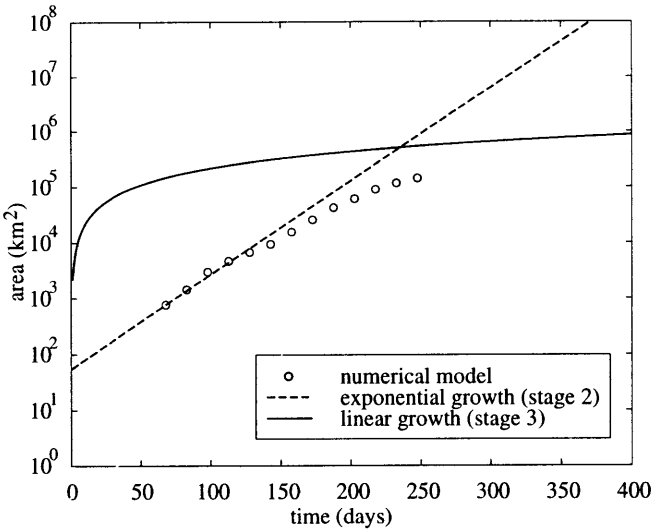

Figure 2.10: Exponential (dashed lines) and linear (solid lines) growth phases (stages 2 and 3 of section 1) of tracer area for a theoretical point release of passive tracer in a turbulent flow and model results (open circles) for the seven frames in Figure 7. Theoretical curves are for $\kappa_s = 10.0$ m^2 s^{-1}, $\gamma_{\rm rms} = 4.5 \times 10^{-7}$ s^{-1}, $\kappa_e = 1 \times 10^3$ m^2 s^{-1}. Model results are plotted with a time offset of approximately 70 days to compensate for the finite size of the initial release.

scaling results to estimate the effective small-scale diffusivity. As noted above, this period is characterized by a fairly well-defined streak width that permits unambiguous (although perhaps biased) estimates of κ_s.

2.5 Discussion

The above analysis suggests that the predictions of section 2.1.1 can be calibrated with numerical simulations and used to make unbiased estimates of κ_s based on observations from a tracer release experiment. If λ is used as a proxy for the rms strain rate, an unbiased estimate of κ_s obtains for $\sigma^2_{\rm rms} = \kappa_s/(\lambda/2)$. For practical purposes, this is a very useful result, and in principle, we could stop here. However, there are some interesting questions that merit further consideration. How are the different measures of the strain rate related to one another? Is the calibration factor in the above result sensitive to spatial and temporal variations of the strain rate and streak width? Could a bias also occur if we overestimate the mean streak width as a

result of the merging of tracer streaks? We now address these questions in turn.

2.5.1 Streak Growth Rates and Strain Rates

To understand the relationship between the streak growth rate and the strain rate, consider our earlier expression (2.9) for streak length in a time dependent but spatially constant strain field. In that case, the mean strain rate may be defined as $\langle\gamma\rangle = \frac{1}{t}\int_0^{t'}\gamma(t)dt$, and is equal to the streak growth rate, i.e., $\lambda = \alpha\langle\gamma\rangle$, with $\alpha = 1$. As pointed out by *Garrett* [1983], however, this equality depends on what one uses as a measure of the strain rate. For example, he used $\gamma_{\rm rms} = \langle\frac{\partial u}{\partial x}^2 + \frac{\partial v}{\partial y}^2\rangle^{\frac{1}{2}}$, which for the time dependent problem would imply an exponential growth coefficient $\alpha = 1/\sqrt{2}$. Yet another measure of the strain rate, suggested by *Haidvogel and Keffer* [1984], is given by the diagonalized strain tensor, $\gamma_{\rm rms} = \langle -\frac{\partial u}{\partial x}\frac{\partial v}{\partial y} + \frac{1}{4}\left(\frac{\partial u}{\partial y} + \frac{\partial v}{\partial x}\right)^2\rangle^{\frac{1}{2}}$, which would require still another value for α.

In the general case of a temporally and spatially varying strain field, it is not immediately clear which, if any, of the above strain rates is the *best* estimator of the strain rate needed to evaluate κ_s. Intuitively we might expect some average of the along-streak component of the strain rate, γ_s, to be most appropriate and most nearly equal to the mean streak growth rate. Some evidence for this can be found in our numerical results if we compare the along-streak component of the strain rate, γ_s, computed directly from the model stream function to the streak growth rate, λ, estimated from the model tracer fields. Averaging over the area stained by the tracer (the area within the highest contour encompassing 95% of the tracer) for $t = 3$ months of our representative model, we find $\langle\gamma_s\rangle = 2.8 \times 10^{-7} \pm 7.1 \times 10^{-9}$ s^{-1}, where the uncertainty is given by the standard error (Figure 2.11). This is about 60% smaller than the average streak growth rate estimated directly from the tracer, i.e., for this definition of the strain rate, $\lambda \approx 2\langle\gamma_s\rangle$. *Ledwell et al.* [1998] suggested that the mean streak growth rate may be weighted by the largest strains along the streak and should be larger than the averaged along-streak strain rate.

If we similarly compute the averaged strain rate as defined by the diagonalized strain

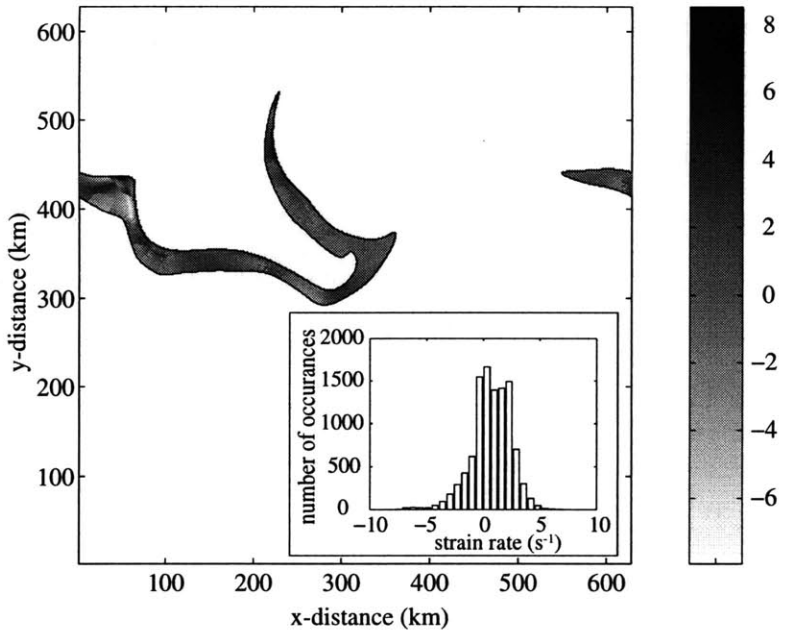

Figure 2.11: Along-streak component of model strain rate computed within the 95% contour of tracer (solid line) for $t = 3$ (frame 4) of Figure 7. The rms strain rate is $\langle \gamma_s \rangle = 2.8 \times 10^{-7} \pm 7.2 \times 10^{-7}$ s^{-1}; the inset shows a histogram of the strain rates computed at each model grid point.

tensor, we find values which are 3 to 6 times larger than the streak growth rate. Thus, while the averaged along-streak component of the strain rate is somewhat smaller than the streak growth rate, the diagonalized strain tensor is many times larger. A similar result was reported by *Pope* [1990] for simulations of three-dimensional turbulence, namely his mean "maximum extensive strain" was 3 times the "mean strain rate on a material line." From this we conclude that, for estimating the small-scale diffusivity from *Garrett's* [1983] theory, the along-streak component of the strain rate is a more appropriate measure of the strain rate than the diagonalized strain tensor.

2.5.2 Temporal and Spatial Variations

Locally, along some segment of a tracer streak, we expect that a balance obtains between some (possibly weighted) average of the directional strain rate and the small-scale diffusivity, i.e.,

$\sigma^2_{\text{rms}} = \kappa_s/\langle\gamma_s\rangle$. However, the directional strain rate (and in fact any of the above measures of the strain rate) varies significantly on scales which are small compared with the streak width, which violates the assumption that the strain rate is uniform within a given streak (Figure 2.11). In fact, a histogram of the directional strain rates (inset to Figure 2.11), shows both negative as well as positive values of γ_s, i.e., the flow is not even always divergent in the along-streak direction. At first, this may seem counter-intuitive; after all, it is the sign of the divergence that should determine the along/cross-streak direction of the tracer. However, such changes in the direction of the strain rate on scales smaller than the streak width are consistent with the splitting and bifurcating of tracer streaks seen in both the observations and the numerical solutions (Figures 2.1 and 2.7).

How these small-scale spatial variations in the strain rate affect estimates of κ_s is unclear. Even if we could construct some appropriate spatial average, we must still contend with the mixed temporal variations in the strain rate (see also *Pope* [1990] for a discussion of temporal variations in strain in three-dimensional turbulence). This is illustrated by (2.8), which shows that the covariance between the strain rate and the cross-streak variance may be important. For example, for a slowly varying strain rate (slow compared to the advective time scale, $1/\gamma$), the strain rate and streak width are approximately in balance and are negatively correlated. In that case, neglecting the covariance term would lead to an overestimate of κ_s, consistent with results from our numerical experiments.

Using (2.9) as a solution for the cross-streak variance, σ_y (and letting $\gamma < 0$), we may also compare the case of a slowly varying strain rate to one which varies rapidly in time. Consider a time dependent strain rate of the form $\gamma = \gamma_o[1 + \sin(\frac{2\pi}{T}t)]$. For $T \ll 1/\gamma_o$, we find that the long-term mean $\langle\sigma_y^2\rangle$ closely resembles the solution for a constant strain rate with $\gamma \equiv \gamma_o$, as does the same sinusoidal solution with $T \approx 1/\gamma_o$ (Figure 2.12). On the other hand, a slowly varying strain rate, $T \gg 1/\gamma_o$, leads to a mean $\langle\sigma_y^2\rangle$ which is significantly greater than the steady solution. The reason for this can be seen by considering the form of the exponential

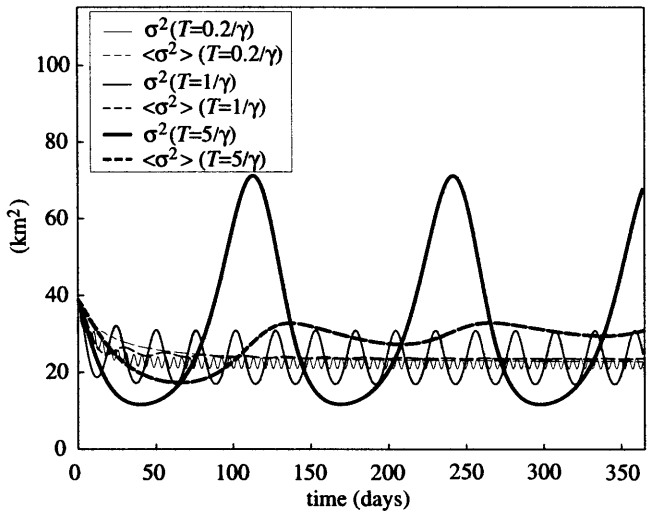

Figure 2.12: Theoretical solution for a sinusoidally varying strain rate showing a mean cross-streak variance which is biased high when the strain rate varies slowly in time. Solid lines represent the instantaneous cross-streak variances, σ_y^2, for $\gamma(t)$ oscillating with periods $T = 0.2 \times \frac{1}{\gamma}$, $T = \frac{1}{\gamma}$, and $T = 5 \times \frac{1}{\gamma}$. Dashed lines represent the running mean of the corresponding cross-streak variances, $\langle \sigma_y^2 \rangle$.

growth rate in this case, $\Gamma = \int_0^{t'} \gamma(t)dt = \gamma_o\{t - \frac{1}{2\pi/T}[\cos(\frac{2\pi}{T}t) + 1]\}$. This shows that for $T \leq 1/\gamma_o$, for time $t \gg 1/\gamma_o$, Γ/t approaches γ_o, which is precisely the mean value of $\gamma(t)$.

The above example suggests that rapid variations in $\gamma(t)$ do not significantly alter the long-term/steady balance between the streak width and the strain rate. However, slow variations in the strain rate may bias high our estimates of κ_s. Returning to our numerical results, it is interesting to assess in which regime our solutions lie. To determine this, we calculate directly the time dependent strain rate following a marked fluid parcel (Figure 2.13). This reveals that the along-streak component of the strain varies considerably on time scales greater than or equal to $1/\gamma$. We thus conclude that temporal variations in the strain rate may account for as much as 30% of the bias in our estimate of κ_s. (Whether this estimate is affected by small-scale spatial variations is unclear.)

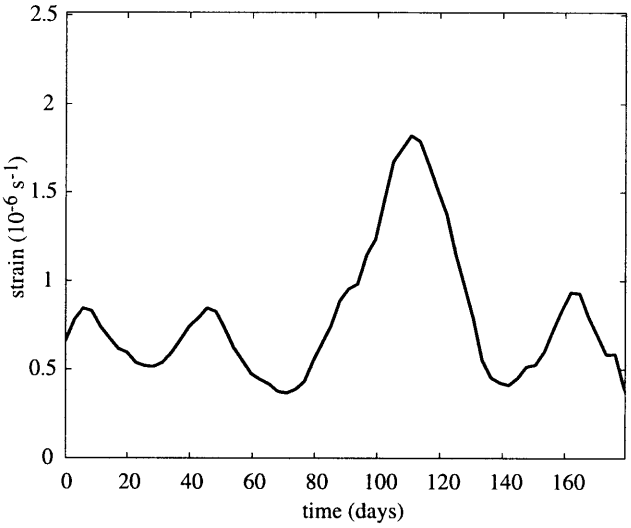

Figure 2.13: The along-streak component of the model strain rate following a Lagrangian particle. Order one fluctuations are readily apparent on time scales that are long compared with $1/\gamma \approx 26$ days, suggesting that the strain rate and streak width are likely to be negatively correlated.

2.5.3 Merging of tracer streaks

A third and final possible bias in our estimates of small-scale diffusivity stems from the merging of tracer streaks which must occur in order for the tracer to fill in the patch (see Figure 2.7). When two streaks merge, each effectively loses its identity, leaving a single streak which is initially wider than either of the component streaks. From an observer's perspective, the inability to distinguish individual streaks from those which have resulted from a recent merger could lead to an overestimate of the streak width, which would lead in turn to the overestimation of κ_s. We were careful to avoid this bias in our analysis of simulated tracer, but of course we had nearly complete information about the model tracer. This may not always be possible in real oceanic tracer release experiments. However, the careful planning and execution of sampling surveys combined with an understanding of the time and space scales of the mesoscale flow should help avoid this bias.

2.6 Summary and Conclusions

In this study we have shown that the dispersal of passive tracer in the NATRE experiment can be described using the ideas laid out by *Garrett* [1983], and that such tracer experiments can be simulated realistically using an appropriately calibrated numerical model.

The streakiness phase of the NATRE tracer patch was consistent with an exponential growth of tracer area for values of small-scale diffusivity, $\kappa_s = 3$ m^2 s^{-1} and streak growth rate $\lambda = 3 \times 10^{-7}$ s^{-1}, as previously estimated by *Ledwell et al.* [1993, 1998]. Large-scale effective eddy diffusivities computed from the NATRE float observations were $(\kappa_{e11}, \kappa_{e22}) = (1.5 \pm 0.7,\ 0.7 \pm 0.4) \times 10^3$ m^2 s^{-1} for (zonal, meridional) components. These values agree with estimates based on the growth of the second moments of the tracer patch by *Ledwell et al.* [1998] and describe the approximately linear growth of the patch area at long times.

Statistics computed from the NATRE float data were used to characterize the kinematics of the mesoscale flow. Mean velocities of $(\overline{u}, \overline{v}) = (-1.2 \pm 0.3,\ -0.9 \pm 0.2)$ cm s^{-1} estimated from the float data were roughly consistent with those estimated by *Ledwell et al.* [1998] from movement of the tracer patch. The ensemble-averaged EKE were $\frac{1}{2}\overline{\langle u'^2_{(1,2)} \rangle} = (8.1 \pm 1.0,\ 8.0 \pm 0.9)$ cm^2 s^{-2}. The first zero crossing of the transverse SCF occurred at approximately 70 km, while (zonal, meridional) integral time scales estimated from the integral of the LACFs were $I_{(11,22)} = (10.6 \pm 4.8,\ 5.4 \pm 2.8)$ days.

A two-layer quasigeostrophic vorticity model was used to simulate the stirring and mixing of a passive tracer in a turbulent flow. The model was calibrated so that the basic statistics of the model floats agreed as closely as possible with those computed from the NATRE floats (EKE and spatial and Lagrangian auto-correlation functions). The rate of dispersal of model tracer was then examined in order to assess the quantitative agreement between the theoretical model of *Garrett* [1983] and tracer dispersal in a fully turbulent flow. The dispersal of model tracer was found to be consistent with an exponential growth phase, followed by a reduced growth rate, perhaps approaching a linear regime for long times. Using the streak growth rate

estimated directly from the tracer as a proxy for the rms strain rate in *Garrett's* [1983] formula for the cross-streak balance (as must be done in any real tracer release study, since $\gamma_{\rm rms}$ cannot be measured directly), we found that a factor of 2 is required to obtain an unbiased estimate of the effective small-scale diffusivity, κ_s (i.e., κ_s is otherwise biased high by a factor of 2). An appropriate measure of the strain rate in Garrett's theory may be the averaged along-streak component of the strain rate, which we found was roughly half the streak growth rate computed directly from the tracer patch. The rms strain rate computed from the diagonalized strain tensor was 3 to 6 times larger than the streak growth rate, and is therefore less appropriate. A second possible source of bias in estimates of κ_s from tracer observations results from the temporal and spatial variations in the strain field, particularly the negative correlation between streak width and strain rate, which are necessarily neglected in *Garrett's* [1983] theory.

These assessments of the spatial and temporal effects in our numerical experiments suggest that estimates of the effective small-scale diffusivity, κ_s, inferred from the NATRE tracer by *Ledwell et al.* [1993] may have been too large by about a factor of 2, and *Ledwell et al.* [1998] have adjusted their estimates downward in light of these results.

A third potential source of bias brought to light by our numerical simulations is that as tracer streaks begin to merge, it may not be possible from local measurements to distinguish individual streaks from recently merged (and broader) streaks. Whether such a bias occurred in computations of κ_s from the NATRE field data is not known, but it is considered unlikely.

Given the agreement between the theoretical predictions of *Garrett* [1983] and our numerical results, we conclude that no known biases could account for the order of magnitude discrepancy between the effective small-scale diffusivity estimated from NATRE ($\kappa_s \approx 3$ m^2 s^{-1}) and that predicted for shear dispersion by internal waves ($\kappa_s \approx 0.08$ m^2 s^{-1}). It is more likely that this discrepancy is due to the presence of some real but as yet unidentified horizontal mixing process acting on scales of 1–10 km.

Part II

Lateral Dispersion over the New England Continental Shelf

Chapter 3

Introduction

Part I of this thesis examines the mixing and stirring of Lagrangian particles and a passive tracer in the open ocean, and attempts to quantify the effects of the mesoscale strain and diffusion at scales of 1–10 km. Part II of this thesis examines lateral dispersion on scales of 1–10 km in the coastal ocean. Here, dye studies from the Coastal Mixing and Optics (CMO) program are used to quantify the rates of lateral dispersion in the coastal ocean, and to understand what mechanisms determine these rates under a limited range of stratification and forcing conditions.

3.1 Diffusion and Dye Studies in Coastal Waters

Numerous tracer release studies have been performed by previous investigators in coastal environments as well as in freshwater lakes. However, very few of these have been in a stratified environment. Noteworthy exceptions to this include studies by Kullenberg (1971), Vasholz and Crawford (1985), Wanninkhof et al. (1997), Houghton (1997), Geyer and Ledwell (1995, 1997), and the CMO dye experiments discussed in the present work. Of these, the CMO dye experiments discussed in the present study, and the Massachusetts Bay experiments by Geyer and Ledwell (1995, 1997) are the most comprehensive in that they include detailed observations of the vertical and horizontal distributions of the dye patches concurrent with CTD observations,

full-depth velocity observations and other environmental parameters. These experiments thus provide an invaluable opportunity to evaluate a wide range of dispersion models.

As described by Richardson (1926) and Richardson and Stommel (1948), the effective horizontal diffusivity observed in both the atmosphere and the ocean depends on the scale of the phenomenon in question. This result was concisely summarized in a diffusion diagram by Stommel (1949) which showed that the effective horizontal diffusivity, κ_H, on scales ranging from $l = 0.2 - 100$ m varied approximately as $\kappa_H \propto l^{\frac{4}{3}}$ (Richardson, 1926, also showed a similar diagram for his atmospheric observations). This $\frac{4}{3}$ power law was predicted by similarity theories of turbulence of Kolmogorov (1941) and Batchelor (1950). More recently, a collection of empirical data from dye experiments in the surface mixed layer was compiled by Okubo (1971). These experiments, ranging in scale from 100 m to 100 km, also showed that the effective diffusivity increased as a function of horizontal scale, in this case $\kappa_H \propto l^{1.1}$. (As suggested by Okubo, his findings do not rule out the possibility that the $\frac{4}{3}$ power law of diffusivity could be valid locally for some time and length scales.)

The diffusion diagrams of Okubo (1971) have been used by many investigators as a benchmark for comparing experimental results from a wide range of space and time scales. Such diagrams provide not only a clue to the behavior of oceanic dispersion, but also a practical means of comparing and predicting the dispersion at different scales. However, as suggested by Okubo (1971), "any interpretation of the diffusion diagrams must remain provisional until the mechanisms or physical process giving rise to diffusion are well understood." The present study is an attempt to understand the mechanisms and physical processes that control horizontal dispersion over the continental shelf.

3.2 Goals and Outline

Two main questions are addressed in this study:

1) What are the rates of lateral dispersion over the continental shelf on spatial scales of 1–10 km and time scales of less than 5 days?

2) What are the mechanisms that determine these rates?

In Chapter 4, an extensive description of the field data from the Coastal Mixing and Optics dye studies is presented. Rates of lateral dispersion inferred from these data are estimated in Chapter 5 for each of the dye experiments using a simple model of vertical and horizontal shears and strains. In Chapter 6, two existing paradigms of lateral dispersion are examined, vertical shear dispersion, and dispersion by lateral intrusions. It is shown that in general, these mechanisms can not account for the small-scale lateral dispersion observed during the CMO dye studies. In Chapter 7, an alternative mechanism of lateral dispersion is proposed, dispersion vortical motions. Such motions are caused by the relaxation of mixed layers created by episodes of diapycnal mixing. It is shown that in some cases this mechanism could account for the observed dispersion, and warrants further study. In Chapter 8, the key results of Part II are summarized, and a brief discussion is given of some of the outstanding questions raised by this work.

Chapter 4

The Coastal Mixing and Optics Dye Studies

This chapter describes the field observations of the three CMO dye cruises and provides a detailed account of the observed vertical and lateral distributions of tracer which will be used in subsequent chapters to examine a variety of possible lateral dispersion mechanisms. Section 4.1 provides a general description of the CMO study site, including a brief overview of the regions climatology. The 1995, 1996, and 1997 cruises are discussed independently in Sections 4.2–4.4. For each cruise, environmental conditions including local hydrography, wind, and velocity structure are examined. For each experiment, the injection and subsequent dye surveys are then described, along with data from the ARGOS drifters, and the vertical diffusivity is discussed. The lateral dispersion is addressed in Chapter 5.

4.1 Overview of the Field Program

4.1.1 The CMO Study Site

The CMO study site was approximately 100 km south of Martha's Vineyard, MA in the region known as the "mud patch" (Figure 4.1). The central and along-shore mooring sites were located along the 70 m isobath, while the inshore and offshore moorings were at about 65 m

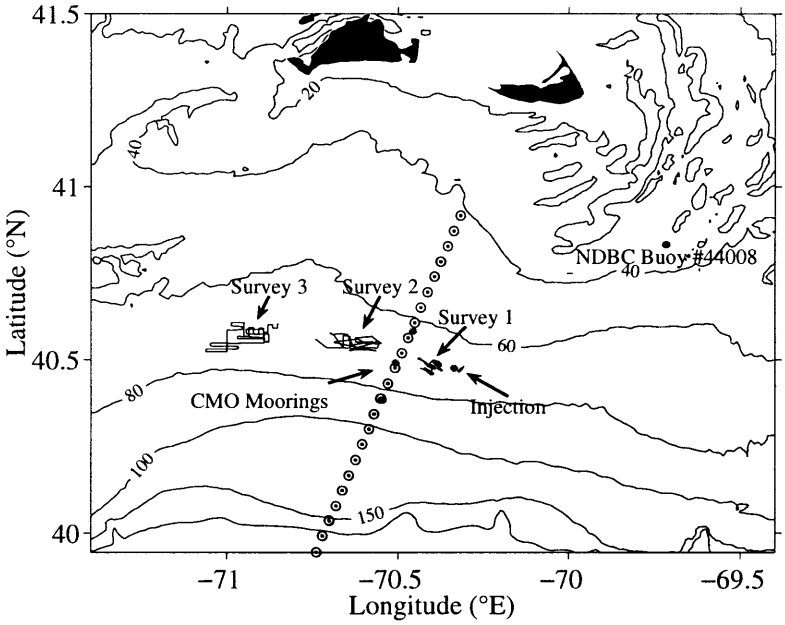

Figure 4.1: Overview of the CMO study site showing the mooring locations and the survey tracks from the September 1996 fluorescein dye experiment. Bullets extending across the shelf indicate the station locations of a hydrographic section made during the same cruise. The NDBC Surface Buoy #44008 is also shown.

and 85 m, respectively. The dye experiments were performed near the 70 m isobath, between the along-shore and central CMO mooring sites. Details of each dye experiment are given in Table 4.1. For each experiment, a single streak of dye was released along an isopycnal surface using a towed injection system. Along with the dye, three to six drogues were also released at the target depth and tracked via ARGOS transmitters. The drogue positions were used along with near real-time shipboard ADCP observations both to assist in locating the dye patch and as an aid to planning sampling strategies during the dye surveys. ADCP data were also logged for later analysis.

After each dye release, three-dimensional surveys of the dye patch were conducted using a sampling sled that was tow-yo'd behind the ship at 2–4 kts. The winch operated at speeds between 30–60 m min^{-1}, which provided a vertical profile every 100–200 m along the ship track. The sampling system included either a rhodamine or fluorescein fluorometer (depending on the type of dye released), a chlorophyll fluorometer, and a Seabird CTD. These instruments

	dates	Dye	Injection Lat, Lon	targ σ_θ	targ depth	surveys
experiment 1	Sept 11–14, 1995	rhodamine	40.44°N, 70.49°W	25.20 kg/m^3	40 m	2
experiment 2	Sept 6–10, 1996	rhodamine	40.46°N, 70.32°W	24.063	35	3
experiment 3	Sept 12–16, 1996	fluorescein	40.47°N, 70.32°W	24.30	46	3
experiment 4	Aug 1–6, 1997	rhodamine	40.48°N, 70.33°W	24.6	18	3
experiment 5	Aug 7–12, 1997	fluorescein	40.48°N, 70.49°W	26.14	62	3

Table 4.1: Overview of dye experiments performed during the Coastal Mixing and Optics program.

sampled at rate of 6 Hz, providing an average vertical resolution of 10 cm.

Hydrographic sections extending across the shelf were made at the beginning and sometimes the end of each cruise. These stations provided detailed descriptions of local conditions and were used to determine where to inject the dye and to help plan subsequent dye sampling strategies. Meteorological data were also logged for each of the cruises using the shipboard Improved Meteorological (IMET) package. In addition, data were obtained from nearby buoys of the National Oceanic and Atmospheric Administration / National Data Buoy Center (NOAA / NDBC).

4.1.2 Climatology

The climatology of the New England shelf has been well documented in the literature (e.g., Moody et al., 1984; Beardsley et al., 1985; Brown et al., 1985; Linder and Gawarkiewicz, 1997) and will not be discussed in detail here. However, since the tides and the large-scale flow across the shelf appear to have had a significant influence on the observed dye dispersion, these warrant some discussion.

The principal lunar tide, M_2, rotates clockwise and is slightly polarized in the along-shelf direction (ellipticity ≈ 1.4) over the New England shelf. This component dominates the tidal variability, with an along-shelf amplitude of approximately 35 cm s^{-1} at the CMO study site.[1] The larger lunar elliptic tide, N_2, is similar to the M_2, except that it has a smaller

[1]The tidal amplitudes summarized here were obtained from tidal ellipses and surface current maps by Moody

amplitude, approximately 4–6 cm s^{-1} in the along-shelf direction. The N_2 and the M_2 tides combine to produce a monthly modulation of the tidal current. The principal solar tide, S_2, is also similar to the M_2, but with along-shelf amplitude of about 3–5 cm s^{-1}, and results in a fortnightly modulation when combined with the M_2. The luni-solar diurnal, K_1, and the principal lunar diurnal, O_1, tides are also clockwise and slightly polarized in the along-shelf direction (ellipticity $\approx$ 1.4). Along-shelf amplitudes of these constituents are approximately 7–10 cm s^{-1} and 3–6 cm s^{-1}, respectively.

During summer stratification, the hydrography is characterized by two robust features, the shelf-slope front and the cold pool. The shelf-slope front forms the boundary between the cooler, fresher water over the continental shelf and the warmer, more saline water farther off-shore. On average, the foot of the front is located near the 100 m isobath, while the surface outcrop is 50–80 km farther offshore (Wright, 1976). There is also observational evidence that the cross-shore positions of the foot and surface outcrop vary considerably. For example, Halliwell and Mooers (1979) showed that the position of the surface outcrop fluctuates by as much as $\pm$35 km from its mean position. Observations of Houghton et al. (1988) also showed that the foot of the front may readily undergo cross-shelf excursions of 20 km or more. The dynamics of such fronts, including their formation and stability, have been studied extensively by Chapman (1986), Chapman et al. (1986), Chapman and Beardsley (1989), Chapman and Lentz (1994, 1996), and other investigators, and will not be discussed here.

The cold pool is generally located immediately inshore of the shelf-slope front, and is typically found at mid-depths or near the bottom. This relatively cold water, less than about 10–12 ^oC, is apparently a remnant of the winter mixed layer which has been left behind by summer stratification (Houghton et al., 1982).

Mean flows along the inshore side of the front are generally westward along-shelf with amplitudes of approximately 10 ± 20 cm s^{-1} (Beardsley et al., 1985). Geostrophic flows asso-

et al. (1984), and do not necessarily represent depth averaged currents. Barotropic tidal amplitudes estimated from shipboard ADCP observations for each of the CMO dye cruises are given in subsequent sections.

ciated with the cold pool are also generally westward, and are of order 10 cm s^{-1}, although eastward counter-flows may occasionally be present between the cold pool and the shelf-slope front where isopynals reverse their slope (Sections 4.2.1 and 4.3.1).

4.2 1995 Pilot Dye Cruise

The pilot cruise for the CMO dye experiments was performed aboard the R/V Oceanus (leg 273) from year days 252–257 (September 9–14), 1995. Hydrography, shipboard ADCP, dye, and drogue data were collected and used to test and further develop the injection and sampling systems. This section describes these data.

4.2.1 Environmental Conditions

Hydrography

An initial assessment of the hydrography of the CMO study region is shown in Figure 4.2. Ten stations extending from approximately the 35 m to the 310 m isobath were occupied over a 29 hour period from days 252–254.

The shelf-slope front extended upward and off-shore from approximately the 100 m isobath and presumably outcropped beyond the offshore extent of our survey. The cold pool was evident in both temperature and salinity, distinct from the shelf-slope front, although it was not a pronounced feature in this transect. (For comparison, see the September 1996 hydrography shown in Figures 4.12 and 4.14).

An additional feature visible in this transect, although it is more transient than the shelf-slope front or the cold pool, is a warm saline surface intrusion emanating from off-shore. Such intrusions, presumably fed by Gulf Stream water, are not uncommon to the region (Linder, 1996). However, due to their extreme temporal variability, these features are not well described by long term means and are poorly documented by climatological studies.

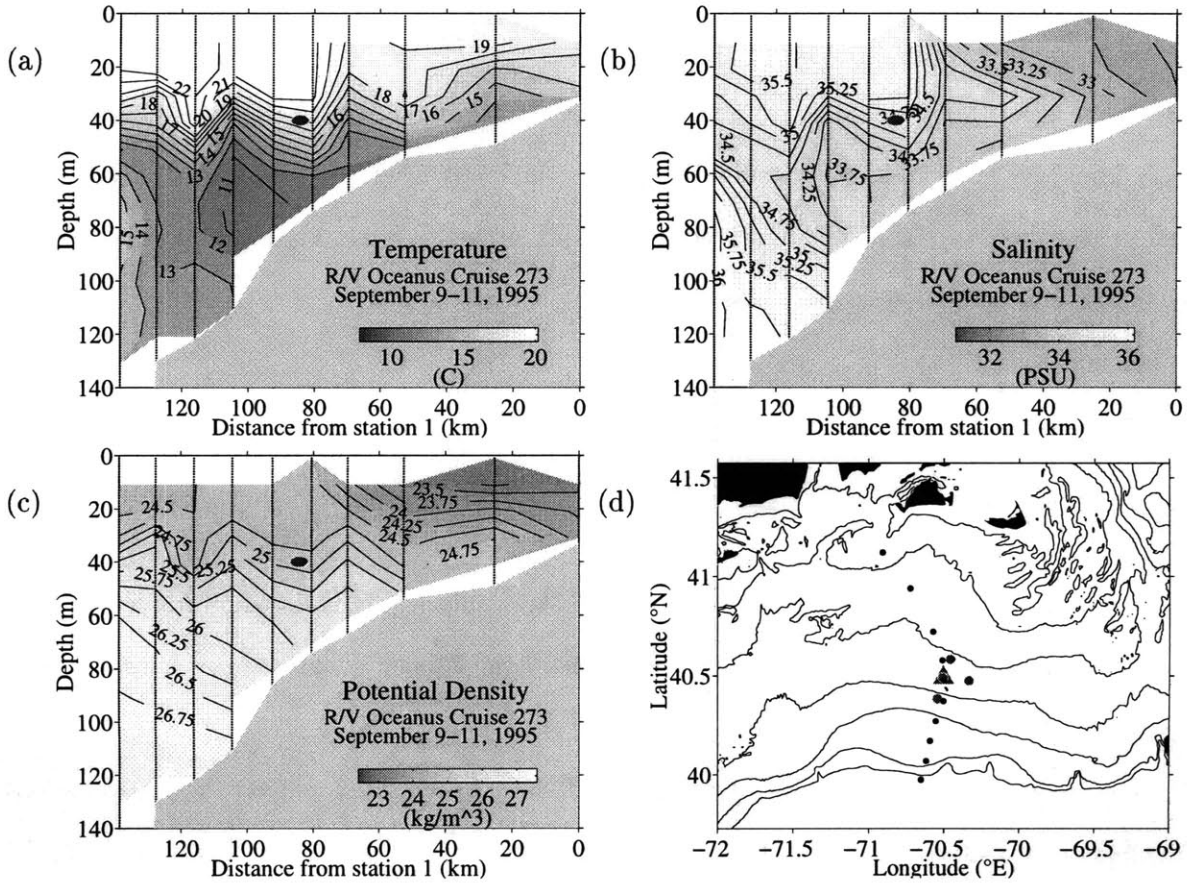

Figure 4.2: Hydrography data collected on days 252–254, 1995. Contour plots show the (a) temperature, (b) salinity, and (c) potential density, with station locations marked by vertical lines. The approximate location of the dye injection relative to the hydrography is shown as bold ellipse. Station locations are shown in plan view (d) (small circles) along with the planned CMO mooring locations (large circles). (Moorings were not deployed until summer 1996.)

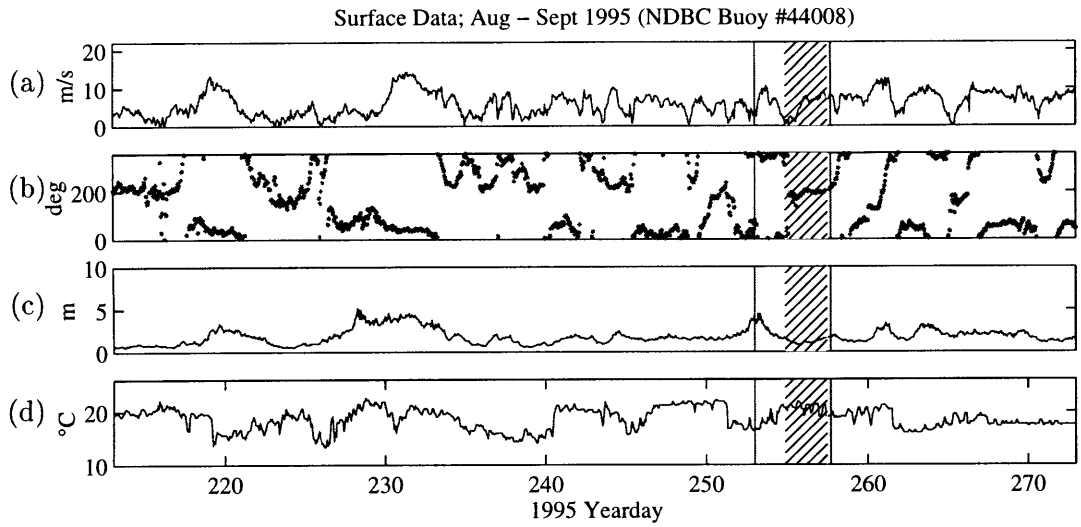

Figure 4.3: Wind (a) speed and (b) direction, (c) significant wave height, and (d) sea surface temperature for days 213–273 (August 1–September 30), 1995 from NDBC Buoy #44008 (Nantucket Shoals). Vertical lines mark the start and end times of the 1995 CMO dye cruise. Hatched areas mark the period corresponding to the 1995 rhodamine dye experiment.

Surface Conditions

Shipboard meteorological data were not logged during the September 1995 cruise; however, wind speed and direction data were obtained from NOAA / NDBC Surface Buoy #44008, located just southeast of Nantucket at 40.50^o N, 69.43^o W (Nantucket Shoals, approximately 80 km northeast of the CMO study site; Figure 4.1).[2] Winds during the 1995 study were moderate, averaging around 5 m s^{-1} for at least two weeks prior to the cruise (Figure 4.3). During the week-long cruise, average wind speeds were approximately 8 m s^{-1} except for a brief relaxation on day 254 during which the wind direction shifted by 180 degrees. Shipboard ADCP observations show that concurrent with this wind event there was a period of enhanced shear across the main pycnocline, consistent with the onset of inertial oscillations (Figure 4.4). This event occurred as the dye was being injected, and may have had a significant impact on

[2]A comparison of wind records from this buoy with shipboard wind data collected during the 1996 dye cruise shows that wind speed and direction between the two platforms were approximately equal (Figure 4.15). Based on this comparison, the wind record from buoy #44008 is assumed to be a reasonable proxy for surface conditions at the CMO site in 1995.

the initial dispersion of the dye patch (Chapters 6 and 7).

Shipboard ADCP Observations

Velocity data were logged continuously during the 1995 cruise from a narrow-band (150 kHz) shipboard ADCP. Data were averaged in 2.5 minute intervals and over 4 m depth bins ranging from roughly 14 m to 58 m (20–85% of the water depth; Figure 4.4). A conservative estimate of the accuracy of these averages is 3–7 cm s^{-1}. Precision in the velocity was better, so that the shear at the same scales should be accurate to within about 0.01 s^{-1}. Here the velocity data show strong barotropic and baroclinic tides as well as significant shears across the main pycnocline which was at about 40 m depth.

Spectral analysis of the barotropic velocity estimated by vertically averaging the ADCP data shows significant energy around the tidal and inertial frequencies (Figure 4.5). Although the velocity record for this cruise was not long enough to resolve clearly individual harmonic constituents in this frequency band, it is nevertheless useful to perform a harmonic analysis on these data to obtain a rough sense of tidal and inertial amplitudes, and for the purpose of detiding the data. A least squares fit to the barotropic velocity was done using the M_2, and K_1 tidal frequencies to represent the semidiurnal and diurnal tides, the local inertial frequency ($f = \frac{2\pi}{18.2}$ hrs^{-1}), and a steady mean. This fit shows that the M_2 tide was slightly polarized in the along-shelf direction (ellipticity ≈ 1.4), with an along-shelf amplitude of about 14 cm s^{-1}. This is about half the value for the surface amplitude given by Moody et al. (1984), which may reflect the importance of baroclinicity in this region. The K_1 component was approximately circular, with amplitude of about 6 cm s^{-1} roughly consistent with Moody et al. (1984).[3] Inertial amplitudes estimated from this fit were approximately 4 cm s^{-1}, slightly polarized onshore

[3]A more sophisticated method of separating temporal from spatial variability in shipboard ADCP data was suggested by Candela et. al (1992). However, for the ADCP surveys made during the CMO dye cruises, this method was found to be extremely sensitive to the choice of horizontal structure functions and did not yield useful results. This is not to be viewed as a shortcoming in Candela et. al's (1992) method, but rather as an indication that our shipboard surveys were not of broad enough scale to resolve cross or along-shelf variations in tidal phase and amplitude (e.g., Moody et al., 1984).

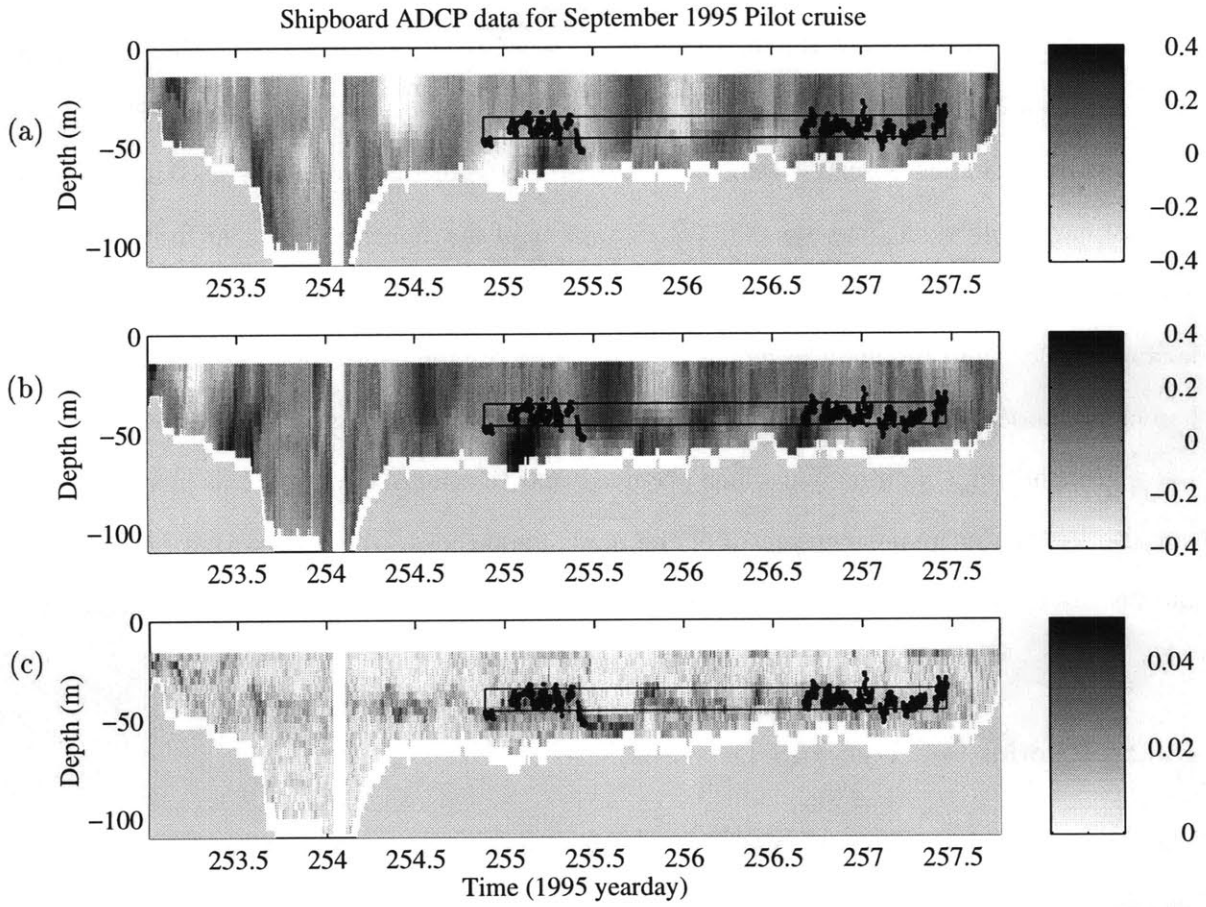

Figure 4.4: (a) Zonal and (b) meridional components of velocity and (c) the amplitude of the vertical shear from shipboard ADCP data from the September 1995 dye cruise. The depth and time of the rhodamine dye experiment is marked by a box in each panel. The length of the box indicates the time between the injection and the end of the final sampling survey. The height of the box indicates the vertical extent of the patch during the final dye survey. The depth of the target density surface during the injection and two subsequent surveys is shown as a dotted line.

(ellipticity $\approx$ 1.4). The mean flow was approximately 5 cm s^{-1} to the northwest. Together, the fitted constituents account for approximately 90% of the variance in the barotropic mode.

For the period between the dye injection and the end of the final sampling survey, an empirical orthogonal function (EOF) analysis for the vertical structure of these data was performed (Figure 4.5). In this analysis, the first EOF mode was forced to be barotropic, while the baroclinic modes are determined by the data. The barotropic mode accounts for 70%–80% of the overall variance in the observed velocity, while 15%–20% of the variance is accounted for by the first baroclinic mode, and less than 3% in any one of the higher modes. The first baroclinic mode shows a zero crossing at approximately 37 m, which corresponds roughly to the depth of maximum shear and the main pycnocline. Time series of mode amplitudes show that the first baroclinic mode is largely dominated by inertial oscillations, as might be expected given the 180 degree shift in wind direction which occurred near the end of day 254. This inertial energy can also be seen in frequency spectra of the mode amplitudes, which show that both the 1st and 2nd baroclinic modes contain significant energy around the tidal and inertial bands.

4.2.2 Rhodamine Dye and Drogues

The pilot dye experiment was conducted between days 254–257 1995. Rhodamine dye was released in a single streak near the planned CMO central mooring site (moorings were not deployed until summer 1996), and sampled twice over a period of 3 days. Three ARGOS drifters with holey sock drogues tethered at 40 m depth were deployed at regular intervals during the injection as an aid to tracking the movement of the dye patch. The ship track during the injection and sampling surveys is shown in Figure 4.6 along with the drogue trajectories.

Stratification remained fairly constant over the course of the experiment, as shown by the mean density and buoyancy frequency profiles for each survey (Figure 4.7). Buoyancy frequencies ranged from 0 to 20 cph, with typical values of 12 cph at the level of the dye (Figure 4.7b).

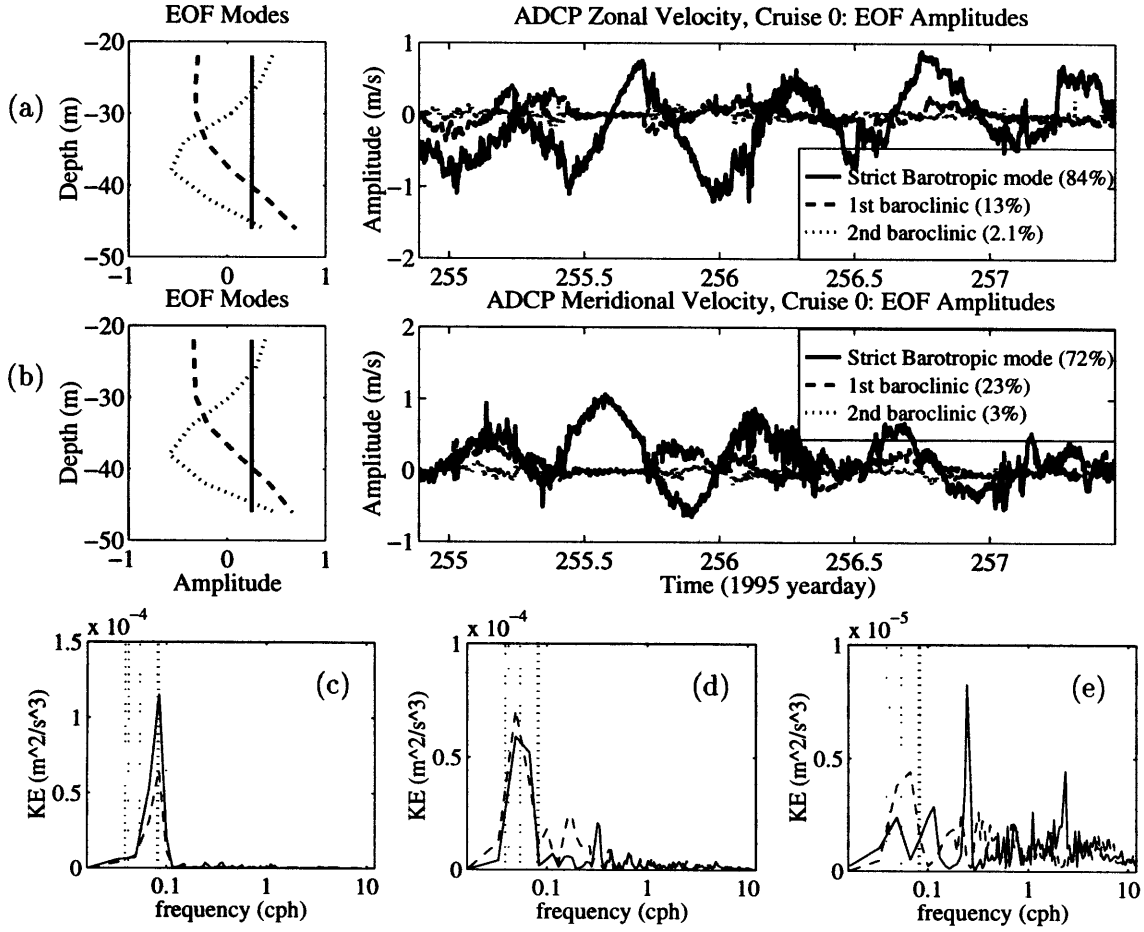

Figure 4.5: (a) Zonal and (b) meridional components of the barotropic mode and first two baroclinic modes computed from an EOF analysis of the 1995 dye cruise shipboard ADCP data. (c,d,e) Spectra for the three modes; solid and dashed lines are zonal and meridional components, respectively. Dotted lines over the spectra mark the O_1, K_1, inertial, M_2, and S_2 frequencies.

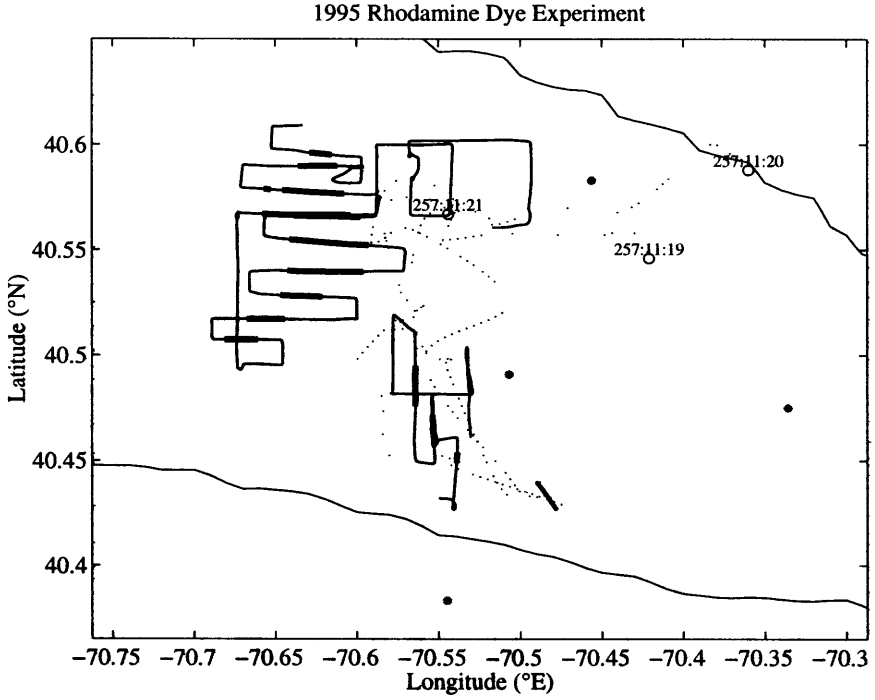

Figure 4.6: Overview of the 1995 pilot dye study showing the ship track (thin solid lines) during the injection and two subsequent dye surveys. The injection streak and the portions of the survey tracks where dye was found are plotted as bold lines. The trajectories of the three Argos drifters which were released along with the tracer are indicated by dotted lines. The 60 m and 80 m bathymetric contours are also shown, along with the locations of each of the planned CMO mooring sites (solid circles; note, moorings were not deployed until summer 1996).

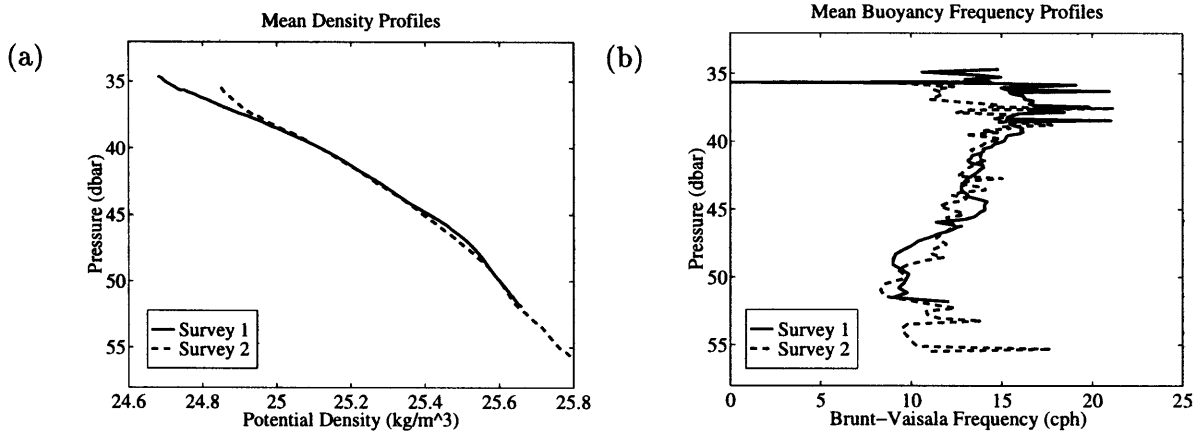

Figure 4.7: (a) Mean density profiles and (b) mean buoyancy frequency profiles for the injection and two surveys of the 1995 rhodamine dye experiment showing a relatively constant stratification over the course of the experiment.

Injection

The injection cast began with a CTD profile down to 65 m in an overall water depth of approximately 75 m (Figure 4.8a). The injection sled was then brought as close as possible to the target density surface, $\sigma_\theta = 25.2$ kg m^{-3}, or approximately 48 m depth, and a total of 100 kg of dye released over a period of about one hour while the ship was under way at approximately 1 kt. Analysis of the CTD data indicated that the standard deviation of the density during the injection was 0.031 kg m^{-3}. Based on the average density vs. pressure relationship computed from the same CTD data, this corresponded to a standard deviation in pressure of 0.25 dbar.

In dye experiments, the exact dimensions of the initial streak are difficult to determine. Laboratory studies by *Lin and Pao* [1979] of dye dispersal in the wake of a towed vehicle showed that after a few buoyancy periods the width is approximately 5 times the height. Applying this guideline to this experiment gives minimum vertical and horizontal thicknesses of $4\sigma_z \approx 1.0$ m and $4\sigma_w \approx 5.0$ m, respectively, about an hour after the injection.

Time series of pressure, temperature, salinity, and density for the period when the dye was being pumped are shown in Figure 4.8. Some variability in the depth of the target density surface is seen in the pressure record, although no trend is apparent. The variations of temperature and salinity along the target density surface indicate horizontal gradients of temperature and salinity of 0.5 ^{o}C and 0.1 PSU, respectively, over the 2 km scale of the injection. These variations are also seen in the T-S diagram as scatter along the target density surface (Figure 4.8b). As discussed in Chapters 6 and 7, these gradients provide information about the local circulation and potentially about the mechanisms of lateral dispersion.

Survey 1

The initial survey of the pilot dye experiment consisted of six meridional tow-yo transects performed between 3 and 10 hours after injection (Figure 4.9). For each transect, tow-yo

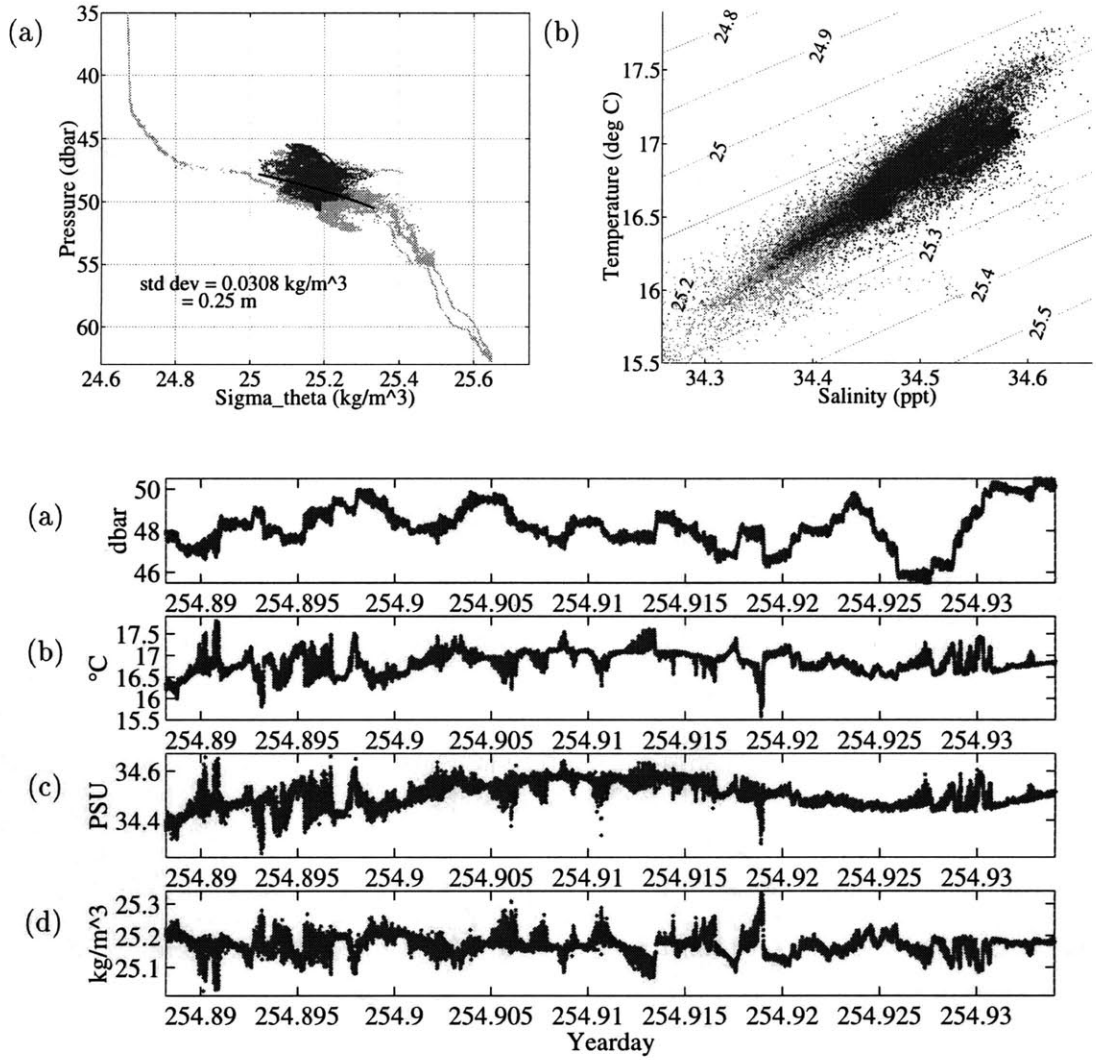

Figure 4.8: (a) Density profile, (b) Temperature-Salinity diagram, and time series of (c) pressure, (d) temperature, (e) salinity, and (f) potential density for the dye injection of the September 1995 pilot study. In (a,b) the full CTD data are plotted in a lighter shade while, the data during the period when the dye was being pumped are plotted in a darker shade. The solid line plotted over the density profile in panel (a) represents a mean profile based on a polynomial fit to the central portion of the data. Standard deviations in density and pressure during the injection period are also written on the figure. In (c-f) the data are only plotted for the period when the dye was being pumped.

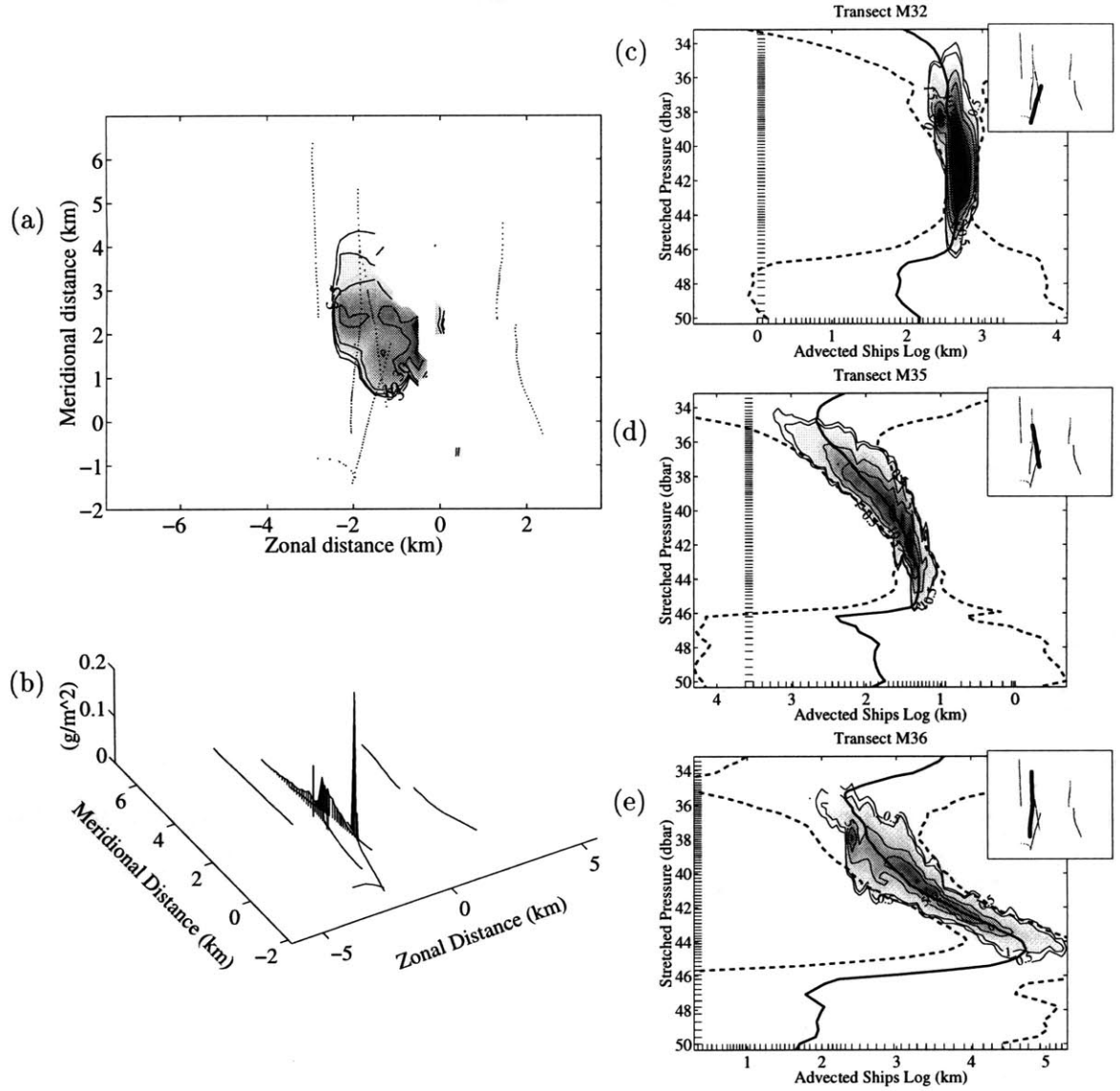

Figure 4.9: Overview of Survey 1 of the 1995 pilot study. (a) Kriging map (kg km^{-2}) and (b) stick plot (g m^{-2}) of vertical integral of tracer after applying ADCP correction. In (b) a vertical line is drawn at the location of each vertical profile with the length of the line indicating the magnitude of the vertical integral of tracer at that location. (c–e) Meridional transects of the dye patch, after applying ADCP correction. Contour lines and shading indicate dye concentration in ppb, with ticks along the left and bottom of each panel marking the vertical and horizontal resolution of the binned data. The thick solid line in each panel marks the center of mass as a function of depth, while thick dashed lines show the width, $4\sigma(z)$, of the patch as a function of depth. In all cases, transects have been plotted so that the right of the figure is eastward. The insets to (c–e) show a plan view of station locations for the entire survey, with the relevant transect indicated by a bold line.

casts were "snipped" into individual up and down profiles, and a horizontal position for each profile was computed as the distance from the starting point of the dye injection. A Lagrangian correction was then applied to these positions using the integrated ADCP velocity at the target depth. This accounts for the advection of the dye patch throughout each survey.

Dye concentration was computed as a function of potential density, and then transformed back into a vertical distance coordinate using the mean potential density vs. pressure relationship averaged over each survey. (This effectively removes variability due to internal waves from vertical diffusivity estimates.) In contrast to traditional CTD rosette casts, the CTD sensors on the dye sampling sled were always on the leading edge of the sled's instrument package and did not suffer from wake effects of the sled. Therefore, both up and down casts are used in the present analysis. However, measurements may have suffered from potential flow effects, i.e., stagnant flow at the leading edge of the sled, for which no correction has been made.

The first survey of the 1995 pilot study yielded three transects in which significant concentrations of dye were found (Figure 4.9). Integration of the shipboard ADCP data as described above suggests that these three transects sampled nearly the same water; hence they provide little information regarding the zonal extent of the patch. In this respect, the first survey was somewhat incomplete. However, despite the poor coverage, useful information can still be gleaned from these data. The patch was fairly well homogenized and somewhat Gaussian in shape both in the horizontal and vertical directions. The significant vertical tilting of the patch between the first and third transects also suggests the possible importance of vertical shears (Chapter 6).

Survey 2

The second survey for the pilot experiment was performed between 42 and 61 hours after the injection and consisted of twelve zonal transects through the dye patch (Figure 4.10). A plan-view map of the vertical integral of tracer using two-dimensional kriging is shown in Figure 4.10a (this mapping procedure follows Ledwell et al., 1998; and Journel and Hui-

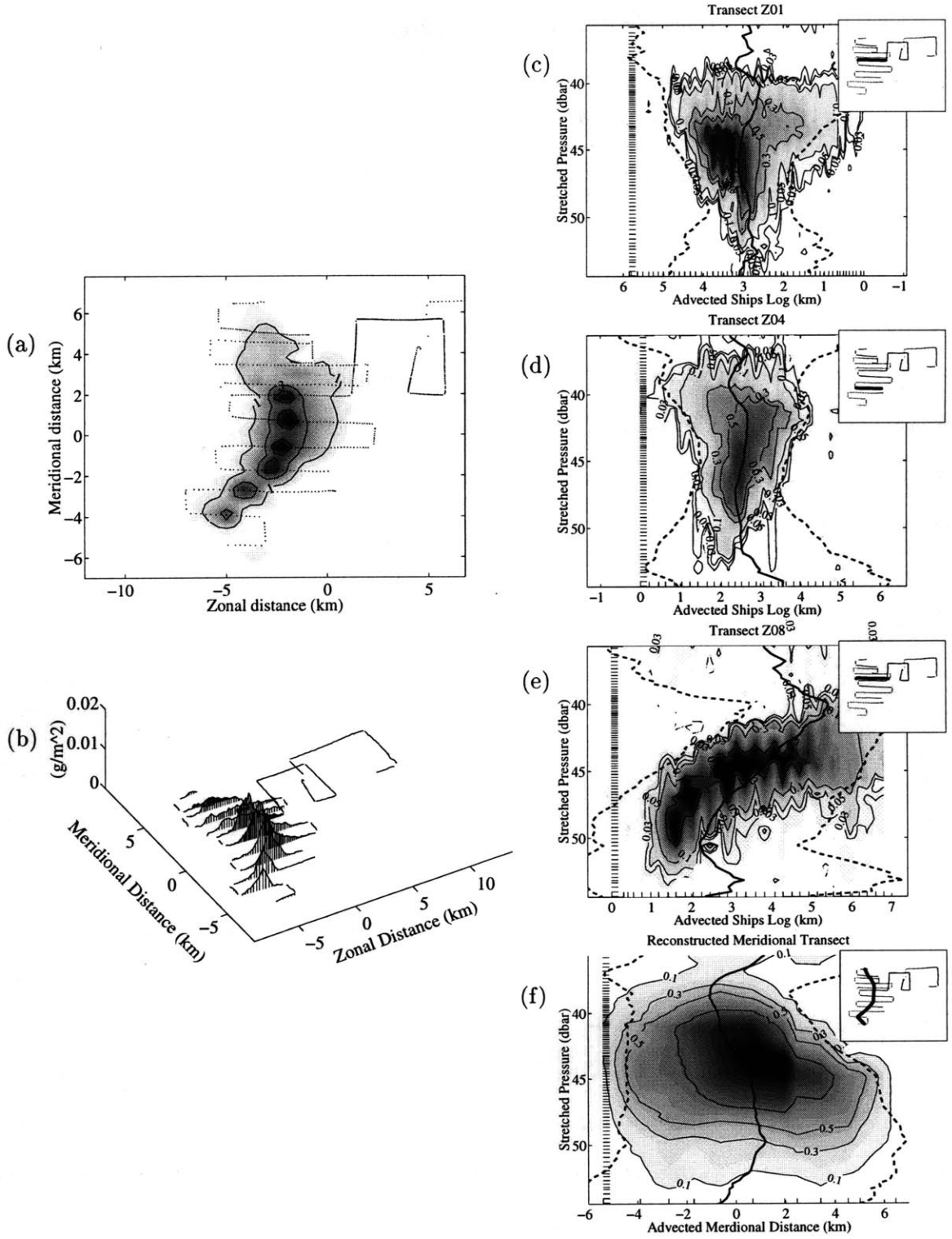

Figure 4.10: Overview of Survey 2 of the 1995 pilot study. Key is similar to Figure 4.9. Only selected zonal transects are shown in (c–e). (f) Meridional transect constructed from dye concentration along the center of mass in the zonal direction. Note the different horizontal scales.

jbregts, 1978; and is a generalized form of the objective analysis described by Bretherton et al., 1976.) This shows that the patch boundary was well delimited during this survey. A mass budget based on this map indicates that all of the dye patch was found during this survey.

Transects for this survey show that the patch remained fairly homogeneous in both the horizontal and vertical directions. However, superimposed on the broader-scale dye distribution some variability in the concentration can also be seen with scales of a few hundred meters horizontally and a few meters vertically. Significant vertical tilting of the patch can again be seen over the course of the survey, this time in the zonal rather than meridional direction, consistent with the direction of the transects. Horizontal elongation of the patch is also evident, with the major axis oriented in approximately the north/south direction. A meridional section was constructed from the these data. The dye concentration plotted as a function of meridional distance along the center of mass in the zonal direction is shown in Figure 4.10f. This section also shows significant vertical tilting of the dye patch.

Drogues

Three holey sock drogues deployed during this experiment were released along with the dye: one at the beginning of the injection, one at the mid-point, and one at the end (Figure 4.6). ARGOS positions were obtained 4-5 times per day and had an estimated accuracy of 0.5-1.0 km. The drogues stayed with the tracer patch for most of the experiment, except for the final day when two of them drifted eastward at approximately 10-20 cm s^{-1}. Windage may have contributed to this drift; however, windage can not explain why the drogues were transported at different rates. Unfortunately, the limitations of both the spatial and temporal resolution of these data make it difficult to infer a horizontal velocity shear from the drogues alone.

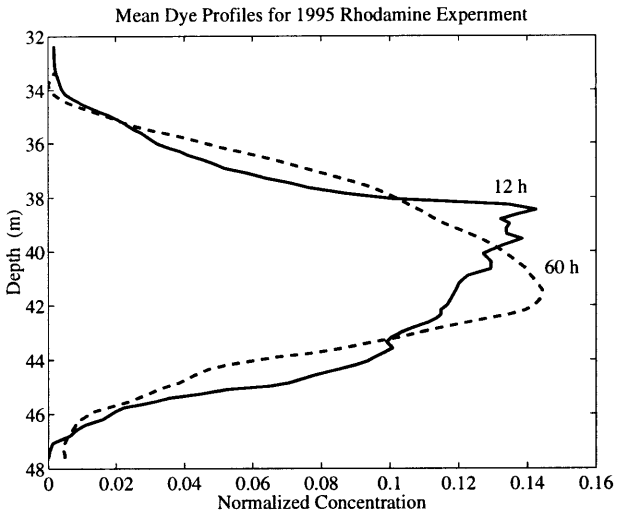

Figure 4.11: Vertical profiles of dye concentration normalized by the vertical integral of tracer for the September 1995 dye study.

Vertical Dispersion

Mean vertical profiles for the two surveys of this experiment are shown in Figure 4.11. For both the surveys the mean vertical variance was $\sigma_z^2 \approx 6.9$ m^2, which corresponds to a mean vertical extent of $4\sigma_z \approx 10.5$ m. Some possible explanations for the consistency of this variance between the two surveys are offered in the next chapters.

Bounds on the vertical dispersion for this experiment are obtained from the estimated initial condition and the above vertical variances. If the first survey is used as the initial condition, then the zero growth in variance between the first and second surveys yields a lower bound on the vertical diffusivity of zero. However, since the large vertical variance estimated for survey 1 may have been an artifact of the poor spatial coverage of that survey, the vertical diffusivity might better be estimated without those data. Assuming that the initial condition was a delta function in z, and considering the variance from the second survey, a Fickian diffusion model yielded an upper limit on the diffusivity of $\kappa_z \leq 1.5 \times 10^{-5}$ m^2 s^{-1}.

4.3 1996 Dye Cruise

The second cruise of the CMO dye studies was performed aboard the R/V Oceanus (leg 287) from yeardays 248–262 (September 4–18), 1996. Data were collected from CTD casts, the dye injection and sampling systems, the shipboard ADCP, shipboard meteorological instruments, and drogues. Two dye experiments were performed, the first using rhodamine and the second using fluorescein. During this cruise, and also the 1997 cruise, dissipation rates of temperature variance and turbulent kinetic energy were also measured by Oakey and Greenan (1998); these observations are discussed briefly in Chapter 7.

4.3.1 Environmental Conditions

Hydrography

Hydrographic transects were made during the 1996 cruise on days 249, 252, and between days 261–262. The first transect consisted of 23 stations extending from approximately the 40 m to the 420 m isobath (Figure 4.12). As in the 1995 hydrographic section, the shelf-slope front is seen to intersect the bottom at around the 100 m isobath and extend toward the surface farther off-shore. The cold pool is also visible in the temperature record, again just inshore of the shelf-slope front. Unlike the 1995 section, however, this section shows no warm saline water intruding from offshore in the surface layers. In fact, on average, the shelf water was as much as 5 ^{o}C colder and 2–3 PSU fresher during this section compared to that of 1995. Some of the differences in water properties are undoubtedly due to the passage of hurricane Edouard between days 245–246, 1996, which likely caused significant mixing over the shelf.

The second hydrographic transect was conducted on day 252 between surveys of the rhodamine dye experiment and consisted of 9 stations between the 60 m and 80 m isobaths (Figure 4.13). This transect was a subset of the stations occupied during the transect on day 249. Its purpose was to provide a rapidly sampled hydrographic survey in the vicinity of the rhodamine dye shortly after it was injected.

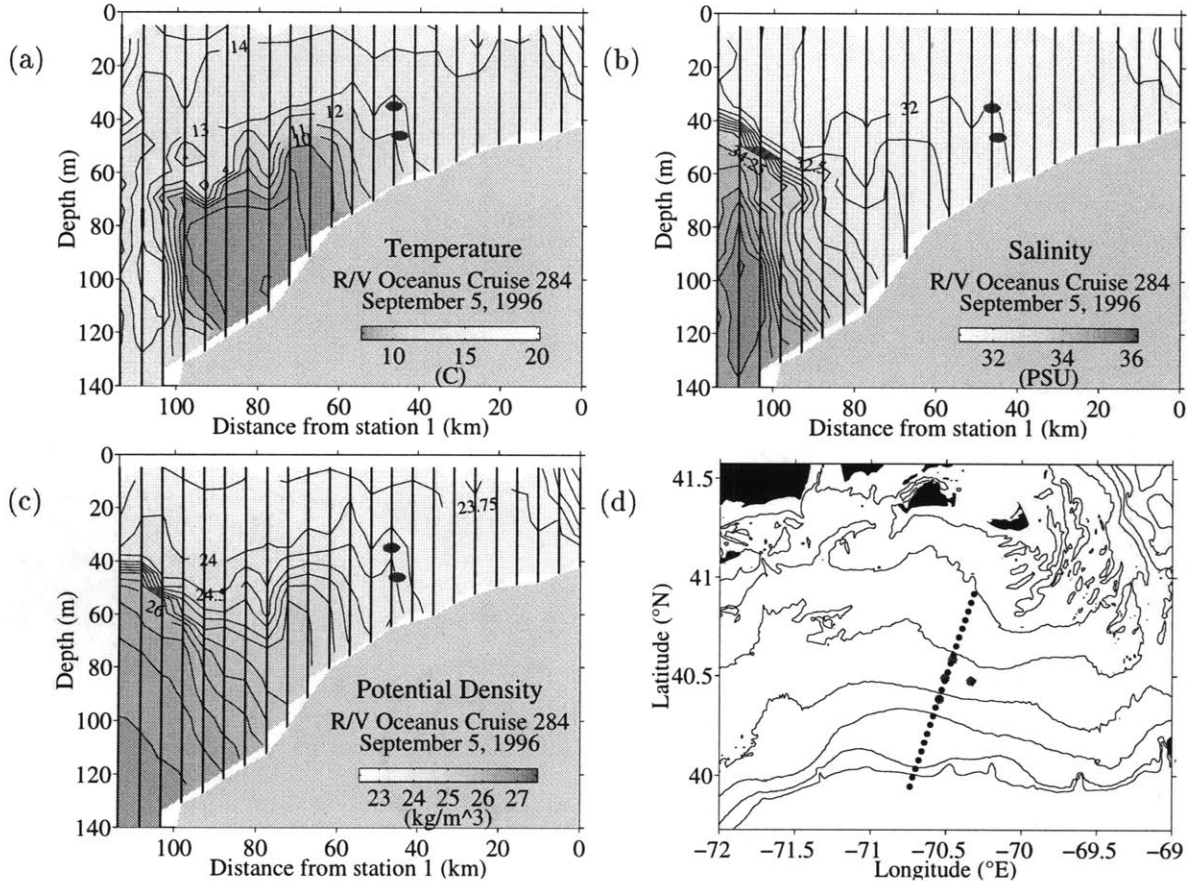

Figure 4.12: Hydrography data collected on day 249, 1996. The relative locations of the rhodamine and fluorescein dye injections are shown as bold ellipses. Key is similar to Figure 4.2.

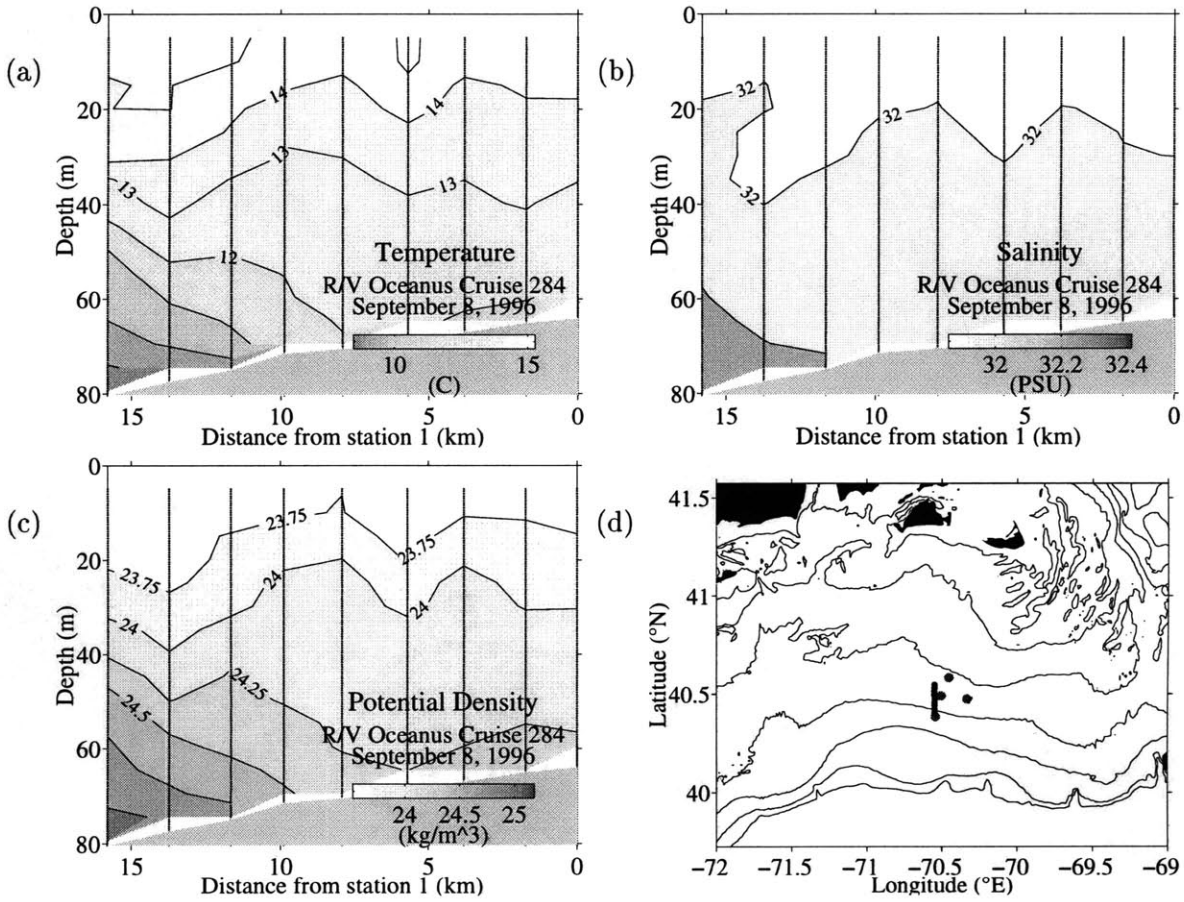

Figure 4.13: Hydrography data collected on day 249, 1996. Key is similar to Figure 4.2.

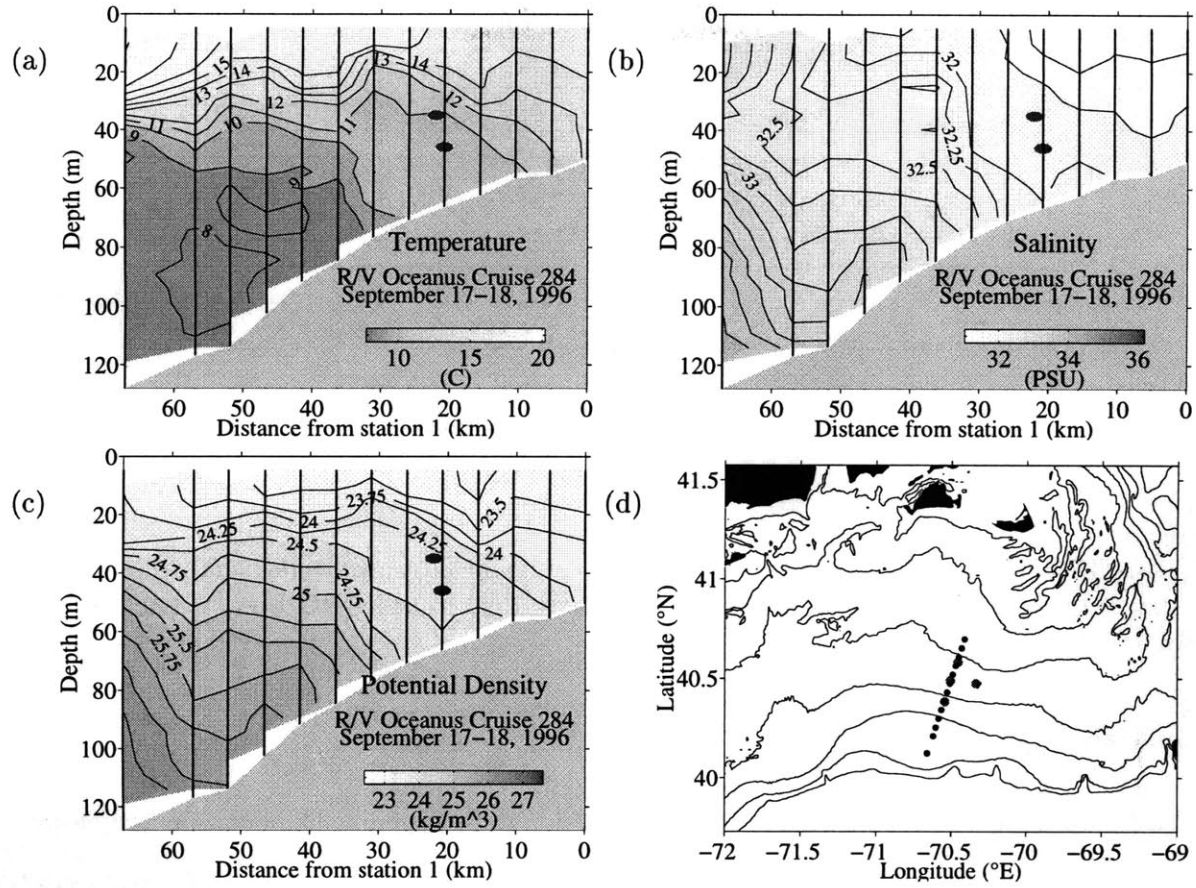

Figure 4.14: Hydrography data collected on days 261–262, 1996. Key is similar to Figure 4.2.

The final hydrographic survey was performed on days 261–262 during the return trip to Woods Hole, MA. The 13 stations occupied in this transect were a subset of the stations occupied during the first hydrographic survey of this cruise, and extended from the 50 m to the 120 m isobath (Figures 4.14). In this transect, the shelf-slope front is much less pronounced compared to previous transects; however, the foot of the front is still located near the 100 m isobath. Figure 4.14a shows significant warming in the upper water column relative to the first transect of this cruise. This 2 ^{o}C difference is presumably the result of surface heat fluxes. Buoyancy frequencies for this transect ranged from 0 – 20 cph, with typical values remaining around 10 cph near the dye study area.

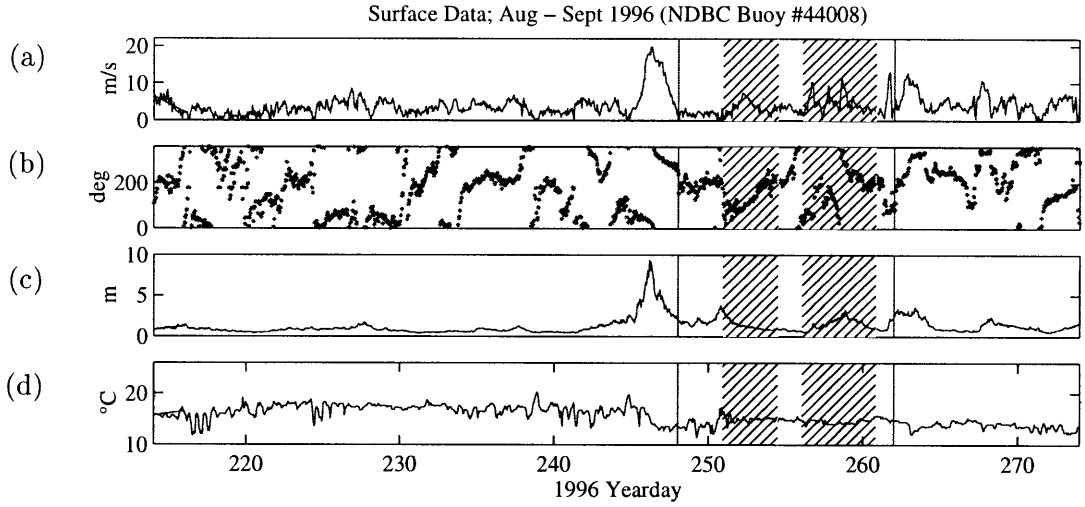

Figure 4.15: Wind (a) speed and (b) direction, (c) significant wave height, and (d) sea surface temperature for days 214–274 (August–September) 1996 from NDBC Buoy #44008. Key is similar to Figure 4.3.

Surface Conditions

During the 1996 dye cruise, wind speed and direction were logged by shipboard meteorological sensors as well as from NOAA / NDBC Buoy #44008 (Figure 4.15). Because wind records from these two sensors appear to be well correlated for the entire duration of the dye cruise, only the NDBC data are displayed as they provide a longer record.

Buoy data for days 214–274, 1996 generally show light winds, of order 3–5 m s^{-1}, compared to the same period in 1995, with the notable exception of two major wind events. The first of these events, between days 245–246 was due to the passing of hurricane Edouard almost directly over the CMO study site. During this period, the Nantucket NDBC buoy shows sustained winds of up to 20 m s^{-1}, with corresponding significant wave heights reaching nearly 10 m and sea surface temperature dropping from approximately 18 ^{o}C to less than 15 ^{o}C. The effects of Edouard can also be seen in the hydrographic section taken on day 249, which shows a fairly well-mixed upper water column, in marked contrast to the same period in 1995 (Figure 4.12).

The second wind event relevant to the 1996 dye studies was due to hurricane Hortense,

which passed about 400 km to the east of the study site between days 256 and 259. During this period, wind speeds reached over 10 m s^{-1} in a series of three bursts, each lasting nearly 12 hours. Although wave heights during this time generally remained below 4 m, significant vertical mixing is believed to have resulted due to inertial oscillations. This is evidenced by shipboard ADCP data, which show significant velocity shears, around 0.02–0.03 s^{-1}, extending throughout the water column (Figure 4.16).

Shipboard ADCP Observations

Velocity data were collected for the duration of the 1996 cruise, except for the brief transit to and from the CMO site, this time using a broad-band (300 kHz) shipboard ADCP (Figure 4.16). Data were averaged over 3.0 minute intervals and over 2 m depth bins ranging from 11 m to approximately 63 m. A conservative estimate for the accuracy of these averages is 3–7 cm s^{-1}. Again, precision is believed to be much better, so that shear at the same scales should be accurate to within 0.002 s^{-1}. Data loss for the ADCP during this cruise was approximately 10–15% due to difficulty with bottom tracking.

Spectral analysis of the barotropic velocity shows clearly defined peaks in tidal energy in the diurnal and semidiurnal bands, while no significant peak is visible at the local inertial frequency (Figure 4.17). Visual inspection of time series of the barotropic velocity reveals a fortnightly signal in both the zonal and meridional components. Based on these considerations, the following tidal, inertial, and mean constituents are included in a harmonic analysis of these data: M_2, S_2, O_1, K_1, f, and a mean flow.

As in the 1995 cruise, it was found that the M_2 tide was slightly polarized in the along-shelf direction (ellipticity $\approx$ 1.4), but here with an along-shelf amplitude of about 8 cm s^{-1} which is significantly smaller than the 14 cm s^{-1} of the previous year. All other tidal components analyzed had amplitudes between 2–5 cm s^{-1}, and ellipticities ranging from 1.1–1.7. Inertial wave amplitudes estimated from this fit were 2 cm s^{-1} and were polarized in the along-shelf direction (ellipticity $\approx$ 1.3). The mean flow was strongly westward along the shelf with an

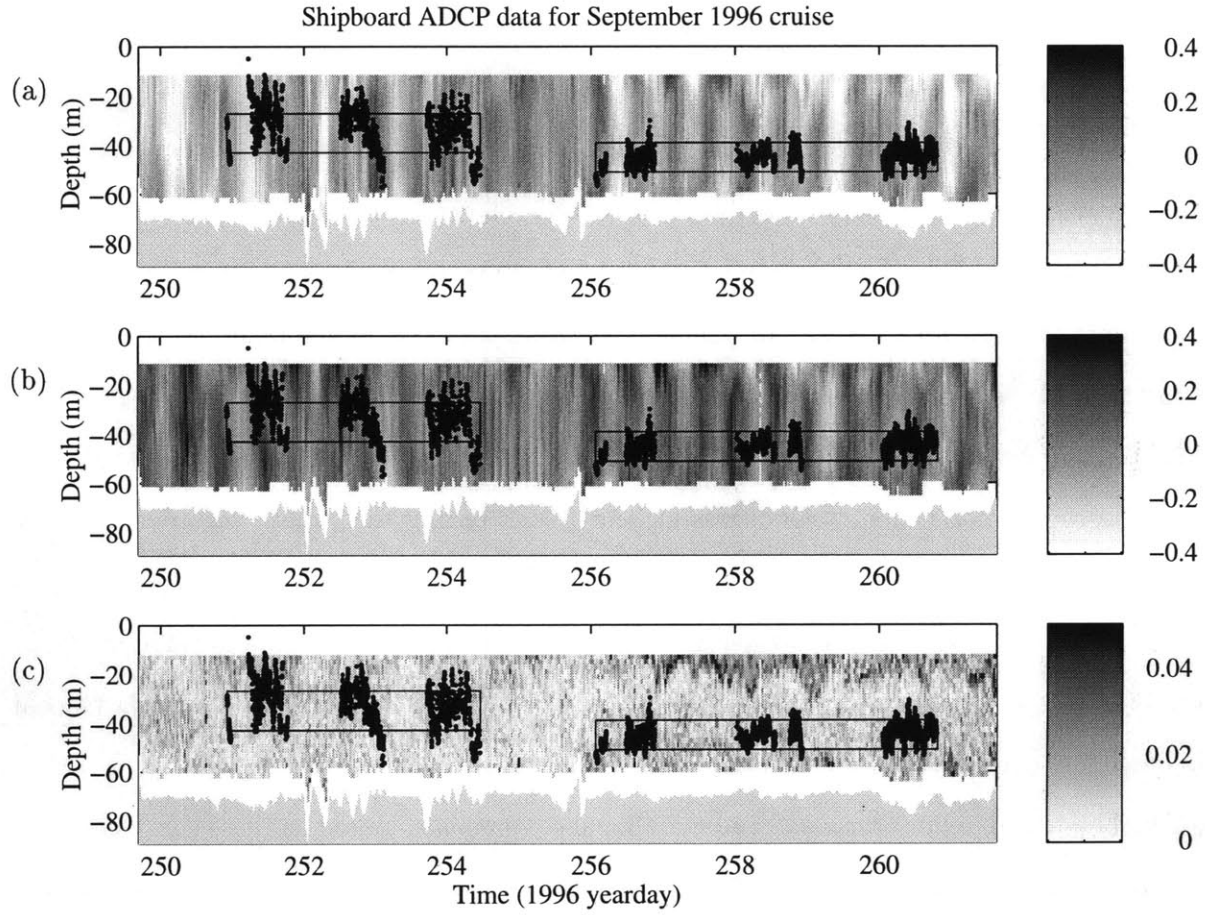

Figure 4.16: (a) Zonal and (b) meridional components of velocity and (c) the amplitude of the vertical shear from shipboard ADCP data collected during the 1996 dye cruise. Key is similar to Figure 4.4.

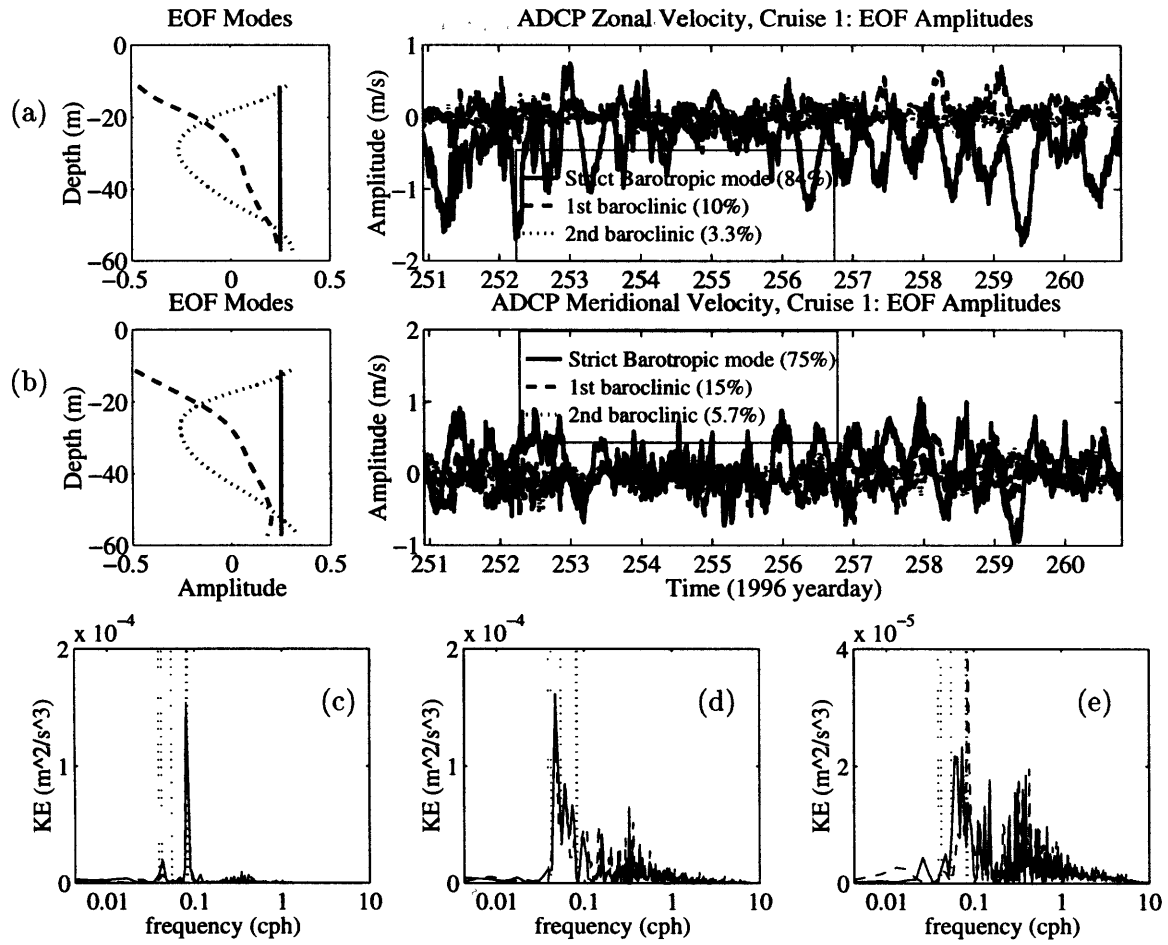

Figure 4.17: (a) Zonal and (b) meridional components of the barotropic mode and first two baroclinic modes computed from an EOF analysis of the 1996 dye cruise shipboard ADCP data. (c,d,e) Spectra for each of the three modes. Key is similar to Figure 4.5.

amplitude of 11 cm s^{-1}. Together the fitted constituents account for about 40% of the total variance in the barotropic mode.

For the period between the first injection and the end of the last survey of the second experiment, an EOF analysis for the vertical structure shows that the barotropic mode accounts for 75%–85% of the overall variance in these data. The first and second baroclinic modes account for 10%–15% and 4%–6% of the variance, respectively (Figure 4.17). Time series of mode amplitudes show that the first baroclinic mode is largely dominated by inertial oscillations, most markedly between days 257–261. Again this is seen frequency spectra of the

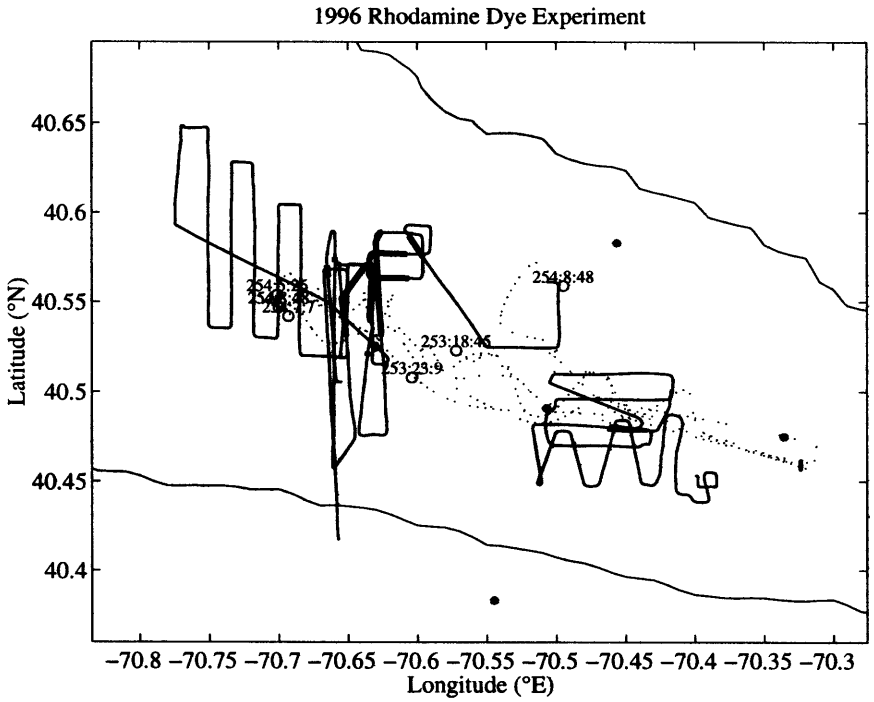

Figure 4.18: Overview of the 1996 rhodamine dye experiment showing the ship track during the injection and three subsequent dye surveys. Key is similar to Figure 4.6.

mode amplitudes, which show that both the 1st and 2nd baroclinic modes are quite energetic in the tidal and inertial bands.

4.3.2 Experiment 1: Rhodamine Dye and Drogues

The first dye experiment of the 1996 cruise was conducted between days 251–255. Rhodamine dye was released in a single streak and subsequently sampled over the course of five days during three surveys. Six holey sock drogues were also released during or immediately following the injection. An overview of surveys during this experiment along with the drogue trajectories is shown in Figure 4.18. As in 1995, stratification remained fairly constant over the course of the experiment, as shown by the mean density and buoyancy frequency profiles (Figure 4.19). However, in this experiment, average buoyancy frequencies at the level of the dye were lower, only 5–6 cph compared to about 12 cph in 1995. (Figure 4.19b).

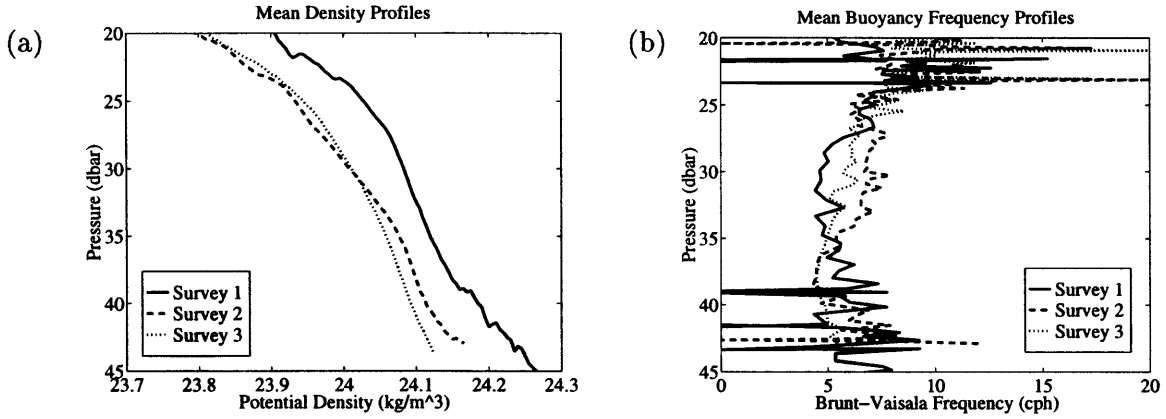

Figure 4.19: (a) Mean density profiles and (b) mean buoyancy frequency profiles for the injection and two surveys of the 1996 rhodamine dye experiment showing a relatively constant stratification over the course of the experiment.

Injection

The injection cast for the 1996 rhodamine dye experiment was performed on day 251 while the ship was steaming southward at 1 kt. The injection cast began with a CTD profile to 50 m in an overall water depth of 70 m (Figure 4.20). The injection sled was then brought to the target density surface, $\sigma_\theta = 24.063$ kg m^{-3}, or 40 m depth, and a total of 100 kg of dye released over a period of one hour. The standard deviation in density for this injection was 0.0035 kg m^{-3}, which due to the low stratification in this part of the water column corresponded to a standard deviation in pressure of 2.5 dbar.

Time series of the CTD data indicate that the depth of the target density surface steadily increased during the injection, from 30 m when pumping began to over 45 m an hour later (Figure 4.20c–e). It is not clear to what extent this change in depth is the result of a temporal or spatial trend, i.e., whether it is the result of internal waves or some geostrophically balanced flow. (If interpreted as a strictly spatial trend, the corresponding tilt in isopycnals would be in the opposite sense as seen in the hydrographic survey of day 249; Figure 4.12). Despite these variations in the depth of the target surface, the time series show that the temperature and salinity remain fairly constant during the injection. This is also seen in the T-S plot of these

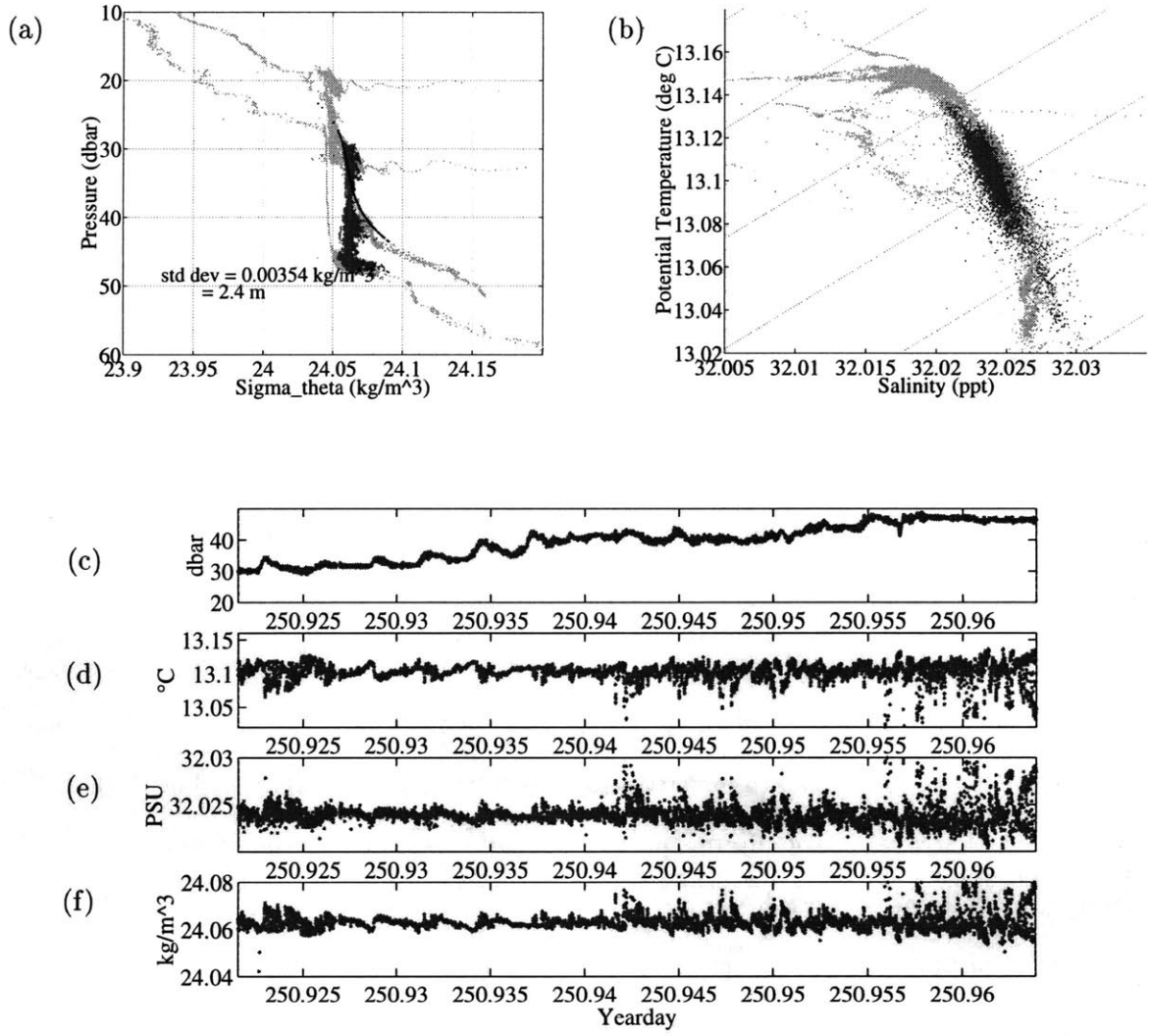

Figure 4.20: (a) Density profile, (b) temperature-salinity diagram, and time series of (c) pressure, (d) potential temperature, (e) salinity, and (f) potential density for the dye injection of the 1996 rhodamine dye experiment. Key is similar to Figure 4.8.

data, which shows minimal scatter along the target isopycnal (Figure 4.20b).

Survey 1

The first survey of the 1996 rhodamine dye experiment was performed between 7 and 20 hours after injection and yielded ten transects with significant dye concentrations (Figure 4.21). Six meridional and two zonal transects spanned the whole patch, and two provided incomplete sections of the dye. A mass budget indicated that virtually all of the dye was found during this survey.

As in the 1995 experiment, the dye appeared well-homogenized in both the horizontal and vertical directions, although again some smaller-scale variability in concentration can be seen in individual transects. Significant vertical tilting was again evident in both the meridional and zonal transects. Figures 4.21a and b show that the patch was also slightly elongated in the southwest/northeast direction; however, estimates of the major and minor axes discussed in Chapter 5 indicate only a slight ellipticity.

Survey 2

The second survey for the 1996 rhodamine dye experiment was performed between 38 and 53 hours after injection. Due to problems with the real-time data display on-board the ship, this survey provided only eight transects through the dye patch (Figure 4.22). Of these, only one, transect M05 (Figure 4.22f), appears to have spanned the dye patch. A mass budget indicates that only 45% of the dye was accounted for in this survey.

In contrast to the fairly smooth dye distributions seen in the 1995 experiment and in the first survey of this experiment, transects from this survey show significant patchiness in the tracer distribution, both zonally and meridionally. The non-Gaussian distributions seen in Figure 4.22c–f show multiple distinct maxima in the tracer concentration in both zonal and meridional transects.

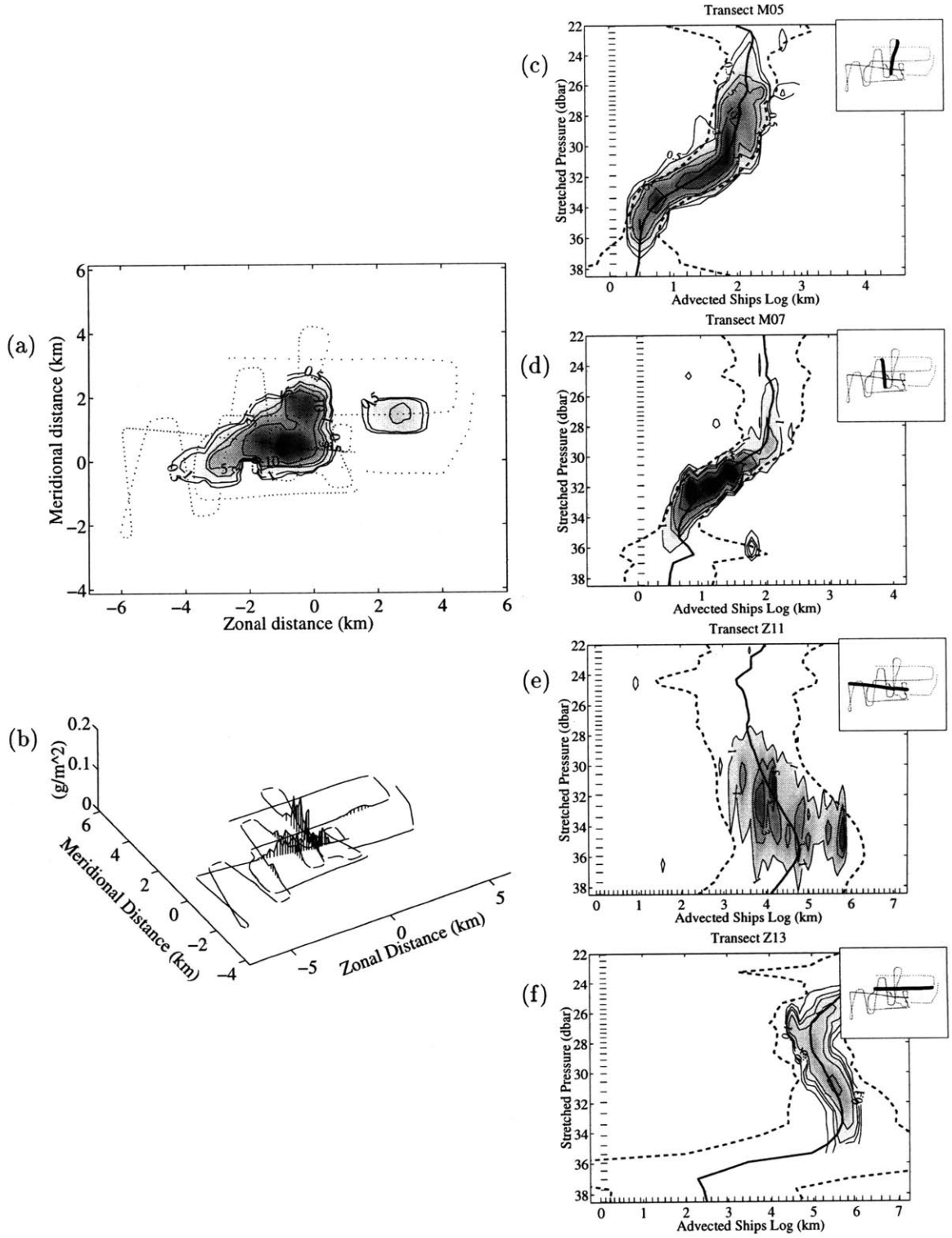

Figure 4.21: Overview of survey 1 of the 1996 rhodamine dye study. Key is similar to Figure 4.9. Note the different horizontal scales.

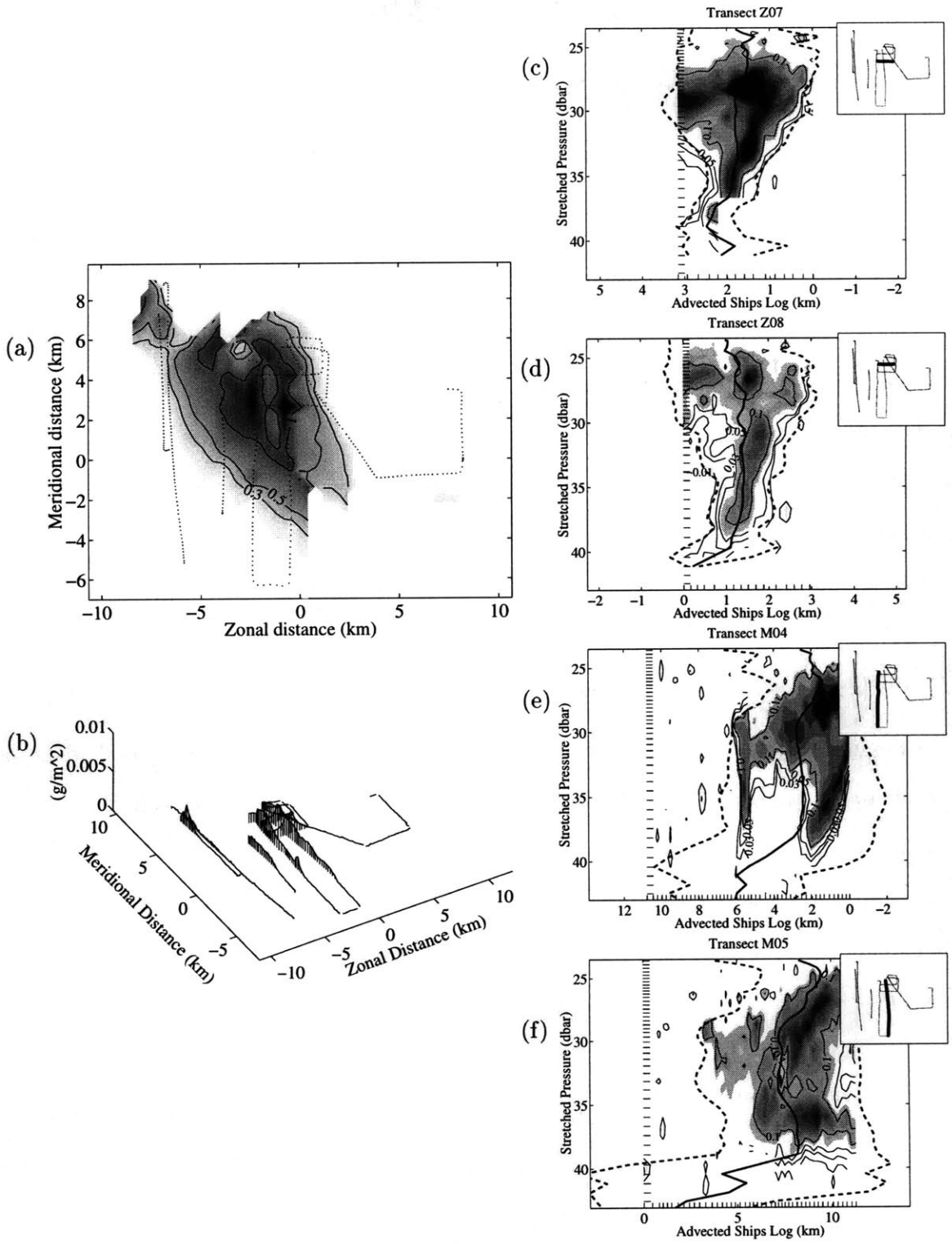

Figure 4.22: Overview of survey 2 of the 1996 rhodamine dye study. Key is similar to Figure 4.9. Note the different horizontal scales.

Survey 3

The final survey of the 1996 rhodamine dye experiment was performed between 67 and 85 hours after injection, and provided nine transects through the dye patch (Figure 4.23). This was the most complete survey performed in this experiment due to the regular spacing between transects and because it clearly delimited the patch boundaries. However, a mass budget indicates that approximately 38% of the dye was found during this survey.

The meridional transects in Figures 4.23c–e show significant homogenization of the patch compared to the previous survey, although patchiness is still evident. Some vertical tilting of the tracer patch is also seen in these transects, although it is not nearly as pronounced as that observed in the 1995 experiment. A zonal section through the patch was re-constructed in a manner similar to Survey 2 of the 1995 experiment, and also shows vertical tilting. A northwest/southeast elongation of the patch is also evident in this survey.

Drogues

Four drogues tethered at 35 m were released at regular intervals during the period when the dye was being pumped. Two additional drogues tethered at the same depth were also released on opposite sides of the injection streak, transverse to the streak axis so as to effectively form a cross. Figure 4.18 shows the trajectories of all six drogues relative to the dye patch. Again, the drogues appeared to track the patch, although their positions relative to one another changed over time.

Vertical Dispersion

Mean vertical profiles of dye from each of these surveys are shown in Figure 4.24. For the first survey, the mean vertical variance was $\sigma_z^2 \approx 12.9$ m^2, which corresponds to a mean vertical extent of $4\sigma_z \approx 14.4$ m. By the final survey, the variance had grown to $\sigma_z^2 \approx 22.8$ m^2, or a vertical extent of $4\sigma_z \approx 19.1$ m. Using a Fickian diffusion model, a best-fit to the data implies

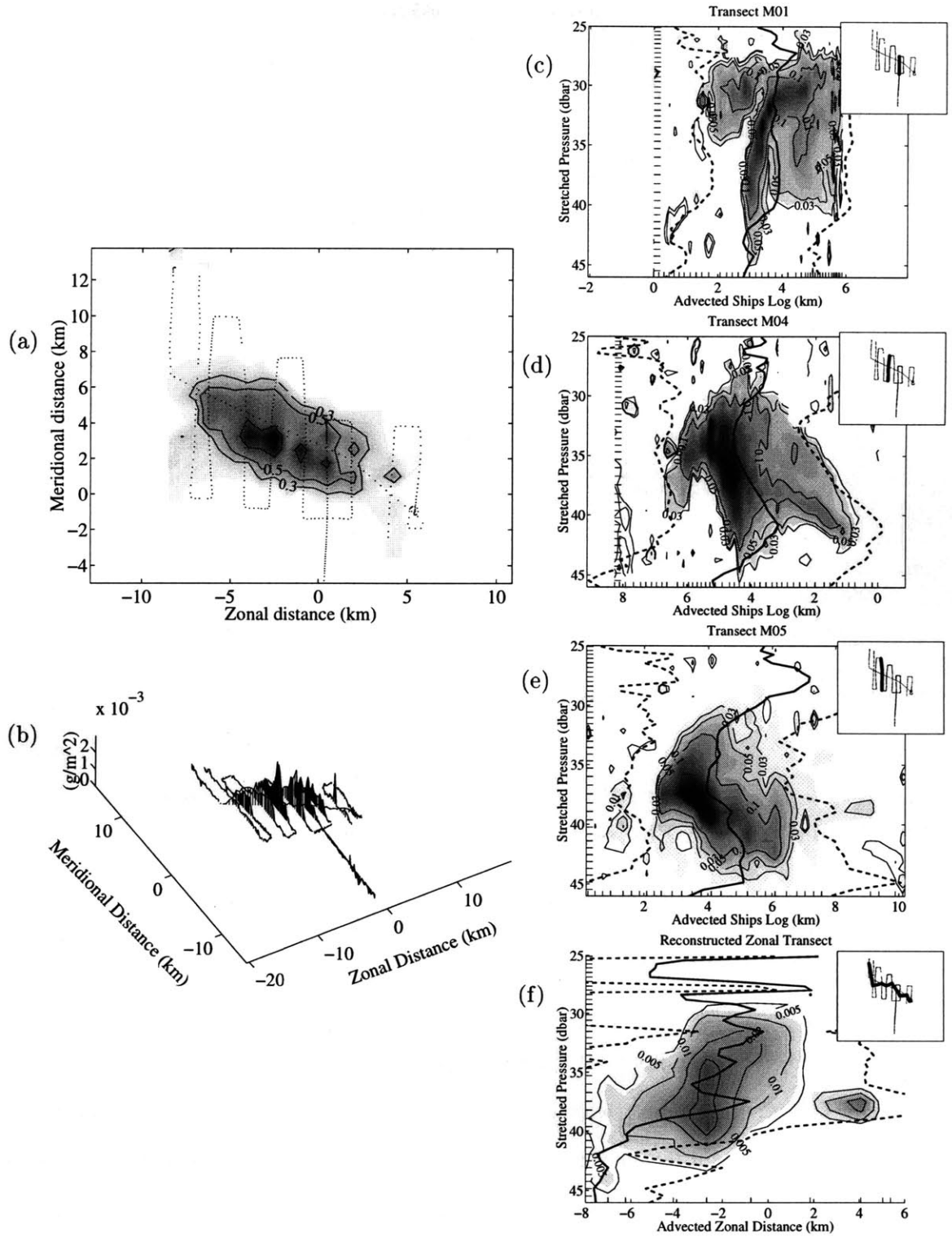

Figure 4.23: Overview of survey 3 of the 1996 rhodamine dye study. Key is similar to Figure 4.9. Note the different horizontal scales.

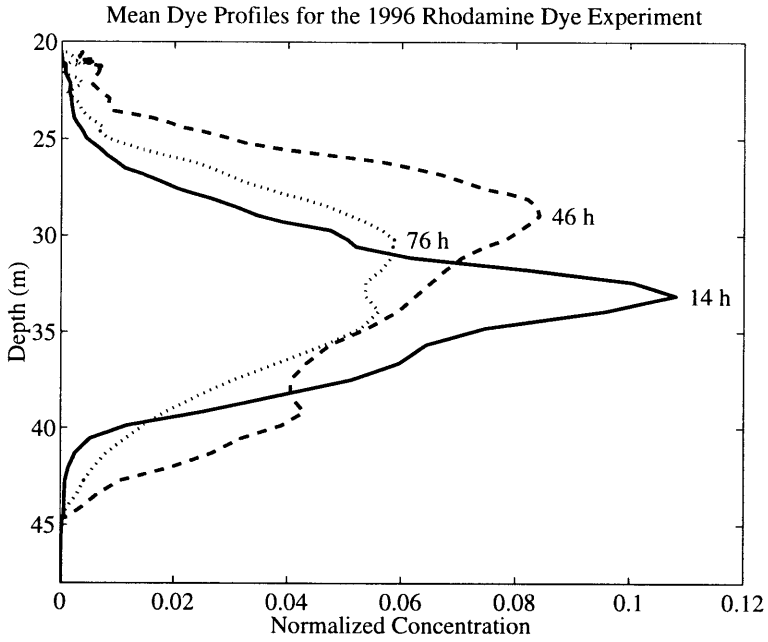

Figure 4.24: Vertical profiles of dye concentration normalized by the vertical integral of tracer for the 1996 rhodamine dye study.

a vertical diffusivity of $\kappa_z = 1\text{–}3 \times 10^{-5}$ m^2 s^{-1}.

4.3.3 Experiment 2: Fluorescein Dye and Drogues

The second dye experiment of the 1996 cruise was conducted between days 257–261. Fluorescein dye was released in a series of closely spaced streaks, and subsequently sampled during three surveys. The injection for this experiment was not as clean as the previous one due to clogging problems with the injection system. Also, due to the threat of hurricane Hortense, three holey sock drogues were released during the second survey rather than during the injection. Survey tracks during the three surveys along with the limited drogue trajectories are shown in Figure 4.25. As in the previous experiments, stratification remained fairly constant. (Figure 4.26). Buoyancy frequencies ranged from 8 to 15 cph, with typical values of 12 cph at the level of the dye. (Figure 4.26b).

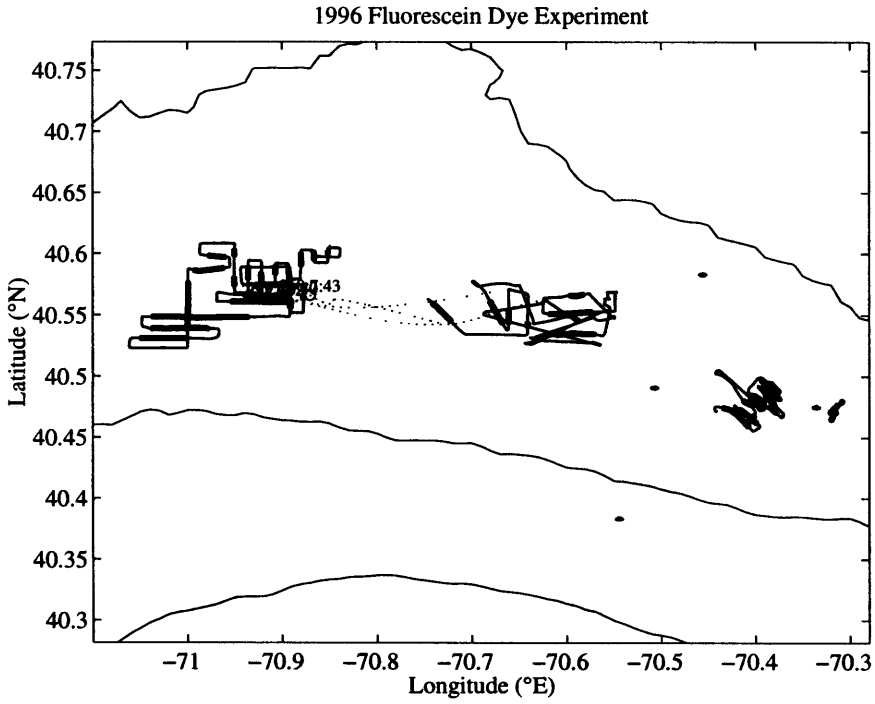

Figure 4.25: Overview of the 1996 fluorescein dye experiment showing the ship track during the injection and three subsequent dye surveys. Key is similar to Figure 4.6.

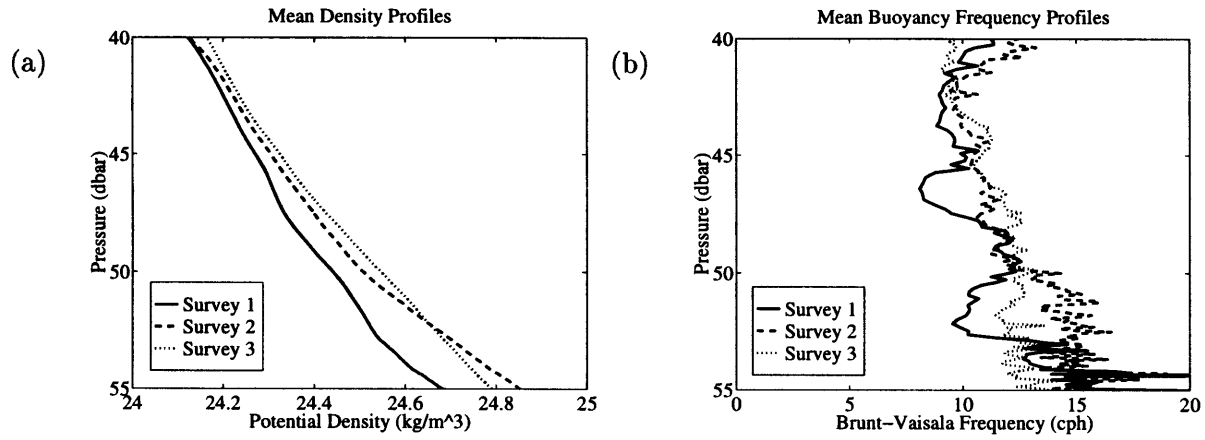

Figure 4.26: (a) Mean density profiles and (b) mean buoyancy frequency profiles for the injection and two surveys of the 1996 fluorescein dye experiment showing a relatively constant stratification over the course of the experiment.

Injection

Injection began on day 257 with the ship under way at 1 kt, at a northeast heading of 50 degrees. Due to clogging in the injection system, the dye pumps were stopped and re-started several times, so that the injection streak was discontinuous. After three failed injection attempts, each lasting less than 10 min, the system was recovered and modified to flow more freely. The ship was then re-positioned, and the injection completed in two additional pumping sequences lasting 15 min and 35 min, respectively. The total inject time was about 1 hour spread over a 4 hour time period.

The target density for this injection was $\sigma_\theta = 24.03$ kg m^{-3}, which corresponded to a depth of 50 m. During subsequent surveys of the patch, the target surface was at 46 m depth. Again, 100 kg of dye were released along the target surface, with a standard deviation of 0.0067 kg m^{-3}, or 0.19 dbar. Density profiles during injection are shown in Figure 4.27. Accounting for the separation of the injection streaks, the overall length of the injection was between 0.4–1.0 km based on a Lagrangian-corrected map of the injection.

The T-S diagram of injection CTD data shows localized clusters of data points associated with the different periods when the dye was being pumped. These clusters imply a change in water mass properties from one portion of the injection streak to another. This variability can also be seen in the time series of the CTD data, and indicates a trend of colder, fresher water to the northeast (Figure 4.27). The time series also indicate that the depth of the target density surface was greater at the end of the injection than at the beginning, although it is again unclear whether this is a result of spatial or temporal variability.

Survey 1

The first survey of the 1996 fluorescein dye experiment was performed between 10 and 20 hours after the start of the injection (Figure 4.28). Ten transects oriented in the northwest/southeast direction and one short transect in the southwest/northeast direction yielded significant con-

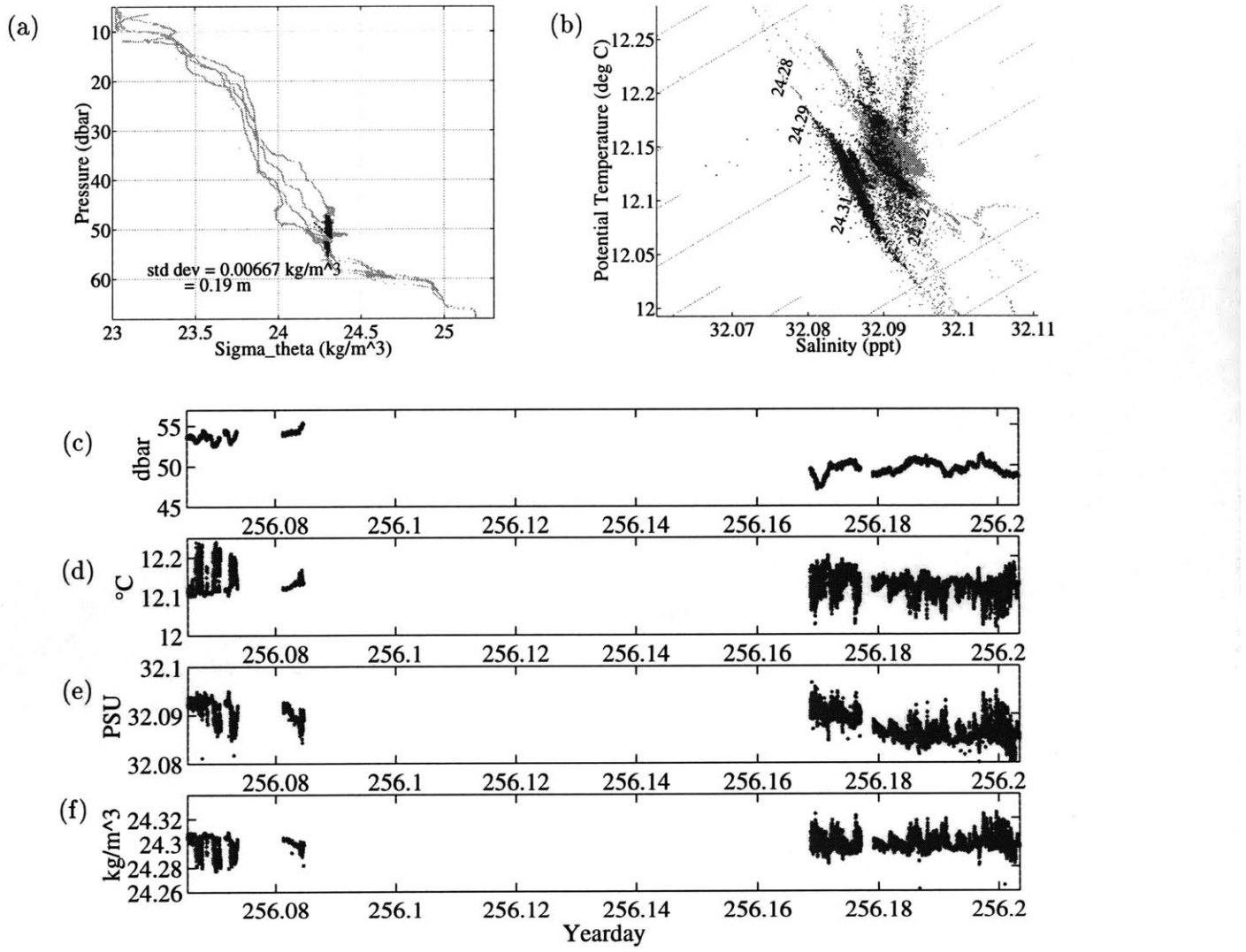

Figure 4.27: (a) Density profile, (b) Temperature-Salinity diagram, and time series of (c) pressure, (d) potential temperature, (e) salinity, and (f) potential density for the 1996 fluorescein dye experiment. Key is similar to Figure 4.8.

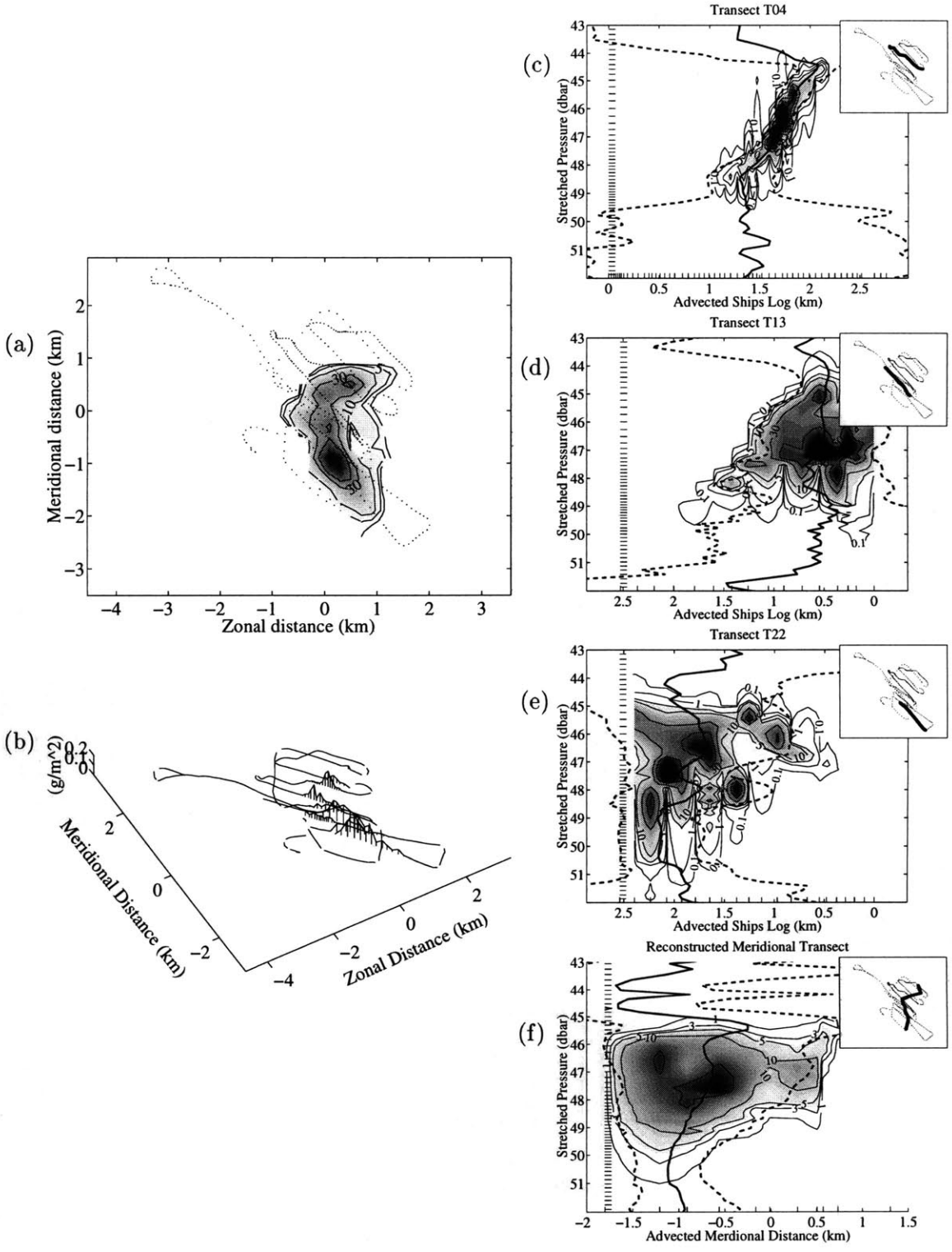

Figure 4.28: Overview of survey 1 of the 1996 fluorescein dye study. Key is similar to Figure 4.9. Note the different horizontal scales.

centrations of dye. The patch was well delimited by this survey and was somewhat elongated in the north/south direction. A mass budget shows that all of the dye was accounted for.

Although in some transects the dye patch appears homogeneous and even Gaussian in shape, other transects show dye distributions which are quite patchy and disjointed (Figure 4.28e,f). These distributions lie in the southwest part of the patch where the injection itself was more inhomogeneous. Consequently, it is more likely that patchy distribution stems from the sporadic release of dye rather than from some stirring mechanism which acted on the patch after the injection. As in earlier experiments, significant vertical tilting of the dye patch is evident throughout this survey. A meridional transect was re-constructed as in earlier experiments and also shows vertical tilting (Figure 4.28f).

Survey 2

The second survey for the 1996 fluorescein dye study was performed between 47 and 68 hours after the start of the injection, and yielded three zonal and four meridional transects containing dye (Figure 4.29). A mass budget indicates that all of the dye was found during this survey.

As in the first survey, homogeneous and patchy dye distributions are visible, depending on the transect examined. It is unclear whether this patchiness is again a remnant of the injection discontinuity or if it is due to some physical process acting on the dye.

Survey 3

The third and final survey of the 1996 fluorescein experiment was performed between 95 and 114 hours after the start of the injection (Figure 4.30). This was the most complete survey of this experiment, incorporating twenty-one transects that delimited the dye patch very well. A mass budget shows that 70% of the patch was found.

Numerous transects of this survey show significant homogenization of the tracer patch, both in the horizontal and vertical directions. However, some transects show two or three distinct disconnected patches. Overall, the majority of the dye was located at the southwest

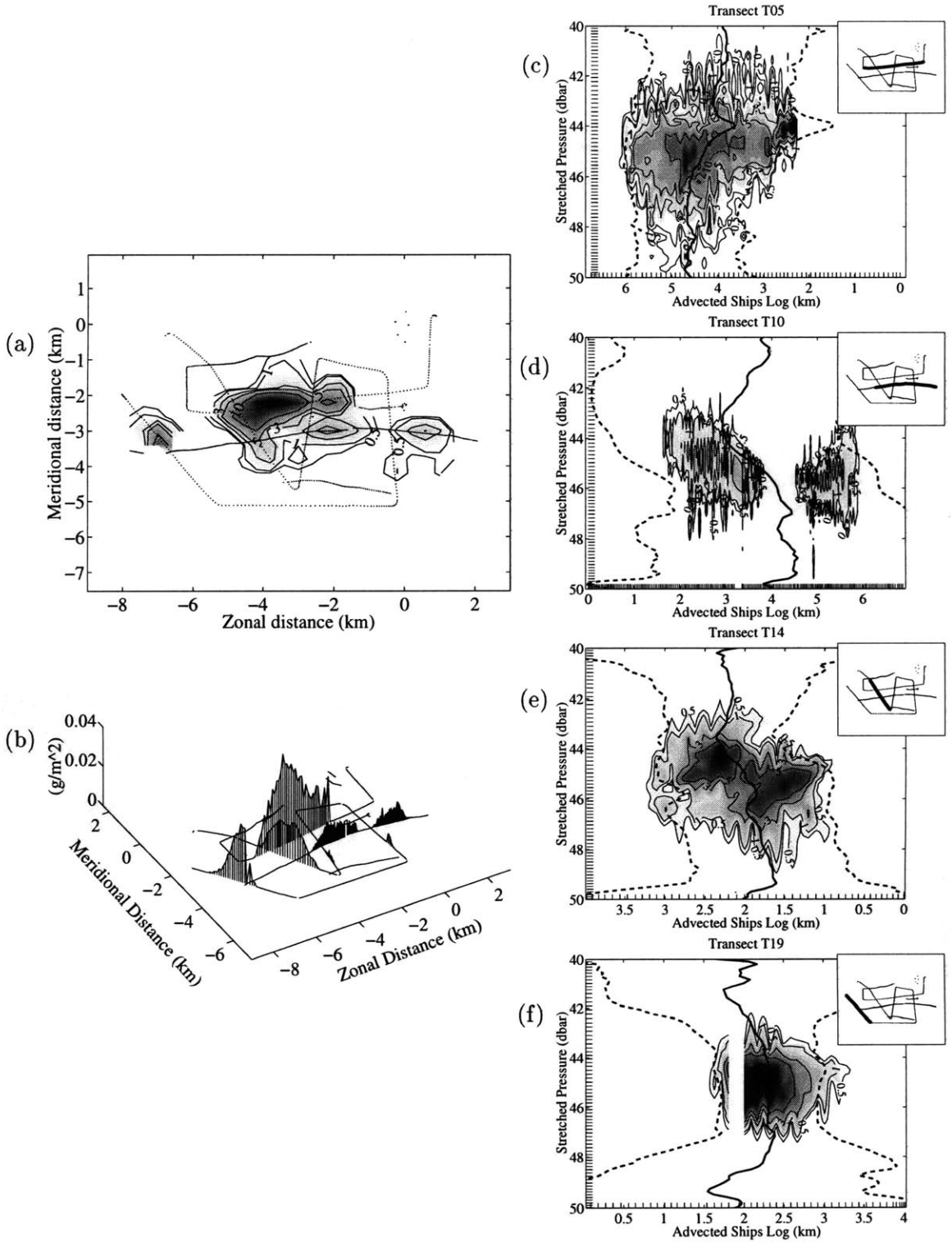

Figure 4.29: Overview of survey 2 of the 1996 fluorescein dye study. Key is similar to Figure 4.9. Note the different horizontal scales.

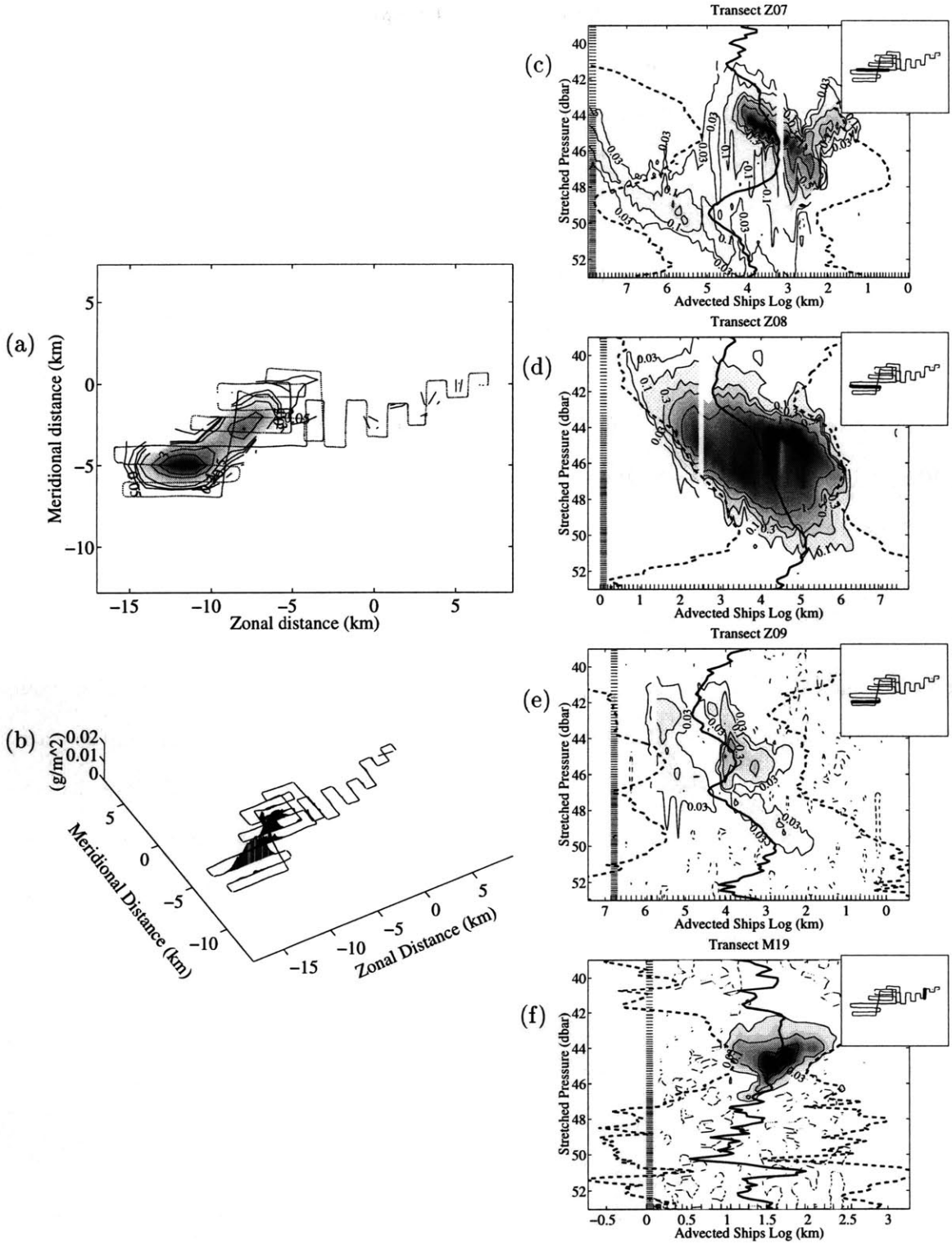

Figure 4.30: Overview of survey 3 of the 1996 fluorescein dye study. Key is similar to Figure 4.9. Note the different horizontal scales.

end of the patch, while a long thin streamer of dye extended over 10 km to the northeast. As discussed in Chapter 5, this extreme elongation of the patch suggests the presence of a significant horizontal strain or shear acting on the patch.

Drogues

The three drogues were released during the second survey rather than during the injection. Drogue release was delayed because hurricane Hortense was expected to pass through the region shortly after the injection. Fortunately, Hortense altered course to the east and the dye survey schedule was not significantly affected. The drogues tracked the patch well (Figure 4.25). However, because of the uncertainty in their positions and the short duration of deployment, they cannot provide much more information.

Vertical Dispersion

Average vertical profiles for each survey show a clear evolution of the patch over the course of the experiment (Figure 4.31). As in the other experiments, an upper bound on the vertical diffusivity was estimated by assuming a delta function initial condition for the dye. However, in this case the mean vertical profile from the third survey showed an asymmetry such that the upper half of the profile had a smaller variance than the lower. Using this profile as a final condition and assuming a Fickian diffusion model, the upper bound for the vertical diffusivity in the upper portion of the patch is $\kappa_z = 0.2 \times 10^{-5}$ m^2 s^{-1}, while in the lower portion the upper bound is $\kappa_z = 0.9 \times 10^{-5}$ m^2 s^{-1}.

4.4 1997 Dye Cruise

The third cruise of the CMO dye studies was performed aboard the R/V Oceanus (leg 309) between days 211–225 (July 30–August 13) 1997. Data were collected from CTD casts, the dye injection and sampling systems, the shipboard ADCP, shipboard meteorological instruments,

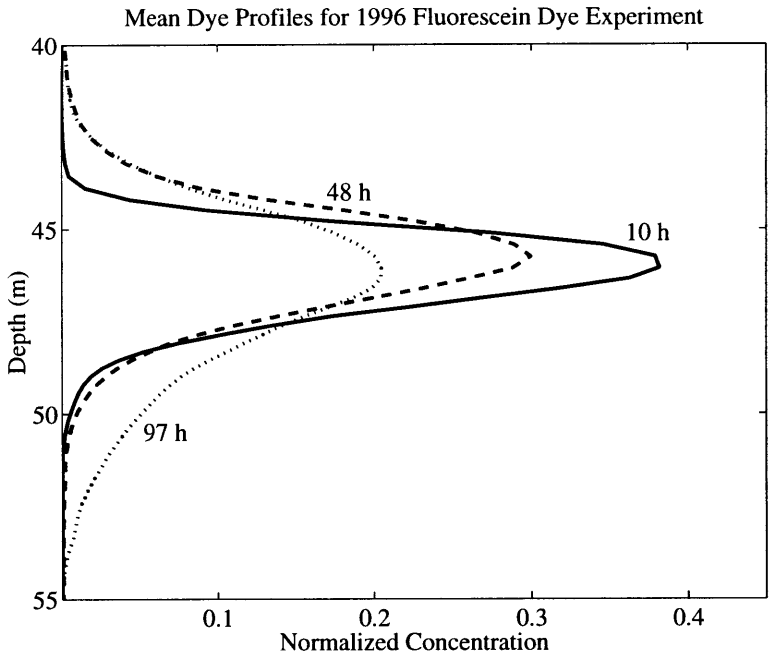

Figure 4.31: Vertical profiles of dye concentration normalized by the vertical integral of tracer for the 1996 fluorescein dye study.

and drogues. Again, two dye experiments were performed, the first using rhodamine and the second using fluorescein. Only data from the rhodamine experiment will be presented here.[4]

4.4.1 Environmental Conditions

Hydrography

Hydrographic transects were made at the beginning and end of the 1997 cruise. The first transect consisted of eighteen CTD stations extending from the 50 m to the 120 m isobath. This transect was made over a 14 hr period from days 211–212 (Figure 4.32). As seen in the salinity section of Figure 4.32b, the shelf-slope front intersected the bottom close to the 90 m isobath, approximately 10 km inshore of its climatological mean position. As in the hydrography from previous years, the cold pool was on the inshore edge of the shelf-slope front

[4]The 1997 fluorescein dye experiment was performed within the bottom boundary layer rather than higher in the water column like the other experiments. The present study focuses on lateral dispersion in the mid-water column; the additional dynamics associated with boundary layer flows are beyond the scope of this work.

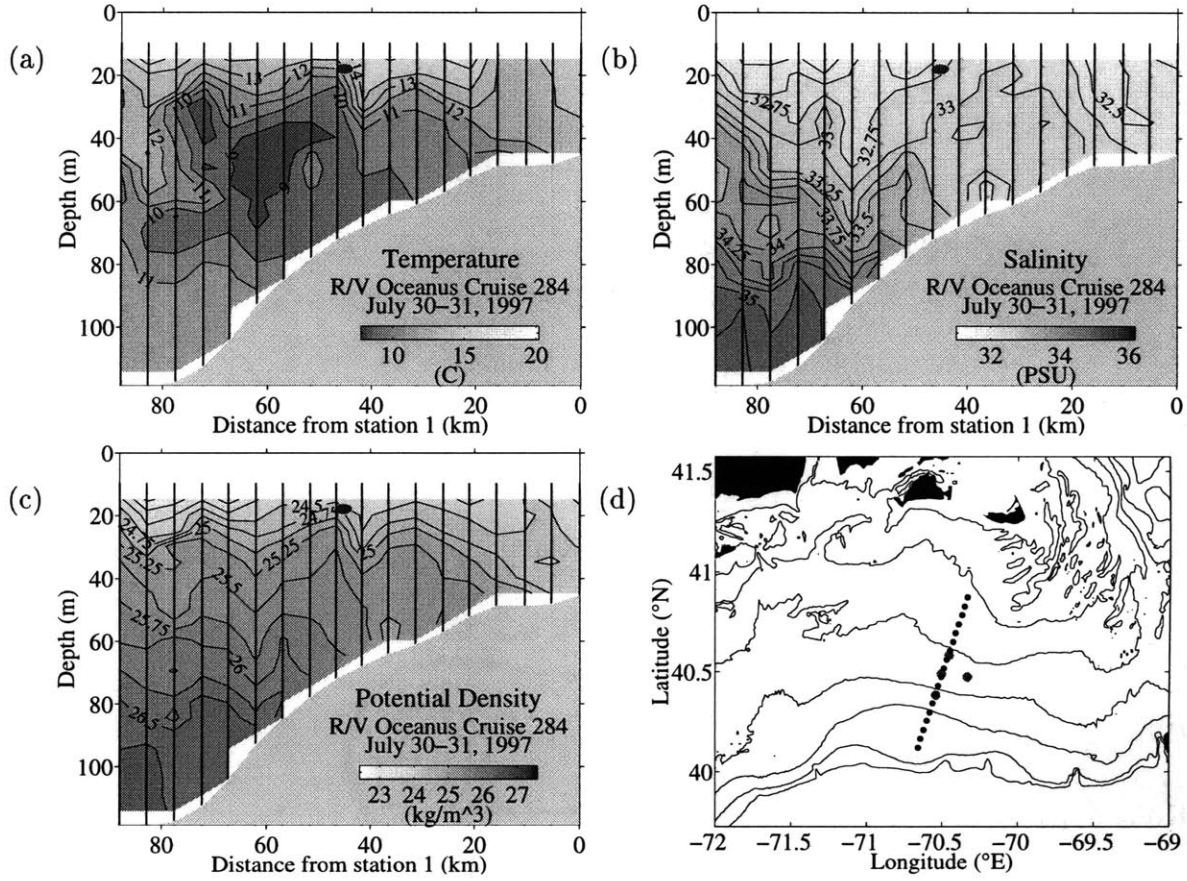

Figure 4.32: Hydrography data collected on days 211–212, 1997. Key is similar to Figure 4.2.

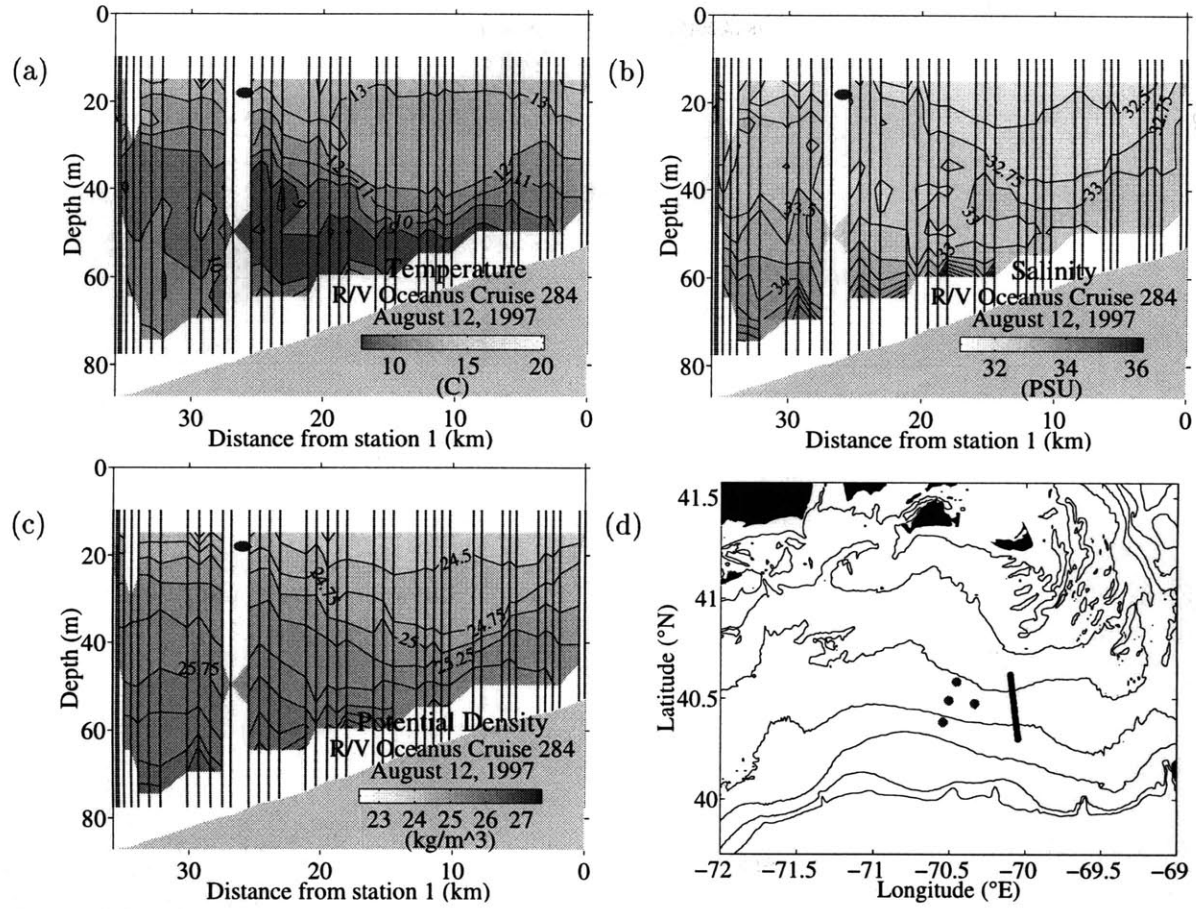

Figure 4.33: Hydrography data collected from a tow-yo transect on day 224, 1997. Key is similar to Figure 4.2.

and was the dominant feature in the temperature signal. However, unlike the 1995 and 1996 hydrography, in 1997 the cold pool extended inshore to the 60 m isobath.

A second hydrographic transect (a tow-yo transect) was made during the return trip to Woods Hole on day 224, and consisted of forty-one profiles between the 50 and 90 m isobaths (Figure 4.33). This transect shows a cold pool structure which is very similar to the first transect.

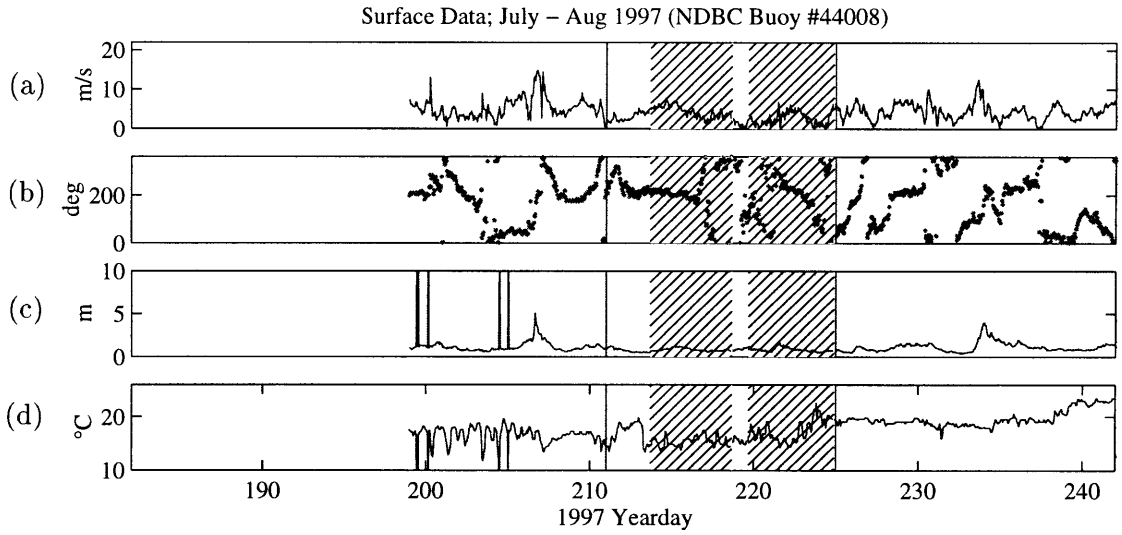

Figure 4.34: Wind (a) speed and (b) direction, (c) significant wave height, and (d) sea surface temperature for (July 18–August 31) 1997 from NDBC buoy #44008 (Nantucket Shoals). Key is similar to Figure 4.3.

Surface Conditions

Wind speed and direction were logged by shipboard meteorological sensors until the anemometer failed approximately halfway through the cruise. Surface data were also obtained from NOAA / NDBC Buoy #44008 (Figure 4.34) for days 199–243 (July 18–August 31). As for the previous cruises, only the NDBC data are displayed since they provide a longer record. Throughout the cruise, wind speeds fluctuated between 3–5 m s^{-1}, occasionally dropping to zero. Seas were very calm, with significant wave heights seldom in excess of 2 m.

Shipboard ADCP Observations

Velocity data were collected for the duration of the 1997 cruise using a broad-band 300kHz shipboard ADCP (Figure 4.35). Data were averaged over 3.0 minute intervals and over 2 m depth bins similar to the 1996 cruise.

Spectral analysis of the barotropic velocity again shows well-defined peaks in the diurnal and semidiurnal bands, while a small peak is also evident at the local inertial frequency (Fig-

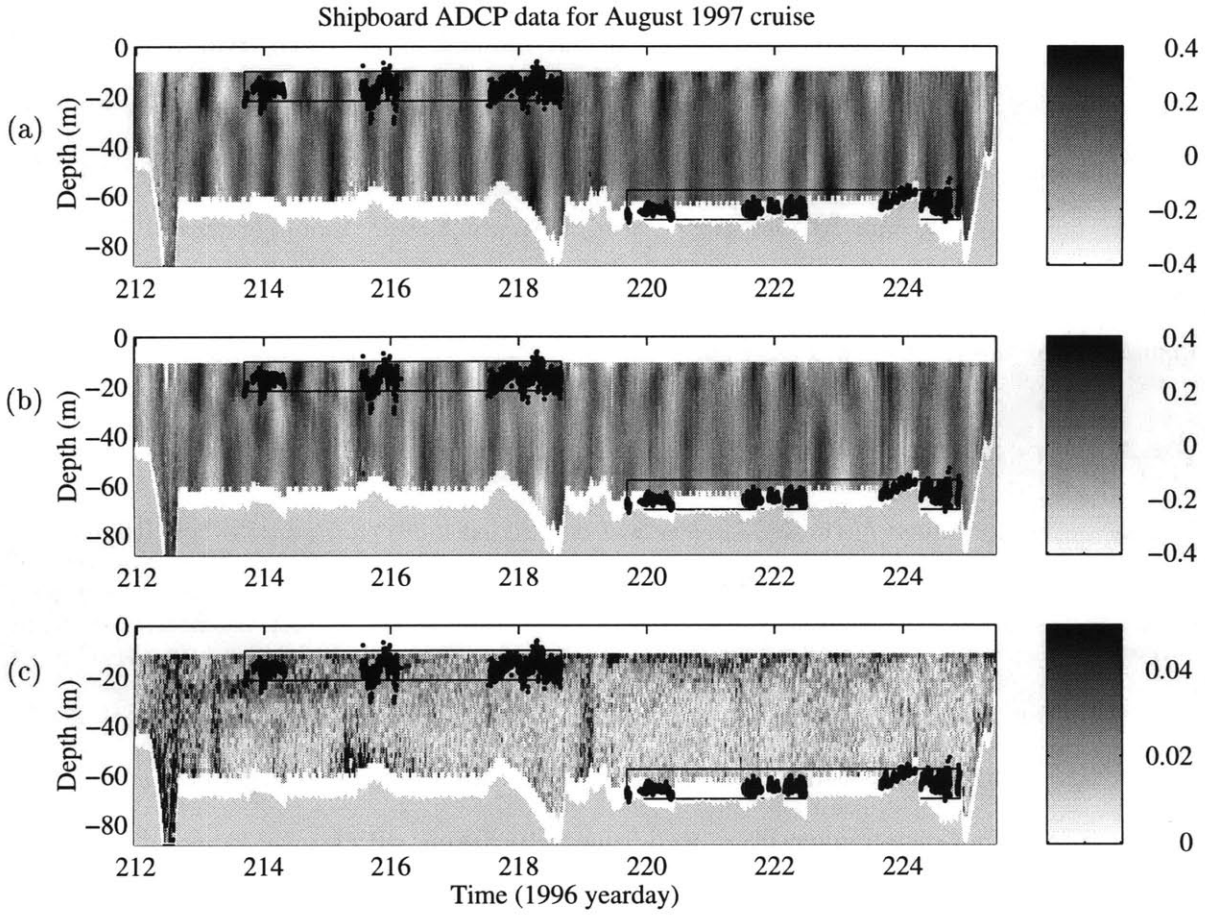

Figure 4.35: (a) Zonal and (b) meridional components of velocity and (c) the amplitude of the vertical shear from shipboard ADCP data collected during the 1997 dye cruise. Key is similar to Figure 4.4.

ure 4.36). A harmonic analysis for M_2, S_2, O_1, K_1, f, and a mean flow gives an M_2 tidal amplitude of 11 cm s^{-1}, and between 2–5 cm s^{-1} for the other tidal constituents. Inertial wave amplitudes were 2 cm s^{-1} and were roughly circular. The mean flow was eastward and slightly offshore, with amplitude of 4 cm s^{-1}. Together the fitted constituents account for 77% of the variance in the barotropic mode.

For the period between the first injection and the end of the last survey of the second experiment, an EOF analysis for the vertical structure shows that the barotropic mode accounts for about 80% of the overall variance in these data. The first and second baroclinic modes account for 11%–15% and 3%–4%, respectively (Figure 4.36). Time series and frequency spectra of mode amplitudes show that the first and second baroclinic modes were largely dominated by inertial oscillations (Figure 4.36).

4.4.2 Experiment 1: Rhodamine Dye and Drogues

The first dye experiment of the 1997 cruise was conducted between days 213–218. Rhodamine dye was released in a single streak and subsequently sampled over the course of five days during three surveys. Six holey sock drogues were also released during the injection. An overview of surveys during this experiment along with the drogue trajectories is shown in Figure 4.37. As in previous experiments, stratification was remained constant over the course of the experiment (Figure 4.38). Buoyancy frequencies ranged from 10 to 20 cph, with typical values of 13–18 cph at the level of the dye (Figure 4.7b).

Injection

The injection cast for the rhodamine experiment was performed on day 213 while the ship was headed due south at 1 kt. The target density surface was $\sigma_\theta = 24.6$ kg m^{-3}, and corresponded to a depth of 20 m (Figure 4.39). Again 100 kg of dye were released over a period of 1 hour, giving an injection streak about 2 km in length. The standard deviation of density during the injection was 0.05 kg m^{-3}, which corresponds to a standard deviation in pressure of 0.23 dbar.

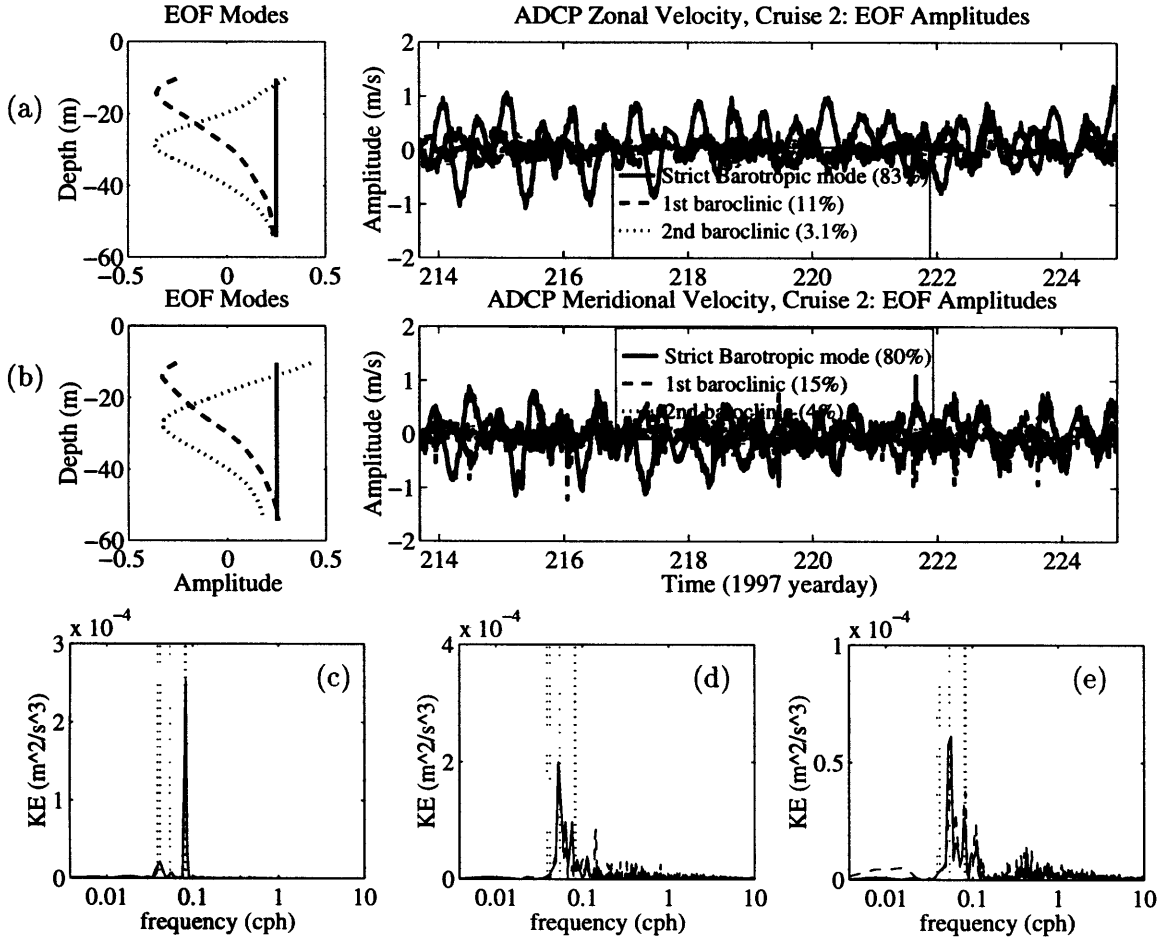

Figure 4.36: (a) Zonal and (b) meridional components of the barotropic mode and first two baroclinic modes computed from an EOF analysis of the 1997 dye cruise shipboard ADCP data. (c,d,e) Spectra for each of the three modes. Key is similar to Figure 4.5.

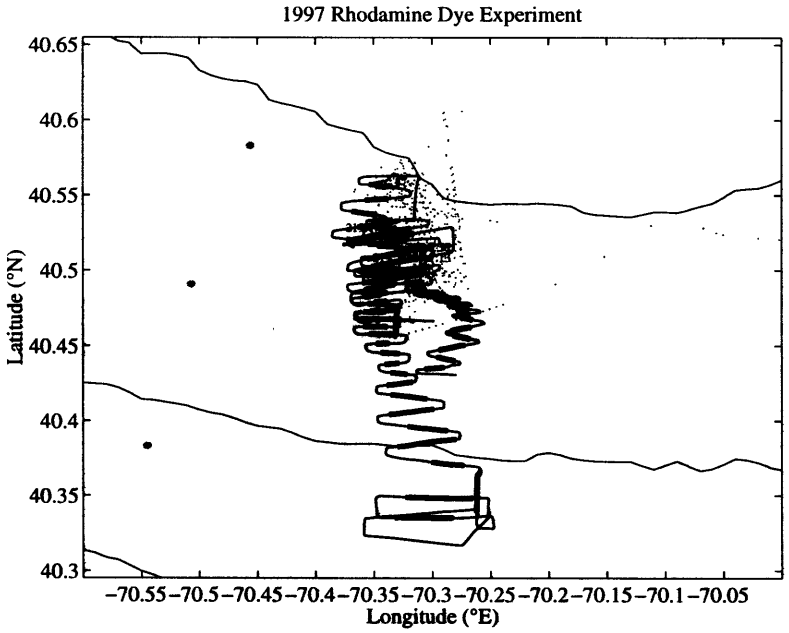

Figure 4.37: Overview of the 1997 rhodamine dye experiment showing the ship track during the injection and three subsequent dye surveys. Key is similar to Figure 4.6.

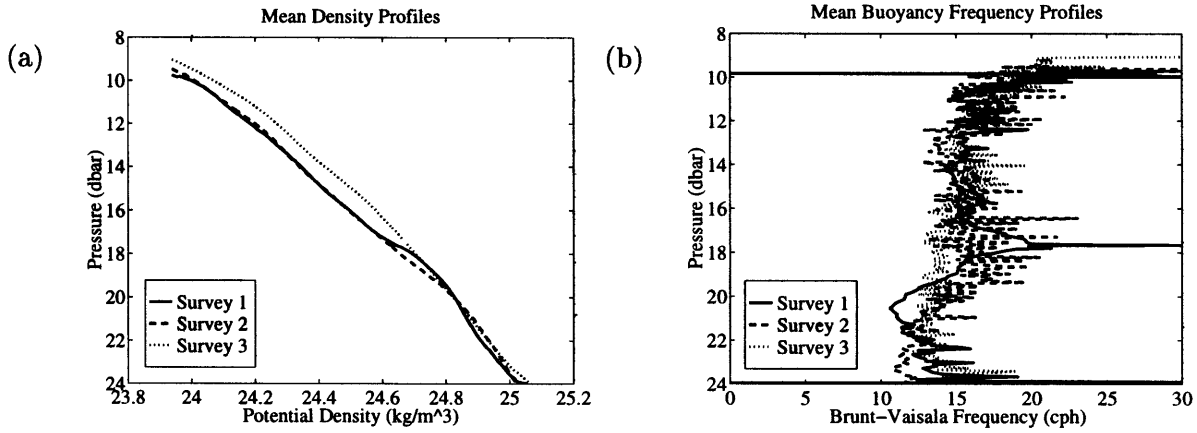

Figure 4.38: (a) Mean density profiles and (b) mean buoyancy frequency profiles for the injection and two surveys of the 1997 rhodamine dye experiment showing a relatively constant stratification over the course of the experiment.

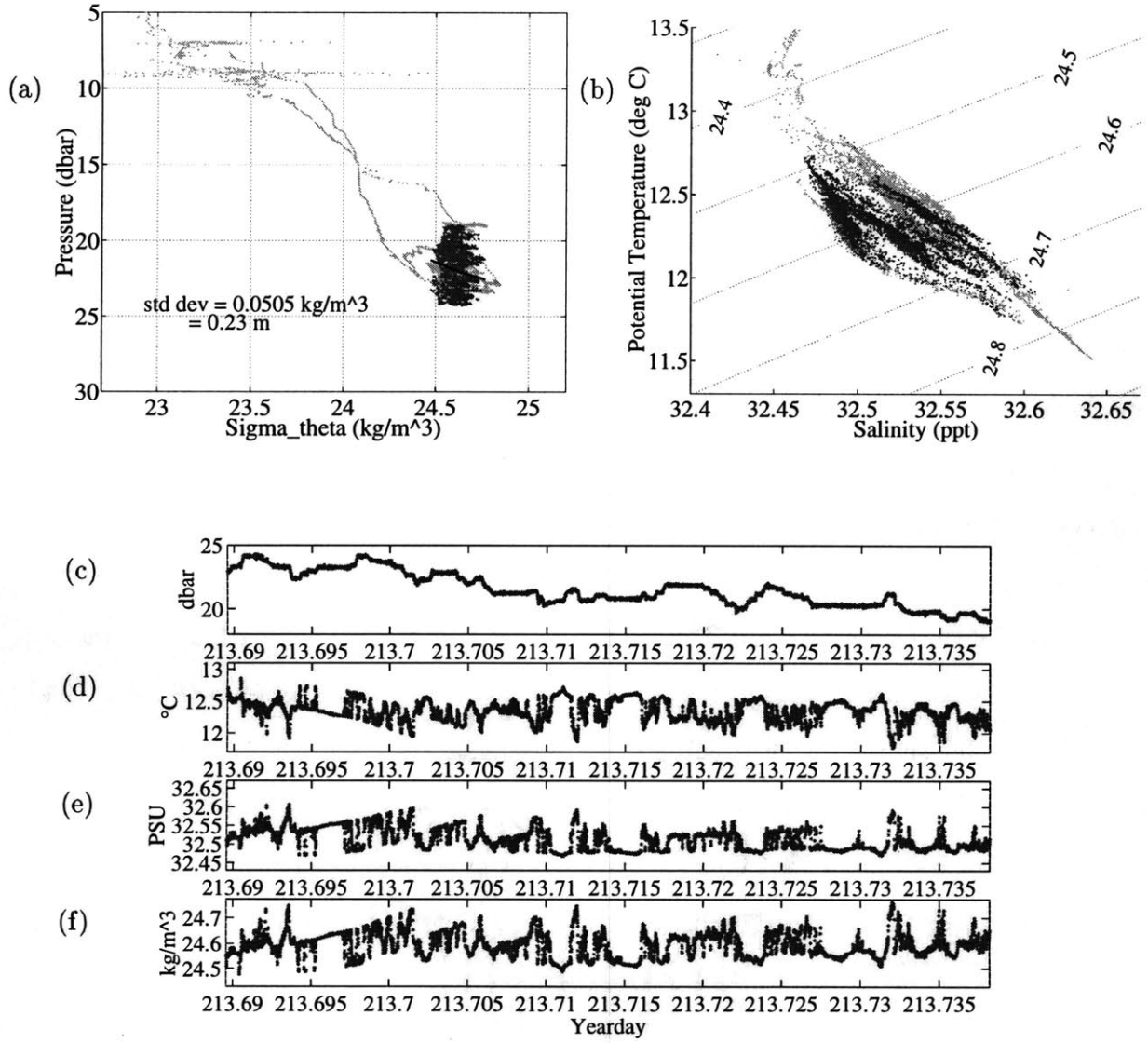

Figure 4.39: (a) Density profile, (b) Temperature-Salinity diagram, and time series of (c) pressure, (d) potential temperature, (e) salinity, and (f) potential density for the dye injection of the 1997 rhodamine dye experiment. Key is similar to Figure 4.8.

Time series of the CTD data show that the target density surface gradually shoaled from 22 m to 18 m over the course of the injection. This trend was roughly consistent with the isopycnal tilting associated with the inshore edge of the cold pool as seen in the hydrographic sections. Also, temperature and salinity show slight cooling ($\approx$ 0.3 ^{o}C) and freshening ($\approx$ 0.05 PSU) as the injection proceeded offshore.

Survey 1

The first survey of the 1997 rhodamine dye experiment was performed between 3 and 15 hours after injection and consisted of 16 east/west transects through the dye patch (Figure 4.40). The patch boundary was well-delimited by this survey, with a mass budget calculation indicating that 81% of the dye was found.

A number of interesting features are seen in Figure 4.40. Patch elongation in the meridional direction is evident (Figure 4.40a,b). During the first half of the survey, transects across the northern portion of the patch were tilted in the east/west direction (Figure 4.40c). Over the course of the survey, the tilting gradually reversed direction (Figure 4.40d). By the end of the survey, the deeper half of the patch was tilted in the opposite sense (Figure 4.40e). The boomerang-shaped dye distributions seen in Figures 4.40e and f further indicate that a significant portion of the vertical shear was higher than mode one, consistent with the findings of the EOF analysis on the ADCP data. Also noteworthy is that in many of these transects, the patch was rather disjointed, exhibiting three or four well-defined tracer concentration maxima within a single transect (Figure 4.40c,d,e).

Survey 2

The second survey for the 1997 rhodamine dye experiment was performed between 44 and 59 hours after injection and consisted of twelve zonal transects through the dye patch (Figure 4.41). Again the patch boundary was well-delimited by this survey, with a mass budget calculation indicating that all of the dye was found.

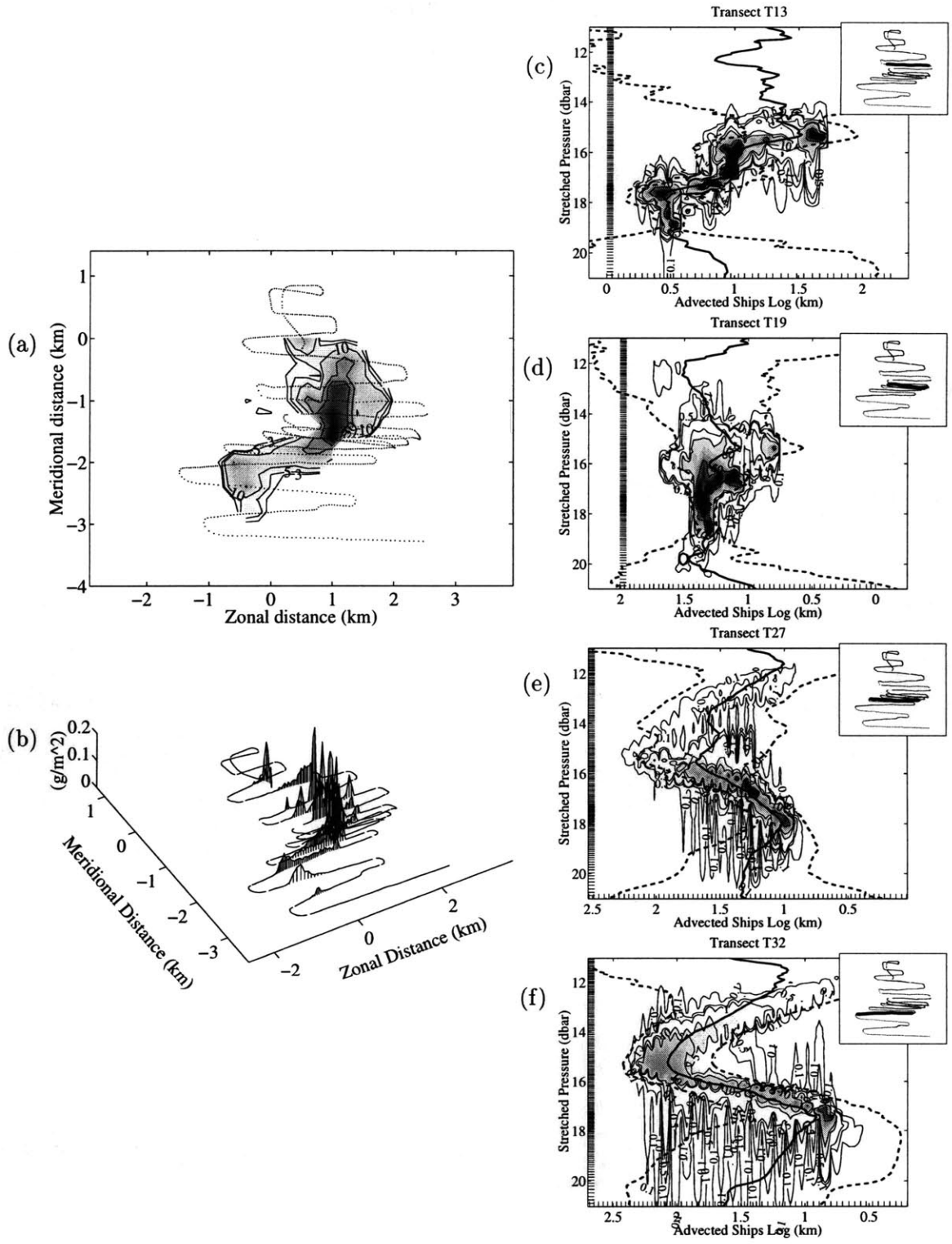

Figure 4.40: Overview of survey 1 of the 1997 rhodamine dye study. Key is similar to Figure 4.9.

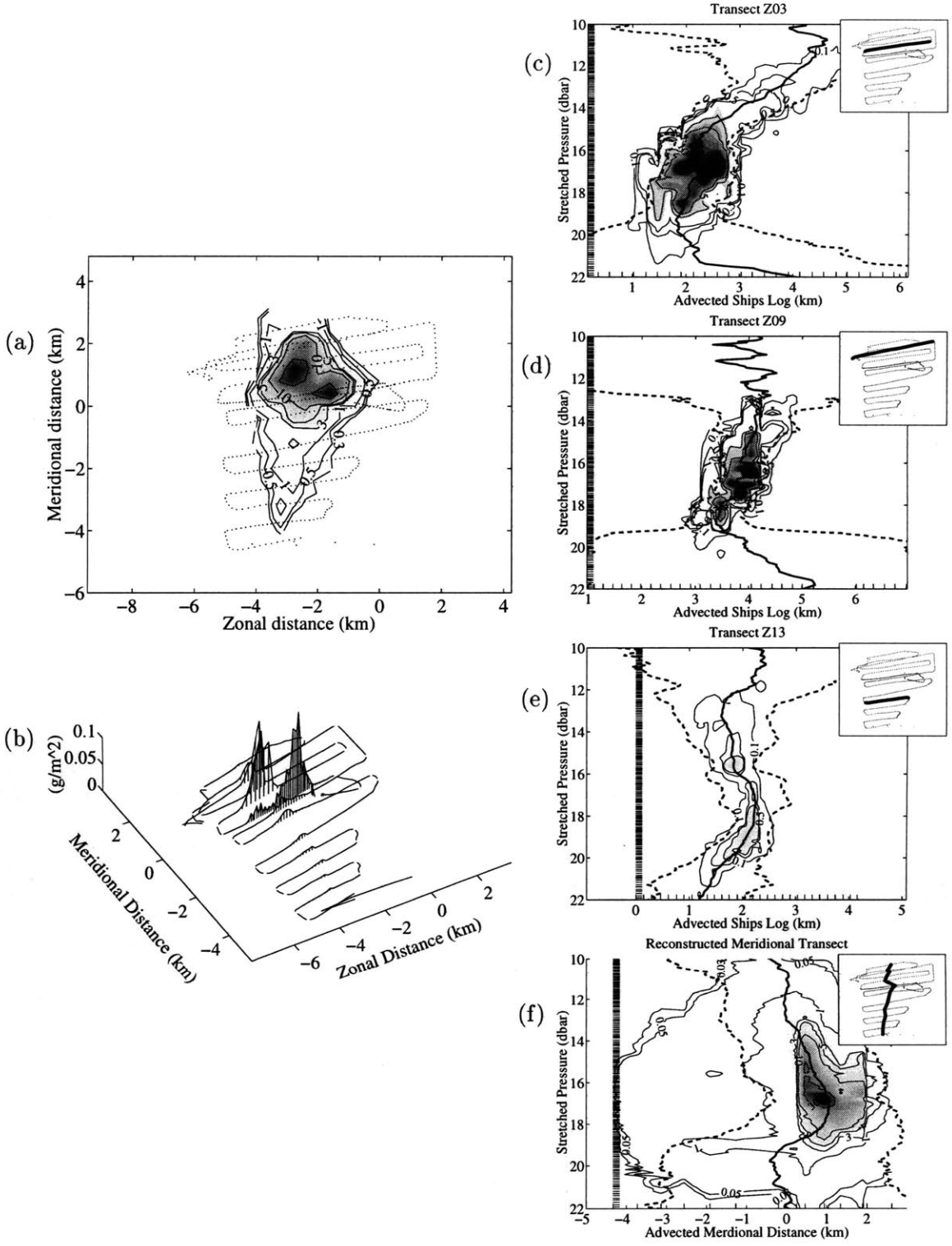

Figure 4.41: Overview of survey 2 of the 1997 rhodamine dye study. Key is similar to Figure 4.9.

Individual transects from this survey again show some patchiness, although the dye was more homogeneous than in the previous survey. Again horizontal elongation in the meridional direction is apparent, and a slight vertical tilting of the patch in the zonal direction was seen during the first few transects. A reconstructed meridional transect shows minimal tilting (Figure 4.41f).

Survey 3

The final survey of the 1997 rhodamine dye experiment was performed between 92 and 119 hours after injection and consisted of thirty-three zonal transects through the dye patch (Figure 4.42). Once again the patch was well delimited by the survey, with a mass budget calculation indicating that all the dye was found.

Patchiness is again evident in numerous transects of this survey (Figure 4.42e). In the zonal direction, no tilting is apparent. However, as the survey progressed southward, the depth of peak dye concentration increased, indicating a meridional tilt of the dye patch.

Drogues

Six drifters with drogues tethered at 20 m were released at regular intervals while the dye was being pumped. The drifters remained with the dye patch for the duration of the experiment, with the exception of one which drifted rapidly to the east, presumably after losing its drogue. Although the patch was stretched over 20 km meridionally by the end of the experiment, all the drogued drifters stayed with the northern half of the patch. Considering that the shallower part of the dye patch remained to the north while the deeper part was sheared to the south, it is not clear why the drogues, which were deep relative to the dye patch, did not drift further south.

Vertical Dispersion

Average vertical profiles for each survey are shown in Figure 4.43. For the first survey, the

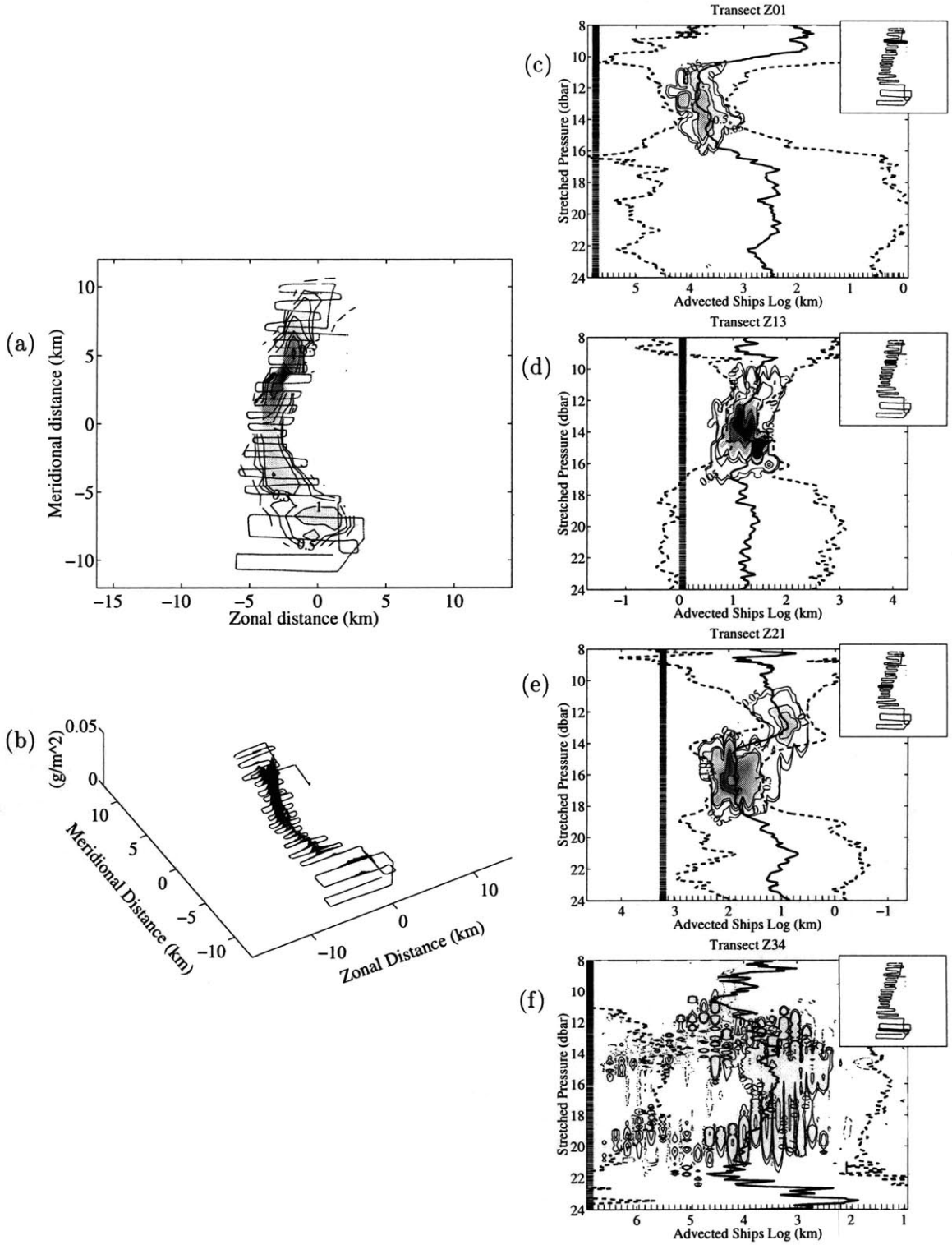

Figure 4.42: Overview of survey 3 of the 1997 rhodamine dye study. Key is similar to Figure 4.9. Note the different horizontal scales.

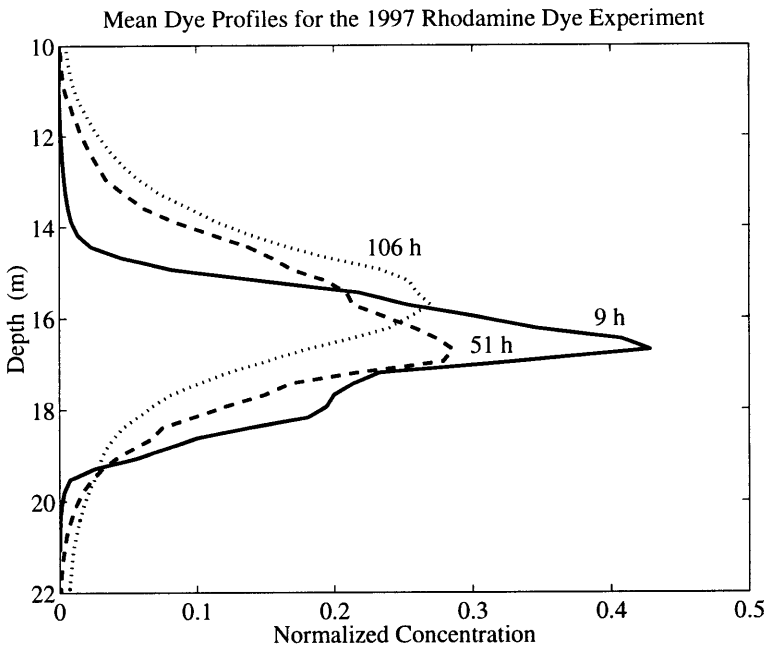

Figure 4.43: Vertical profiles of dye concentration normalized by the vertical integral of tracer for the 1997 rhodamine dye study.

mean vertical variance was $\sigma_z^2 \approx 1.25$ m^2, which corresponds to a mean vertical extent of $4\sigma_z \approx 4.5$ m. By the final survey, the variance had grown to $\sigma_z^2 \approx 3.9$ m^2, or a vertical extent of $4\sigma_z \approx 7.9$ m. The vertical diffusivity from these data based on a Fickian diffusion model was $\kappa_z = 0.1\text{–}0.4 \times 10^{-5}$ m^2 s^{-1}.

Chapter 5

An Assessment of Lateral Dispersion

In this chapter the lateral dispersion observed during the CMO dye experiments is examined in detail. In Sections 5.1 and 5.2 different measures of dispersion are defined, and a conceptual framework for lateral dispersion analysis is presented. In Section 5.3 this framework is used to infer horizontal strain rates and diffusivities for each of the dye experiments described in Chapter 4.

5.1 Reversible and Irreversible Processes

In any discussion of diffusion or dispersion, it is important to distinguish among different measures of the spreading of a dye patch. In practice, our definitions of diffusion and dispersion will depend on the underlying processes and the space and time scales of interest. In the present analysis lateral dispersion will be classified in two types, "reversible" and "irreversible" dispersion. Reversible dispersion refers to spreading of tracer by purely advective processes, e.g., some arrangement of vertical and horizontal shears or strains that displace the dye without diffusing it. Such processes are reversible in the sense that they do not alter the concentration of tracer following fluid parcels. Hence in principle it is always possible for the advection to reverse

direction and restore the tracer to its initial distribution. (Note, this means that the reversible dispersion may be negative at times.) In contrast, irreversible dispersion does change the tracer concentration of individual fluid parcels and cannot be reversed. Molecular diffusion is the most elementary irreversible dispersion process. However, in practice irreversible dispersion may additionally include stirring by small-scale shears and strains, and diffusive processes that were not resolved in the observations (i.e., some stirring plus molecular diffusion will insure irreversibility before any real reversal occurs).

5.2 Measures of Lateral Dispersion

In the context of the CMO dye experiments, two types of lateral dispersion will be examined. The first is parameterized by an effective horizontal diffusivity, κ_ζ, estimated from the vertically-integrated tracer. This will be used as a measure of the overall (total) horizontal spreading of the dye patch, and can be thought of as a sum of reversible and irreversible processes in the sense that it includes both the advective effects of vertical shears, and the effective diffusion due to small-scale mixing and stirring processes. This total dispersion is relevant in problems where the lateral but not the vertical extent of the tracer is of interest. It is also useful for comparison with mixed layer studies in which global horizontal variances are identical to the depth-dependent variances, and for comparison with historical dye studies where the vertical integral of tracer was the only observed quantity.

A second measure of lateral dispersion is the effective irreversible horizontal diffusivity, κ_{irrev}, estimated from the dye concentration along the target density surface. This diffusivity takes into account the depth-dependence of the tracer and represents the irreversible dispersion of the dye patch in the sense that it includes only those processes that spread the dye along isopycnal surfaces. For example, κ_{irrev} does not include the advective effects of vertical shears since these represent relative motions of isopycnals. However, it does include horizontal diffusion due to vertical shear dispersion, i.e., the interaction between vertical shear and ver-

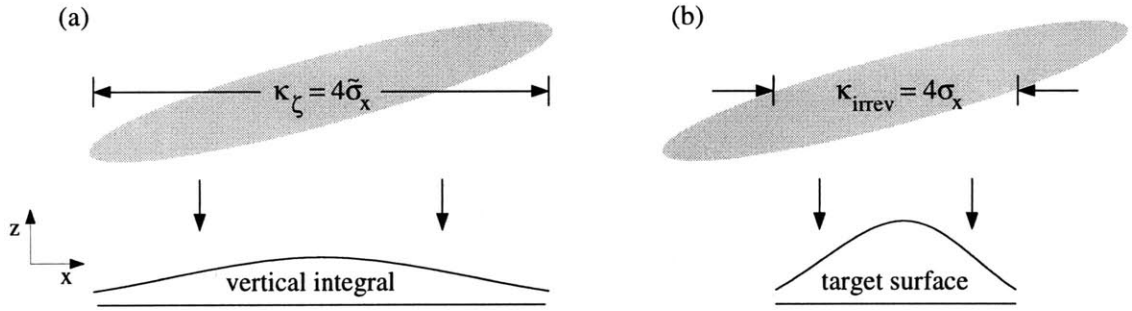

Figure 5.1: Schematic showing the distinction between reversible and irreversible dispersion as described in the text.

tical diffusion, since this involves spreading of dye along isopycnals. The effects of larger-scale along-isopycnal strains are also not included as part of κ_{irrev}, but rather will be treated explicitly in the forthcoming analysis. As discussed in Chapters 6 and 7, the irreversible dispersion κ_{irrev} is useful for comparing the observed tracer dispersion along the target density surface to a variety of theoretical models, not the least of which is shear dispersion. A schematic showing the distinction between κ_ζ and κ_{irrev} is shown in Figure 5.1.

5.2.1 Lateral Moments

As a measure of dispersion, the growth of the horizontal variances of the tracer patch are estimated using both the vertically-integrated tracer and the tracer along the target density surface. The horizontal moments for the vertically-integrated tracer, $\zeta(x, y)$, are defined as

$$M_{pq} = \int_{-\infty}^{+\infty} \int_{-\infty}^{+\infty} x^p y^q \zeta(x, y) dx dy. \tag{5.1}$$

The moments of interest are:

$$\begin{aligned}
M &= M_{00} && \text{total tracer within mapping region} \\
X_{\text{com}} &= M_{10} && \text{center of mass in zonal direction} \\
Y_{\text{com}} &= M_{01} && \text{center of mass in meridional direction} \\
\sigma_x^2 &= (M_{20} - M_{10}^2)/M && \text{zonal variance relative to center of mass} \\
\sigma_y^2 &= (M_{02} - M_{01}^2)/M && \text{meridional variance relative to center of mass} \\
\sigma_{xy} &= (M_{11} - M_{10}M_{01})/M && \text{zonal-meridional covariance relative to center of mass}
\end{aligned} \tag{5.2}$$

The horizontal moments along the target density surface are exactly analogous, except that the vertically-integrated tracer in (5.1) is replaced by the tracer concentration along the target density surface, $\theta(x, y)$.

As noted in Chapter 4, the tracer patches generally did not spread isotropically in the zonal and meridional directions. Instead, they were elongated in one direction or another, often at some angle with respect to the zonal or meridional directions. For a Gaussian distribution, the variances along the major and minor axes are related to the zonal and meridional variances through the relations

$$\begin{aligned}
\sigma_a^2 &= \tfrac{1}{2}[\sigma_x^2 + \sigma_y^2 + \tfrac{\sigma_{xy}}{\cos(\phi)\sin(\phi)}] && \text{variance a long the major axis} \\
\sigma_b^2 &= \tfrac{1}{2}[\sigma_x^2 + \sigma_y^2 - \tfrac{\sigma_{xy}}{\cos(\phi)\sin(\phi)}] && \text{variance a long the minor axis} \\
\phi &= \tfrac{1}{2}\arctan\left(\tfrac{2\sigma_{xy}}{\sigma_x^2 - \sigma_y^2}\right) && \text{angle of rotation.}
\end{aligned} \tag{5.3}$$

The variances along the target density surface are again analogous. A schematic of how these different variances relate to one another is shown in Figure 5.2.

5.2.2 Lateral Diffusivities and Strain Rates

In light of the observed elongation of the tracer patches, the growth of the horizontal patch variances will be modeled in terms of an effective horizontal diffusivity plus a horizontal strain. For a two dimensional linear strain, γ, and assuming a constant, isotropic horizontal diffusivity,

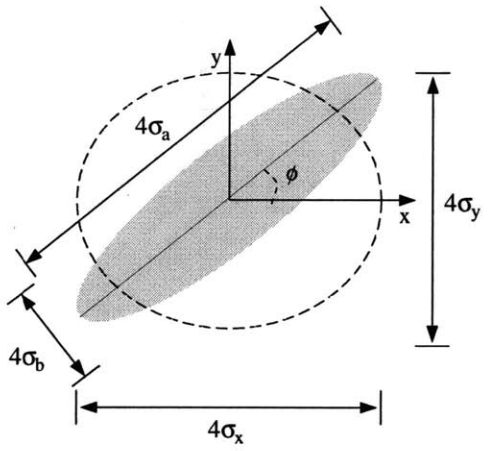

Figure 5.2: Schematic of the relationship between horizontal moments of equations (5.2) and (5.3).

κ, the advection-diffusion equation for a tracer, C, can be written as

$$\frac{\partial C}{\partial t} - \gamma x \frac{\partial C}{\partial x} + \gamma y \frac{\partial C}{\partial y} = \kappa \frac{\partial^2 C}{\partial x^2} + \kappa \frac{\partial^2 C}{\partial y^2}, \tag{5.4}$$

(see also equations 2.4–2.7 of Part I). Multiplying by x^2 and integrating over all x, or by y^2 and integrating over all y, equations for the tracer variances, σ_x^2 and σ_y^2 in the x and y directions, respectively, are

$$\frac{d\sigma_x^2}{dt} + 2\gamma\sigma_x^2 = 2\kappa \tag{5.5}$$

$$\frac{d\sigma_y^2}{dt} - 2\gamma\sigma_y^2 = 2\kappa, \tag{5.6}$$

with solutions

$$\sigma_x^2 = \sigma_{xo}^2 e^{-2\gamma t} + e^{-2\gamma t} \int_0^t 2\kappa e^{2\gamma t} dt, \tag{5.7}$$

$$\sigma_y^2 = \sigma_{yo}^2 e^{2\gamma t} + e^{2\gamma t} \int_0^t 2\kappa e^{-2\gamma t} dt. \tag{5.8}$$

This model can be applied to both the vertically-integrated tracer, $\zeta(x, y)$, and the tracer along the target density surface, $\theta(x, y)$, to obtain estimates of the effective total diffusivity, κ_ζ, and

description of variable	notation for vertically-integrated tracer	notation for tracer along target density surface
dye concentration	$\zeta = \zeta(x, y)$	$\theta = \theta(x, y)$
variances relative to the center of mass, and angle of rotation	$\tilde{\sigma}_x^2, \tilde{\sigma}_y^2, \tilde{\sigma}_{xy}, \tilde{\sigma}_a^2, \tilde{\sigma}_b^2, \tilde{\phi}$	$\sigma_x^2, \sigma_y^2, \sigma_{xy}, \sigma_a^2, \sigma_b^2, \phi$
horizontal strain rate	$\tilde{\gamma}$	γ
effective horizontal diffusivity	κ_ζ	κ_{irrev}

Table 5.1: Notation used in discussion of horizontal dispersion; see equations (5.2) – (5.8).

the effective irreversible diffusivity, κ_{irrev}. In the interest of clarity, the notation summarized in Table 5.1 will be adopted in order to distinguish between each of these measures of dispersion.

5.3 Observed Lateral Dispersion

5.3.1 Vertically Integrated Tracer

The variances, $\tilde{\sigma}_x^2$, $\tilde{\sigma}_y^2$, for each experiment were computed based on the kriging maps of the vertically-integrated tracer shown in Chapter 4, and are plotted in Figure 5.3. The variances $\tilde{\sigma}_a^2$ and $\tilde{\sigma}_b^2$ along the major and minor axes calculated from (5.8) are plotted in Figure 5.4. In these figures, a wide range of growth rates can be seen among the different experiments, as well as significant anisotropy within individual experiments.

Using these horizontal variances and (5.7) and (5.8), the strain rate and horizontal diffusivity can be estimated as follows. Given an initial and final along-streak variance (i.e., the distance along the major axis of the patch), equation (5.8) implies that if the strain rate, $\tilde{\gamma}$, is known then the along-streak diffusivity, κ_ζ, can be inferred, or vice-versa. Put another way, for a given initial condition, (5.8) says what combinations of $\tilde{\gamma}$ and κ_ζ could explain the observed final along-streak variance; a larger value of $\tilde{\gamma}$ implies a smaller value of κ_ζ and vice-versa. This

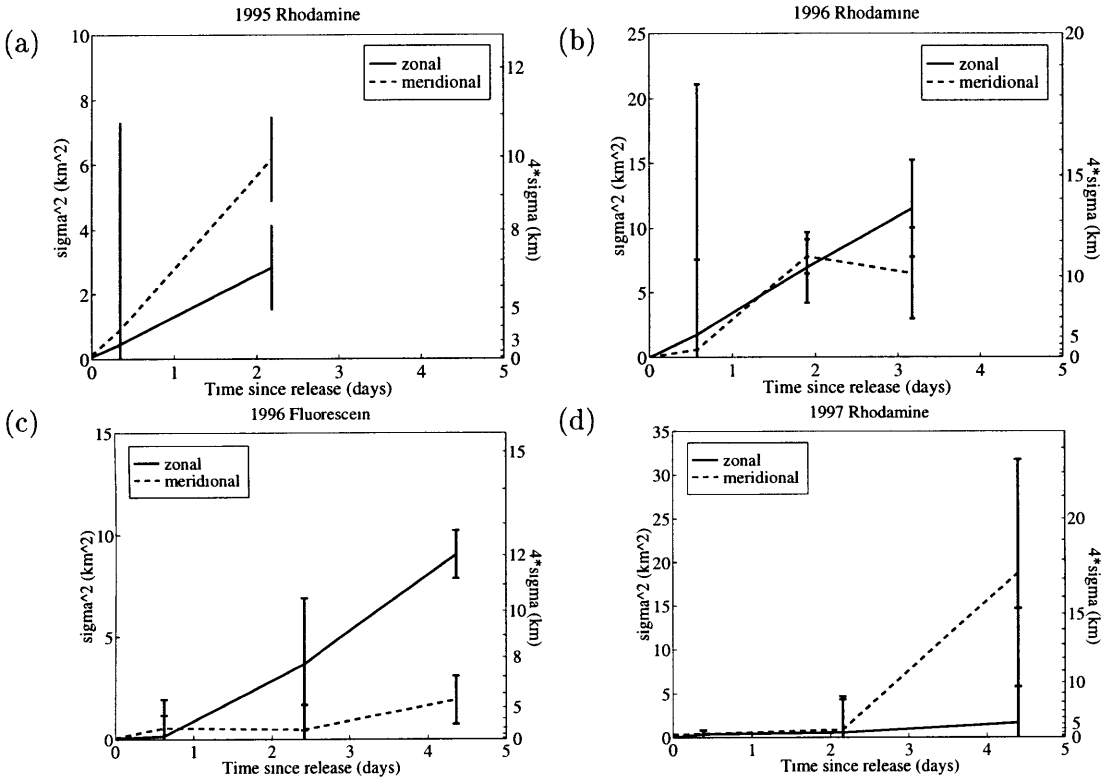

Figure 5.3: Zonal and meridional variances, $\tilde{\sigma}_x^2$, $\tilde{\sigma}_y^2$, estimated from the vertically-integrated tracer for the (a) 1995, (b,c) 1996, and (d) the first 1997 CMO dye experiments. Note the different vertical scales.

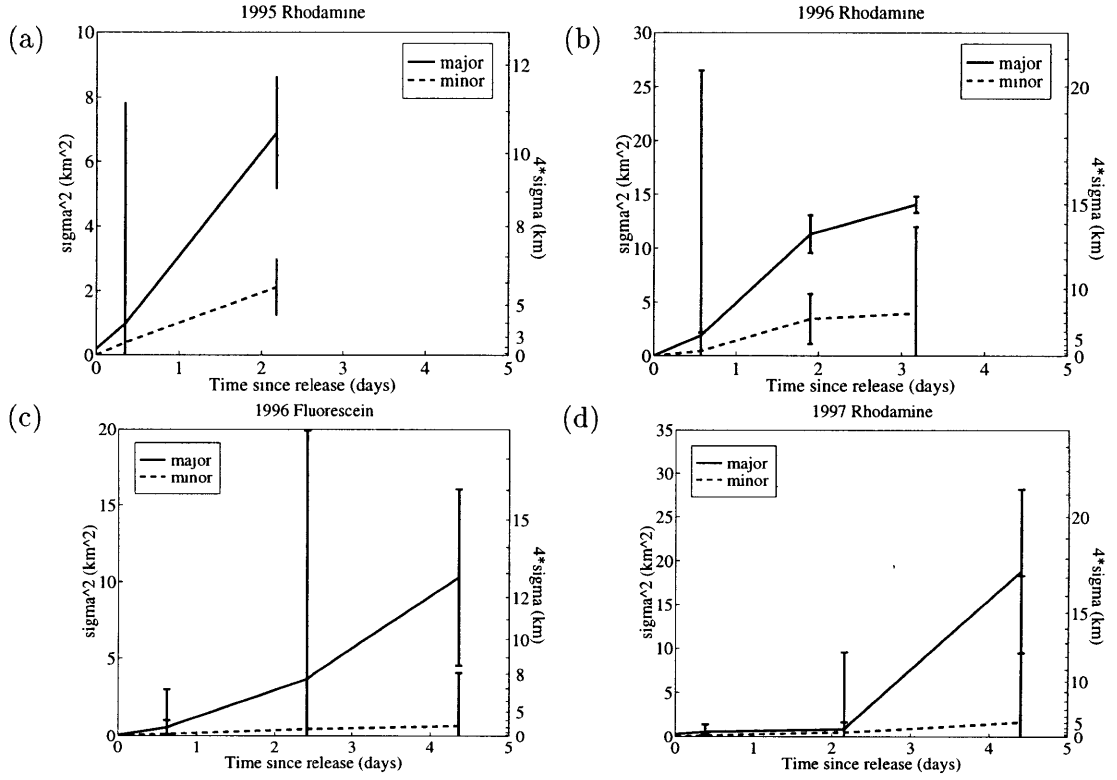

Figure 5.4: Patch variances along the major and minor horizontal axes, $\tilde{\sigma}_a^2$, $\tilde{\sigma}_b^2$, estimated from the vertically-integrated tracer for the (a) 1995, (b,c) 1996, and (d) the first 1997 CMO dye experiments. Note the different vertical scales.

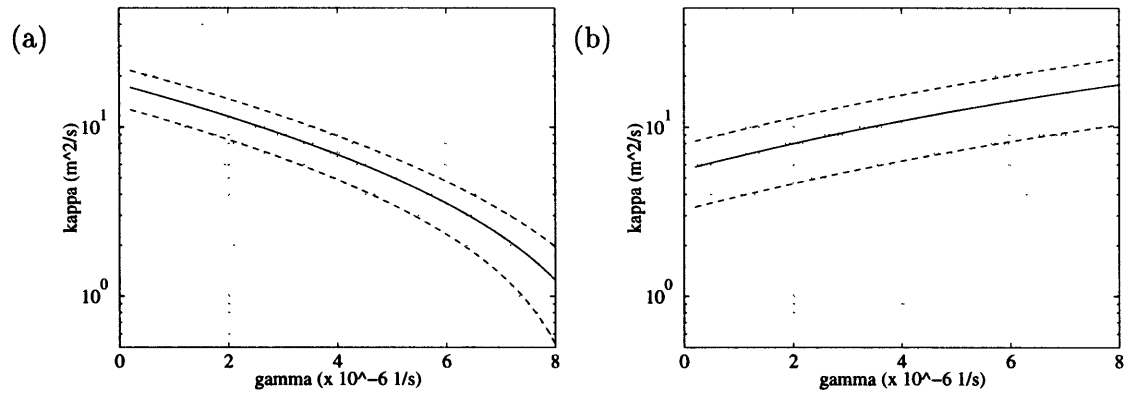

Figure 5.5: Graphic representation of possible combinations of $\tilde{\gamma}$ and κ_ζ that could explain the observed growth of the 1995 rhodamine dye patch in (a) the along-streak (meridional) and (b) the cross-streak (zonal) direction. Solid curves are the best estimates based on estimated variances (Figure 5.4) while dashed curves indicate uncertainties.

range of combinations can be expressed as a negative-sloping curve in $\tilde{\gamma}$–κ_ζ space (Figure 5.5a). For a different final condition, a different curve will result; the larger the final condition, the further the curve will be shifted towards larger $\tilde{\gamma}$ or larger κ_ζ. A different initial condition will lead to a different family of curves. For example, a smaller initial condition requires a larger $\tilde{\gamma}$ or a larger κ_ζ to yield the same final condition.

Similar reasoning can be applied to the cross-streak direction (Figure 5.5b). In that case a larger strain rate, i.e., more negative in the cross-streak direction, requires a larger diffusivity to maintain the same patch width so that the curves have a positive slope. The larger the final condition, the further the curves will be shifted towards smaller $\tilde{\gamma}$ or larger κ_ζ.

Using these families of curves, the strain rate, $\tilde{\gamma}$, and the small-scale diffusivity, κ_ζ, can be estimated from the intersections of the along- and cross-streak curves (Figure 5.6a).[1] The resulting estimates for this example are $\tilde{\gamma} = 2.9$ (1.3 to 4.8) $\times 10^{-6}$ s^{-1} and $\kappa_\zeta = 9.2$ (5.8 to 12.6) m^2 s^{-1}, where the uncertainties are given by the intersections of the upper- and lower-bound curves for the final patch variances. Similar plots for each of the dye experiments

[1]Although it has been assumed here that the along- and cross-streak strain rates are equal and opposite and that the horizontal diffusivity is isotropic, this is not required as long as the relationships between the along- and cross-streak strain and diffusivity are known.

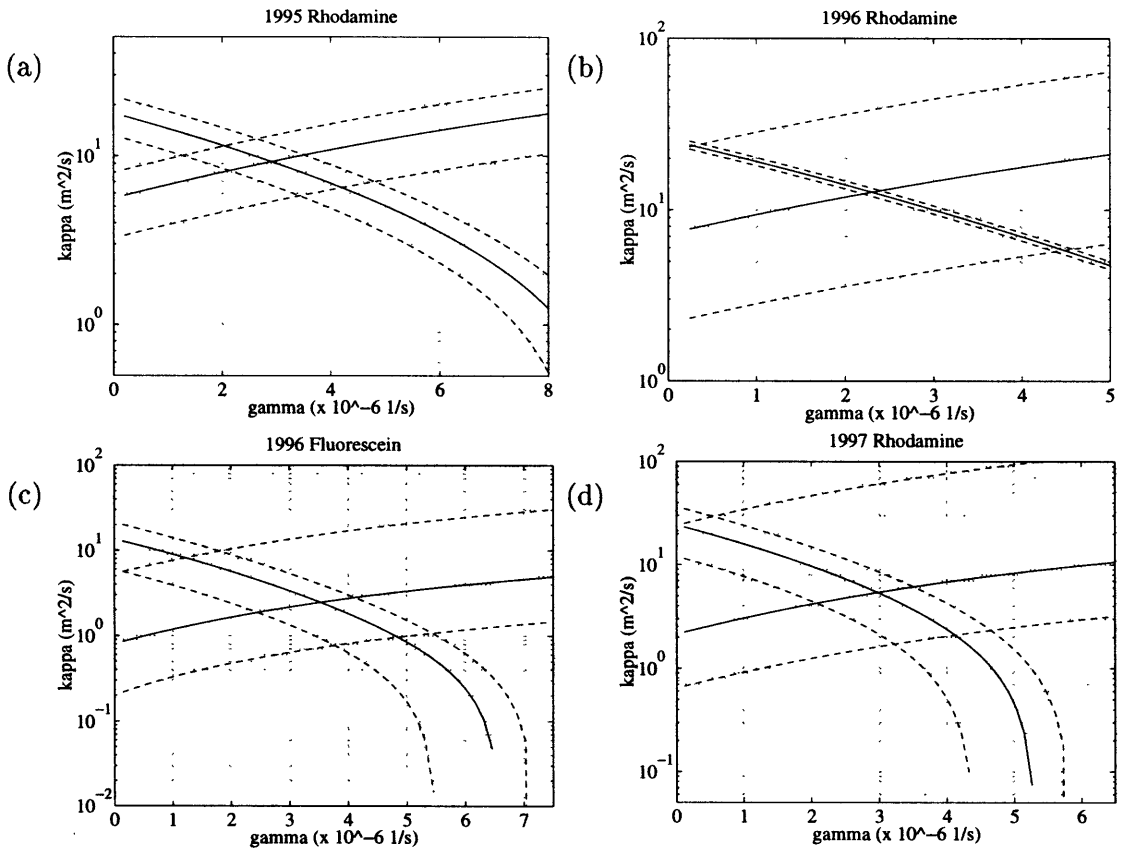

Figure 5.6: Graphical representation of possible combinations of $\tilde{\gamma}$ and κ_ζ that could explain the observed growth of tracer variance for the (a) 1995, (b,c) 1996, and (d) the first 1997 CMO dye experiments.

described in Chapter 4 are shown in Figure 5.6. Estimates of $\tilde{\gamma}$ and κ_ζ for other experiments are listed in Table 5.2 and range from $\tilde{\gamma} = 2.3 \times 10^{-6}$ to 3.5×10^{-6} s^{-1}, and $\kappa_\zeta = 2.5$ to 12.7 m^2 s^{-1}.

5.3.2 Depth Dependent Tracer

In the previous section, lateral dispersion was described in terms of the moments of the vertically-integrated tracer. In that case horizontal strains on scales of 1–10 km were treated as advective processes while vertical shears and small-scale diffusive processes were parameterized in terms of an effective horizontal diffusivity. In this section a similar analysis is performed using the tracer along the target density surface, $\theta(x, y)$. Here vertical shears are

	$\tilde{\gamma} \times 10^{-6}$ (s^{-1})	κ_ζ (m^2 s^{-1})
experiment 1	2.9 (1.3 to 4.8)	9.2 (5.8 to 12.6)
experiment 2	2.3 (0.2 to 4.6)	12.7 (5.7 to 24.2)
experiment 3	3.5 (0.2 to 5.4)	2.5 (0.7 to 9.8)
experiment 4	3.0 (0.0 to 4.6)	5.4 (1.7 to 30.0)

Table 5.2: Horizontal strain rate, $\tilde{\gamma}$, and horizontal diffusivity, κ_ζ, estimated from the vertically-integrated tracer.

resolved as advective processes while only irreversible processes are parameterized in terms of a horizontal diffusivity. For the CMO dye studies, the irreversible diffusivity will include small-scale stirring, i.e., horizontal shears on scales less than the scale of the dye patch (1–10 km). The irreversible diffusivity will also include the diffusive effects of shear dispersion as well as molecular diffusion.

As in the above analysis, tracer variances along the target density surface in the direction of the major and minor axes, σ_a^2, and σ_b^2, were estimated. However, this time patch widths (and thus patch variances) were obtained by eye using the raw data from the final survey of each experiment described in Chapter 4 (the appropriate kriging parameters for mapping tracer along the target density surface have not been determined; Figure 5.7). As expected for a tracer which is being vertically sheared, these variances were generally smaller than those computed from the vertically-integrated tracer.

The horizontal strain rate and the irreversible component of the horizontal diffusivity were again estimated using (5.7) and (5.8), this time using the variances estimated along the target density surface rather than the vertically-integrated tracer. The relevant curves in γ–κ_{irrev} space are shown in Figure 5.8. The resulting estimates of γ and κ_{irrev} range from $\gamma = 1.9 \times 10^{-6}$ to 4.0×10^{-6} s^{-1}, and $\kappa_{\text{irrev}} = 0.3$ to 4.9 m^2 s^{-1} and are listed in Table 5.3.

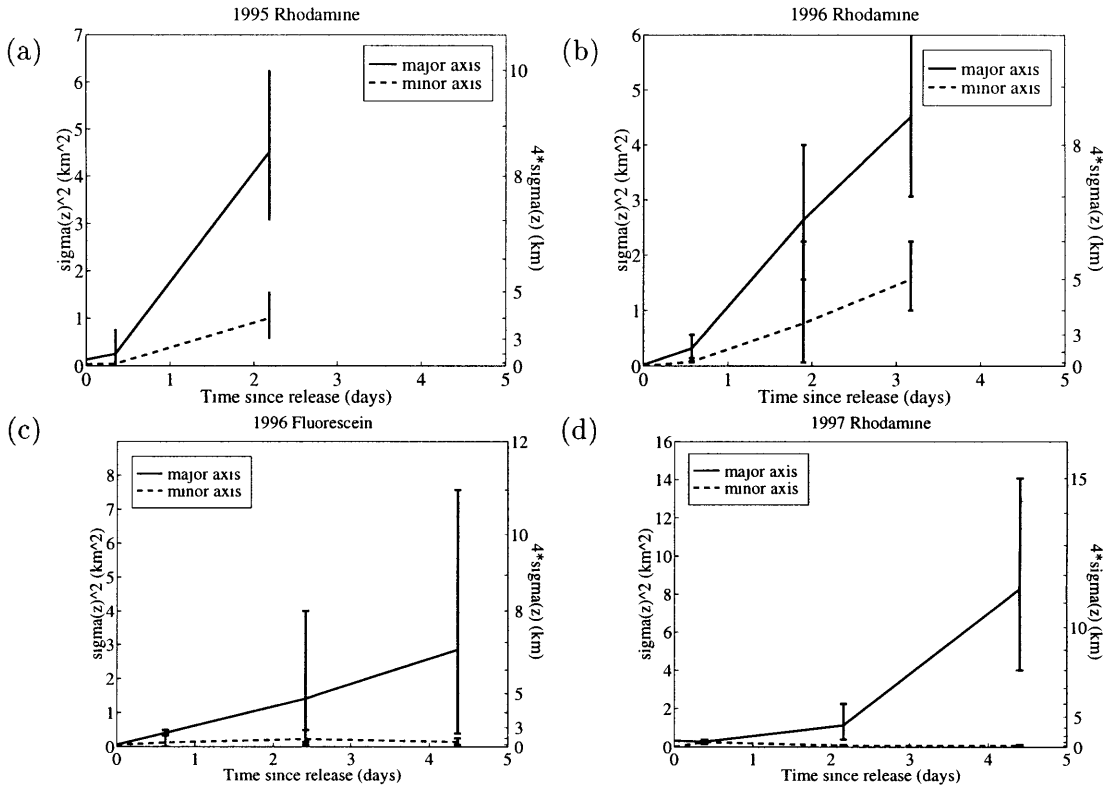

Figure 5.7: Patch variances in the directions of the major and minor horizontal axes, σ_a^2, σ_b^2, for the (a) 1995, (b,c) 1996, and (d) the first 1997 CMO dye experiments. Note the different vertical scales.

	$\gamma \times 10^{-6}$ (s^{-1})	κ_{irrev} (m^2 s^{-1})
experiment 1	3.7 (1.6 to 5.8)	4.9 (2.9 to 7.3)
experiment 2	1.9 (0.6 to 3.3)	4.6 (3.0 to 6.5)
experiment 3	3.5 (0.5 to 5.4)	0.5 (0.1 to 1.1)
experiment 4	4.0 (2.8 to 4.8)	0.3 (0.1 to 0.6)

Table 5.3: Horizontal strain rate, γ, and irreversible component of horizontal diffusivity, κ_{irrev}, estimated from the vertical integral of tracer.

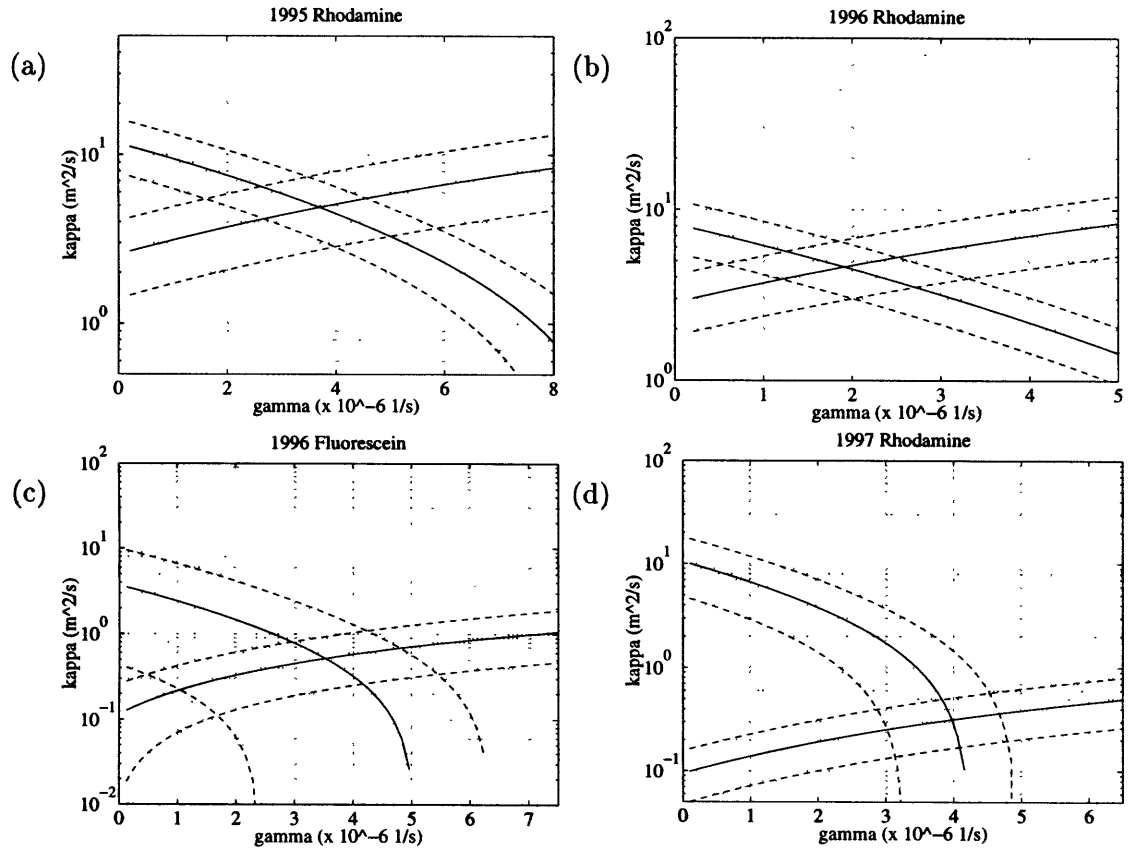

Figure 5.8: Graphical representation of possible combinations of γ and κ that could explain the observed growth of tracer variance for the (a) 1995, (b,c) 1996, and (d) the first 1997 CMO dye experiments.

Again the strain rates for the four experiments are relatively consistent with one another. In addition, estimates of γ based on the tracer along the target density surface are roughly consistent with the $\tilde{\gamma}$ inferred above from the vertically-integrated tracer. However, estimates of κ_{irrev} are smaller (2 to 18 times) than the total effective diffusivity, κ_ζ. This is consistent with the conceptual model described in Section 5.2, i.e. that the overall (total) diffusivity, κ_ζ, represents the sum of some irreversible diffusivity, κ_{irrev}, plus a reversible component due to the vertical shear. The fact that the two estimates of the large-scale horizontal strain rate, γ and $\tilde{\gamma}$, are in agreement is consistent with the idea that these parameters represent the same horizontal straining process.

5.4 Summary of Lateral Dispersion Analysis

In this chapter lateral dispersion during the CMO dye experiments was found to be consistent with a horizontal strain at scales of 1–10 km acting in conjunction with lateral dispersion on smaller scales. Two classifications of horizontal dispersion were made. Reversible dispersion referred to the effects of purely advective processes such as vertical shears that were resolved in the observations. Irreversible dispersion referred to stirring by small-scale shears and strains, and diffusive processes that were not resolved in the observations.

The total dispersion (reversible plus irreversible) estimated from the vertically-integrated tracer ranged from $\kappa_\zeta = 2.5$ to 12.7 m^2 s^{-1}. The irreversible dispersion estimated from the tracer along the target density surface was between 2 and 18 times smaller, and ranged from $\kappa_{\text{irrev}} = 0.3$ to 4.9 m^2 s^{-1}. For both the total dispersion and the irreversible dispersion, concomitant estimates of horizontal strains at scales of 1–10 km ranged from $\gamma = 1.9 \times 10^{-6}$ to 4.0×10^{-6} s^{-1}.

The above estimates of dispersion must be interpreted with care since they are specific to the space and time scales of the present dye experiments and since they assume a particular model of the physical processes involved. For example, the total dispersion, κ_ζ, parameterizes

the advective effects of vertical shear in terms of a Fickian diffusion coefficient. In the most general sense, this may be more or less appropriate, depending on how the vertical shear varies in time. For example, in the absence of vertical or horizontal diffusion, a steady vertical shear would lead to a quadratic growth in time of the horizontal tracer variance. In that case, a Fickian diffusion parameterization which assumes a linear growth of tracer variance would be inappropriate. Alternatively, if the vertical shear varied non-linearly with time, the horizontal variance may exhibit much more complicated time dependence. In that case, no single measure of dispersion, Fickian or other, could be considered any more or less appropriate.

In the above analysis, effective Fickian diffusivities, κ_ζ and κ_{irrev}, were used to parameterize the growth of the horizontal moments of the vertically-integrated tracer and the tracer along the target density surface, respectively. Although in some cases they may not represent the physics well, such parameterizations provide a useful means of comparison with other studies. Having quantified these rates of dispersion, the next two chapters are devoted to understanding the mechanisms responsible for this observed dispersion. In particular, Chapters 6 and 7 will focus on understanding the mechanisms responsible for the irreversible diffusivities, κ_{irrev}, since these by definition represent small-scale processes which were unresolved in the CMO observations and are the least understood.

Chapter 6

An Evaluation of Existing Dispersion Models

The CMO dye experiments described in Chapters 4 and 5 represent some of the most comprehensive and detailed observations to date of tracer release studies in the coastal ocean. As such, these experiments provide an invaluable opportunity to evaluate a wide range of dispersion models. In this chapter, two mechanisms of lateral dispersion proposed by previous investigators will be examined: shear dispersion (Section 6.1) and diffusion by lateral intrusions (Section 6.2). Previous applications and discussions of these models include a wide range of scales and environments such as lakes, rivers, estuaries, marginal seas, continental shelves and the deep oceans. The applicability of a particular model depends, of course, on the particular environment under study, and must be evaluated on a case by case basis. The purpose of this chapter is to determine what mechanisms are important over the continental shelf.

The main result of this chapter is that neither the classic paradigm of shear dispersion nor mixing due to lateral intrusions can account for the lateral dispersion observed during the CMO dye experiments. Consequently, this chapter is a compilation of *negative* results, in effect demonstrating that there must exist some other mechanism of lateral dispersion at work in the coastal ocean. In Chapter 7 a plausible alternative mechanism will be proposed which could

explain the observed dispersion.

6.1 Shear Dispersion

A notable feature in all of the dye experiments described in Chapter 4 was a dramatic change in the vertical tilt of the dye patch during successive surveys of the tracer, presumably due to a vertical shear. In some cases, the shear appeared to be persistent throughout the experiment, creating horizontal displacements as large as 2–5 km between the shallowest and deepest parts of the dye patch (e.g., Figures 4.10f and 4.30d.) In other cases, the shear appeared to oscillate, reversing the tilt of the dye patch within the few hours it took to complete a single survey (e.g., Figure 4.40). In light of these observations, a natural candidate as a lateral dispersion mechanism in the CMO region is vertical shear dispersion.

In this section the role of vertical shear dispersion in the CMO dye studies is examined. In Section 6.1.1, theoretical models of shear dispersion are reviewed. In Section 6.1.2, each of the dye experiments discussed in Chapters 4 and 5 is then examined in turn to determine the relative contribution to lateral dispersion by shear dispersion. The main result of this analysis is that shear dispersion can *not* explain the observed lateral dispersion in the CMO dye experiments. Instead, some other mechanism is required to contribute an effective small-scale horizontal diffusivity of order 0.2–4.0 $m^2\ s^{-1}$.

6.1.1 Theoretical Background

The Taylor and Saffman Limits

As originally described by Taylor (1953) in his studies of pipe flow dispersion, the interaction between a longitudinal flow and a transverse diffusivity can lead to an enhanced longitudinal diffusivity which is inversely proportional to the transverse diffusivity. This problem has been widely studied since Taylor's original work, with subsequent investigators considering a variety of variations of the original pipe flow problem (e.g., Elder, 1959; Chatwin, 1975).

Taylor's ideas have also found much relevance in geophysical flows, including fresh water lakes, rivers, estuaries, and the coastal ocean (e.g., Bowden, 1965; Csanady, 1966). One underlying assumption of the latter studies, which typically involved shallow or well-mixed waters, was that the time scale of the transverse (vertical) diffusion was small compared to the advective time scale of the flow. Consequently, vertical gradients of tracer were mixed away before the transverse (horizontal) velocity could advect the tracer a significant distance. In that case, the effective horizontal diffusivity is predicted to be inversely proportional to the vertical diffusivity (henceforth this is referred to as Taylor's limit).

As first discussed by Saffman (1962), however, this inverse proportionality may not apply to an unbounded or semi-bounded fluid if the time scale of the transverse diffusivity is much larger than the advective time scale. Rather, in this case the longitudinal diffusivity is predicted to be directly proportional to the transverse diffusivity (henceforth, Saffman's limit).

Solutions for Sinusoidal Shears

An extensive treatment of shear dispersion in the ocean which encompassed both the Taylor and Saffman limits in an unbounded fluid was given by Young et al. (1982). They derived solutions for the effective horizontal dispersion in a vertical shear flow which varies sinusoidally in both time and depth, i.e, for a horizontal velocity, $u(z,t)$, of the form

$$u(z,t) = \frac{\alpha}{m}\sin(mz)\cos(\omega t), \tag{6.1}$$

where m is the vertical wavenumber, ω is the frequency, and α is the shear amplitude. In this case, the long-term growth of the horizontal tracer variance, σ_x^2, can be expressed as

$$\frac{1}{2}\frac{d\sigma_x^2}{dt} = \kappa_x + \frac{\kappa_z\alpha^2}{2(\omega^2 + m^4\kappa_z^2)}, \tag{6.2}$$

where, and κ_x and κ_z are explicit horizontal and vertical diffusivities, respectively, and the second term on the right hand side represents the effective horizontal diffusivity due to shear

dispersion (Young et al., 1982). For large vertical wavenumbers, $m^2 \gg \omega/\kappa_z$, the shear dispersion term in (6.2) reduces to $\alpha^2/2m^4\kappa_z$, which represents Taylor's limit. For small vertical wavenumbers, $m^2 \ll \omega/\kappa_z$, the shear dispersion term becomes $\kappa_z\alpha^2/2\omega^2$, which represents Saffman's limit.

More generally, (6.2) shows that in an unbounded fluid, shear dispersion is most effective at low frequencies and low vertical wavenumbers. This means that for a given shear amplitude, α, and vertical diffusivity, κ_z, taking $m = 0$ in (6.2) yields an upper bound on the contribution of shear dispersion to the growth in the horizontal variance. The analysis below exploits this result.

Solutions for Time-dependent Linear Shears

Equation (6.2) describes the long-term effective diffusivity of an oscillatory shear flow. It was noted that taking $m = 0$ in this expression yields an upper bound on the contribution of shear dispersion to the growth in the horizontal variance. However, this result rigorously applies only as an average over an integral number of, or sufficiently many periods and wavelengths.

A more practical solution for the purposes of the present study, one which holds for arbitrary time was given by Smith (1982). He solved the advection-diffusion equation exactly for the case of a linear shear (i.e., $m = 0$ in equation 6.1) of arbitrary time dependence. In two dimensions, the problem is expressed as

$$\frac{\partial C}{\partial t} + u(z,t)\frac{\partial C}{\partial x} = \kappa_x \frac{\partial^2 C}{\partial x^2} + \kappa_z \frac{\partial^2 C}{\partial z^2}, \tag{6.3}$$

where C represents the concentration of tracer, κ_x and κ_z are the explicit horizontal and vertical diffusion coefficients, and the horizontal velocity, $u(z,t)$, now varies linearly with depth,

$$u = u_o(t) + z\alpha(t). \tag{6.4}$$

(The analogous problem in three dimensions was also solved by Smith, 1982, but will not be

discussed here.)

As shown by Smith (1982), a greatly simplified solution to (6.3) may be obtained with the introduction of an advected horizontal coordinate,

$$X = x - \int_0^t u_o(t')dt' - zG(t). \tag{6.5}$$

The second term on the rhs of (6.5) represents advection by the mean flow, while the third term represents the vertical tilt of the tracer patch, characterized by a distortion factor, G, which is yet to be determined. Applying this change of variables to (6.3), and noting that for a time-dependent linear shear a Gaussian initial condition yields a Gaussian solution, the solution of (6.3) can be written in the form

$$C = \frac{M}{2\pi\sigma_x\sigma_z} e^{\left[-\frac{X^2}{2\sigma_x^2} - \frac{z^2}{2\sigma_z^2}\right]}, \tag{6.6}$$

where M is the total mass of tracer, and $\sigma_x^2(t)$ and $\sigma_z^2(t)$ are the horizontal and vertical variances, respectively. Substituting (6.5) and (6.6) into (6.3), the following expressions are obtained for the evolution of the horizontal and vertical variances and the distortion factor, G:

$$\frac{1}{2}\frac{d\sigma_x^2}{dt} = \kappa_x + \kappa_z G^2, \tag{6.7}$$

$$\frac{1}{2}\frac{d\sigma_z^2}{dt} = \kappa_z, \tag{6.8}$$

$$\frac{dG}{dt} = \alpha(t) - \frac{2\kappa_z G}{\sigma_z^2}. \tag{6.9}$$

Given a shear, $\alpha(t)$, of arbitrary time dependence, and diffusivities κ_x and κ_z, this system of ODEs can be solved exactly:

$$\sigma_x^2 = \sigma_{x_o}^2 + 2\kappa_x t + 2\kappa_z \int_0^t G^2 dt', \tag{6.10}$$

$$\sigma_z^2 = \sigma_{z_o}^2 + 2\kappa_z t, \tag{6.11}$$

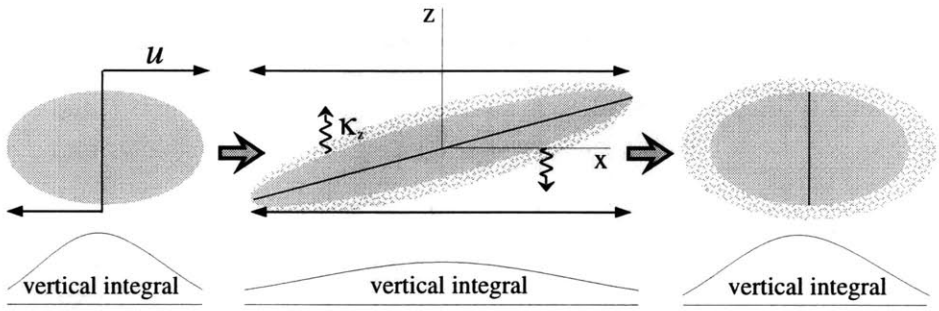

Figure 6.1: Schematic of linear shear dispersion model showing a dye patch which undergoes tilting by a vertical shear at the same time that it is being vertically diffused. The net effect, shown at the far right, is an effective horizontal dispersion which remains even if the advection is reversed.

$$G = \frac{1}{t - \tilde{t}} \int_0^t (t' - \tilde{t})\alpha(t')dt' \qquad (\tilde{t} = -\frac{\sigma_{z_o}^2}{2\kappa_z}). \tag{6.12}$$

The last term on the rhs of (6.10) represents the effective horizontal diffusivity due to shear dispersion and is analogous to the second term on the rhs of (6.2) in the limit of $m = 0$. Equation (6.12) shows that the distortion factor, G, represents a weighted mean shear, or effectively a measure of the vertical tilt of the center of mass of the tracer patch. Also noteworthy is that the vertical variance (6.11) does not depend on the vertical shear. A schematic of the linear dispersion model is shown in Figure 6.1.

6.1.2 Comparison with Observations

The theoretical ideas discussed in Section 6.1.1 imply that a linear shear dispersion model ($m = 0$ in equation 6.2) provides an upper bound on lateral dispersion due to shear dispersion. Analytical solutions by Smith (1982) further provided an exact solution for the evolution of a passive tracer in the presence of a linear shear of arbitrary time dependence. This solution will now be used to determine upper bounds on the contribution of shear dispersion to the lateral dispersion observed during the CMO dye studies.

Two questions are addressed: 1) What are the relative contributions of shear dispersion by mean, inertial, diurnal, and semidiurnal shears? 2) Can the total contribution of shear

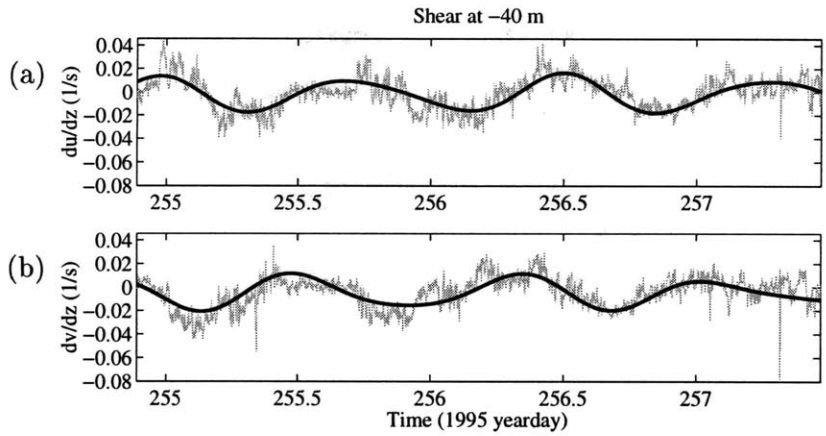

Figure 6.2: Time series of (a) zonal and (b) meridional shears at 40 m depth for the 1995 rhodamine dye study. A least squares fit for mean plus oscillatory shears with inertial, diurnal, and semidiurnal frequencies is plotted over the raw data for each component.

dispersion as estimated using the full time series of ADCP shears explain the observed lateral dispersion in these experiments? The general approach will be to use the shears observed at the mean depth of the target density surface in the above solutions for shear dispersion in a time dependent linear shear field. In all cases, an upper bound on the vertical diffusivity inferred from the dye will be used, thus further reinforcing that these predictions represent upper bounds on shear dispersion (see Section 6.1.1). Each of the dye experiments described in Chapters 4 and 5 are now examined.

September 1995 Rhodamine Dye Study

In the 1995 rhodamine dye experiment, the target density surface was within the main pycnocline at a depth of approximately 40 m, which was roughly the depth of maximum shear (Figures 4.4 and 4.5). Time series of the shear at 40 m are shown in Figure 6.2 along with a least squares fit to these data for mean plus oscillatory shears with inertial, diurnal, and semidiurnal frequencies.

Using these shears and an upper bound on the vertical diffusivity, κ_z, estimated from the dye, (6.10)–(6.12) were integrated numerically to obtain predictions for the zonal and

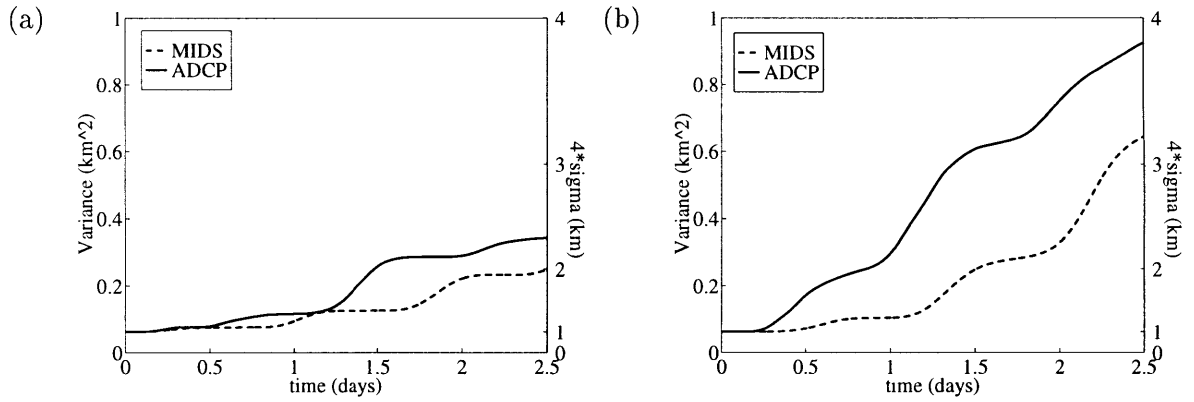

Figure 6.3: Theoretical predictions for (a) zonal and (b) meridional shear dispersion in the 1995 rhodamine dye study (see also Table 6.1). Dashed curves are for a Mean plus Inertial, Diurnal, and Semidiurnal (MIDS) shears as estimated from a least squares fit to the data (Figure 6.2). Solid curves are similar predictions using the full ADCP time series.

meridional variances, σ_x^2 and σ_y^2, as a function of time. To further maintain the shear dispersion prediction as an upper bound, upper bounds on the initial condition of patch variances, $\sigma_{x_o}^2$, $\sigma_{y_o}^2$, and $\sigma_{z_o}^2$, were also used. Figure 6.3 shows the theoretical shear dispersion predictions for the 1995 rhodamine dye study. In these predictions, $\kappa_z = 1.5 \times 10^{-5}$ m^2 s^{-1}, $\sigma_{x_o}^2 = \sigma_{y_o}^2 = 0.0625$ km^2 ($4\sigma_x = 4\sigma_y = 1$ km), and $\sigma_{z_o}^2 = 0.39$ m^2 ($4\sigma_z = 2.5$ m).

The contributions of shear dispersion by mean and oscillatory shears for this experiment are listed in Table 6.1. For convenience of notation, the effective dispersion of each of the fitted constituents is quoted in terms of an effective diffusivity, $\kappa = \frac{1}{2}\frac{\Delta\sigma_{(x,y)}^2}{\Delta t}$. Alternatively, since a diffusion parameterization for mean shear dispersion can be misleading, the total change in variance over the course of the experiment, $\Delta\sigma_{(x,y)}^2$, is also given. The latter provides the same information as the the former, except that it is not normalized by the time scale of the experiment. A different time scale which is useful for comparing mean and oscillatory shear dispersion is the time it takes for mean shear dispersion (which grows as t^3) to dominate the effects of oscillatory shear dispersion (which grows as t). This transition time scale is also listed in Table 6.1 for each of the fitted oscillatory shears.

The predictions using the least-squares fit show that in the zonal direction, mean shear

		ADCP	MIDS	M	I	D	S
effective diffusivity ($m^2\ s^{-1}$)	zonal	0.65	0.41	0.23	0.17	2.4×10^{-3}	4.3×10^{-3}
	meridional	2.0	1.1	0.93	0.12	1.1×10^{-2}	4.9×10^{-3}
$\Delta\sigma^2_{(x,y)}$ (km^2)	zonal	0.28	0.18	0.10	7.2×10^{-2}	1.0×10^{-3}	1.9×10^{-3}
	meridional	0.88	0.46	0.40	5.3×10^{-2}	4.8×10^{-3}	2.1×10^{-3}
transition time (days) zonal, meridional		–	–	–	2.1, 0.91	0.25, 0.27	0.34, 0.18

Table 6.1: Theoretical predictions for (zonal, meridional) shear dispersion in the 1995 rhodamine dye study (see also Figure 6.3). Individual components are the mean shear (M), inertial oscillations (I), and diurnal (D) and semidiurnal (S) tides. First and second rows give, respectively, the effective diffusivity, and the growth in patch variance over the course of the experiment. The third row gives the time scale at which mean shear dispersion dominates oscillatory shear dispersion for each of the fitted constituents.

contributed approximately the same to shear dispersion as did the combined oscillatory shears. In the meridional direction, oscillatory shear dispersion was similar to the zonal direction, while mean shear dispersion was somewhat larger. It is interesting to note that the dominant contribution in the oscillatory shears was from inertial oscillations.

Comparing these predictions to the effective irreversible diffusivities estimated from the observations (Chapter 5; Table 5.3), the total dispersion by mean plus oscillatory shears in the zonal direction, $\kappa_{\mathrm{MIDS}} \approx 0.41\ m^2\ s^{-1}$, accounts for less than 10% of the observed irreversible diffusivity. The total dispersion in the meridional direction, $\kappa_{\mathrm{MIDS}} \approx 1.1\ m^2\ s^{-1}$, was somewhat larger, but still only accounts for about 22% of the observed irreversible diffusivity. Similar predictions using the full ADCP time series are slightly higher, $\kappa_{\mathrm{ADCP}} \approx 0.65\ m^2\ s^{-1}$ and $2.0\ m^2\ s^{-1}$, for the zonal and meridional directions, respectively. However, these still only account for approximately 13%–41% of the irreversible diffusivity inferred from the observations.

The above predictions show that shear dispersion was not the dominant mechanism of lateral dispersion during the 1995 rhodamine dye study (remember that the shear dispersion

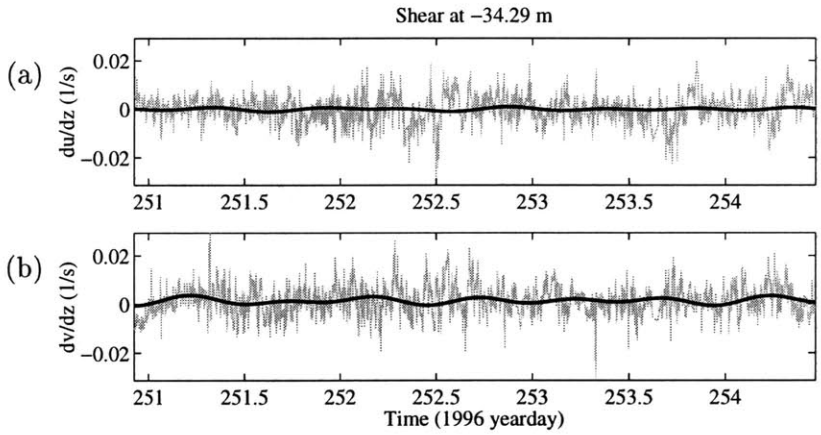

Figure 6.4: Time series of (a) zonal and (b) meridional shears at 35 m depth for the 1996 rhodamine dye study. A least squares fit for mean plus oscillatory shears with inertial, diurnal, and semidiurnal frequencies is plotted over the raw data for each component.

prediction was also an upper bound). Shear dispersion accounts for at most 13%–41% of the irreversible diffusivity inferred from the observations, i.e., 59%–87% of this dispersion must have been due to some other mechanism. Put another way, this result shows that some mechanism must have contributed an effective horizontal diffusivity of $\kappa_{\text{missing}} \approx 3 - 4\ \text{m}^2\ \text{s}^{-1}$.

September 1996 Rhodamine Dye Study

The target density surface of the 1996 rhodamine dye experiment was at a depth of approximately 35 m. The time series for the shear at this depth are shown in Figure 6.4 along with a least squares fit for a mean plus inertial, diurnal and semidiurnal harmonics. Using an upper bound on the vertical diffusivity, $\kappa_z = 3.5 \times 10^{-5}\ \text{m}^2\ \text{s}^{-1}$, and an initial patch size of $4\sigma_x = 4\sigma_y = 1$ km and $4\sigma_z = 2.5$ m, (6.10)–(6.12) were again integrated numerically to obtain upper bounds on the diffusivity due to shear dispersion (Figure 6.5).

The predictions using the least-squares fit show that in the zonal direction, the mean shear contributed approximately three times as much to shear dispersion as did the combined oscillatory shears (Table 6.2). However, the total contribution of the mean and oscillatory shears was quite small, $\kappa_{\text{MIDS}} \approx 3.0 \times 10^{-3}\ \text{m}^2\ \text{s}^{-1}$. Oscillatory shear dispersion in the meridional

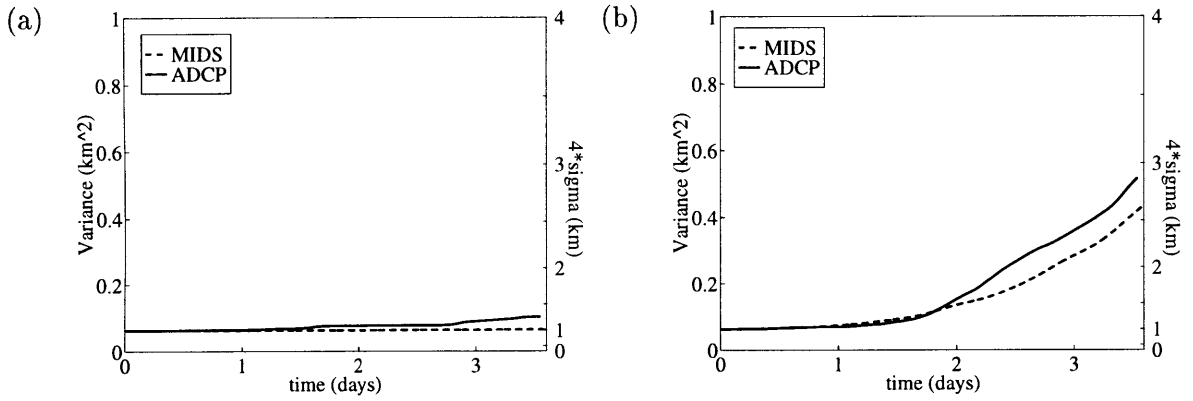

Figure 6.5: Theoretical predictions for (a) zonal and (b) meridional shear dispersion in the 1996 rhodamine dye study (see also Table 6.2). Key is similar to Figure 6.3.

		ADCP	MIDS	M	I	D	S
effective diffusivity ($m^2\ s^{-1}$)	zonal	0.06	0.003	0.002	3.3×10^{-4}	2.6×10^{-4}	2.0×10^{-4}
	meridional	0.73	0.56	0.55	1.5×10^{-3}	7.0×10^{-4}	1.0×10^{-3}
$\Delta\sigma^2_{(x,y)}$ (km^2)	zonal	0.04	0.002	0.001	2.1×10^{-4}	1.6×10^{-4}	1.2×10^{-4}
	meridional	0.45	0.35	0.34	9.3×10^{-4}	4.4×10^{-4}	6.2×10^{-4}
transition time (days) zonal, meridional		–	–	–	1.4, 0.19	1.2, 0.13	1.1, 0.15

Table 6.2: Theoretical predictions for (zonal, meridional) shear dispersion in the 1996 rhodamine dye study (see also Figure 6.5). Key is similar to Table 6.1.

direction was approximately the same as in the zonal direction, while mean shear dispersion was two orders of magnitude larger (Table 6.2).

Comparing these predictions to estimates of the irreversible diffusivity made from the observations (Chapter 5; Table 5.3), the total dispersion by mean plus oscillatory shears in the zonal direction, $\kappa_{\mathrm{MIDS}} \approx 3.0 \times 10^{-3}$ m^2 s^{-1}, accounts for only about 0.1% of the observed dispersion. The total shear dispersion in the meridional direction was again larger, $\kappa_{\mathrm{MIDS}} \approx 0.56$ m^2 s^{-1}, but still only accounts for about 12% of the observed dispersion. Again the predictions using the full ADCP time series are somewhat higher, $\kappa_{\mathrm{ADCP}} \approx 0.06$ m^2 s^{-1} and 0.73 m^2 s^{-1} for the zonal and meridional directions, respectively. However, these still only account for approximately 1%–16% of the observed dispersion.

As in the 1995 experiment, the above predictions show that in the 1996 rhodamine dye experiment shear dispersion was not the dominant mechanism of lateral dispersion. In this case, shear dispersion accounts for less than 16% of the irreversible diffusivity inferred from the observations. This implies that some other mechanism must have contributed an effective horizontal diffusivity of order $\kappa_{\mathrm{missing}} \approx 4$ m^2 s^{-1}.

September 1996 Fluorescein Dye Study

For the 1996 fluorescein dye experiment, the time series of shear at the depth of the target density surface (46 m) are shown in Figure 6.6 along with a least squares fit to these data. Using a vertical diffusivity of $\kappa_z = 0.9 \times 10^{-5}$ m^2 s^{-1}, and an initial patch size of $4\sigma_x = 4\sigma_y = 1$ km and $4\sigma_z = 2.5$ m, (6.10)–(6.12) were again integrated numerically to obtain upper bound predictions for shear dispersion.

Shear dispersion predictions for the zonal and meridional variances using the least-squares fit are shown in Figure 6.7, and listed in Table 6.3. Again mean shear dispersion dominated oscillatory shear dispersion in both the zonal and meridional directions. The total contribution of shear dispersion was $\kappa_{\mathrm{MIDS}} \approx (0.15, 0.06)$ m^2 s^{-1} for the (zonal, meridional) directions.

Comparing these predictions to estimates of the observed irreversible diffusivity (Chapter 5;

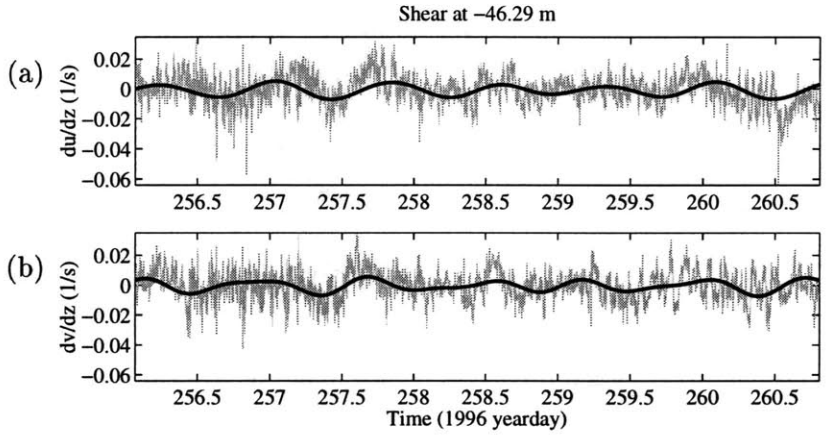

Figure 6.6: Time series of (a) zonal and (b) meridional shears at 46 m depth for the 1996 fluorescein dye study. A least squares fit for a mean plus oscillatory shears with inertial, diurnal, and semidiurnal frequencies is plotted over the raw data for each component.

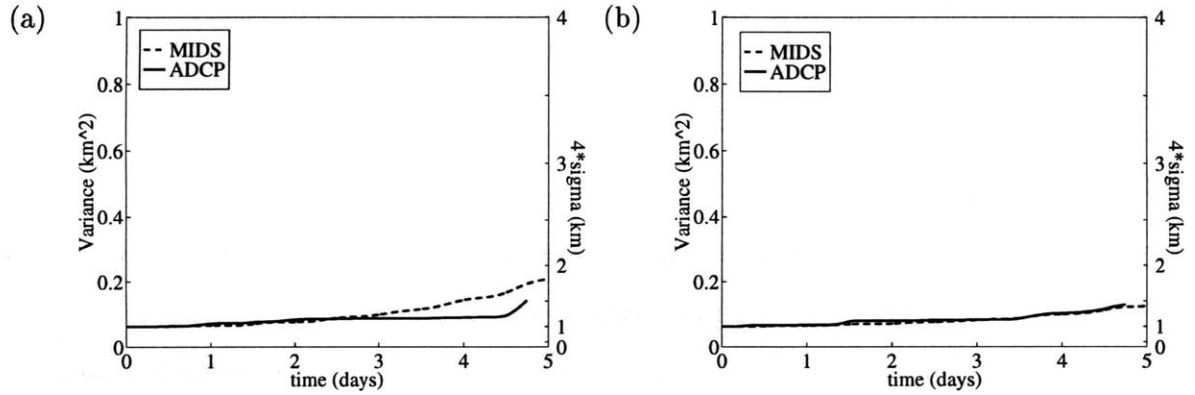

Figure 6.7: Theoretical prediction for (a) zonal and (b) meridional shear dispersion in the 1996 fluorescein dye study (see also Table 6.3). Key is similar to Figure 6.3.

		ADCP	MIDS	M	I	D	S
effective diffusivity ($m^2\ s^{-1}$)	zonal	0.09	0.15	0.14	9.9×10^{-3}	2.5×10^{-3}	3.7×10^{-5}
	meridional	0.08	0.06	0.05	6.6×10^{-3}	1.4×10^{-3}	7.7×10^{-4}
$\Delta\sigma^2_{(x,y)}$ (km^2)	zonal	0.08	0.13	0.12	8.5×10^{-3}	2.1×10^{-3}	3.2×10^{-5}
	meridional	0.07	0.05	0.05	5.7×10^{-3}	1.2×10^{-3}	6.6×10^{-4}
transition time (days) zonal, meridional		–	–	–	1.3, 1.8	0.67, 0.82	0.08, 0.60

Table 6.3: Theoretical predictions for (zonal, meridional) shear dispersion in the 1996 fluorescein dye study (see also Figure 6.7). Key is similar to Table 6.1.

Table 5.3), the total shear dispersion in the zonal and meridional directions again account, respectively, for only 30% and 12% of the observed dispersion. The predictions using the full ADCP time series gave similar results. Thus these predictions show that once again shear dispersion can not account for the observed lateral dispersion. However, for this experiment, the irreversible dispersion estimated from the observations was an order of magnitude smaller than for the previous experiments. Hence, in this case, the implied diffusivity by some other mechanism is also an order of magnitude smaller, approximately $\kappa_{\text{missing}} \approx 0.35 - 0.44\ m^2\ s^{-1}$.

August 1997 Rhodamine Dye Study

The target density for the 1997 rhodamine dye experiment corresponded to a depth of approximately 18 m. Time series for the shears at this depth and their corresponding least-squares fits are shown in Figure 6.8. Again an upper bound on the vertical diffusivity, $\kappa_z = 0.4 \times 10^{-5}\ m^2\ s^{-1}$, was used along with an initial patch size of $4\sigma_x = 4\sigma_y = 1$ km and $4\sigma_z = 2.5$ m. Predictions for shear dispersion are shown in Figure 6.9 and listed in Table 6.4.

The predictions from the least-squares fit suggest that oscillatory shear dispersion in the

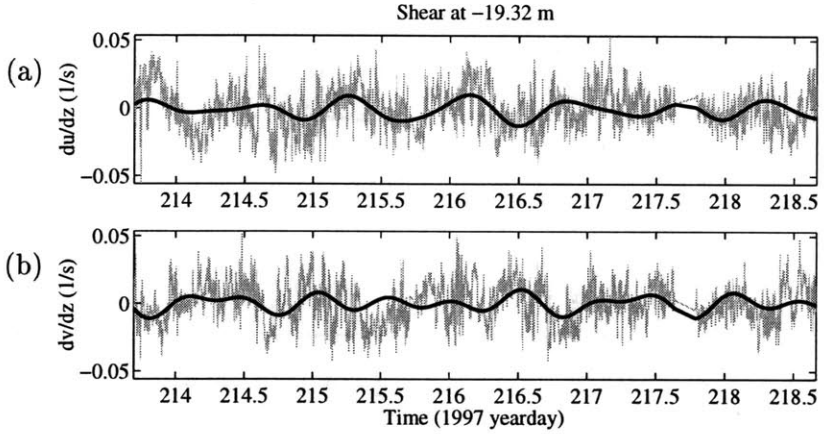

Figure 6.8: Time series of (a) zonal and (b) meridional shears at 35 m depth for the 1997 rhodamine dye study. A least squares fit for a mean plus oscillatory shears with inertial, diurnal, and semidiurnal frequencies is plotted over the raw data for each component.

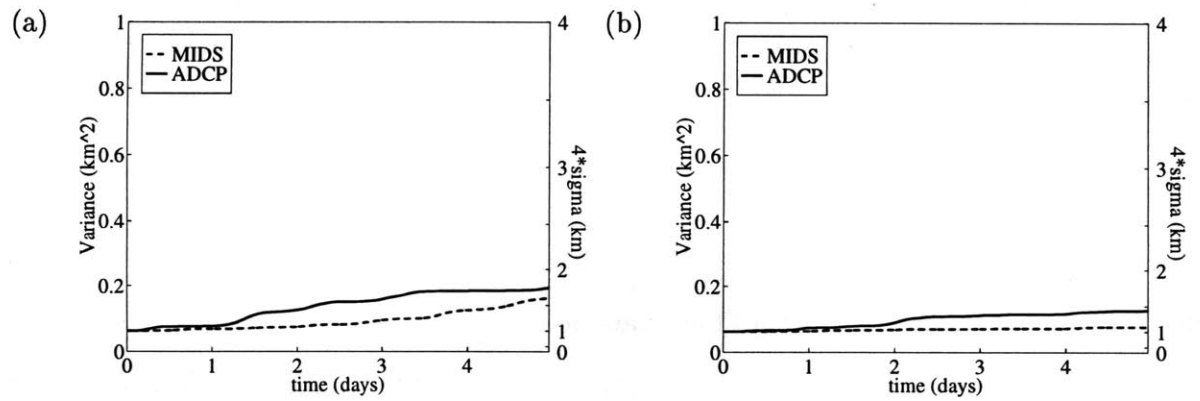

Figure 6.9: Theoretical prediction for (a) zonal and (b) meridional shear dispersion in the 1997 rhodamine dye study (see also Table 6.2). Key is similar to Figure 6.3.

		ADCP	MIDS	M	I	D	S
effective diffusivity ($m^2\ s^{-1}$)	zonal	0.15	0.089	0.07	1.1×10^{-2}	2.2×10^{-3}	1.2×10^{-3}
	meridional	0.077	0.019	0.005	4.2×10^{-3}	8.7×10^{-3}	8.0×10^{-4}
$\Delta\sigma^2_{(r,y)}$ (km^2)	zonal	0.13	0.076	0.06	9.6×10^{-3}	1.9×10^{-3}	1.0×10^{-3}
	meridional	0.066	0.016	0.004	3.6×10^{-3}	7.5×10^{-3}	6.8×10^{-4}
transition time (days) zonal, meridional		–	–	–	1.9, 4.6	0.85, 6.7	0.62, 2.0

Table 6.4: Theoretical predictions for (zonal, meridional) shear dispersion in the 1997 rhodamine dye study (see also Figure 6.9). Key is similar to Table 6.1.

zonal and meridional directions were again approximately equal. In the zonal direction, mean shear dispersion was larger than oscillatory shear dispersion, while in the meridional direction it was smaller. In both zonal and meridional directions, the full ADCP time series gave somewhat higher predictions than the MIDS, i.e., $\kappa_{\rm ADCP} = (0.15,\ 0.077)\ m^2\ s^{-1}$, respectively, compared to $\kappa_{\rm MIDS} = (0.089,\ 0.012)\ m^2\ s^{-1}$. However, again these under-predict the irreversible dispersion estimated from the observations, with the ADCP prediction accounting in this case for 50% and 25% of the zonal and meridional dispersion, respectively.[1] Similar to the 1996 fluorescein experiment, the dispersion estimated for this experiment was an order of magnitude smaller than for the 1995 and 1996 rhodamine experiments. Hence, the missing diffusivity was approximately $\kappa_{\rm missing} \approx 0.15 - 0.23\ m^2\ s^{-1}$.

Summary of Comparison with Observations

Several conclusions can be drawn from this analysis. First, using estimates of mean, inertial, semidiurnal and diurnal shears obtained from a least-squares fit to the observed shears, a

[1]Based on the above calculations, it could be argued that shear dispersion *can* explain the observed dispersion in the 1997 rhodamine dye experiment, since at least the zonal shear dispersion prediction lies within the uncertainty of observed dispersion estimates. However, since the shear dispersion estimates represent upper bounds, as described at the beginning of this section, this is considered unlikely.

linear shear dispersion model predicts that over time scales of 2.5–5 days mean and oscillatory shear dispersion over the continental shelf were comparable in magnitude. Second, and most importantly, this analysis shows that shear dispersion alone does not account for the lateral dispersion observed in the dye experiments. Most notably, the analyses of the 1995 and 1996 rhodamine dye studies suggest that some other mechanism was required to contribute an additional horizontal diffusivity of $\kappa_{\text{missing}} \approx 3 - 4 \text{ m}^2 \text{ s}^{-1}$. The observed horizontal diffusivity in the 1996 fluorescein and the 1997 rhodamine experiments was somewhat smaller. Hence the additional diffusivity required in those cases was $\kappa_{\text{missing}} \approx 0.15 - 0.44 \text{ m}^2 \text{ s}^{-1}$. These estimates of κ_{missing} represent a lower bound on the missing diffusivity in these experiments, insofar as the above predictions were an upper bound on shear dispersion.

6.1.3 Further Considerations

In Section 6.1.2, a time dependent linear shear model was used to estimate upper bounds on the lateral dispersion due to shear dispersion. Time series of shear collected by shipboard ADCP were used in combination with upper bounds on the vertical diffusivities estimated directly from the dye experiments. The above analysis is now expanded to incorporate two important considerations. First, the effects of a time dependent vertical diffusivity are examined. Second, it may be noted that the shear dispersion predictions of the previous section were made using the shear at a fixed depth which was equal to the mean depth of the target density surface. These predictions are now compared to similar predictions using the shear across the target surface, this time keeping account of how the depth of this surface fluctuated in time. The analysis of this section shows that the predictions of the previous section are not significantly modified when these two effects are accounted for.

Time-Dependent Vertical Diffusivity

In the above analysis, the shear dispersion contribution to the horizontal variance would be modified if the vertical diffusivity also varied in time. This can occur, for example, if the

vertical diffusivity is related to the shear amplitude through a Richardson number criterion.

The effect of a time-dependent diffusivity may readily be examined using the linear shear dispersion model of Section 6.1.1. Letting $\kappa_z = \kappa_z(t)$ in (6.7)–(6.9), the solution becomes

$$\sigma_x^2 = \sigma_x^2(t_o) + 2\int_{t_o}^{t} \kappa_x(t') + G^2(t')\kappa_z(t')dt', \tag{6.13}$$

$$\sigma_z^2 = \sigma_z^2(t_o) + 2\int_{t_o}^{t} \kappa_z(t')dt', \tag{6.14}$$

$$G = \frac{\int_{t_o}^{t} \alpha(t')\sigma_z^2(t')dt'}{\sigma_z^2(t)}. \tag{6.15}$$

To understand the role of $\kappa_z(t)$ in these solutions, consider an idealized case where the vertical diffusivity is proportional to the magnitude of the shear, i.e., $\kappa_z = \xi^2\|\alpha\|$, where ξ is some scale factor with units of length squared, consistent with a crude model of a Richardson number criterion for shear instability. Since from (6.15) the tilt factor, G, varies in quadrature with α, it follows that G is also in quadrature with κ_z. Thus (6.13) shows that the shear dispersion effect for a time dependent diffusivity is less than the effect from a constant diffusivity with magnitude equal to the mean of the time dependent diffusivity.

Extending this idea to a shear in two horizontal dimensions, the effects of a time dependent vertical diffusivity become more complex. Rather than developing the analogous three dimensional solution, consider the following three cases which illustrate the basic effects (Figure 6.10). In all cases assume, as above, that the vertical diffusivity varies proportionally (or at least in phase with) the amplitude of the shear.

In the first case, consider a vertical shear across two horizontal dimensions in which the x and y components of shear are perfectly in phase (Figure 6.10a). The result is similar to the single shear case. Namely, the shear dispersion effect for a time dependent diffusivity is less than the effect from a constant diffusivity with magnitude equal to the mean of the time dependent diffusivity. This is true regardless of the relative amplitudes of the two shear components.

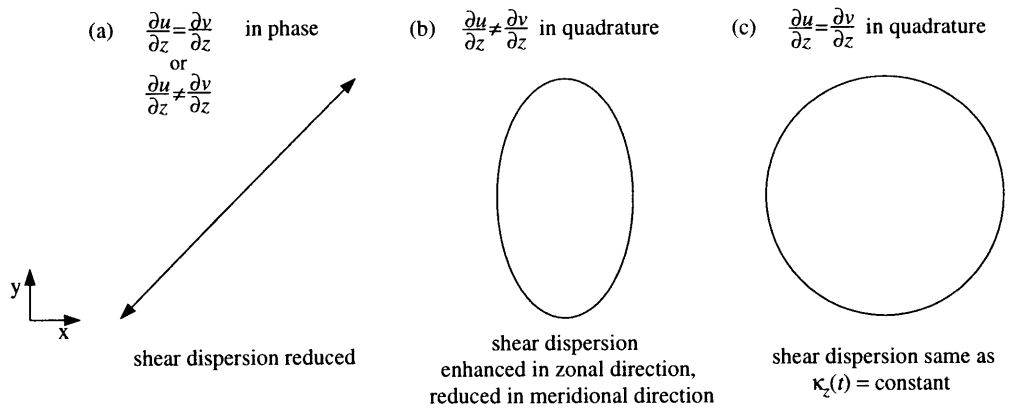

Figure 6.10: Schematic of possible combinations of vertical shear components in two horizontal dimensions. Assuming vertical diffusivity which varies proportionally to the shear amplitude, the shear dispersion effect will be enhanced or reduced as a function of the relative phase and amplitudes of the two components of shear.

In the second case, suppose the horizontal shears are unequal but in quadrature (Figure 6.10b). By (6.15) the tilt factor, G, in the direction of the major axis of the shear would be in quadrature with the diffusivity, while the tilt factor in the direction of the minor axis of the shear would be in phase with the diffusivity. This occurs simply because the diffusivity will be in phase with the shear in the major axis. In the direction of the major axis then, the effect of the time dependent vertical diffusivity would again be to decrease shear dispersion. However, in the direction of the minor axis, the converse would be true, i.e., the effect of shear dispersion would be increased.

Finally, as the third case, if the two components of shear are equal but in quadrature (Figure 6.10c). In this case, the amplitude of the shear as well as the vertical diffusivity, $\kappa_z = \xi^2\|\alpha\|$ would be constant in time, as it was before we began this thought experiment.

Based on the above considerations, if the vertical diffusivity is assumed proportional to the shear amplitude, as with a Richardson number criterion, shear dispersion is expected to be reduced/enhanced along the major/minor axes of an elliptical shear compared to the case of a constant vertical diffusivity. In the coastal ocean, elliptical shears may occur due to a baroclinic tide or inertial oscillations. However, during the CMO dye studies, the baroclinic

tides and the inertial shear were not significantly polarized (maximum ellipticity of about 1.17). As a result, re-calculating the shear dispersion predictions, using a time dependent diffusivity which varied as the amplitude of the shear, did not produce significantly different results. This indicates that the incorporation of a time dependent diffusivity is insufficient to account for the discrepancy between the observed irreversible diffusivities estimated in Chapter 5 and the theoretical shear dispersion predictions of Section 6.1.2.

Level vs. Layer Shears

A second consideration in the analysis of Section 6.1.2 is that predictions of shear dispersion are most appropriately made using the shear across a target density layer (layer shear) rather than the shear at a fixed depth (level shear). This distinction may be important if the depth of the target density surface varies significantly over the course of an experiment. The difficulty in obtaining shears at a given layer lies in the fact that ADCP observations alone do not provide information about the depth of a given density surface. CTD observations can provide additional information about isopycnal depths; however, in practice a CTD was not always available to make these measurements.

Based on Figures 4.4, 4.16, and 4.35, it appears that the depth of the target density surface can fluctuate as much as 15 m about its mean level. In light of this, a case study of the 1995 rhodamine dye experiment was carried out to examine how such fluctuations would modify the shear dispersion prediction if the more appropriate layer shear were used instead of the level shear as was done in Section 6.1.2.

In the 1995 rhodamine experiment, a large portion of the baroclinic energy was contained in the first baroclinic mode (Section 4.2.1). In addition, the depth of maximum shear corresponded roughly to the depth of the main pycnocline and thus the target density surface (Figure 6.11). As a test to see whether there was a significant difference between the shear dispersion prediction for a fixed level vs. a fixed layer, the depth of maximum shear was used as a proxy for the depth of the target density surface. In this case, it was found that the shear

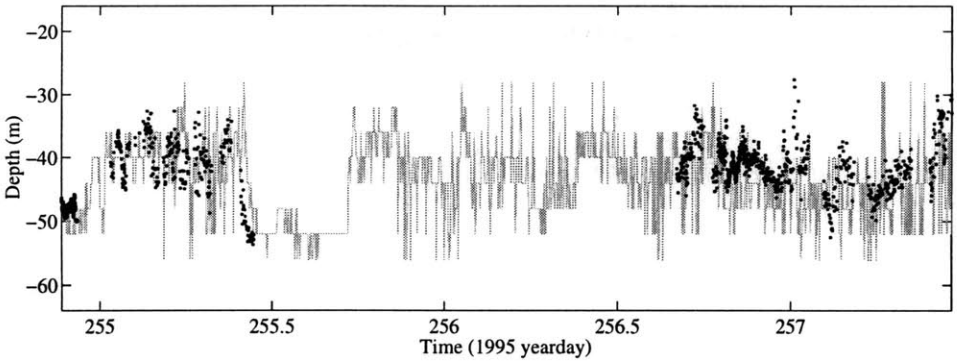

Figure 6.11: Depth of maximum shear (solid line) and depth of the target density surface for the 1995 rhodamine dye experiment.

dispersion prediction for the 1995 dye experiment was *decreased* by about 30% and 50% in the zonal and meridional directions, respectively compared to the level shear case.

The reason that the layer shear gave a lower prediction than the level shear in the 1995 dye experiment is not intuitively obvious. It is because of a few events in which large shears corresponded to large isopycnal displacements. At the onset of these events, the layer and level shears were approximately equal. However, as the layer shear increased, the depth of the target density surface became displaced so that the level shear underestimated the layer shear. Then, although in actuality the layer shear reversed direction and tilted the patch back to its original position, the level shear under-predicted this shear reversal. As a result, the layer shear averaged to zero, while the level shear gave a net shear averaged over these events. In other words, these large oscillatory shear events were aliased by the level shears as mean shear dispersion, thus giving a higher shear dispersion prediction than the layer shear. Thus in this case, the use of a layer shear rather than a level shear would not alter the main conclusion of Section 6.1.2, i.e., that shear dispersion does not explain the observed irreversible dispersion in the CMO dye studies.

Summary of Further Considerations

Two main conclusions can be drawn from the above considerations. First, it was shown that a time-dependent vertical diffusivity can lead to either reduced or enhanced shear dispersion, depending on the relative phase of the two horizontal shear components. Nevertheless, the relatively small anisotropy of the tidal and inertial shears during the CMO dye studies suggested that the effects of this time dependence were small. Second, the difference between layer and level shears was shown to effect these dispersion predictions also. Using the 1995 dye experiment as a case study, however, it was shown that at least for that experiment the main conclusion of Section 6.1.2 is only reinforced. Namely, shear dispersion does not explain the observed lateral dispersion in the CMO dye studies. Instead, some other mechanism is required to contribute a diffusivity of $\kappa_{\text{missing}} \approx 3 - 4$ m^2 s^{-1} for the 1995 and 1996 rhodamine experiments, and $\kappa_{\text{missing}} \approx 0.15 - 0.44$ m^2 s^{-1} for the 1996 fluorescein and the 1997 rhodamine experiments.

6.2 Lateral Intrusions

The analyses of Section 6.1 showed that shear dispersion alone, even with a time-dependent vertical diffusivity and using the appropriate target density layer, does not account for the observed lateral diffusion of the dye. This implies that some other mechanism must contribute to lateral dispersion over the continental shelf. One possibility is mixing due to lateral intrusions.

As first suggested by Stommel and Fedorov (1967) and Stern (1967), horizontal gradients in water mass properties can result in interleaving density currents and/or diffusive interleaving. The effects of these two types of intrusions on the lateral dispersion of the dye are now considered. Although there is evidence for both types of interleaving during the CMO dye studies, the spatial and temporal scales of these intrusions were too large to be effective mixing mechanisms. The intrusions were either of large enough spatial scales to be considered advective phenomena (i.e., large enough to be resolved by the shipboard ADCP), or their time

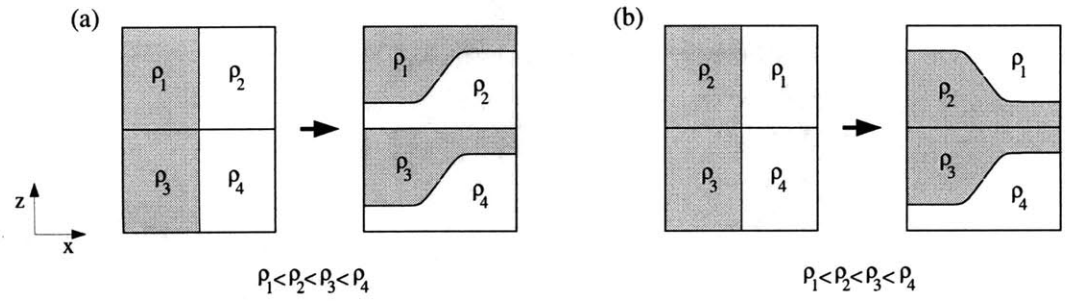

Figure 6.12: Schematic of two possible combinations of density arrangements that could lead to interleaving (following Stommel and Fedorov, 1967; see text).

scales would have been too small to have a significant effect on the dye over the course of the experiments.

6.2.1 Density Driven Intrusions

As originally discussed by Stommel and Fedorov (1967) horizontal density gradients can cause interleaving density currents. This occurs when the density of a water mass at one location is intermediate relative to density layers at a neighboring location. Two water mass distributions which may lead to interleaving are shown schematically in Figure 6.12.

In the first case, two neighboring density profiles are such that initially the surface water to the left is lighter than the surface water to the right (Figure 6.12a). Similarly, the deep water to the left is lighter than the deep water to the right. However, the deep water to the left is heavier than the surface water to the right. If the watermasses in this initial configuration are allowed to adjust to their equilibrium levels, the result is an interleaving of layers as depicted in (Figure 6.12a).

In the second case, two neighboring density profiles are such that initially both the surface and deep waters to the left are heavier than the surface water to the right, but lighter than the deep water to the right (Figure 6.12b). In this case if the watermasses are allowed to

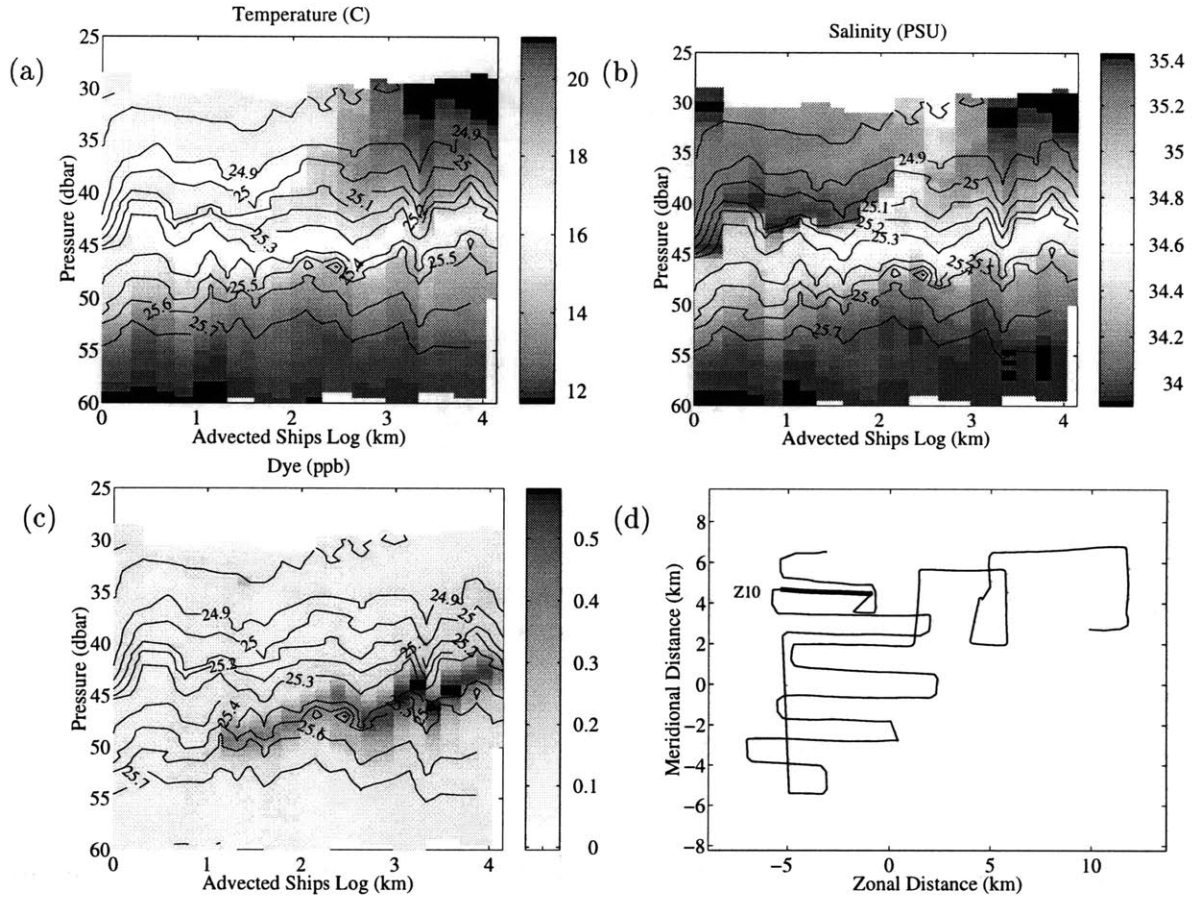

Figure 6.13: (a) Temperature, (b) salinity, and (c) dye concentration along a zonal transect taken during Survey 2 of the 1995 rhodamine dye study, showing evidence of a density-driven intrusion in the vicinity of the dye patch. Over-plotted on each panel are contours of potential density in units of kg m^{-3}. Panel (d) shows the location of this transect (thick line) relative to the rest of the survey.

equilibrate, interleaving will again occur, although, as depicted in Figure 6.12b, the details of the interleaving will be slightly different than in Figure 6.12a.

A necessary condition for density driven intrusions to exist is the presence of horizontal density gradients. Given the near proximity of the shelf-slope front to the CMO study site, it is not surprising that evidence of such intrusions can be seen in data collected during the CMO dye experiments. Figure 6.13 shows an example of one intrusion observed during the final survey of the 1995 pilot dye study. The intrusion had a vertical scale of 5–10 m, and was centered at about 40–50 m depth. Its horizontal scale was at least a few km so that it

extended across the entire transect. The sloping isopycnals associated with this warm saline water intruding toward the west are reminiscent of the two scenarios depicted in Figure 6.12. Associated with this intrusion are horizontal temperature gradients as large as 2 ^{o}C km^{-1} and salinity gradients as large as 1 PSU km^{-1}.

When considering the effect of an intrusion on a dye patch, relative size is a key factor. Here, both the vertical and horizontal scales of the intrusion were comparable to the scales of the tracer patch. Thus, the pressure gradients which drove the intrusion are expected to have had the same advective influence on the dye as they did on the density field. In other words, an intrusion of this magnitude would have differentially advected the dye patch in either the horizontal or vertical direction, or both. In the vertical direction, differential advection on these scales (5–10 m) would have been resolved by our ADCP observations as a vertical shear and would already have been incorporated in the shear dispersion calculations of Section 6.1. In the horizontal direction, these pressure gradients would have been the driving force for the large-scale horizontal shears and strains that elongated the patch in either the zonal or meridional direction. It is thus argued that such a large-scale intrusion (relative to the size of the dye patch) should be considered an *advective* rather than a *diffusive* mechanism in the context of the present work, and thus would not explain the *irreversible* diffusivities estimated in Chapter 5.

6.2.2 Diffusive Interleaving

As first discussed by Stern (1967), horizontal gradients in temperature and salinity may result in interleaving of water masses even in the absence of large-scale horizontal density gradients. This diffusive interleaving occurs when relatively warm/salty water lies next to cold/fresh water. Even when both water masses are stably stratified, a small horizontal displacement of one water mass into the other can create a region which is double-diffusively unstable (Figure 6.14). The ensuing double diffusion may then cause a net salt (and buoyancy) flux, which leads to a local pressure gradient and then to further intrusion. This positive feedback

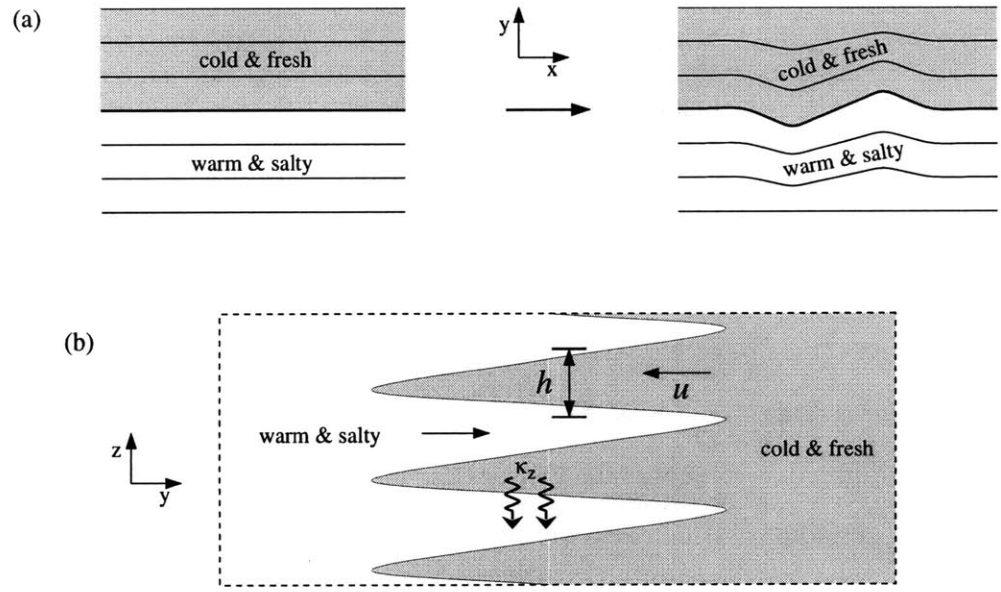

Figure 6.14: Schematic of diffusive interleaving.

mechanism results in a growing instability in which small perturbations lead to self-propagating intrusions (Stern, 1967; Toole and Georgi, 1981).

Evidence for diffusive interleaving in the vicinity of the New England shelf-slope front was reported by Voorhis et al. (1976). Based on CTD casts made while tracking neutrally buoyant floats, they estimated horizontal scales of the intrusions to be of order 10–30 km and layer thicknesses ranging from 1–30 m, with a typical layer thickness of about 10 m. Ruddick and Turner (1979) showed that these vertical scales agree with predictions based on energetics arguments, which imply a vertical scale of approximately 6 m with an uncertainty factor of 2 based on laboratory experiments. Horne (1978) also reported interleaving along the shelf-slope front off Nova Scotia, for which he estimated typical vertical and cross-front scales of order 10 m and 3–5 km, respectively. (As noted by Ruddick and Turner, 1979, the observations by Horne were likely dominated by diffusive fluxes rather than double-diffusive fluxes. Hence the vertical scales may have been set by a different process than those observed by Voorhis et

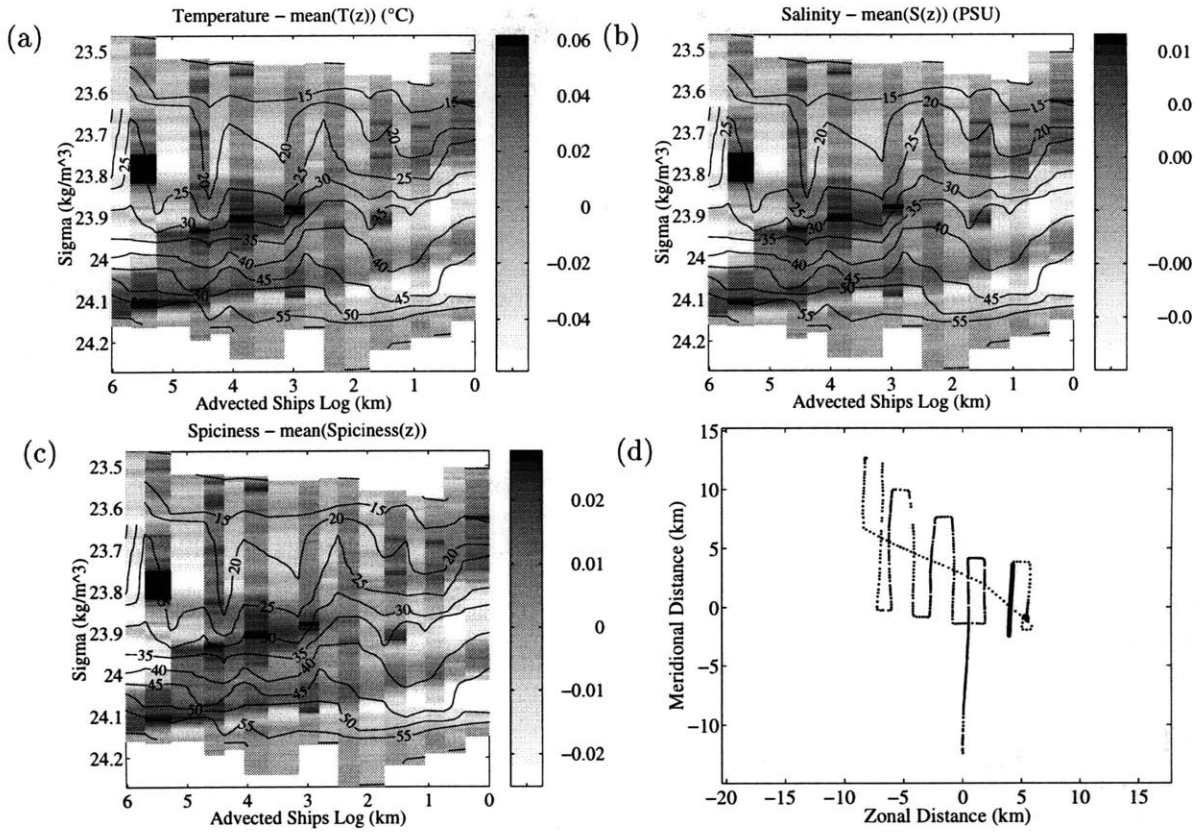

Figure 6.15: (a) Temperature anomaly, (b) salinity anomaly, and (c) spiciness anomaly from a meridional transect taken during Survey 3 of the 1996 rhodamine dye study. A mean property profile has been subtracted from each data array. Contour lines of pressure are plotted in each panel. Panel (d) shows the location of this transect (thick line) relative to the rest of the survey.

al. 1976.)

Given such observational precedence, it is no surprise that evidence for diffusive interleaving was also found during the CMO dye experiments. An example of interleaving from the final survey of the 1996 rhodamine dye study is shown in Figure 6.15. The alternating horizontal bands of relatively high and low temperature and salinity anomalies are readily apparent, and indicate a typical vertical scale of about 10 m, consistent with observations of previous investigators. (The vertical offset seen in alternating profiles is an artifact of stagnating flow at the front of the sampling sled and of the mismatch in the time response in the temperature and salinity sensors.)

Laboratory studies of Ruddick and Turner (1979) suggested that the horizontal propagation speed of double-diffusive intrusions scales approximately as

$$u \approx \frac{1}{200} N h, \tag{6.16}$$

where N is the buoyancy frequency and h is the thickness of the intrusions (this result was first published by Ruddick and Hebert, 1988). From this result, using a typical buoyancy frequency for the CMO site of $N = 0.02$ rad s^{-1} (10 cph), and a layer thickness $h = 10$ m, the inferred propagation speed of the observed intrusions is $u \approx 1 \times 10^{-3}$ m s^{-1}, which is too small to be resolved by shipboard ADCP observations. However, using this velocity scale and an appropriate time scale, an effective horizontal dispersion, $\kappa_h \approx u^2 T$, due to interleaving can be estimated. Assuming as a time scale the time it would take an anomaly to diffuse away due to vertical diffusion (i.e., the effective lifetime of an anomaly), $T \approx h^2/\kappa_z$, the horizontal dispersion becomes,

$$\kappa_h \approx u^2 T = \frac{u^2 h^2}{\kappa_z} = \frac{1}{200^2} \frac{N h^4}{\kappa_z}. \tag{6.17}$$

This approach is similar to that used by Joyce (1977) where the effective horizontal diffusivity due to lateral intrusions is assumed to be in statistical equilibrium the vertical diffusivity.

For a layer thickness of $h = 10$ m, and a vertical diffusivity, $\kappa_z = 10^{-5}$ m^2 s^{-1}, consistent with the dye, the above scaling gives a time scale of $T \approx 100$ days, and a corresponding effective horizontal diffusivity of $\kappa_h \approx 10$ m^2 s^{-1} (Table 6.5). While this horizontal diffusivity is certainly enticing as an explanation for the observed dispersion in the CMO dye studies, the time scale associated with this process is much too long to be relevant to the 3–5 day experiments described in Chapters 4 and 5. On the other hand, assuming a smaller vertical scale of $h = 1$ m, so that the time scale, $T \approx 1$ day, is of the same order as the dye experiments, the effective horizontal diffusivity $\kappa_h \approx 10^{-3}$ m^2 s^{-1} becomes much smaller than that observed from the dye studies. Similar estimates for an intermediate value of $h = 3$ m are given in Table 6.5, and again show that the contribution to the effective horizontal diffusivity would be

	$h = 1$ m	$h = 3$ m	$h = 10$ m
u (m s^{-1})	10^{-4}	3×10^{-4}	10^{-3}
T (days)	1	10	100
κ_h (m^2 s^{-1})	10^{-3}	0.1	10

Table 6.5: Estimated propagation speeds, time scales, and effective horizontal diffusivities for various values of the vertical scale of the intrusions. κ_z is assumed to be of order 10^{-5} m^2 s^{-1}.

too small to explain the observed dispersion.

6.2.3 Summary of Lateral Intrusion Analysis

In summary, considering that the vertical scale of the observed intrusions was comparable to the vertical scale of the dye patches, the effect of large-scale density intrusions on the dye patches was more likely advective rather than diffusive, as discussed in Section 6.2.1. In Section 6.2.2, simple scaling arguments further showed that for diffusive interleaving the time scale associated with intrusions of order $h \approx 10$ m thick would have been much too long to have had a significant effect during the 3–5 day long CMO dye experiments. Intrusions with vertical scales of order a few meters would also have been ineffective as a mechanism of lateral dispersion because the resulting horizontal diffusivities would have been too small.

Chapter 7

Vortical Motions - A Proposed Mechanism of Lateral Dispersion

The analyses of Chapters 5 and 6 suggest that a significant part of the irreversible lateral dispersion observed during the CMO dye experiments can not be explained by the existing paradigms of shear dispersion and dispersion by lateral intrusions of different water masses. In this chapter an alternative mechanism, dispersion by vortical motions caused by the relaxation of diapycnal mixing events, is proposed which could explain these observations. The proposed mechanism relies on the fact that vertical mixing in the ocean is not uniform in space and time. Rather, it is episodic, consisting of isolated events which are the result of breaking internal waves (Figure 7.1). These mixing events lead to an effective lateral dispersion which is caused by the horizontal adjustment and thus displacement of regions of well-mixed fluid.

The first evidence that turbulence in the thermocline occurs in intermittent local patches was obtained off the west coast of Vancouver Island by Grant et al. (1968) using temperature and velocity microstructure probes mounted on the bow of a submarine. Their observations showed patches of turbulence ranging from 30 m to 170 m in horizontal scale, (precise vertical scales of patches could not be obtained from their observations due to the limited number of probes used). Such regions of high mixing can be expected to occur as the result of fluctuating

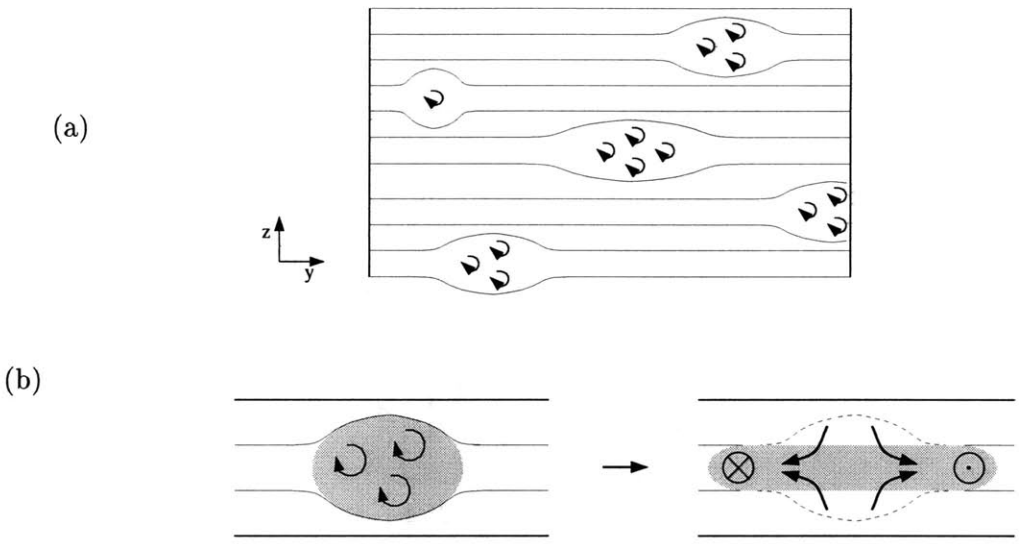

Figure 7.1: Schematic of proposed mechanism of lateral dispersion showing mixing which is episodic in space and time. Panels (b) and (c) show a single mixing event and the ensuing lateral spreading as the stratification adjusts back to its original level.

vertical shears caused by internal and inertial gravity waves. As envisioned by Phillips (1966) and by Garrett and Munk (1972), local shear instabilities are produced when the shear exceeds a critical value set by a Richardson number criterion. A random superposition of waves causes these instabilities to occur episodically in both space and time. This type of behavior was observed, for example, in the summer thermocline of the Mediterranean Sea by Woods (1968) who used divers to photograph dye streaks during internal wave breaking events. Laboratory experiments of Thorpe (1971) and meteorological observations of Browning and Watkins (1970) suggest that the thicknesses of the resulting turbulent layers are such that the layer Richardson number is 0.4 ± 0.1, based on the maximum shear experienced, (Garrett and Munk, 1972).

As a result of episodic mixing, localized regions of low stratification are generated preferentially in regions of high mixing, as described in detail by Woods and Wiley (1972) in their discussion of "billow turbulence". Associated with these stratification anomalies are horizontal pressure gradients which cause the well-mixed regions to adjust laterally, either geostrophically or frictionally, to form "blini" or pancakes (Phillips, 1966; Figure 7.1b). The process of adjustment may lead to two types of motions, a slumping velocity which is directed radially outward,

and in the case of geostrophic adjustment, an azimuthal velocity which is geostrophically balanced. For both types of motions, the net effect of the adjustment is similar; the dye will be displaced laterally.

The effective lateral dispersion associated with the adjustment of mixing events will depend at the very least on the vertical and horizontal scales, and the intensity of the episodic mixing, since these scales ultimately set the scales of the adjustment. Assuming that the ocean is full of these isolated mixing events, the goal is then to express both the mean vertical and horizontal diffusivities in terms of the initial event scales. To begin, the net vertical diffusivity observed in the ocean can be expressed as an average over some number (possibly large) of events. Meanwhile, the sum of the lateral displacements associated with the adjustment of these events can be expressed in terms of an effective horizontal diffusivity. For a single event, this lateral diffusivity is more appropriately described as an advective process. However, for a large number of events, the dispersion can be expressed in terms of a random walk with rms step size equal to the rms horizontal displacement averaged over the events.

The effects of such blini or vortical motions in the open ocean is presently being investigated by Polzin et al. (1998) in the context of shear dispersion and the North Atlantic Tracer Release Experiment (see Part I of this thesis). In the present chapter, the effects of vortical motions in the coastal ocean are explored. In Section 7.1 the observations from the tracer tow-yo surveys described in Chapter 4 are revisited, and the scales of patchiness during the CMO dye studies are examined. Also in Section 7.1, the microstructure observations of Oakey and Greenan (1998), which were made concurrently with the dye experiments, are used to infer spatial scales of localized mixing events. In Section 7.2, a description of lateral dispersion by isolated mixing events and vortical motions is presented. The order of magnitude of the lateral diffusivity due to this mechanism is estimated for a variety of event space and time scales spanning the relevant viscid/inviscid and rotational/non-rotational parameter regimes. The results of this analysis show that the lateral dispersion associated with episodic mixing

and vortical motions could explain the lateral dispersion observed in at least two of the CMO dye studies. Remaining discrepancies between the proposed mechanism and the observations are also discussed. Section 7.3 discusses the role of shear dispersion in the context of vortical motions. Finally, Section 7.4 summarizes the results of this chapter.

7.1 Observed Scales of Mixing

The scales of mixing during the CMO dye studies can be estimated using three distinct measures. First, scales are inferred from the patchiness of the dye which was noted in many of the dye surveys described in Chapter 4 (Section 7.1.1). Second, maps of potential density based on the dye survey tow-yo data are used to estimate spatial scales of isolated regions of low stratification which are assumed to be the result of localized mixing events (Section 7.1.2). Third, the spatial scales of localized mixing events are estimated from dissipation rates of both eddy kinetic energy and temperature variance based on microstructure observations (Section 7.1.3).

7.1.1 Scales Inferred from the Dye Data

One noteworthy feature of the dye data discussed in Chapter 4 is that patchiness could be seen in the dye distributions of all of the experiments, particularly the 1996 and 1997 rhodamine dye studies (e.g., Figures 4.22c,d,e; 4.40c,d).[1] Patchiness occurred in both the horizontal and vertical. In some cases distinctly isolated regions of high dye concentration were observed (e.g., Figure 4.40c), while in other cases the patchiness was superimposed on a background of more diffuse concentrations (e.g., Figure 4.10e).

Inspection of the available tow-yo transects suggests that scales of variability of the dye were between 0.5–10 m vertically and a few hundred meters to more than a kilometer horizontally.

[1]The 1996 fluorescein experiment was also quite patchy. However, since the injection for that experiment was discontinuous, it is not clear whether the observed patchiness stemmed from the sporadic release of dye or from some stirring mechanism (see Section 4.3.3).

It is unclear whether significant variability occurred on scales much smaller than the minimum estimates here. The raw data had a vertical resolution of approximately a 0.1 m and a horizontal resolution of about 100 m, so that layers smaller than this scale, if they existed, would not have been detected.

7.1.2 Tow-yo Transects and Density Anomalies

A second interesting feature of the data collected during the CMO dye surveys is the nature of the stratification. Superimposed on a background of fairly smooth stratification were localized regions of relatively low stratification. The presence of these regions indicates that intense mixing may have occurred on vertical scales of only a few meters. Localized mixing is not the only possible explanation for the existence of these regions; for example, internal wave strain could also explain these observations. However, velocity and temperature microstructure data collected during the CMO dye cruises are consistent with the mixing explanation. Section 7.1.3 discusses this in further detail.

Figure 7.2 shows an example of density profiles showing stratification anomalies in the 1996 fluorescein dye study. All profiles here were taken below the main pycnocline, from about 30–60 m depth. In this particular transect, the well mixed layers ranged from 2–10 m thick vertically and a few hundred meters to a few kilometers horizontally.[2] In many cases, the anomalies were oblique to potential density surfaces. As discussed in Section 7.2.5 this may have had a significant influence on their lateral adjustment. Similar anomalies were observed in the other dye experiments.

7.1.3 Mixed Layers and Microstructure

During the 1996 and 1997 CMO dye cruises, dissipation rates of temperature variance and turbulent kinetic energy were measured using EPSONDE microstructure probes by Oakey and

[2]Note, the larger-scale events are more readily apparent to the eye since these span many profiles. However, events which span only a few profiles are evident upon closer scrutiny.

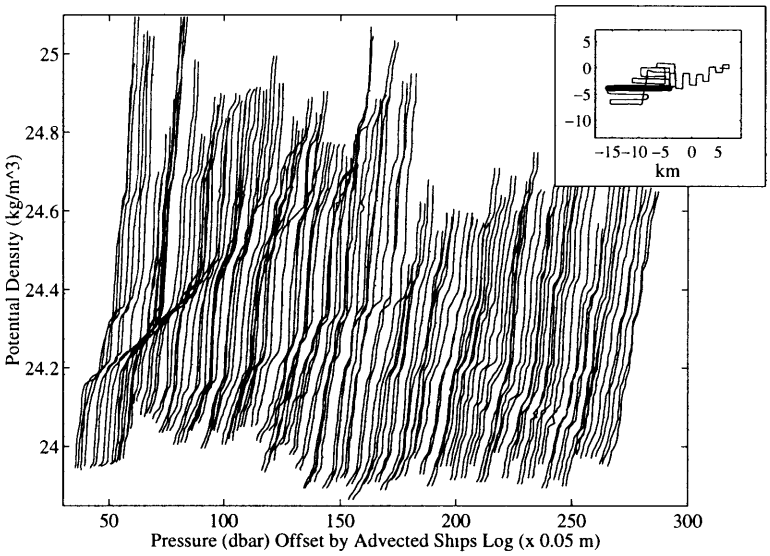

Figure 7.2: Density profiles along Transect Z07 of Survey 3 of the 1996 fluorescein dye experiment showing localized regions of nearly constant density, i.e., low stratification. Pressure is plotted on the x axis and potential density on the y axis so that regions of low stratification appear as horizontal segments of the profiles. Successive profiles are offset by distance along the ship track in an advected coordinate frame. A plan view of the station locations showing the relative location of this transect (bold line) is shown in the subplot.

Greenan (1998). Microstructure data were collected on a schedule of days alternating with the dye surveys for the purpose of making direct comparisons of diapycnal diffusivities from these two methods. These microstructure data are now examined to characterize the vertical and horizontal scales of the regions of energetic mixing.

The locations of the EPSONDE microstructure stations of the 1996 fluorescein dye study are shown in Figure 7.3 along with the ship track during the three surveys (see also Figure 4.25). For each day that EPSONDE data were collected, a region relatively free of fishing gear was selected as the site of repeated stations. Each station consisted of a series of successive profiles taken while the ship was underway at about 1 kt. This provided an effective horizontal resolution of 100–400 m. For the 1996 fluorescein experiment a total of twenty-one EPSONDE stations were occupied, with each station consisting of between twelve and forty-two profiles. Altogether, a total of 522 EPSONDE profiles were taken during the 1996 fluorescein experiment. A comparable number of stations were occupied during the 1996 and 1997 rhodamine

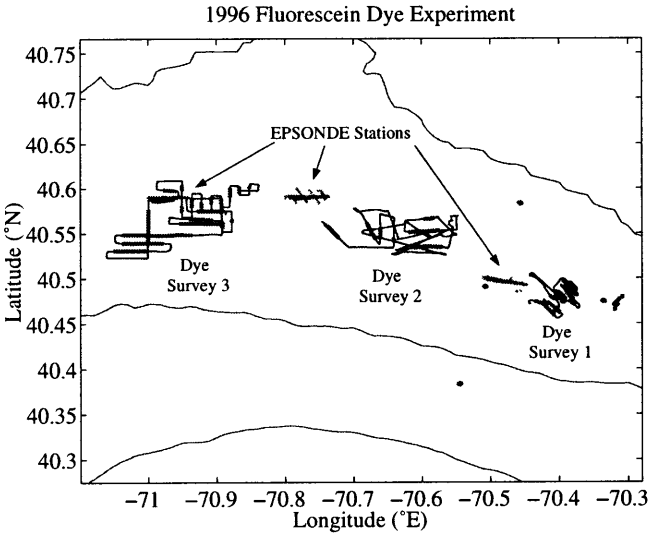

Figure 7.3: Ship track during the 1996 fluorescein dye study showing the locations of the EPSONDE microstructure stations relative to the three dye surveys. (See also Figure 4.25.)

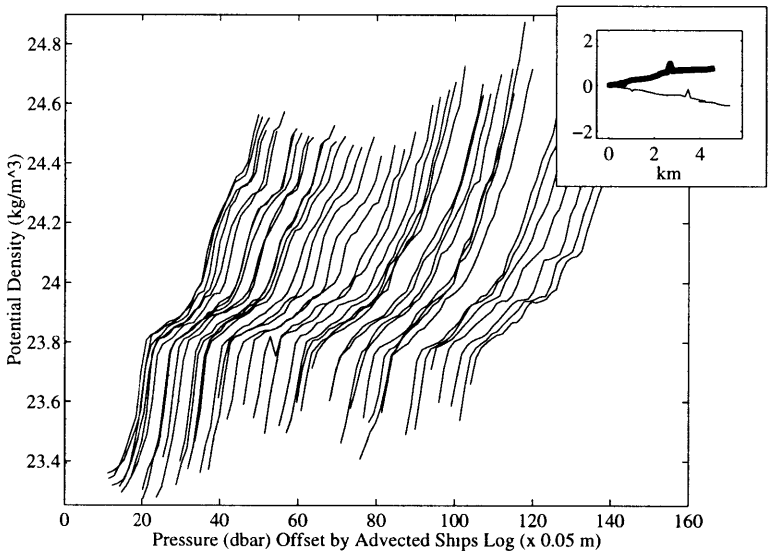

Figure 7.4: Density profiles along EPSONDE station number 24 during the 1996 fluorescein dye experiment showing localized regions of low stratification similar to those observed during the dye surveys (Oakey and Greenan, 1998). A plan view of the station locations is shown in the subplot with the thin line indicating the station locations before accounting for advection and the bold line indicating the advected station locations. Key is similar to Figure 7.2. (Note, the scales here are different than those in Figure 7.2.)

and the 1997 fluorescein experiments.

A series of density profiles taken along a single EPSONDE station line are shown in Figure 7.4. Here the data have been smoothed over approximately 0.5 dbar bins in order to yield the same resolution as the data in Figure 7.2. As in the transects taken during the dye surveys, localized regions of low stratification are seen throughout the water column, particularly below the main pycnocline, which here was at about 20 m depth. Like the tow-yo data, the EPSONDE profiles show that the stratification anomalies had vertical scales of 2–10 m and horizontal scales ranging from a few hundred meters to a few kilometers.

The same data from EPSONDE station number 24 are shown in Figure 7.5, this time in the form of buoyancy frequency profiles, $N^2 = -\frac{g}{\rho_o}\frac{d\rho}{dz}$. In this figure, the data have been averaged over 0.25 s intervals, giving an effective resolution of 0.15 m. Here regions of enhanced finestructure can be seen throughout the water column, with vertical scales again ranging from 2–10 meters and horizontal scales of a few hundred meters to a few kilometers.

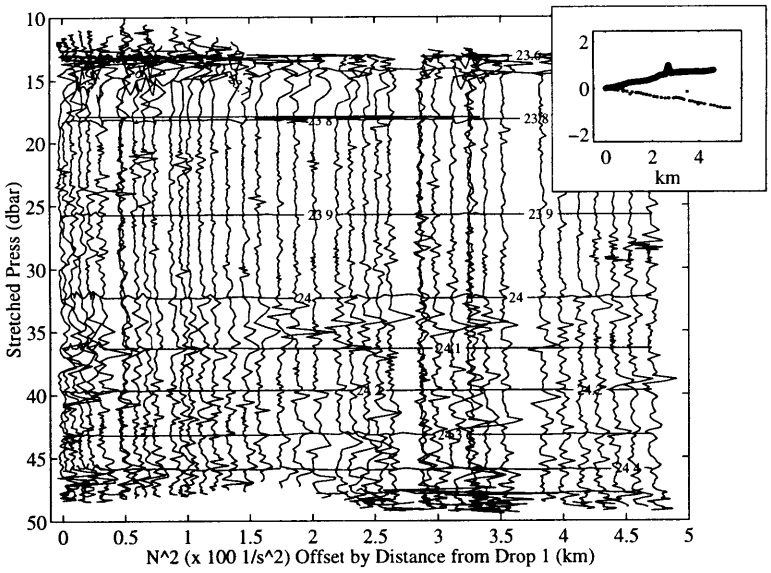

Figure 7.5: Buoyancy frequency profiles along EPSONDE station number 24 during the 1996 fluorescein dye experiment showing localized regions of enhanced finestructure (Oakey and Greenan, 1998).

For each of the buoyancy frequency profiles shown in Figure 7.5, the dissipation rates of turbulent kinetic energy,

$$\epsilon = 7.5\frac{\mu}{\rho}\overline{\left(\frac{\partial u'}{\partial z}\right)^2} \qquad (\mathrm{m^2\ s^{-3}}), \tag{7.1}$$

(e.g., Oakey, 1988) and temperature variance,

$$\chi = 6D\overline{\left(\frac{\partial T'}{\partial z}\right)^2} \qquad (^o\mathrm{C\ s^{-1}}), \tag{7.2}$$

were computed using the full 256 Hz data, and then averaging over 2.0 second intervals (Oakey and Greenan, 1998; Figures 7.6a and b). Here u' and T' represent the high frequency velocity and temperature fluctuations, while $\frac{\mu}{\rho} = 1.3 \times 10^{-6}$ m^2 s^{-1} and $D = 1.4 \times 10^{-7}$ m^2 s^{-1} are the kinematic viscosity of water and the molecular diffusivity of heat, respectively.

Assuming stationarity, homogeneity, and isotropy, the vertical diffusivity of mass, κ_ρ may

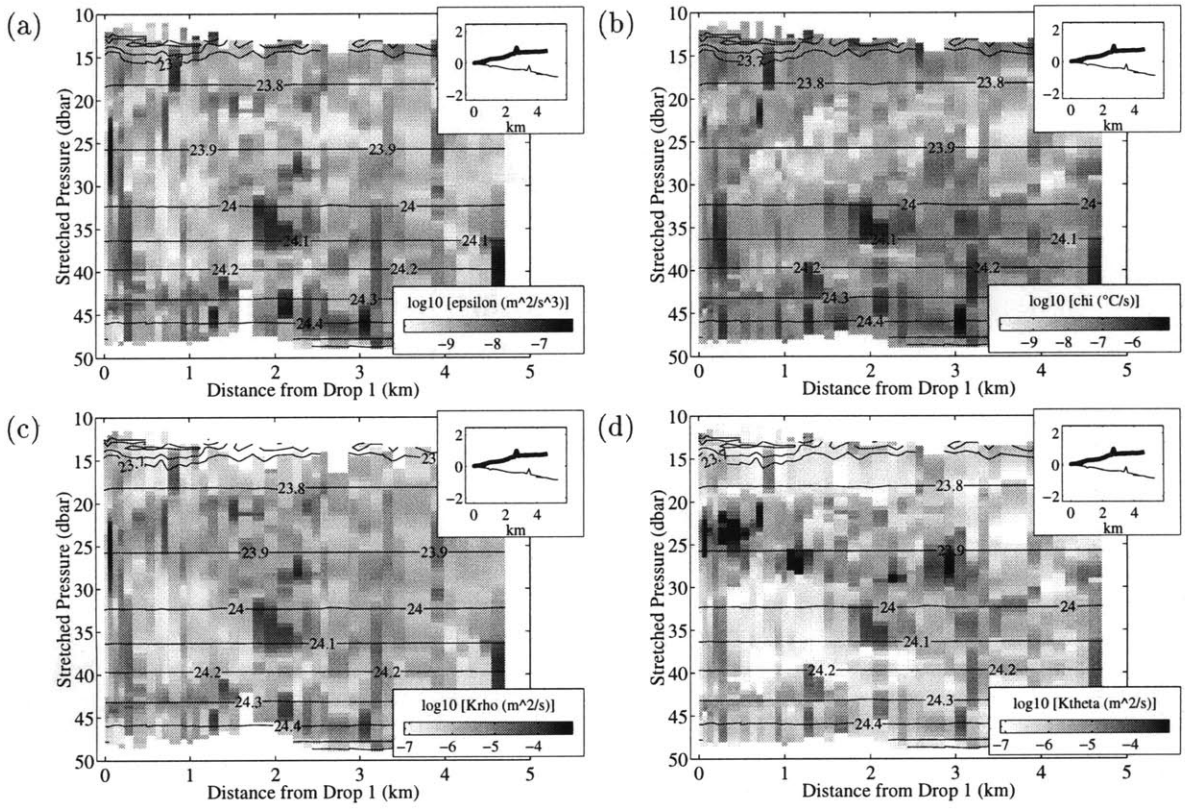

Figure 7.6: (a) Mixing efficiency, ϵ, (b) temperature variance, χ, (c) vertical diffusivity of mass, κ_ρ, and (d) vertical diffusivity of heat, κ_θ, for EPSONDE station number 24 of the 1996 fluorescein dye experiment (Oakey and Greenan, 1998). Here localized regions of high velocity and temperature variance and high vertical diffusivity can be seen superimposed on a relatively quiescent background.

be obtained from the turbulent kinetic energy equation,

$$\kappa_\rho = \Gamma \frac{\epsilon}{N^2} \qquad (\mathrm{m^2\ s^{-1}}), \tag{7.3}$$

where Γ is related to the flux Richardson number, R_f, by

$$\Gamma = \frac{R_f}{(1 - R_f)}, \tag{7.4}$$

(e.g., Osborne, 1980). Critical flux Richardson number arguments suggest that $\Gamma \approx 0.20 - 0.25$ (e.g., Osborne, 1980). Under the same assumptions, the vertical diffusivity of heat, κ_θ, may be obtained from the turbulent heat equation,

$$\kappa_\theta = \frac{\chi}{2\left(\frac{\partial \overline{T}}{\partial z}\right)^2} \qquad (\mathrm{m^2\ s^{-1}}). \tag{7.5}$$

Estimates of κ_ρ and κ_θ made by Oakey and Greenan (1998) are shown in Figure 7.6c and d. As expected, regions of high κ_ρ and κ_θ correspond to regions of enhanced N^2 finestructure shown in Figure 7.5. Assuming that mixing events occurred where κ_ρ and κ_θ were more than an order of magnitude greater than the mean, these data show that episodic mixing events had typical vertical scales of 2–10 m and horizontal scales of a few hundred meters to a few kilometers. Such patches of high diffusivity are a ubiquitous feature of the microstructure data for all the CMO dye experiments. (Microstructure data were not available during the 1995 pilot cruise.) Additional examples of patchy mixing events are shown in Figures 7.7 and 7.8. These further indicate that mixing occurred on a variety of vertical and horizontal scales. In Figure 7.8, the layer centered at approximately 35 m which was oblique to potential density surfaces is similar in both scale and angle of inclination to the layers seen in Figure 7.2.

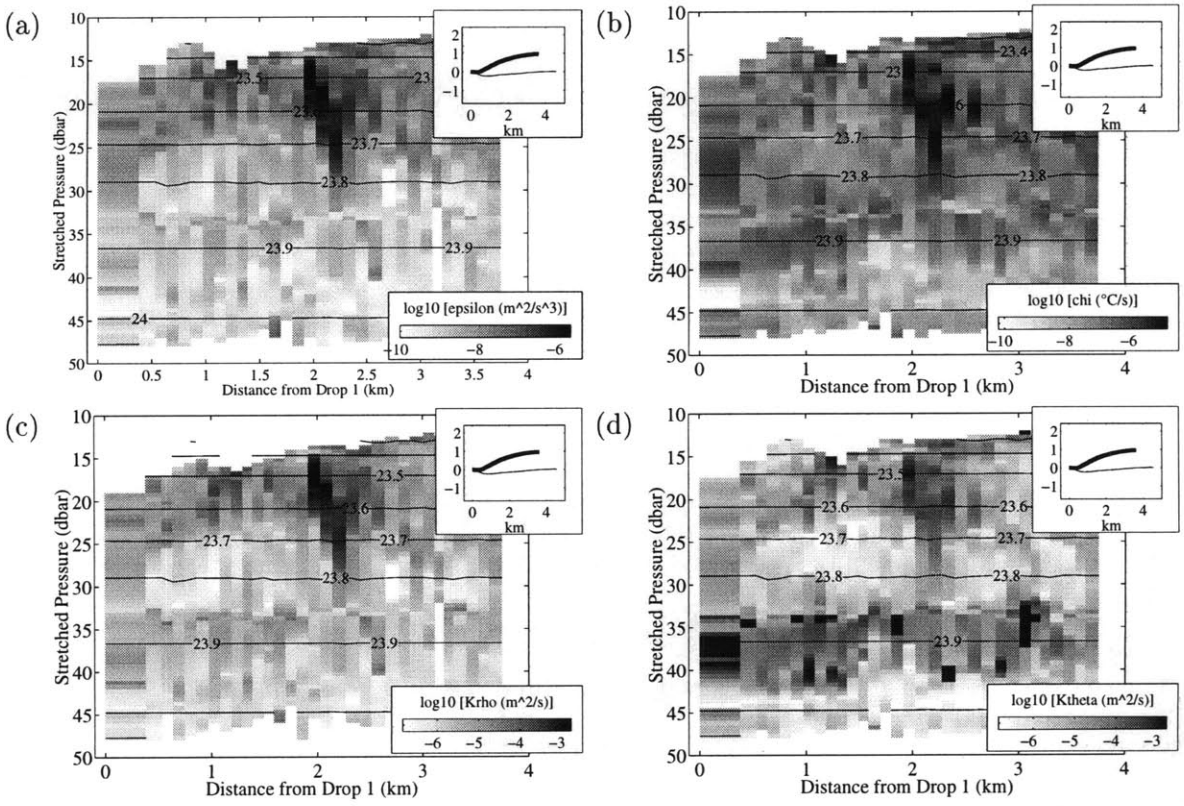

Figure 7.7: (a) Mixing efficiency, ϵ, (b) temperature variance, χ, (c) vertical diffusivity of mass, κ_ρ, and (d) vertical diffusivity of heat, κ_θ, for EPSONDE station number 28 of the 1996 fluorescein dye experiment (Oakey and Greenan, 1998).

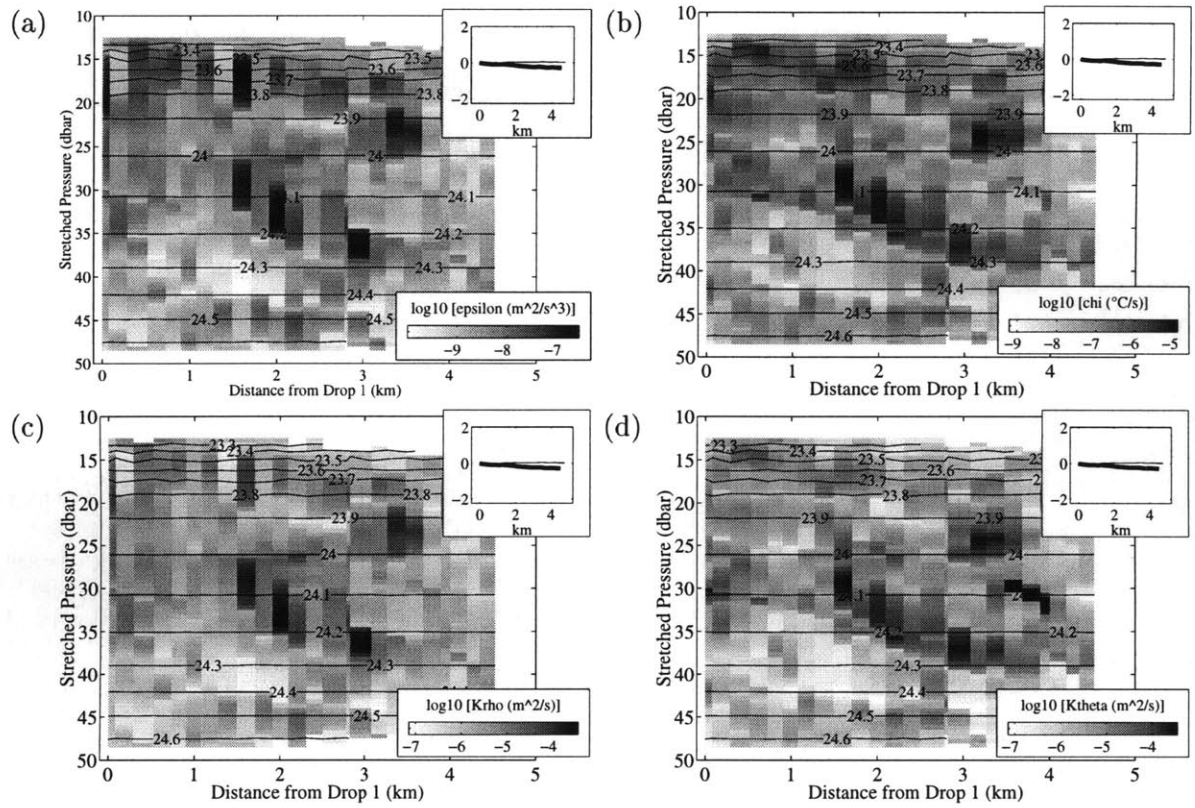

Figure 7.8: (a) Mixing efficiency, ϵ, (b) temperature variance, χ, (c) vertical diffusivity of mass, κ_ρ, and (d) vertical diffusivity of heat, κ_θ, for EPSONDE station number 40 of the 1996 fluorescein dye experiment (Oakey and Greenan, 1998). In this section the large region of high mixing centered at about 30 m depth is oblique to surfaces of constant potential density.

7.1.4 Summary of Observed Scales of Mixing

Patchy mixing was observed in all of the CMO dye experiments. Tow-yo transects from the dye surveys showed regions of low stratification with vertical scales of 2–10 m and horizontal scales ranging from a few hundred meters to a few kilometers. These data along with the dye data suggest that mixing during the CMO dye studies was not uniform or continuous, but rather episodic. This conclusion is supported by estimates of the dissipation of turbulent kinetic energy, ϵ, and temperature variance, χ, inferred from microstructure observations of Oakey and Greenan (1998). Estimates of the vertical diffusivities of mass, κ_ρ, and of heat, κ_θ, also showed event-like mixing at vertical scales of 2–10 m and horizontal scales of a few hundred meters to a few kilometers.

7.2 Relaxation of Diapycnal Mixing Events

Section 7.1 showed that vertical mixing during the CMO dye studies was episodic rather than continuous. This section will show that the adjustment or relaxation of episodic mixing events can lead to an effective horizontal diffusivity which is of the same order as that observed during at least two of the CMO dye studies. In Section 7.2.1, the basic mechanism of lateral dispersion due to episodic mixing and vortical motions will be described. In Section 7.2.2, the net vertical diffusivity caused by mixing events will be parameterized using potential energy arguments. The relative importance of rotation and friction will also be considered based on the observed scales of mixing. In Section 7.2.3, scaling arguments applied to the horizontal momentum equations will be used to estimate the effective horizontal diffusivity for events that adjust geostrophically. In Section 7.2.4, additional scaling regimes for ageostrophic and frictional adjustment will be considered. It will be shown that for events of a given vertical scale, there exists an optimal horizontal scale for which the effective horizontal diffusivity is largest. This scale corresponds to the Rossby radius of deformation. If the mixing event scales are much larger or much smaller than this optimal scale, the effective horizontal diffusivity will

be less than if the events had this preferred scale. Finally, a summary of these scale analyses will be given in Section 7.2.5 along with a discussion of their limitations.

7.2.1 Overview of Basic Mechanism

Consider a single isolated mixing event of scale $2h = 5$ m (i.e., h is the half-height of the region where κ_ρ is more than an order of magnitude greater than the mean), and a horizontal scale of $2L = 1.0$ km (where L is half the diameter of the region of high diffusivity), consistent with the typically observed scales of Section 7.1. The fate of such an event can be understood as follows. If the timescale of the turbulent mixing events is short compared to the relaxation time of the resulting mixed layers, an individual event may be thought of as having two distinct phases, a turbulent mixing phase, and a relaxation or adjustment phase. Associated with the mixing phase, a buoyancy anomaly, ΔN^2, can be defined as the change in the local buoyancy frequency between the onset and cessation of mixing. For perfect mixing, the final stratification within the mixed region would be zero so that $\Delta N^2 = N^2$, where N^2 is the original or mean buoyancy frequency. However, if localized mixing events cause an order 1 change in the local buoyancy frequency, but they do not lead to perfect mixing, a typical value of ΔN^2 would be of order $\frac{1}{2}N^2$. For a given vertical event scale, h, a corresponding event deformation radius associated with the adjustment phase can then be defined as $R = \frac{\Delta N\, h}{f}$ (e.g., Gill, 1981). Taking a typical buoyancy frequency, $N = 10$ cph, as observed during the CMO experiments, and a vertical event scale of $2h = 5$ m, one obtains $R \approx 325$ m. If we assume for the moment that friction is not important during the relaxation of an event (the effects of friction will be considered in Section 7.2.4), this suggests that a typical event of horizontal scale, $2L = 1.0$ km would have adjusted geostrophically, since in that case the horizontal scale is comparable to the deformation scale.

Using the above assumptions, simple scaling arguments can be employed to understand how the relaxation of diapycnal events can lead to horizontal dispersion. Consider the horizontal

momentum equation,

$$\frac{\partial u}{\partial t} + u \cdot \nabla u - fv = -\frac{1}{\rho}\frac{\partial P}{\partial x} + \kappa_B \frac{\partial^2 u}{\partial z^2}, \tag{7.6}$$

Where κ_B represents some ambient background viscosity which may or may not be directly related to the mixing events. Respective terms in this equation can be scaled as follows:

$$\left(\frac{\mathrm{U}}{\mathrm{T}}\right)\left(\frac{\mathrm{U}^2}{\mathrm{L}}\right)(f\mathrm{U})\left(\frac{h^2}{\mathrm{L}}\Delta N^2\right)\left(\kappa_B \frac{\mathrm{U}}{h^2}\right), \tag{7.7}$$

where U, L, and T represent velocity, length, and time scales, respectively, and the scaling for the pressure gradient term has been obtained through use of the hydrostatic equation,

$$\frac{\partial P}{\partial z} = -\rho g. \tag{7.8}$$

Equation (7.6) represents the basic momentum balance associated with the relaxation phase of episodic mixing events. For a single event, we can envision a classic Rossby adjustment problem. The buoyancy anomaly associated with an event will result in a horizontal pressure gradient as represented by the first term on the rhs of (7.7). If the anomaly is rotationally symmetric in the horizontal, and if the influence of friction is small, this pressure gradient will lead to an initial radial spreading of the well-mixed fluid of order the deformation radius (Figure 7.1b). As this initial adjustment occurs, a geostrophic flow will be established in the azimuthal direction such that the mixed region rotates cyclonically. (The spreading and thus a decrease in the potential energy of the well-mixed fluid is required by energy conservation if the fluid is to spin up geostrophically.)

Of relevance in the present context, is that the relaxation of mixing events will lead to lateral displacements of fluid in two directions. First there will be a radial displacement which is directed down pressure gradient and is associated with the slumping of the well-mixed fluid. Second, in the case of geostrophic adjustment, there will be azimuthal displacements associated with the geostrophic flow. Whether the effective dispersion by the adjustment process

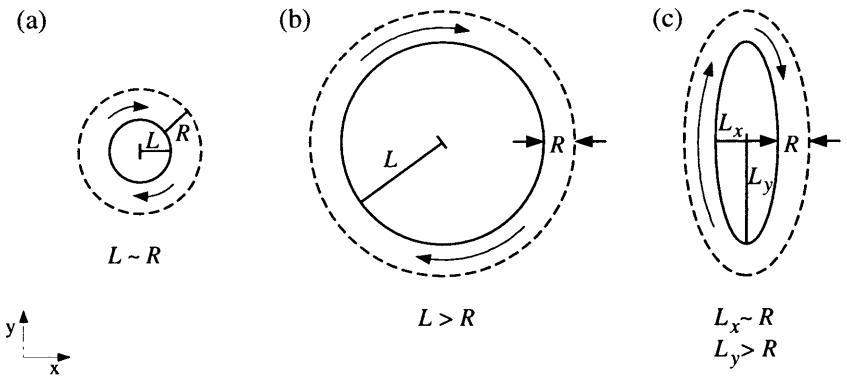

Figure 7.9: Schematic of (a) radially symmetric mixing event of horizontal scale $L \approx R$, (b) radially symmetric mixing event of scale $L > R$, and (c) an elongated mixing event of mixed scales.

is dominated by the slumping displacements or the geostrophic flows will depend on the relative strength and duration of these flows. For example, in the case of inviscid geostrophic adjustment ($L \geq R$), the geostrophic displacements will be greater than the slumping displacements since the vortical motions associated with the geostrophic flow will be greater and persist for much longer than the initial slumping period. Alternatively, in cases where the effects of rotation are small ($L \ll R$), azimuthal displacements will be negligible compared to radial displacements, and thus the horizontal dispersion will be primarily due to the slumping motions. As discussed in Sections 7.2.3 and 7.2.4, the largest lateral dispersion is expected to occur for the case of geostrophic adjustment ($L \approx R$) where vortical motions are important.

In the more general case when mixing events adjust geostrophically but are not horizontally symmetric, the above picture may be additionally modified. Consider an event which is of order the deformation scale in one horizontal dimension, but much larger in the other. In this case, the mixed region will again adjust geostrophically, spreading laterally while setting up a geostrophic flow. However, instead of a symmetric vortex, the adjusted state will be a long band with geostrophic flow in the direction of the longitudinal axis of the mixed region (Figure 7.9c). In this case, the displacements associated with the geostrophic flows are again expected to be larger than the slumping displacements. In addition, they will also be larger

than the displacements associated with a symmetric patch which is of deformation scale. This is because in the case of an elongated patch of mixed fluid, the geostrophic flows can transport fluid much further that a deformation radius in the direction of the major axis of the mixed region (this assumes again that the geostrophic flows persist longer than the initial adjustment). Similar is the case of large symmetric mixed regions.

In summary, depending on the relative sizes of the mixing events and the deformation scale, three regimes for the adjustment of mixing events may occur. First, in the case of a radially symmetric patch of scale $L \approx R$, the slumping displacements will be of the same order as geostrophic displacements (Figure 7.9a). Second, for a patch of scale $L > R$, the displacements caused by the geostrophic flow may be much larger than the initial down-gradient displacements, particularly if the geostrophic flow persists for much longer than the initial adjustment period (Figure 7.9b). Finally, the case for the longitudinal displacements of an elongated patch the displacements by the geostrophic flow may again be much larger than the initial displacements, as discussed in the previous paragraph (Figure 7.9c).

The above considerations can be used to formulate a simple parameterization of the effective horizontal dispersion caused by a collection of random mixing events. However, before embarking on a more extensive analysis of horizontal dispersion it is useful to consider how the vertical scales of episodic mixing events are related to the mean vertical diffusion. We return to the effective lateral dispersion due to episodic mixing events in Section 7.2.3.

7.2.2 Vertical Diffusion and Event Timescales

As suggested by Garrett and Munk (1972), the mean vertical diffusivity, κ_z, in a stratified fluid can be related to the scales of episodic mixing events using potential energy arguments. Consider in one dimension a single isolated mixing event of half-thickness, h (Figure 7.10). For an initial stratification, $\frac{\partial \rho_i}{\partial z}$, and a final stratification, $\frac{\partial \rho_f}{\partial z}$, caused by mixing, the change

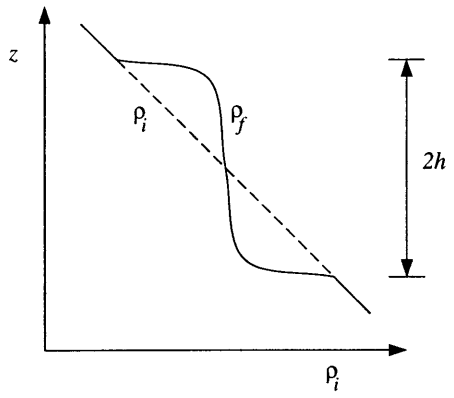

Figure 7.10: Schematic of change in stratification and thus potential energy associated with a single mixing event. The initial stratification, $\frac{\partial \rho_i}{\partial z}$, is indicated by a dashed line, while the final stratification, $\frac{\partial \rho_f}{\partial z}$, is indicated by a solid line.

in potential energy, ΔPE, per unit area associated with this event can be expressed as,

$$\frac{1}{\text{unit area}}\Delta\text{PE} = \frac{g}{3}\left(\frac{\partial \rho_f}{\partial z} - \frac{\partial \rho_i}{\partial z}\right) h^3 = \frac{\rho_o}{3}(N_i^2 - N_f^2)h^3 = \frac{\rho_o}{3}(\Delta N^2)h^3, \tag{7.9}$$

where $N_i^2 = -\frac{g}{\rho_o}\frac{\partial \rho_i}{\partial z}$ and $N_f^2 = -\frac{g}{\rho_o}\frac{\partial \rho_f}{\partial z}$ are the initial and final buoyancy frequencies, respectively, such that $\Delta N^2 = N_i^2 - N_f^2$. If $Q(h)dh$ represents the expected number of events between $h \pm \frac{1}{2}dh$ per unit time per unit depth, then the average change in potential energy per unit volume per unit time, i.e., the buoyancy flux, can be written as

$$\frac{1}{\text{unit area}} \int \Delta\text{PE}\ Q(h)dh = \frac{1}{3}\int \rho_o\ \Delta N^2\ h^3\ Q(h)dh. \tag{7.10}$$

Assuming that this buoyancy flux can equivalently be expressed as a diffusivity, κ_z, times a buoyancy gradient, it follows that

$$\frac{1}{\text{unit area}} \int \Delta\text{PE}\ Q(h)dh = -\kappa_z \frac{\partial(\rho g)}{\partial z} = \kappa_z N^2 \rho_o, \tag{7.11}$$

where $N^2 = N_i^2$ represents the steady background stratification. Substituting (7.10) into (7.11), shows that the vertical diffusivity can be expressed as the sum of isolated mixing

events,

$$\kappa_z = \frac{1}{3}\int \frac{\Delta N^2}{N^2} h^3 Q(h) dh. \tag{7.12}$$

Equation 7.12 provides a simple relation between the effective vertical diffusivity, κ_z, the probability of mixing events of a given scale, $Q(h)dh$, and the buoyancy anomaly associated with these events, ΔN^2. More simply, if events are always of a given thickness, h, and buoyancy anomaly, ΔN^2, (7.12) reduces to

$$\kappa_z = \frac{1}{3}\frac{\Delta N^2}{N^2} h^2 \nu, \tag{7.13}$$

where ν represents the average frequency of events. Equation (7.13) is most useful if the vertical diffusivity is known, as from the dye experiments or microstructure. In this case the frequency of events, ν, can be inferred based on the observed vertical scale, h, and the buoyancy anomaly, ΔN^2, i.e.,

$$\nu = 3\frac{N^2}{\Delta N^2}\frac{1}{h^2}\kappa_z. \tag{7.14}$$

In the CMO dye studies, all variables on the rhs of (7.14) were measurable or calculable, so that ν could be determined.

Equations (7.13) and (7.14) show that for a given vertical diffusivity, κ_z, the larger the thickness of the mixing events, the less frequently they must occur. For example, for the 1996 fluorescein dye experiment, the upper-bound estimate of vertical diffusivity was $\kappa_z = 0.9 \times 10^{-5}$ m^2 s^{-1}. Assuming a typical buoyancy anomaly, $\Delta N^2 = \frac{1}{2}N^2$, and a typical vertical scale, $2h = 2$ m, (7.14) implies an average event recurrence time of $\frac{1}{\nu} = 0.2$ days. However, mixing events of vertical scale $2h = 5$ m would result in a larger event recurrence time, $\frac{1}{\nu} = 1.3$ days. Similar calculations for a variety of combinations of patch thicknesses and vertical diffusivities are listed in Table 7.1. For a reasonable range of vertical scales, h, and vertical diffusivities, κ_z, the inferred event recurrence times range from $\frac{1}{\nu} = 0.2$ days to $\frac{1}{\nu} = 48$ days.

Another time scale which is important to the adjustment of diapycnal mixing events is the frictional time scale, $\frac{h^2}{\kappa_B}$, associated with vertical viscosity. Here we imagine that diapycnal

	$2h = 2$ m	$2h = 5$ m	$2h = 10$ m
$\kappa_z = 0.1 \times 10^{-5}$ m^{2}s^{-1}	$\frac{1}{\nu} = 2$ days	$\frac{1}{\nu} = 12$ days	$\frac{1}{\nu} = 48$ days
$\kappa_z = 1.0 \times 10^{-5}$ m^{2}s^{-1}	$\frac{1}{\nu} = 0.2$ days	$\frac{1}{\nu} = 1.2$ days	$\frac{1}{\nu} = 4.8$ days

Table 7.1: Event recurrence time scales, $\frac{1}{\nu}$, inferred from (7.14) for a range of vertical diffusivities, κ_z, and vertical scales, h.

mixing events occur and relax amidst some background vertical viscosity, κ_B, which may represent either purely molecular processes or small-scale eddy viscosity. (For event-like mixing, we expect $\kappa_B < \kappa_z$, while for mixing which is uniform in space and time, $\kappa_B = \kappa_z$.) For purely molecular viscosity acting on a very thin layer, the horizontal pressure gradients associated with a density anomaly may be balanced by friction and a frictional adjustment may occur. In the case of an eddy viscosity, we might imagine that as small-scale eddies redistribute momentum, so too would they mix away the density anomaly associated with the mixing event. Hence, they would halt the adjustment. In other words, the frictional time scale would limit the amount of time that advection would have to spread the mixed fluid laterally.

Whether friction is likely to affect the adjustment of mixed layers can be readily determined. Table 7.2 lists the diffusion time scales, $\frac{h^2}{\kappa_B}$, for molecular and eddy viscosities through a reasonable range of vertical scales. For the scales of mixing events which occurred during the CMO dye studies, the diffusion times were typically of order a day or more. Thus, for these events friction is not likely to have been important compared to the Earth's rotation. Furthermore, for similar diffusivities, $\kappa_B = \kappa_z$, and vertical scales, h, the frictional time scales, h^2/κ_B, are always larger than the recurrence time scales, $1/\nu$. This means that the relaxation of an event will likely be interrupted by the next event. In an extreme case, if the density anomaly is completely mixed away by a new event, the recurrence of events will thus halt the relaxation long before friction can become a significant factor.

	$2h = 2$ m	$2h = 5$ m	$2h = 10$ m
$\kappa_B = 0.1 \times 10^{-5}$ m^{2}s^{-1} (molecular viscosity)	12 days	72 days	289 days
$\kappa_B = 1.0 \times 10^{-5}$ m^{2}s^{-1} (eddy viscosity)	1.2 days	7.2 days	29 days

Table 7.2: Diffusion time scales, $\frac{h^2}{\kappa_B}$, showing the time it would take for an anomaly of a given vertical scale, h, to diffuse away due to vertical diffusion.

7.2.3 Effective Lateral Dispersion

The size of the deformation radius estimated in Section 7.2.1, implies that the scales of episodic mixing events during the CMO experiments could lead to the geostrophic adjustment of mixed regions. The effective lateral diffusivity associated with a collection of such events is now considered. Additional cases which consider ageostrophic and frictional adjustment will be discussed in Section 7.2.4.

CASE 1: Geostrophic Adjustment

Suppose that patches of mixing occur on horizontal scales comparable to or greater than the deformation radius, and that the recurrence time scale of events, $\frac{1}{\nu}$, is greater than or equal to the rotation time scale, $\frac{1}{f}$, so that events adjust geostrophically without being disturbed by subsequent events. In this case, the dominant balance in the horizontal momentum equations (7.6) and (7.7) will be between the pressure gradient term and the rotation term. The horizontal velocity associated with the adjustment of a mixed layer will thus scale as

$$U \approx \frac{h^2 \Delta N^2}{Lf}. \tag{7.15}$$

Meanwhile, the horizontal displacement of fluid within the adjustment region will be at least of order the deformation radius, $R \approx \frac{h\Delta N}{f}$. (Note, the deformation radius, R, may represent a lower bound on the displacements for reasons discussed in Section 7.2.1.)

For a collection of relaxation events, the effective horizontal diffusivity can be thought of as a random walk of fluid parcels with step size, S, and frequency ν. The diffusivity can thus be expressed as the square of the horizontal displacement times the frequency of events, i.e., $\kappa_H \approx \frac{1}{2}\, S^2\nu$. In the case of geostrophic adjustment, the step size is given by the geostrophic velocity (7.15) times the adjustment time scale, $T = \frac{1}{f}$, i.e.,

$$S = UT \approx \frac{h^2\Delta N^2}{Lf^2} = \frac{R^2}{L}. \tag{7.16}$$

Hence, the horizontal diffusivity thus becomes

$$\kappa_H \approx \left(\frac{1}{2}\right) S^2\nu \approx \left(\frac{1}{2}\right) \frac{h^4\Delta N^4}{L^2 f^4}\nu. \tag{7.17}$$

Substituting for $\Delta N^2 h^2$ in terms of κ_z from (7.14), and for the deformation radius, $R = \Delta N h/f$, (7.17) can equivalently be expressed as

$$\kappa_H \approx \left(\frac{3}{2}\right)\left(\frac{N^2}{f^2}\right)\left(\frac{R^2}{L^2}\right)\kappa_z. \tag{7.18}$$

This shows that the effective horizontal diffusivity can be written in terms of the vertical diffusivity times a scaling factor.

Equation (7.18) can be used to estimate the effective horizontal diffusivity due to the relaxation of episodic mixing events when events are of large enough horizontal scale that they adjust geostrophically. For the CMO experiments, $\left(\frac{N^2}{f^2}\right) \approx (0.1 \text{ to } 1.1) \times 10^5$. For mixing events of horizontal scale of order the deformation radius, $\left(\frac{R^2}{L^2}\right) \approx 1$, (7.18) thus becomes

$$\kappa_H \geq (0.1 \text{ to } 1.1) \times 10^5 \kappa_z. \tag{7.19}$$

Equations (7.18) and (7.19) are perhaps the most important result of this chapter. For the vertical diffusivities estimated in the CMO dye studies, $\kappa_z \approx (0.1 \text{ to } 1.0) \times 10^{-5}$ m^2 s^{-1}, they predict that horizontal diffusivities will be between $\kappa_H \geq (0.01 \text{ to } 1.1)$ m^2 s^{-1}. The lower range of this predicted κ_H would be too small to explain the observed horizontal diffusivities discussed in Chapter 5. However, at least for the 1996 fluorescein and 1997 rhodamine experiments, the upper range is of the right order of magnitude to explain the observed values, $\kappa_{\text{irrev}} = 0.5$ m^2 s^{-1} and 0.3 m^2 s^{-1}, respectively.

Noteworthy is that the above estimates for dispersion by the relaxation of diapycnal mixing events still do not appear to account for the observed dispersion in the 1995 and 1996 rhodamine experiments, $\kappa_{\text{irrev}} = 4.9$ m^2 s^{-1} and 4.6 m^2 s^{-1}, respectively. However, the above results obtain further significance when we consider that these predictions may represent a lower-bound on the effective diffusivity due to vortical motions for the following reasons. First, as discussed in Section 7.2.1, if the mixing events were larger than the deformation scale or were not horizontally symmetric, the geostrophic flows associated with their adjustment could lead to larger horizontal displacements than suggested by the above result. This is because the persistence of these flows may imply a larger time scale than was assumed in the above scaling. Second, if layers adjusted geostrophically, and then slowly decayed due to viscosity, an additional spreading of the mixed fluid would occur during the spin-down of the geostrophic flow (e.g., Gill, 1981). These considerations suggest that dispersion by the relaxation of mixing events may be larger than that suggested by the above scaling, and thus that this mechanism may still be a viable candidate to explain the lateral dispersion observed during the 1995 and 1996 rhodamine dye experiments.

7.2.4 Additional Scaling Regimes

Given that the mixed layers observed during the CMO dye studies occurred on a variety of scales, the effective horizontal diffusivities for the cases of ageostrophic and frictional adjustment will now be examined. In contrast to the above geostrophic scaling, it is presumed in

these cases that geostrophic flows and thus azimuthal displacements are small, and that instead the largest displacements are due to the slumping of the well-mixed fluid. This analysis will show that if mixed layers occur on scales which are much smaller than the deformation radius or are thin enough so that they adjust frictionally, then the effective lateral dispersion due to the relaxation of mixing events will be reduced compared to the case of geostrophic adjustment.

CASE 2: Ageostrophic Adjustment (narrow mixing events)

In the case of mixing events which are narrow in the sense that $L \ll R$, (7.7) shows that the advection time scale, $\frac{L}{U}$, may be small compared to either the recurrence time scale, $\frac{1}{\nu}$ or the rotation time scale, $\frac{1}{f}$. Thus, initially events will spread laterally, unaffected by rotation and the recurrence of events. (Ultimately, however, the adjusting layers become thin enough that friction becomes important.) In this case, the initial adjustment velocity is given by a balance between the advective term and the pressure gradient term,

$$U^2 \approx h^2 \Delta N^2. \tag{7.20}$$

Again using a random walk formulation for the effective horizontal diffusivity, the step size in this case is given by the velocity (7.20) times the adjustment time scale, which now is equal to the advective time scale, $T = \frac{L}{U}$, i.e.,

$$S \approx UT = L. \tag{7.21}$$

Here the effective horizontal diffusivity due to ageostrophic advection becomes

$$\kappa_H \approx \left(\frac{1}{2}\right) S^2 \nu \approx \left(\frac{1}{2}\right) L^2 \nu \approx \left(\frac{1}{2}\right) L^2 \left(\frac{h^2 \Delta N^2}{h^2 \Delta N^2} \frac{f^2}{f^2}\right) \nu \approx \left(\frac{3}{2}\right) \left(\frac{N^2}{f^2}\right) \left(\frac{L^2}{R^2}\right) \kappa_z, \tag{7.22}$$

where again (7.14) and the definition of the deformation radius have been used in the final substitution. Equation (7.22) is similar to the result for geostrophic adjustment, (7.18), except that the scale factor $\left(\frac{L^2}{R^2}\right)$ here replaces $\left(\frac{R^2}{L^2}\right)$ in the previous case. This shows that if mixing events are narrow compared to the deformation scale, $\frac{L^2}{R^2} \ll 1$, then the effective lateral dispersion given by (7.22) is less than that predicted for mixing events of scale $\frac{L^2}{R^2} \approx 1$.

CASE 3: Ageostrophic Adjustment (thin mixing events)

In this case, it is assumed that mixing events are thin enough that their recurrence time scale is small compared to the rotation time scale, but not so thin that friction dominates their initial adjustment. Here the adjustment of events is halted by the recurrence of events. The velocity scale is thus obtained from the acceleration produced by the pressure gradient over a time, $T \approx \frac{1}{\nu}$,

$$U \approx \frac{h^2 \Delta N^2}{L\nu}. \tag{7.23}$$

The step size associated with the adjustment of events then becomes

$$S \approx UT = \frac{h^2 \Delta N^2}{L\nu^2} = \frac{R^2}{L}\frac{f^2}{\nu^2}, \tag{7.24}$$

so that the effective horizontal diffusivity is

$$\kappa_H \approx \left(\frac{1}{2}\right) S^2 \nu \approx \left(\frac{1}{2}\right) \frac{h^4 \Delta N^4}{L^2 \nu^4} \nu \approx \left(\frac{3}{2}\right) \left(\frac{N^2}{\nu^2}\right) \left(\frac{f^2}{\nu^2}\right) \left(\frac{R^2}{L^2}\right) \kappa_z. \tag{7.25}$$

This case is similar to the geostrophic adjustment case except that the rotational time scale, $\frac{1}{f}$, has been replaced by the recurrence time scale, $\frac{1}{\nu}$. By assumption, $\frac{f^2}{\nu^2} \ll 1$, in this case so that the effective diffusion by ageostrophic adjustment of thin patches is less than that predicted in the geostrophic adjustment case.[3]

[3]In this case, it has been assumed that a new mixing event will destroy a previous event, so that the recurrence time scale sets the time scale of adjustment. This leads to a conservative estimate of the horizontal diffusivity in the sense that if a new event does not completely destroy and halt the horizontal adjustment of a previous

CASE 4: Frictional Adjustment

In this final case layers are assumed to be thin in the sense that the frictional time scale, $\frac{h^2}{\kappa_B}$, is small compared to the rotational time scale, $\frac{1}{f}$, the recurrence time scale, $\frac{1}{\nu}$, and the advective time scale, $\frac{L}{U}$. (That the frictional time scale is less than the advective time scale can also be couched in terms of the horizontal scale L, i.e., L must not be so small that the advection term is larger than the friction term.) Thus, the momentum balance is between the horizontal pressure gradient term and the frictional term. Consequently, the horizontal velocity scales as,

$$U \approx \frac{h^4 \Delta N^2}{L \kappa_B}. \tag{7.26}$$

Assuming that the step size associated with the relaxation is given by this velocity times a diffusive time scale,

$$S = UT = \frac{h^4 \Delta N^2}{L \kappa_B} \frac{h^2}{\kappa_B} \approx \frac{R^2}{L} \frac{f^2}{(\kappa_B / h^2)^2}. \tag{7.27}$$

Thus the effective horizontal diffusivity in the case of frictional adjustment becomes

$$\kappa_H \approx \left(\frac{1}{2}\right) S^2 \nu \approx \left(\frac{1}{2}\right) \frac{h^4 \Delta N^4}{L^2 f^2} \frac{f^2}{(\kappa_B / h^2)^4} \nu \approx \left(\frac{3}{2}\right) \left(\frac{N^2}{(\kappa_B / h^2)^2}\right) \left(\frac{f^2}{(\kappa_B / h^2)^2}\right) \left(\frac{R^2}{L^2}\right) \kappa_z. \tag{7.28}$$

This case is again similar to the geostrophic adjustment case except that the rotational time scale, $\frac{1}{f}$, has now been replaced by the diffusive time scale, $\frac{h^2}{\kappa_B}$. In this case, the frictional time scale is much less than the rotational time scale, $\frac{f^2}{(\kappa_B / h^2)^2} \ll 1$, by assumption, so that once again the horizontal diffusivity is less than that obtained for geostrophic adjustment of events.

event, the effective diffusivity, κ_H, will be larger. However, regardless of this, the estimated diffusivity for this case is still smaller than the effective diffusivity in the case of geostrophic adjustment, since $\frac{1}{\nu} \ll \frac{1}{f}$ and $\frac{R^2}{L^2} \leq 1$ by assumption.

7.2.5 Summary of Relaxation of Diapycnal Mixing Events

In this section, the effective horizontal diffusivity due to the relaxation of diapycnal mixing events was estimated using scaling results for a variety of horizontal and vertical scales. Four principal scaling regimes were discussed. In the first case it was assumed that rotation was important so that mixed layers adjusted geostrophically. In Cases 2 and 3, rotation was not important so that mixing events adjusted ageostrophically. In these three cases friction was assumed unimportant. In the final case, mixed layers were assumed to adjust frictionally.

The above scaling results may be summarized as follows. Mixed layers that are the most effective at horizontal mixing are those that adjust geostrophically. Layers which adjust ageostrophically will be inhibited by the recurrence of events, or eventually by friction. The resulting advective scales will thus be smaller than the deformation radius, and the effective horizontal diffusivity will be smaller than in the geostrophic adjustment case. Finally, layers which adjust frictionally will also lead to smaller diffusivities than the geostrophic adjustment cases.

Thus the conclusion of this analysis is that an upper bound on the effective horizontal diffusivity by the relaxation of diapycnal mixing events is given by the geostrophic scaling of (7.18). The optimal horizontal scale of events is the internal deformation radius, $L \approx R$, and the optimal vertical scale is thick enough that events are infrequent in the sense that $\frac{1}{\nu} \geq \frac{1}{f}$. Most importantly, in the case of geostrophic adjustment of mixing events, the above scale analysis suggests that the effective horizontal diffusivities caused by the relaxation of diapycnal mixing events may be large enough to explain the irreversible diffusivities observed during CMO, at least for the 1996 fluorescein and 1997 rhodamine dye experiments. This is true if the typical scale of mixed layers, L, was of the same order as the deformation radius, R, which it was.

The above predictions for lateral dispersion by the relaxation of diapycnal mixing events apparently still do not account for the observed dispersion in the 1995 and 1996 rhodamine

dye experiments. However, two additional considerations must be mentioned with regard to the above scaling which indicate that these predictions may represent lower bounds. First as noted in Section 7.1.2, the density anomalies observed during the CMO dye studies were frequently oblique rather than parallel to potential density surfaces. The implication of this to the adjustment of localized mixed layers is that the effective horizontal scales of the layers, $L' \leq L$, will be reduced relative to the case where layers are not tilted. In the case of the geostrophic scaling, (7.18), the predicted horizontal diffusivity would thus be increased for large tilted layers, since the scale factor $\frac{R^2}{L'^2} \geq \frac{R^2}{L^2}$. Similar are the cases for the second ageostrophic scaling (CASE 3; equation 7.25) and the frictional adjustment (CASE 4; equation 7.28), where the horizontal diffusivities also were proportional to $\frac{R^2}{L^2}$. However, the opposite is true for the ageostrophic adjustment of narrow patches, (CASE 2; equation 7.22), since in that case the diffusivity is proportional to $\frac{L^2}{R^2}$.

The second consideration is that as discussed in Section 7.2.1, mixed layers may be considerably larger than the deformation scale, or elongated in one horizontal dimension. In this case, the geostrophic scaling given by (7.18) may underpredict the effective lateral spreading of tracer if the geostrophic flow persists for much longer than an inertial period, since in that case the lateral advection of the mixed fluid may be larger than the deformation scale. Hence, for both of these considerations, the effective lateral diffusivity associated with the relaxation of mixing events is expected to be increased compared to the basic geostrophic case.

7.3 Shear Dispersion and the Vortical Mode

The scaling arguments of Section 7.2 show that horizontal displacements associated with the relaxation of diapycnal mixing events can lead to significant lateral dispersion. A second mechanism of lateral dispersion which can be caused by these mixing events is vertical shear dispersion. Although vertical shear dispersion was discussed in detail in Chapter 6, the effective shear dispersion due to isolated mixing events was not well represented by those predictions.

The relatively low frequency shears associated with these events would have been aliased as high frequency shears due to the relatively small spatial scales of the events. This is discussed below.

In Section 7.2, it was assumed that associated with any single mixing event there is a corresponding flow, U, caused by the ensuing geostrophic or ageostrophic or frictional adjustment. To lowest order, this flow will occur on the same vertical scale, h, as the mixing event itself. Hence, associated with the adjustment of an event will be a vertical shear of order

$$\alpha \approx U/h. \tag{7.29}$$

This vertical shear combined with the vertical diffusivity make up the shear dispersion of interest. This section will show that the relaxation of diapycnal mixing events leads to shear dispersion which is less than or of the same order as the effective lateral dispersion due to the horizontal displacements associated with such events. To consider this effective shear dispersion, a scaling approach will be used which combines the results of the shear dispersion analysis of Chapter 6 with the scaling analysis of Section 7.2.

Assuming a linear shear dispersion model, (6.2) implies that the effective horizontal diffusivity for an oscillatory shear of amplitude, α, and frequency, ω, scales as

$$\kappa_H \approx \frac{\alpha^2}{\omega^2}\kappa_B. \tag{7.30}$$

Here the effective background vertical diffusivity, κ_B, has been used instead of the mean diffusivity, κ_z, because κ_B is expected to be the diffusivity present during the relaxation of the mixed layers. Alternatively, for a steady linear shear acting over a time, T, (6.10)–(6.12) imply that the rate of change of tracer variance, i.e., the effective horizontal diffusivity scales as

$$\kappa_H \approx \alpha^2 T^2 \kappa_B. \tag{7.31}$$

(In the latter case, the description of the variance in terms of a horizontal diffusivity is not strictly appropriate since the variance grows as the third power of time; however, the purpose of writing the horizontal variance in this way is so that (7.30) can be compared directly to (7.31)). Comparison of these two expressions shows that for a linear shear, the effective horizontal dispersion by vertical shear dispersion is given by the product of the shear squared, a time scale squared, and the vertical diffusivity. In the case of an oscillator shear, (7.30) shows that the appropriate time scale is given by the frequency of oscillation. In the case of a mean shear, (7.31) shows that the time scale is the duration for which the steady shear persists.

Equation (7.31) can be used to estimate the effective lateral dispersion by shear dispersion in the context of the relaxation of diapycnal mixing events. For these events, the shear associated with the adjustment (and the ensuing geostrophic flow) can be estimated from (7.29). Meanwhile, the duration of the shear can be approximated as the relevant adjustment time scale of events. The geostrophic and ageostrophic scaling regimes discussed in Sections 7.2.3 and 7.2.4 will now be addressed in turn.

CASE 1: Geostrophic Adjustment

The velocity scale for the case of geostrophically adjusting mixed layers was given by (7.15). Using this result, and Equations (7.29) and (7.31),

$$\kappa_H \approx \frac{h^2 \Delta N^4}{L^2 f^4} \kappa_B \leq \left(\frac{N^2}{f^2}\right)\left(\frac{R^2}{L^2}\right)\kappa_z, \tag{7.32}$$

where it has been assumed that the time scale $T \approx \frac{1}{f}$. This time scale is a lower bound on the duration of the shear associated with geostrophic adjustment in the sense that geostrophic flows may persist for considerably longer than an inertial period (see also Section s-basic-scaling). The last inequality in (7.32) obtains since $\kappa_B \leq \kappa_z$, and $\Delta N^2 \leq N^2$, by definition (Section 7.2.2). The effective shear dispersion due to the relaxation of diapycnal mixing events is thus of the same order as or less than the effective horizontal dispersion due to horizontal

displacements associated with these same events (see Equation 7.18).

CASE 2: Ageostrophic Adjustment (narrow mixing events)

Similar scaling can be applied to the ageostrophic adjustment cases. With the assumed time scale, $T \approx \frac{1}{\nu}$, representing the duration of the shear, the velocity scale given by (7.20) and the above scaling for shear dispersion yield

$$\kappa_H \approx \frac{\Delta N^2}{\nu^2}\kappa_B \leq \left(\frac{N^2}{\nu^2}\right)\kappa_z. \tag{7.33}$$

Again this represents an effective horizontal dispersion which is less than or of the same order as that obtained before (see Equation 7.22).

CASE 3: Ageostrophic Adjustment (thin mixing events)

Again assuming a time scale, $T \approx \frac{1}{\nu}$, the velocity scale given by (7.23) and the above shear dispersion scaling yield

$$\kappa_H \approx \frac{h^2\Delta N^4}{L^2\nu^4}\kappa_B \leq \left(\frac{N^2}{\nu^2}\right)\left(\frac{f^2}{\nu^2}\right)\left(\frac{R^2}{L^2}\right)\kappa_z. \tag{7.34}$$

Once again the effective horizontal dispersion is less than or of the same order than that obtained previously (see Equation 7.25).

In summary, the relaxation of diapycnal mixing events causes an effective lateral dispersion due to vertical shear dispersion as well as an effective dispersion due to the horizontal displacements associated with the relaxation of the mixing events. Given the relatively small horizontal scale of these mixing events compared to the larger-scale patch surveys, it is likely that the shipboard ADCP observations would alias the shears associated with these events as unsteady shears with time scales which are small compared to the time scale of the events. Thus, the shear dispersion estimates of Chapter 6 would have underestimated the shear dispersion associated with these events. In this section, it was shown that for the geostrophic and

ageostrophic scaling regimes examined in Sections 7.2.3 and 7.2.4, the shear dispersion associated with the relaxation of diapycnal mixing events is less than or of the same order as the effective lateral dispersion which results from horizontal advection during event relaxation.

7.4 Summary of Proposed Mechanism

In this chapter the effective horizontal dispersion due to the relaxation of diapycnal mixing events was examined. Observations of potential density from the CMO dye studies as well as microstructure data collected concurrently showed that mixing occurred episodically in space and time. Based on estimated dissipation rates of turbulent kinetic energy and temperature variance, the scales of energetic mixing events were estimated to be a few hundred meters to a few kilometers in the horizontal and 2–10 m in the vertical.

Scale analysis applied to the horizontal momentum balance suggests that for a given vertical diffusivity, there exists an optimal scale of mixing events for which a maximum effective horizontal diffusivity results. This maximum diffusivity is predicted to occur for events of horizontal scales comparable to the deformation radius and vertical scales large enough that events adjust geostrophically. For the CMO dye experiments, the predicted horizontal diffusivity due to the relaxation of mixing events ranged from $\kappa_H \approx (0.01 \text{ to } 1.1)$ m^2 s^{-1}. The upper range represented here is roughly consistent with the observed horizontal diffusivities for the 1996 fluorescein and 1997 rhodamine dye experiments, $\kappa_{\text{irrev}} = 0.5$ m^2 s^{-1} and 0.3 m^2 s^{-1}, respectively. However, it is still somewhat smaller than the observed dispersion during the 1995 and 1996 rhodamine dye experiments, $\kappa_{\text{irrev}} = 4.9$ m^2 s^{-1} and 4.6 m^2 s^{-1}, respectively. Some possible explanations for this were given in Section 7.2.3 and are discussed in the next chapter.

The relaxation of diapycnal mixing events also contributes to lateral dispersion by vertical shear dispersion. However, given the relatively small scale of these events compared to the scale of the dye surveys, it is likely that the relatively low frequency vertical shears associated

with these events would have been aliased as high frequency shears by shipboard ADCP observations. In the cases of geostrophic and ageostrophic adjustment, scaling arguments show that shear dispersion associated with the adjustment of diapycnal mixing events would be less than or of the same order as the effective dispersion due to advective effects.

Despite their large range in magnitude, the above predictions suggest that lateral dispersion by vortical motions may be important in the ocean. However, based on the CMO dye experiments alone, a definitive test of this mechanism is not possible since the temporal and spatial resolutions of the observations were often comparable to or greater than the scales of the mixing events. Nevertheless, it is interesting to speculate about what the observed tracer distributions may tell us about the mechanisms responsible for the dispersion. For example, as discussed in Chapter 4 and Section 7.1.1, evidence of mixing on scales of 0.5–10 m vertically and a few hundred meters to a few kilometers horizontally could be seen in the data from the dye surveys in the form of patchiness in the dye concentrations. Suppose, however, that the vertical mixing during a particular experiment was due primarily to one (or very few) large events. In this case the distribution of tracer may instead look quite homogeneous compared to the case of many smaller events. In the extreme case of a single large mixing event, the dye would mix rapidly in the vertical for a brief time and then not at all. Meanwhile, in the horizontal direction the dye would appear to spread continuously as the well-mixed fluid relaxed laterally. (Note that this is reminiscent of the 1995 rhodamine dye experiment described in Chapter 4.) In this case, the horizontal adjustment would more appropriately be described as an advective process. However in practical terms, without sufficient temporal information about the lateral spreading, this advection may be indistinguishable from a smaller-scale diffusive process.

Of additional interest is that the scaling results of Section 7.2.3 show a range of values for the scale factors, particularly the stratification, which span an order of magnitude. That the stratification can have such a large influence on the rate of lateral dispersion can be understood by noting that the aspect ratio associated with internal waves is order $\frac{N}{f}$. However, it is

not clear how changes in stratification might otherwise affect the generation or relaxation of diapycnal mixing events. This is the subject of further study.

In conclusion, the full range of temporal and spatial scales of the mixing events and the details of the adjustment are not well constrained by the observations. However, based on the best estimates of the relevant parameters, simple scaling arguments show that the relaxation of diapycnal mixing events is a viable candidate to explain the lateral dispersion observed during the CMO dye studies.

Chapter 8

Summary and Discussion of Part II

In Part II of this thesis, rates and mechanisms of lateral dispersion over the New England Continental shelf were investigated using data from the Coastal Mixing and Optics dye studies and theoretical models of lateral dispersion. In Chapter 4, an extensive description of the field data was given for four dye experiments conducted during the CMO dye cruises. Rates of lateral dispersion were determined in Chapter 5 for each of these dye studies using a simple model of vertical and horizontal shears and strains. In Chapter 6, two existing paradigms of lateral dispersion were examined, vertical shear dispersion, and dispersion by interleaving water-masses. It was shown that these mechanisms can not account for the irreversible small-scale lateral dispersion observed during the CMO dye studies. In Chapter 7, an alternative mechanism of lateral dispersion was proposed, dispersion by the relaxation of mixed layers created by episodes of diapycnal mixing. It was shown that for this mechanism, the scales of mixing observed during the CMO dye studies were the same as the optimal scales for lateral dispersion by this mechanism, and that in at least some cases this mechanism could account for the observed dispersion. The present chapter recapitulates the major results of these analyses and offers a brief discussion of some of implications and outstanding questions raised by this work.

8.1 Analysis of Data from the CMO Dye Studies

The CMO dye experiments were performed over the New England continental shelf during three one- or two-week cruises, the first in September 1995, the second in September 1996, and the third in August 1997. The four experiments examined in this study were performed at mid-depths near the 70 m isobath, and inshore of both the shelf-slope front and the cold pool. A fifth experiment was performed near the bottom boundary layer, and was not discussed.

Environmental conditions for each experiment were assessed using hydrographic data, a shipboard ADCP, and shipboard and moored meteorological sensors. Harmonic analysis of the barotropic currents yielded barotropic tidal amplitudes ranging from 8–14 cm s^{-1}. Mean flows were primarily in the along-shelf direction, and ranged from 11 cm s^{-1} westward during the 1996 experiments to 4 cm s^{-1} eastward during the 1997 experiments. Empirical Orthogonal Function analysis of the ADCP data showed that for all three cruises 70%–85% of the variance in the velocity data was accounted for by the barotropic mode, while 10%–20% was accounted for by the first baroclinic mode, and less than 6% in higher modes. Power spectra of the EOF mode amplitudes showed that the first baroclinic mode was dominated by inertial oscillations during the 1995 cruise, and both tidal and inertial oscillations during the 1996 and 1997 cruises.

In the four experiments analyzed here, the dye injection was performed inshore of the shelf-slope front, typically near the inshore edge of the cold pool. Stratification at mid-depths remained approximately constant during each of the dye experiments, but varied from one experiment to the next. Typical buoyancy frequencies ranged from $N \approx 6 - 18$ cph. In each experiment, dye was injected along a target density surface and then mapped during two to three surveys over a period of 3–5 days. Vertical diffusivities inferred from the dye surveys ranged from 0.1–3.0 $\times 10^{-5}$ m^2 s^{-1}. Three-dimensional sampling surveys showed that significant vertical tilting of the dye patches occurred over the course of each of the experiments. In some cases, horizontal displacements as large as 2–5 km between the shallowest and deepest parts of the dye patch were observed. In addition to tilting vertically, patches also became

elongated horizontally, often at some angle with respect to the zonal or meridional directions. Typically the major horizontal axis of the patch was between two and four times as large as the minor horizontal axis.

In light of this vertical tilting and horizontal elongation of the dye patches, reversible and irreversible components of the lateral dispersion of the dye were defined using a simple model of vertical shear and horizontal strain. Total diffusivities (reversible plus irreversible) estimated from the vertical integral of tracer ranged from $\kappa_\zeta = 2.5$ to 12.7 $m^2\ s^{-1}$. Irreversible diffusivities estimated from the dye along the target density surface were somewhat smaller, and ranged from $\kappa_{irrev} = 0.3$ to 4.9 $m^2\ s^{-1}$. For both the total dispersion and the irreversible dispersion, concomitant estimates of the larger-scale horizontal strain at scales of 1–10 km ranged from $\gamma = 1.9 \times 10^{-6}$ to $4.0 \times 10^{-6}\ s^{-1}$.

8.2 Existing Paradigms of Lateral Dispersion

Using the field data from the CMO dye studies, the role of vertical shear dispersion as a mechanism of lateral dispersion was examined using a linear shear dispersion model. Here upper-bound estimates of the vertical diffusivities inferred from the dye, and of the initial horizontal and vertical patch variances were used to obtain upper-bound estimates of the effective lateral dispersion due to shear dispersion. The model predicts that on time scales of 2.5–5.0 days, mean and oscillatory shear dispersion over the continental shelf were generally comparable in magnitude. Most importantly, however, this analysis showed that shear dispersion alone can *not* account for the irreversible diffusivities observed during the CMO dye studies. Upper-bound predictions for shear dispersion accounted for between 1% and 50% of the observed lateral dispersion, i.e., in some cases, the shear dispersion predictions were more than an order of magnitude smaller than the observed dispersion. The inclusion of a time-dependent vertical diffusivity, as well as the use of level vs. layer shears in this model further strengthened this result. This suggests that some other mechanism was required to contribute additional

horizontal diffusivities of $\kappa_{\text{missing}} \approx 3 - 4$ m^2 s^{-1} for 1995 and 1996 rhodamine dye studies, and $\kappa_{\text{missing}} \approx 0.15 - 0.44$ m^2 s^{-1} for the 1996 fluorescein and the 1997 rhodamine dye studies.

A second mechanism examined as a possible explanation for the observed horizontal dispersion was mixing due to lateral intrusions. Two types of intrusions were considered: interleaving density currents, and diffusive interleaving of different water masses. In the case of interleaving density currents, it was found that the vertical scales of the intrusions were comparable to the vertical scales of the dye patches so that the intrusions' affect on the dye patches was more likely advective rather than diffusive. In the case of diffusive interleaving, scaling arguments showed that intrusions with vertical scales of order $h \approx 10$ m would have had diffusive time scales which were much too long compared to the 3–5 day dye studies. Alternatively, intrusions with vertical scales of order a few meters would also have been ineffective because the resulting diffusivities would have been too small.

8.3 A Proposed Mechanism of Lateral Dispersion

The above analysis suggested that a significant part of the irreversible dispersion observed during the CMO dye studies could not be explained by the existing paradigms of shear dispersion and dispersion by lateral intrusions. In light of these results, an alternative mechanism of lateral dispersion, dispersion by vortical motions caused by the relaxation of episodic mixing events, was proposed which in at least two of the four experiments could account for the observed dispersion.

Dye concentrations observed during the CMO dye studies showed patchiness on vertical scales of 1–10 m and horizontal scales of a few hundred meters to a few kilometers. Observations of potential density from the CMO dye studies as well as microstructure data collected concurrently further showed that mixing occurred episodically in space and time. Based on dissipation rates of both turbulent kinetic energy and temperature variance, and corresponding estimates of the vertical diffusivities of mass and heat, scales of episodic mixing events were

estimated to be 2–10 m in the vertical and a few hundred meters to a few kilometers in the horizontal.

Scaling arguments showed that for episodic mixing, the mean vertical and horizontal diffusivities could be expressed in terms of the vertical scale of the events, h, the horizontal scale, L, the event frequency, ν, and the buoyancy frequency anomaly, ΔN. For a given vertical diffusivity, κ_z, scale analysis applied to the horizontal momentum balance further showed that there exists an optimal scale of mixing events for which a maximum effective horizontal dispersion results. In the CMO dye studies, this maximum diffusivity is predicted to occur for events of horizontal scales comparable to the deformation radius and vertical scales large enough so that events adjust geostrophically. The dye surveys and microstructure data suggest that these optimal scales obtained during the CMO dye studies. The predicted horizontal diffusivity due to vortical motions ranged from $\kappa_H \approx (0.01 \text{ to } 1.1)$ m^2 s^{-1} and was within the range of diffusivities required in the 1996 fluorescein and 1997 rhodamine experiments, $\kappa_{\text{irrev}} = 0.5$ m^2 s^{-1} and 0.3 m^2 s^{-1}, respectively, although it was still somewhat smaller that the observed dispersion in the 1995 and 1996 rhodamine experiments $\kappa_{\text{irrev}} = 4.9$ m^2 s^{-1} and 4.6 m^2 s^{-1}, respectively. Whether the latter discrepancy is due to the predicted diffusivities being a lower-bound, or whether there is yet another mechanism of lateral dispersion at work is unclear.

Beyond this basic scaling, a number of additional factors were also considered. First, based on scaling arguments, the effect of friction on the lateral adjustment of events was small for the parameter range of interest in the CMO dye studies. Second, although mixing events with horizontal scales much larger than the optimal scale were frequently observed, these layers were often tilted with respect to isopycnals. Hence such events would have had effective horizontal scales which were much closer to the optimal scale. Third, for mixing events which are horizontally asymmetric, geostrophic flows along the major axis of the mixed region may be persistent and lead to larger displacements and dispersion than was predicted by the basic scaling. Finally, the relaxation of mixing events may also contribute to lateral dispersion by

vertical shear dispersion, although scaling predicts that this effect will be less than or equal to the effective dispersion due to advective effects.

8.4 Discussion

In summary, Part II of this thesis showed that the lateral dispersion observed during the CMO dye experiments could have been caused by the relaxation of episodic mixing events. However, this mechanism still warrants further investigation for reasons which will now be discussed.

The most compelling evidence for the proposed mechanism of dispersion by the relaxation of diapycnal mixing events is that the microstructure observations of Oakey and Greenan (1998) showed mixing which was episodic in both space and time. That the resulting regions of well-mixed fluid will subsequently adjust laterally has been firmly established by previous investigators both theoretically and in the laboratory (e.g., Gill, 1981; Thomas and Linden, 1996; Griffeths and Hopfinger, 1984; Ivey, 1987). However, the observations from the CMO dye experiments do not provide a definitive test of this process for two reasons. First, the resolution of the dye surveys were often comparable to the scales of the mixing events, so that even if episodic mixing had been the *only* mechanism of lateral dispersion, the patchiness of the dye distributions would not have been well-resolved in either space or time. Instead, individual mixing events were sampled at most once every two days, and only along a single two-dimensional transect during each survey. In addition, it is possible that diffusion due to other processes such as shear dispersion further smoothed out the dye distributions, masking what would otherwise be even more patchy distributions. Second the velocities associated with the relaxation of mixing events could not be measured directly. For the geostrophic adjustment scaling discussed in Section 7.2.3, assuming a buoyancy anomaly of $\Delta N^2 = \frac{1}{2}N^2$ with $N^2 = 10$ cph, a mixing event of vertical scale $2h = 5$ m and horizontal scale of order the deformation radius, $L \approx R$, would result in a geostrophic velocity of approximately 0.03 m s^{-1} (see Equation 7.15). The vertical shear associated with an event of this scale would be of

	κ_z ($\times 10^{-5}$ m^{2}s^{-1})	κ_{irrev} (m^{2}s^{-1})	N (cph)	tide	rms shear (s^{-1})	$\frac{N^2}{\text{shear}^2}$
experiment 1	0 to 1.5	4.9 (2.9 to 7.3)	12	spring→neap	0.014	2.2
experiment 2	1 to 3	4.6 (3.0 to 6.5)	5 to 6	neap→spring	0.006	2.6
experiment 3	0.2 to 0.9	0.5 (0.1 to 1.1)	12	spring→neap	0.010	4.4
experiment 4	0.1 to 0.4	0.3 (0.1 to 0.6)	13 to 18	spring	0.015	3.5

Table 8.1: Overview of vertical and horizontal diffusivities inferred from the CMO dye experiments along with important environmental parameters which may have affected this dispersion.

order $\frac{U}{h} \approx 0.01$ s^{-1}, which is well within the estimated accuracy, 0.002 s^{-1}, for the broad-band ADCP used during the 1996 and 1997 cruises. However, the rms shears associated with the ambient internal wave field are expected to be at least this large and would readily mask this signal (Gargett et al., 1981). One way of avoiding this difficulty might have been to remain on station following a fluid parcel and to average over a time period which is long compared to the typical internal wave period.

It is interesting to note that in the four dye experiments examined in this study the vertical and lateral diffusivities varied by an order of magnitude, despite the fact that all the experiments were performed during similar times of year. The reason for this is not fully understood, although some clues can be found in the environmental forcing. Table 8.1 summarizes the results of each of the experiments along with some of the key environmental parameters: the mean buoyancy frequencies, N, (from Chapter 4), the rms shear (estimated from the least squares fits in Chapter 6), and the spring / neap phase of the tide (inferred from lunar phase over the course of each experiment). Noteworthy is that the vertical diffusivities are roughly correlated with the horizontal diffusivities. This is consistent with the predictions of dispersion by vortical motions as well as vertical shear dispersion. Also of interest is that the vertical diffusivities are not simply correlated with either the buoyancy frequency or the shear. How-

ever, they are roughly correlated with a crude measure of the Richardson number, taken as the mean buoyancy frequency squared divided by the mean shear squared. Whether this correlation holds for more refined estimates of the Richardson number has not been investigated, nor have the the temporal and spatial dependence of the vertical shear been explored in detail. Suffice it to say that the diffusivities do not appear to be correlated with the spring / neap cycle of the tides. Also, little is known about the effect of solitary internal waves which were not resolved in the shipboard ADCP data, but are known to exist over this region of the shelf.

In light of the large variability of vertical and horizontal diffusions rates, and the apparent complexity of the mechanisms responsible for this dispersion, further work on the problem of dispersion in the ocean is needed. A more definitive test of what mechanisms control dispersion over the continental shelf could be made using dye experiments of higher resolution both spatially and temporally. As a test of dispersion by vortical motions, such observations could be used to track localized regions of the dye patch, showing the evolution of individual mixing events from their generation through their horizontal adjustment to their ultimate decay. In addition, quantities such as Ertel potential vorticity could be estimated in order to determine whether significant vortical motions indeed exist and persist on scales which could lead to significant horizontal mixing. The vorticity analysis might follow the approach of Kunze and Sanford (1993) who used the phase difference between relative vorticity and vortex stretching to distinguish vortical motions from internal waves. Initial investigations of such processes and the feasibility of making such observations in the coastal ocean could also be conducted using direct numerical simulations or laboratory experiments. These approaches could be used to address questions like how the relaxation following an isolated mixing event is affected by motions associated with the ambient internal wave field? Such studies would further our understanding of how geostrophic and ageostrophic adjustment occurs in the midst of other oceanic processes and provide additional footing for the ideas proposed in the present work.

Chapter 9

Conclusions

In both the North Atlantic Tracer Release Experiment and the Coastal Mixing and Optics dye studies, it was found that the observed rates of lateral dispersion on scales of order 1–10 km were greater than those predicted by existing theories of lateral dispersion in the ocean. For NATRE, this was shown by Ledwell et al. (1993, 1998). Part I of this thesis verified and refined the method of inference used to obtain this result. In that case, a balance between the convergent mesoscale strain field and the small-scale lateral diffusion gave a value of the small-scale diffusivity which was more than an order of magnitude larger than that predicted for shear dispersion by high frequency internal waves by Young et al. (1982). For the CMO dye studies, lateral dispersion due to vertical shear dispersion was also estimated. Using shears obtained from a shipboard ADCP and upper bounds of the vertical diffusivity inferred from the dye data, it was also found that shear dispersion could not account for the observed lateral dispersion.

In Part II of this thesis, data from the CMO dye experiments suggested a different mechanism of lateral dispersion in the ocean, diffusion by vortical motions caused by the relaxation of diapycnal mixing events. Order-of-magnitude estimates showed that if mixing events adjusted geostrophically, they would lead to an effective lateral dispersion of 0.01–1.1 $m^2\ s^{-1}$. These values were within the range required by the observations for at least two of the four experiments

examined. However, the observations from the CMO dye studies did not provide a definitive test of this mechanism since the actual adjustment process was not directly observable. A few other outstanding questions still remain.

1) How does episodic mixing effect lateral dispersion in the main pycnocline of the open ocean? This is related to the questions addressed in Part I of this thesis. Can the relaxation of episodic mixing events, either as described here or as envisioned by Polzin et al. (1998) account for the forty-fold discrepancy between the diffusivity on scales of 1–10 km estimated by Ledwell et al. (1998) and the predictions for internal wave shear dispersion by Young et al. (1982)? The present study showed that in the optimal case, the relaxation of episodic mixing gives $\kappa_H \approx \left(\frac{3}{2}\right)\left(\frac{N^2}{f^2}\right)\left(\frac{R^2}{L^2}\right)\kappa_z$. Young et al. (1982) predicted $\kappa_H \approx \left(\frac{N^2}{f^2}\right)\kappa_z$ for high-frequency internal waves (note that they also suggested that sub-inertial shears may be important). Even in the optimal case of $\frac{R^2}{L^2} \approx 1$, the present results thus still imply a lateral diffusivity which is much too small compared to the observations. This is a subject of ongoing research.

2) Dispersion by episodic mixing is most effective at high stratification, but what happens for low stratification? Will another mechanism such as shear dispersion take over? What about other time and/or space scales? For example, the scale analysis of Chapter 6 suggests that lateral intrusions may become important for larger time scales. Or, as discussed in Part I, on larger spatial scales, lateral dispersion may be significantly enhanced by shearing and straining due to mesoscale strains. Other mechanisms may also be important at different length and time scales. These include chaotic mixing (e.g., Aref, 1983; Ottino, 1990) and stirring by a random internal wave field (Sanderson and Okubo, 1988). These mechanisms require further study.

In summary, the NATRE and CMO dye studies have shown that the mechanisms or physical processes which govern lateral dispersion in the ocean are anything but well understood. Although the present results are suggestive, a definitive test is still required to determine under what conditions dispersion due vortical motions and the relaxation of isolated mixing events

is important in the ocean. As discussed in Chapter 7, the scales of mixing events and hence predictions of the effective dispersion caused by this mechanism can readily be determined from microstructure observations. Further observational efforts should be aimed at determining whether indeed this mechanism or rather some other mechanism dominates the dispersion. Such efforts should include dye experiments in which the relatively small time and space scales of mixing events and relaxation are well resolved. As suggested by Polzin et al. (1998), comparison of small-scale shear and strain spectra may also be useful for further quantifying the efficiency of mixing by this mechanism. Process studies using numerical simulations may also aid in these efforts.

References

Aref, H., 1983. Integrable, chaotic, and turbulent vortex motion in two-dimensional flows. *Ann. Rev. Fluid Mech.*, **15**, 345–389.

Babiano, A., C. Basdevant, and R. Sadourny, 1985. Structure functions and dispersion laws in two-dimensional turbulence. *J. Atmos. Sci.*, **42**, 941–949.

Babiano, A., C. Basdevant, B. Legras, and R. Sadourny, 1987. Vorticity and passive-scalar dynamics in two-dimensional turbulence. *J. Fluid Mech.*, **183**, 379–397.

Basdevant, C., B. Legras, R. Sadourny, and M. Béland, 1981. A study of barotropic model flows: intermittency, waves and predictability. *J. Atmos. Sci.*, **38**, 2305–2326.

Batchelor, G. K., 1950. The application of the similarity theory of turbulence to atmospheric diffusion. *Quart. J. Roy. Met. Soc.*, **76**, 133–146.

Beardsley, R. C., D. C. Chapman, K. H. Brink, S. R. Ramp, and R. Schlitz, 1985. The Nantucket Shoals Flux Experiment (NSFE79). Part I: A basic description of the current and temperature variability. *J. Phys. Oceanogr.*, **15**, 713–748.

Bennett, A. F., 1987. A Lagrangian analysis of turbulent diffusion. *Rev. Geophys.*, **25**, 799–822.

Bennett, A. F. and D. B. Haidvogel, 1983. Low-resolution numerical simulation of decaying two-dimensional turbulence. *J. Atmos. Sci.*, **40**, 738–748.

Bowden, K. F., 1965. Horizontal mixing in the sea due to a shearing current. *J. Fluid Mech.*, **21**, 83–95.

Bretherton, F. P., R. E. Davis, and C. B. Fandry, 1976. A technique for objective analysis and design of oceaographic experiments applied to MODE-73. *Deep Sea Res.*, **23**, 559–582.

Brown, W. S., N. R. Pettigrew, and J. D. Irish, 1985. The Nantucket Shoals Flux Experiment (NSFE79). Part II: The structure and variability of across-shelf pressure gradients. *J. Phys. Oceanogr.*, **15**, 749–771.

Browning, K. A. and C. D. Watkins, 1970. Observations of clear air turbulence. *Nature*, **227**, 260–263.

Candela, J., R. C. Beardsley, and R. Limeburner, 1992. Separation of tidal and subtidal current in ship-mounted acoustic doppler current profiler observations. *J. Geophys. Res.*, **97**, 769–788.

Canuto, C., M. Y. Hussaini, A. Quarteroni, and T. A. Zang, 1988. *Spectral Methods in Fluid Dynamics*. Springer-Verlag, New York.

Chapman, D. C., 1986. A simple model of the formation and maintenance of the shelf/slope front in the Middle Atlantic Bight. *J. Phys. Oceanogr.*, **16**, 1273–1279.

Chapman, D. C. and R. C. Beardsley, 1989. On the origin of shelf water in the Middle Atlantic Bight. *J. Phys. Oceanogr.*, **19**, 384–391.

Chapman, D. C. and S. J. Lentz, 1994. Trapping of a coastal density front by the bottom boundary layer. *J. Phys. Oceanogr.*, **24**, 1464–1479.

Chapman, D. C., J. A. Barth, R. C. Beardsley, and R. G. Fairbanks, 1986. On the continuity of the mean flow between the Scotian Shelf and the Middle Atlantic Bight. *J. Phys. Oceanogr.*, **16**, 758–772.

Chatwin, P. C., 1975. On the longitudinal dispersion of passive contaminant in oscillatory flows in tubes. *J. Fluid Mech.*, **71**, 513–527.

Colin de Verdiere, A., 1983. Lagrangian eddy statistics from surface drifters in the eastern North Atlantic. *J. Mar. Res.*, **41**, 375–398.

Csanady, G. T., 1966. Accelerated diffusion in the skewed shear flow of lake currents. *J. Geophys. Res.*, **71**, 411–420.

Davis, R. E., 1983. Oceanic property transport, Lagrangian particle statistics, and their prediction. *J. Mar. Res.*, **41**, 163–194.

Davis, R. E., 1985. Drifter observations of coastal surface currents during CODE: The statistical and dynamical views. *J. Geophys. Res.*, **90**, 4756–4772.

Davis, R. E., 1987. Modeling eddy transport of passive tracers. *J. Mar. Res.*, **45**, 635–666.

Eckart, C., 1948. An analysis of the stirring and mixing processes in incompressible fluids. *J. Mar. Res.*, **7**, 265–275.

Elder, J. W., 1959. The dispersion of marked fluid in turbulent shear flow. *J. Fluid Mech.*, **5**, 544–560.

Ewart, T. E. and W. P. Bendiner, 1981. An observation of the horizontal and vertical diffusion of a passive tracer in the deep ocean. *J. Geophys. Res.*, **86**, 10,974–10,982.

Fischer, H. B., E. J. List, R. C. Y. Koh, J. Imberger, and N. H. Brooks, 1979. *Mixing in Inland and Coastal Waters.* Academic Press, San Diego, Calif.

Freeland, H. J., P. B. Rhines, and T. Rossby, 1975. Statistical observations of the trajectories of neutrally buoyant floats in the North Atlantic. *J. Mar. Sci.*, **33**, 383–404.

Gargett, A. E., P. J. Hendricks, T. B. Sanford, T. R. Osborn, and A. J. Williams III, 1981. A composite spectrum of vertical shear in the upper ocean. *J. Phys. Oceanogr.*, **11**, 1258–1271.

Garrett, C., 1983. On the initial streakiness of a dispersing tracer in two- and three-dimensional turbulence. *Dyn. Atmos. Oceans*, **7**, 265–277.

Garrett, C. and W. Munk, 1972. Oceanic mixing by breaking internal waves. *Deep-Sea Res.*, **19**, 823–832.

Geyer, W. R. and J. R. Ledwell, 1995. Sea Grant Completion Report R/O-17, Vertical Mixing Processed in Massachusetts Bay, 13 pp.

Geyer, W. R. and J. R. Ledwell, 1997. Sea Grant Completion Report R/O-24, Boundary Mixing in Massachusetts Bay, 21 pp.

Gill, A. E., 1981. Homogeneous intrusions in a rotating stratified fluid. *J. Fluid Mech.*, **103**, 275–295.

Grant, H. L., A. Moilliet, and W. M. Vogel, 1968. Some observations of the occurrence of turbulence in and above the thermocline. *J. Fluid Mech.*, **34**, 443–448.

Griffiths, R. W. and E. J. Hopfinger, 1984. The structure of mesoscale turbulence and horizontal spreading at ocean fronts. *Deep Sea Res.*, **31**, 245–269.

Haidvogel, D. B. and I. M. Held, 1981. Homogeneous quasi-geostrophic turbulence driven by a uniform temperature gradient. *J. Atmos. Sci.*, **37**, 2644–2660.

Haidvogel, D. B. and T. Keffer, 1984. Tracer dispersal by mid-ocean mesoscale eddies. Part I. Ensemble Statistics. *Dyn. Atmos. and Oceans*, **8**, 1–40.

Halliwell, G. R. and C. N. K. Mooers, 1979. The space-time structure and variability of the shelf water-slope water and Gulf Stream surface temperature fronts and associated warm-core eddies. *J. Geophys. Res.*, **83**, 1366–1372.

Holloway, G. and S. S. Kristmannsson, 1984. Stirring and transport of tracer fields by geostrophic turbulence. *J. Fluid Mech.*, **141**, 27–50.

Horne, E. P. W., 1978. Interleaveing at the subsurface front in the slope water off Nova Scotia. *J. Geophys. Res.*, **83**, 3659–3671.

Houghton, R. W., 1997. Lagrangian flow at the foot of a shelfbreak front using a dye tracer injected into the bottom boundary layer. *Geophys. Res. Lett.*, **24**, 2035–2038.

Houghton, R. W., R. Schlitz, R. C. Beardsley, B. Butman, and J. L. Chamberlin, 1982. The Middle Atlantic Bight cold pool: evolution of the temperature structure during summer 1979. *J. Phys. Oceanogr.*, **12**, 1019–1029.

Houghton, R. W., F. Aikman III, and H.W. Ou, 1988. Shelf-slope frontal structure and cross-shelf exchange at the New England shelf-break. *Cont. Shelf Res.*, **8**, 687–710.

Ivey, G. N., 1987. Boundary mixing in a rotating, stratified fluid. *J. Fluid Mech.*, **183**, 25–44.

Journel, A. G. and Ch. J. Huijbregts, 1978. *Mining geostatistics.* Academic Press, New York.

Kolmogorov, A. N., 1941. The local structure of turbulence in incompressible viscous fluid for very large Reynolds' numbers. *Comptes Rendus Acad. Sci. U.S.S.R.*, **30**, 301–305.

Kullenberg, G., 1971. Vertical diffusion in shallow waters. *Tellus*, **23**, 129–135.

Kullenberg, G., 1972. Apparent horizontal diffusion in stratified vertical shear flow. *Tellus*, **24**, 17–28.

Kunze, E. and T. B. Sanford, 1993. Submesoscale dynamics near a seamount. Part I: Measurements of Ertel Vorticity. *J. Phys. Oceanogr.*, **23**, 2567–2588.

Ledwell, J. R., A. J. Watson, and C. S. Law, 1993. Evidence for slow mixing across the pycnocline from an open-ocean tracer-release experiment. *Nature*, **364**, 701–703.

Ledwell, J. R., A. J. Watson, and C. S. Law, 1998. Mixing of a tracer released in the pycnocline. *J. Geophys. Res.* In press.

Lin, J. T. and Y. H. Pao, 79. Wakes in stratified fluids. *Ann. Rev. Fluid Mech.*, **11**, 317–338.

Linder, C. A., 1996. A climatology of the Middle Atlantic Bight Shelfbreak Front. Masters, Massachusetts Institute of Technology, Cambridge, MA, and Woods Hole Oceanographic Institution, Woods Hole, MA, Joint Program.

Linder, C. A. and G. Gawarkiewicz, 1998. A climatology of the shelfbreak front in the Middle Atlantic Bight. *J. Geophys. Res.* In press.

M., J. T., 1977. A note on the lateral mixing of water masses. *J. Phys. Oceanogr.*, **7**, 626–629.

Maltrud, M. E. and G. K. Vallis, 1991. Energy spectra and coherent structures in forced two-dimensional and beta-plane turbulence. *J. Fluid Mech.*, **228**, 321–342.

McWilliams, J. C., 1990. The vortices of two-dimensional turbulence. *J. Fluid Mech.*, **219**, 361–385.

Moody, J. A., B. Butman, R. C. Beardsley, W. S. Brown, P. Daifuku, J. D. Irish, D. A. Mayer, H. O. Mofjeld, B Petrie, S. Ramp, P. Smith, and W. R. Wright, 1984. Atlas of tidal elevation and current observations on the northeast American Continental Shelf and Slope. U. S. Geol. Surv. Bull. 1611, 122 pp.

Oakey, N. S., 1988. Estimates of mixing inferred from temperature and velocity microstructure. In Nihoul, J. C. J. and B. M. Jamart, editors, *Small-scale Turbulence and Mixing in the Ocean, Proceedings of the 19th international Liege colloquium on ocean hydrodynamics*, volume 46 of *Elsevier Oceanography Series.*

Oakey, N. S. and B. J. W Greenan, 1998. Mixing in a coastal environment: A view from microstructure measurements. In *EOS Transactions, American Geophysical Union, 1998 Ocean Sciences Meeting*, volume 79.

Okubo, A., 1971. Oceanic diffusion diagrams. *Deep Sea Res.*, **18**, 789–802.

Osborn, T. R., 1980. Estimates fo the local rate of vertical diffusion from dissipation measurements. *J. Phys. Oceanogr.*, **10**, 83–89.

Ottino, J. M., 1990. Mixing, chaotic advection, and turbulence. *Ann. Rev. Fluid Mech.*, **22**, 207–253.

Pedlosky, J., 1979. *Geophysical Fluid Dynamics.* Springer-Verlag, New York.

Phillips, O. M., 1966. *Dynamics of the upper ocean.* Cambridge University Press, 1 edition.

Polzin, K. L., E. Kunze, J. M. Toole, and R. W. Schmitt, 1998. The partition of small-scale energy into internal waves and geostrophic motions. In preparation.

Pope, S. B., 1990. Lagrangian microscales in turbulence. *Phil. Trans. R. Soc. Lond. A*, **333**, 309–319.

Press, W. H., S. A. Teukolsky, W. T. Vetterling, and B. P. Flannery, 1986. *Numerical Recipes.* Cambridge University Press, New York, N.Y.

Rhines, P. B., 1977. The dynamics of unsteady currents. In Goldberg, E. D., I. N. McCane, J. J. O'Brien, and J. H. Steele, editors, *The Sea*, volume 6, chapter 7, pages 189–318. Wiley, New York.

Richardson, L. F., 1926. Atmospheric diffusion shown on a distance-neighbour graph. *Proc. Roy. Soc., London, A*, **110**, 709–737.

Richardson, L. F. and H. Stommel, 1948. Note on eddy diffusion in the sea. *J. Meteor.*, **5**, 238–240.

Ruddick, B. R. and D. Hebert, 1988. The mixing of meddy "Sharon". In Nihoul, J. C. J. and B. M. Jamart, editors, *Small-scale Turbulence and Mixing in the Ocean, Proceedings of the 19th international Liege colloquium on ocean hydrodynamics*, volume 46 of *Elsevier Oceanography Series.*

Ruddick, B. R. and J. S. Turner, 1979. The vertical length scale of double-diffusive intrusions. *Deep-Sea Res.*, **26A**, 903–913.

Saffman, P. G., 1962. The effect of wind shear on horizontal spread from an instantaneous ground source. *Quart. J. Roy. Met. Soc.*, **88**, 382–393.

Sanderson, B. G. and A. Okubo, 1988. Diffusion by internal waves. *J. Geophys. Res.*, **93**, 3570–3582.

Smith, R., 1982. Dispersion of tracers in the deep ocean. *J. Fluid Mech.*, **123**, 131–142.

Stern, M. E., 1967. Lateral mixing of water masses. *Deep-Sea Res.*, **14**, 747–753.

Stommel, H., 1949. Horizontal diffusion due to oceanic turbulence. *J. Mar. Res.*, **8**, 199–255.

Stommel, H. and K. N. Fedorov, 1967. Small scale structure in the temperature and salinity near Timor and Mindanao. *Tellus*, **19**, 306–325.

Sundermeyer, M. A., 1995. Mixing in the North Atlantic Tracer Release Experiment: Observations and Numerical Simulations of Lagrangian Particles and Passive Tracer. Master's thesis, MIT, Cambridge, MA / WHOI, Woods Hole, MA, Joint Program in Physical Oceanography.

Sundermeyer, M. A. and J. F. Price, 1998. Lateral mixing and the North Atlantic Tracer Release Experiment: Observations and numerical simulations of Lagrangian particles and a passive tracer. *J. Geophys. Res.* In press.

Taylor, G. I., 1921. Diffusion by continuous movements. *Proc. Lond. Math. Soc. A*, **20**, 196–212.

Taylor, G. I., 1953. Dispersion of soluble matter in solvent flowing slowly through a tube. *Proc. Roy. Soc. London*, **A219**, 186–203.

Thomas, P. J. and P. F. Linden, 1996. A laboratory simulations of mixing across tidal fronts. *J. Fluid Mech.*, **309**, 321–344.

Thorpe, S. A., 1971. Experiments on the instability of stratified shear flows: miscible fluids. *J. Fluid Mech.*, **46**, 299–319.

Toole, J. M. and D. T. Georgi, 1981. On the dynamics and effects of double-diffusively driven intrusions. *Prog. Oceanog.*, **10**, 123–145.

Townsend, A. A., 1951. The diffusion of heat spots in isotropic turbulence. *Proc. R. Soc. London*, **Ser. A, 209**, 418–430.

Trask, R. P. and N. J. Brink, 1993. Cruise report R/V Oceanus cruise # 240, leg 3. Subduction 1 Mooring Deployment Cruise, 17 June – 5 July, 1991. WHOI Technical Report 93-12, Woods Hole Oceanographic Inst., Woods Hole, Mass.

Vasholz, D. P. and L. J. Crawford, 1985. Dye dispersion in the seasonal thermocline. *J. Phys. Oceanogr.*, **15**, 695–711.

Voorhis, A. D., D. C. Webb, and R. C. Millard, 1976. Current structure and mixing in the shelf/slope water front south of New England. *J. Geophys. Res.*, **81**, 3695–3708.

Wanninkhof, R., G. Hitchcock, W. J. Wiseman, G. Vargo, P. B. Ortner, W. Asher, D. T. Ho, P. Schlosser, M. Dickson, R. Masserini, K. Fanning, and J. Zhang, 1997. Gas ex-

change, dispersion , and biological productivity on teh west Florida shelf: Results from a Lagrangian tracer study. *Geophys. Res. Lett.*, **24**, 1767–1770.

Woods, J. D., 1968. Wave-induced shear instability in the summer thermocline. *J. Fluid Mech.*, **32**, 791–800.

Woods, J. D. and R. L. Wiley, 1972. Billow turbulence and ocean microstructure. *Deep-Sea Res.*, **19**, 87–121.

Wright, W. R., 1976. Nantucket Shoals Flux Experiment data report I. Hydrography. NOAA Technichal Memorandum NMFS-F/NEC-23, National Marine Fisheries Service, Woods Hole, MA. 105 pp.

Young, W. R., P. B. Rhines, and C. J. R. Garrett, 1982. Shear-flow dispersion, internal waves and horizontal mixing in the ocean. *J. Phys. Oceanogr.*, **12**, 515–527.